TOWARDS A HIGH-PERFORMANCE COMPUTING FINITE ELEMENT SIMULATION FRAMEWORK FOR VIRTUAL TESTING OF COMPOSITE STRUCTURES

Adrià Quintanas Corominas

Doctoral Thesis

Towards a High-Performance Computing Finite Element Simulation Framework for Virtual Testing of Composite Structures

Adrià Quintanas Corominas

2019

Advisors:

Dr. Albert Turon Travessa
Universitat de Girona
Girona, Spain

Dr. Eva Casoni Rero
Barcelona Supercomputing Center
Barcelona, Spain

Dr. Jose Reinoso Cuevas
Universidad de Sevilla
Sevilla, Spain

This manuscript is submitted in partial fulfillment of the requirements for the degree of Doctor of Philosophy by the Universitat de Girona

Adrià Quintanas Corominas

Towards a High-Performance Computing Finite Element Simulation Framework for Virtual Testing of Composite Structures

Doctoral Thesis, 2019

Doctoral Program in Technology

Advisors: Dr. Albert Turon Travessa Dr. Eva Casoni Rero and Dr. Jose Reinoso Cuevas

Universitat de Girona

AMADE Research Group

Escola Politècnica Superior

Dept. d'Enginyeria Mecànica i de la Construcció Industrial

Carrer Universitat de Girona, 4. Campus de Montilivi

17003 Girona

A tots aquells apassionat del que fan.

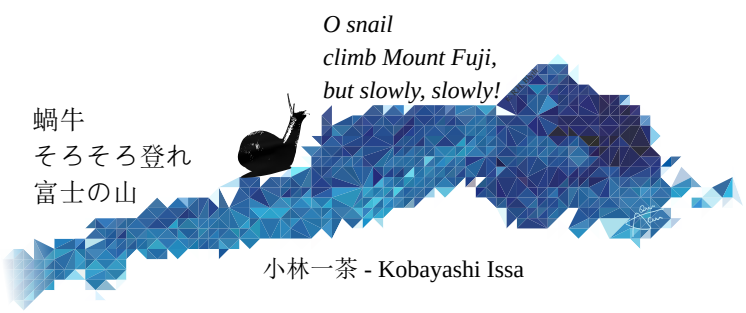

蝸牛
そろそろ登れ
富士の山

O snail
climb Mount Fuji,
but slowly, slowly!

小林一茶 - Kobayashi Issa

Agraïments

First of all, I would like to express my sincere gratitude to my advisors, Albert Turon, Eva Casoni and Jose Reinoso, for not only encouraging my research but also for their infinite patience. Their pieces of advice have helped me in the learning path of becoming a researcher. Although now is not advisor of my thesis, these words of gratitude also are for Joan Andreu Mayugo, who also helped me a lot during these years.

Beyond my advisors, I thank the members, technicians and researches of AMADE, for bringing me their support and the opportunity to learn from them. In the same vein, I would also like to thank the people of the CASE department in the BSC, especially the fathers of Alya, Mariano Vázquez and Guillaume Houzeaux.

My gratitude also is for Professor Marco Paggi, from the IMT School of Advanced Studies Lucca in Italy, for the opportunity of doing a research stay there. I also extend this gratitude to all the students who made more pleasant my stay in Lucca: Sara, Annalisa, Beyza, Matteo (future novel price), Dimitris, Matteo (the president), Emiliano, Jacopo, Maria Rosaria, among others. Without them, it would have been harsher.

Canviant a un idioma més familiar i proper, vull donar les gràcies a tots aquells que han compartit aquest llarg camí amb mi. En especial, vull agrair als companys de ruta d'AMADE per els seus valors, les seves idees i les paraules d'ànims. Tant els que hem compartit día rere día durant els últims anys: en Jordi, l'Aravind, en Javi, en Sergio, en Santi, en Jose i en Rodrigo; com els que s'han incorporat o marxat recentment: la Laura, la Magda, l'Adrián, en Yi, en Juan Jose, l'Annie i en Younes. En aquest mateix sentit, vull donar agrair l'ajuda brindada des de Barcelona per en Gerard i en Matías. A part de tots aquests companys i amics de feina, aquest llarg camí ha estat en certa manera compartit per els meus amics de Via Lúdica, els del local de Figueres i la família d'Alma Cubrae. A tots ells vull donar-los les gràcies per la seva paciència estoica per afrontar el meu anàlisis-paràlisis, així com les meves interpretacions excèntriques. Per últim, haig de donar les gràcies aquells amics que, tot i veure'ns poc, sé que, quan l'ocasió ho permet, hi són per poder comentar la ruta a seguir: en Jordi, la Clara, en Pau, en Carles, en Jaco i la Núria.

Amb un to més íntim, vull donar les gràcies pel suport àcid, dosis de realitat i relativisme forçat als meus amics: l'Albert, en Xavi i en Joan. Continuant amb aquest to més íntim, vull expressar un profund agraïment al suport, comprensió i infinita paciència que ha demostrat

tenir la meva estimada Anna. Sense ella, aquest llarg camí moltes vegades convertit en muntanya russa emocional, hagués estat encara més feixuc. Per tots ells, no només hi ha aquestes breus paraules d'agraïment, sinó també un profund sentiment d'estima i admiració. Per acabar aquest grupet íntim, i encara que algú li pugui semblar estrany, vull donar les gracies a la Haru, qui m'ha tret a passejar cada dia des de que vaig tornar d'Itàlia.

Per anar finalitzant aquestes paraules, vull destacar i donar les gràcies al paper jugat per part de la meva família. Gràcies al seu suport incondicional el llarg camí que ha suposat, aquesta etapa ha arribat a bon port, i a més sense perdre el cap. Especialment, vull agrair al meu pare Josep Maria, la meva mare Maria Gracia, al meu germà Albert, l'avi Joan i la iaia Flora, per haver-me ensenyat i transmès la capacitat de lluita i sacrifici, però també d'estima pel que un fa.

A tothom que he anomenat en aquestes paraules d'agraïment, i els que m'he descuidat, vull remarcar-los que sense ells no hagués arribat al punt de poder escriure aquesta tesis. Tots ells m'han ajudat a avançar i fer un pas endavant per poder arribar al final del camí, posant punt i final a aquesta etapa d'aprenentatge. És per això que ...

Thank you! Grazie mille! Muchas gracias! Moltes gràcies!

Preface

The work contained in this thesis was conducted mainly in the AMADE research group (Department of Mechanical Engineering and Industrial Construction, Universitat de Girona, Spain) in collaboration with the CASE department (Barcelona Supercomputing Center, Barcelona, Spain) and GESM (Department of Continuum Mechanics, Universidad de Seville, Spain). The thesis was carried out under the grant FPU15/06287 of the *Formación de Profesorado Universitario (FPU)* program from the *Ministerio de Ciencia, Innovación y Universidades* of the *Gobierno de España*.

Part of the research presented in this thesis was developed during the candidate stay at the IMT School for Advanced Studies Lucca (Lucca, Italy), which was supervised by the Prof. Marco Paggi and partially funded by the AMADE research group.

Declaration

Universitat de Girona

Dr. Albert Turon Travesa, Associate Professor at Universitat de Girona, Dr. José Reinoso Cuevas, Associate Professor at Universidad de Sevilla, and Dr. Eva Casoni Rero, Established Researcher at Barcelona Supercomputing Center,

hereby CERTIFY that:

The work entitled *Towards a High-Performance Computing Finite Element Simulation Framework for Virtual Testing of Composite Structures*, submitted for the degree of Doctor of Philosophy by Adrià Quintanas Corominas, has been conducted under our supervision and fulfills the requirements for the mention of *International Doctorate*.

Dr. Albert Turon Travessa
Universitat de Girona
Girona, Spain

Dr. Eva Casoni Rero
Barcelona Supercomputing Center
Barcelona, Spain

Dr. Jose Reinoso Cuevas
Universidad de Sevilla
Sevilla, Spain

Girona, June 18, 2019

List of Publications

The present thesis is as a compendium of peer-reviewed scientific papers in accordance with the regulations of the Universitat de Girona to obtain the degree of Doctor in Philosophy. Parts of these papers are used directly or indirectly through this document. As part of the assessment, co-authors statements have been made available to the assessment committee and are also available at the Escola de Doctorat of the Universitat de Girona.

The scientific papers supporting the main body of the present thesis are the following:

Paper A

Quintanas-Corominas, A., P. Maimí, E. Casoni, A. Turon, J.A. Mayugo, G. Guillamet, and M. Vázquez (2018). *A 3D transversally isotropic constitutive model for advanced composites implemented in a high performance computing code*. In: *European Journal of Mechanics - A/Solids* 71, pp. 278–291 (ISSN: 0997-7538)

Published

Impact factors according to the 2017 Journal Citation Reports: 2.881, ranked 17/134 in category *Mechanics* (1st quartile)

Paper B

Quintanas-Corominas, A., J. Reinoso, E. Casoni, A. Turon, and J.A. Mayugo (2019a). *A phase field approach to simulate intralaminar and translaminar fracture in long fiber composite m aterials*. I n: *Composite Structures* 220, pp. 899–911 (ISSN: 0263-8223)

Published

Impact factors according to the 2017 Journal Citation Reports: 4.101, ranked 5/26 in category *Materials Science, Composites* (1st quartile)

Paper C

Quintanas-Corominas, A., J. Reinoso, E. Casoni, A. Turon, M. Paggi, and J.A. Mayugo (2019b). *A phase field approach enhanced with a cohesive zone model for modelling delamination induced by matrix cracking*. In: *Computer Methods in Applied Mechanics and Engineering* (ISSN: 0045-7825)

Published

Impact factors according to the 2017 Journal Citation Reports: 4.441, ranked 5/86 in category *Engineering, Multidisciplinary* (1st quartile), ranked 7/134 in category *Mechanics* (1st quartile), and ranked 2/103 in category *Mathematics, Interdisciplinary applications* (1st quartile)

List of Figures

List of Tables

Contents

Abstract

In many industrial applications, and especially in the automotive and aeronautical sectors, Virtual Testing (VT) of composite structures is foreseen as one of the strategies aimed at reducing the number of tests required to certificate new components. Conceptually, VT consists of the simulation of experimental tests through reliable numerical methods. By this strategy, it is intended to minimise the monetary and temporal costs associated with the certification and design processes and, at the same time, acquire a deeper level of understanding about the mechanical behaviour of composite structures. Thus, the VT ranges simulation from coupon level to subcomponent and component levels.

One of the most used numerical methods to built frameworks for VT of composite structures is the Finite Element Method (FEM). In part, this is because this method provides a versatile framework with reliable predictions in comparison with alternative modelling methods. Although these qualities, the VT of composite materials is a complex nonlinear numerical problem. The different damage mechanisms arising during the failure process increase the complexity of the models involved during the simulation. Moreover, the length scale concerning the damage phenomena imposes the use of thin meshes and refined time discretisation. These facts increase the computational costs of the simulations. Therefore, the VT of composite structures has usually an enormous computational cost, which, if not appropriately managed, can even preclude the simulation.

This doctoral thesis aims at developing and implementing a computational framework for Virtual Testing of Composite Structures in a High-Performance Computing (HPC) environment. By this objective is pretended to overcome the limitation regarding the management of the computational costs. In this sense, this thesis presents different constitutive models, which are based on the continuum damage mechanics theory, and their implementation in a HPC-base FE simulation code named Alya. Regarding the intralaminar region, two models are developed and implemented to capture the onset and progression of the damage on the mesoscopic length scale: (i) a local damage model and (ii) a nonlocal damage model rooted in the phase field approach. In turn, the damage occurring in the intralaminar region is modelled employing a cohesive zone model available in the literature in conjunction with an interface element technology. Finally, a novel formulation is presented, which couples the nonlocal intralaminar model with the cohesive zone model formulation. As an outcome of this thesis, it is presented a novel and complete numerical framework to simulate intralaminar and interlaminar damage of composite structures, implemented in the Alya.

The verification and validation of the models are performed comparing the numerical predictions with analytical and experimental data. The comparisons demonstrate not only the reliability of models but also the potential of the usage an HPC-based FE simulation code such, as Alya, for VT of composite structures.

Resumen

La realización de pruebas virtuales (VT, de las siglas en inglés de *Virtual Testing*) de estructuras de materiales compuestos se ve como una de las posibles estrategias para reducir el número de ensayos experimentales requeridos en la certificación de nuevos componentes en aplicaciones industriales, especialmente en los sectores automotriz y aeronáutico. Conceptualmente, el VT consiste en la simulación de pruebas experimentales mediante métodos numéricos, buscando minimizar los costos monetarios y temporales asociados con los procesos de certificación y diseño, al mismo tiempo que se adquiere un nivel de comprensión más profundo del comportamiento mecánico de las estructuras hechas de materiales compuestos. En este sentido, el VT abarca desde la simulación de pequeñas probetas hasta componentes estructurales.

Uno de los métodos numéricos más utilizados para crear marcos numéricos para el VT de estructuras en compuestos es el Método de los Elementos Finitos (FEM, de las siglas en inglés de *Finite Element Method*). En parte, esto se debe a que, en comparación con métodos alternativos de modelado, éste ofrece un alto grado de versatilidad y precisión. Sin embargo, a pesar de estas cualidades, el VT de materiales compuestos mediante FEM es un problema numérico complejo altamente no lineal. Los diferentes mecanismos de daño que surgen durante el proceso de falla aumentan la complejidad de los modelos involucrados durante la simulación. Además, la escala de longitud relativa a los fenómenos de daño impone el uso de mallas finas y la necesidad de una discretización temporal muy refinada. Estos hechos se traducen en un aumento significativo de los costos computacionales de las simulaciones que, si no se administran adecuadamente, pueden incluso impedir la ejecución de la simulación.

El objetivo de esta tesis doctoral es desarrollar e implementar un marco computacional para pruebas virtuales de estructuras en compuestos en un entorno de computación de alto rendimiento (HPC, de las siglas en inglés de *High-Performance Computing*). Con el uso de un entorno HPC se pretende superar la limitación respecto a la gestión de los costos computacionales. En este sentido, esta tesis presenta la formulación de diferentes modelos constitutivos basados en la teoría de la mecánica de daños continuos, así como su implementación en el código de simulación HPC denominado Alya. Con respecto a la región dentro de la capa (zona intralaminar), se proponen dos nuevos modelos que capturan el inicio y la progresión del daño en la escala de longitud mesoscópica: (i) un modelo de daño local y (ii) un modelo de daño no local arraigado en el enfoque de campo de fase. A su vez, el daño que se produce en la interfaz entre capas (zona interlaminar) se predice empleando un

modelo de zona cohesiva disponible en la literatura, junto con una tecnología de elementos de interfaz. Finalmente, se presenta una nueva formulación que combina el modelo no local para el daño intralaminar con la formulación del modelo de zona cohesiva para el daño interlaminar. Por lo tanto, en esta tesis se desarrolla un marco numérico nuevo y completo para simular el daño intralaminar e interlaminar de estructuras en materiales compuestos, implementado en el código de simulación HPC Alya.

La verificación y validación de los modelos se realiza comparando las predicciones numéricas con los datos analíticos y experimentales. La comparación demuestra tanto la fiabilidad de los modelos formulados, como el potencial de usar el código de elementos finitos de alto rendimiento computacional, Alya.

Resum

En moltes aplicacions industrials, especialment en el sector de l'automoció i l'aeronàutic, es preveu que la realització de proves virtuals (VT, de les sigles en anglès de *Virutal Testing*) d'estructures de materials compòsits sigui una peça clau per a reduir el nombre d'assajos experimentals necessaris per a la certificació de nous components. Conceptualment, el VT consisteix en la simulació de proves experimentals mitjançant mètodes numèrics fiables. Amb aquestes simulacions es pretén minimitzar els costos monetaris i temporals associats als processos de certificació i disseny i, alhora, adquirir un nivell de comprensió més profund sobre el comportament mecànic de les estructures. En aquest sentit, el VT inclou simulacions que van des de provetes fins a components estructurals.

Un dels mètodes numèrics més utilitzats per crear marcs numèrics per el VT d'estructures de materials compòsits és el mètode dels elements finits (FEM, de les sigles en anglès de *Finite Element Method*). Aquest fet es deu en part a que aquest mètode proporciona, en comparació amb mètodes de modelització alternatius, un marc versàtil amb prediccions numèriques fiables. Tot i les qualitats d'aquest mètode, el VT de materials compostos mitjançant FEM és un problema numèric no lineal molt complex. Per una banda, els mecanismes de dany que poden iniciar i créixer durant el procés de fallada augmenten la complexitat dels models constitutius implicats durant la simulació. A més, l'escala de longitud relativa als fenòmens de dany imposa l'ús de malles fines i d'una aproximació temporal molt fina. Aquests fets augmenten els costos computacionals de les simulacions. Per tant, el VT d'estructures de compòsits sol tenir associat un enorme cost computacional, que si no es gestiona adequadament, pot arribar a impedir la realització de la simulació.

Aquesta tesi doctoral té com a objectiu desenvolupar i implementar un marc computacional per a la realització de proves virtuals d'estructures de materials compòsits en un entorn de computació d'alt rendiment (HPC, de les sigles en anglès de *High Performance Computing*). Amb aquest objectiu es pretén superar la limitació quant a la gestió dels costos computacionals. En aquest sentit, aquesta tesi presenta la formulació diversos models constitutius emmarcats dintre la teoria de la mecànica de danys continus així com la seva implementació en el codi de simulació HPC anomenat Alya. La regió dintre la làmina (zona intralminar), es proposen dos models per capturar l'inici i la progressió del dany a l'escala de longitud mesoscòpica: (i) un model de dany local i (ii) un model de dany no local basat en l'enfocament del camp de fase. Pel que fa a la interfície entre dues làmines (zona interlaminar), el dany es prediu emprant un model de zona cohesiva conjuntament amb la

tecnologia d'elements d'interfície. Finalment, aprofitant el caràcter no local del segon model de dany intralminar es proposa una nova estratègia que te en compte l'acoblament entre el dany d'ambdues zones, l'intralminar i l'interlaminar. Per tant, en aquesta tesi es desenvolupa un nou marc numèric complet per a la simulació del dany intralaminar i interlaminar en estructures de material compòsit en un entorn de computació d'alt rendiment mitjançant el codi Alya.

La verificació i validació dels models es realitza comparant les prediccions numèriques amb dades analítiques i experimentals. La comparació demostra la fiabilitat dels models així com el potencial d'utilitzar un codi d'element finit d'elements finits d'alt rendiment computacional.

Part I

Introduction and Methodology

1 Introduction

1.1 Contextual background and motivation

The rise of usage of Fibre-Reinforced Polymer (FRP) composites for structural applications has increased over the last decades, especially in the aerospace, automotive, and wind turbine industries. This increase can be partially explained by their excellent stiffness-to-weight and strength-to-weight ratio in comparison with traditional materials, such as steel and titanium (Barbero 2017). However, the real potential of FRP structures in terms of load-bearing capacities has not fully exploited so far. The difficulty of predicting how damage mechanisms develop up to structural failure, enforce engineers to use high design safety factors and to plan extensive certification campaigns. The outcome is an increase in the costs associated with the design and development processes, making the FRP structures less attractive for some industrial applications.

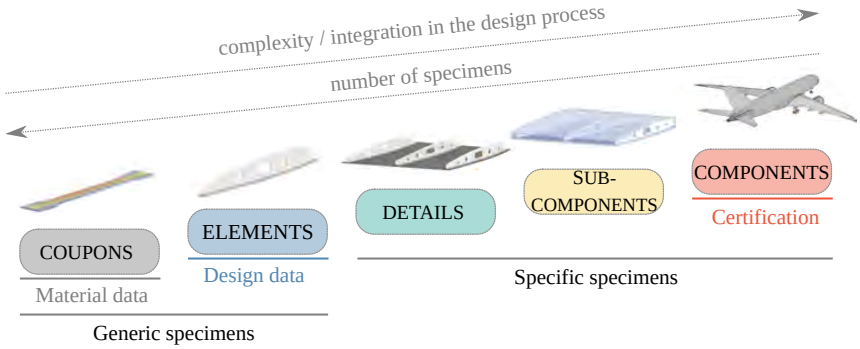

Figure 1.1: Schematic representation of the building block approach applied to the composite structures of the aeronautical sector.

With the aim of reducing the number of certification tests, the scientific and industrial communities have been intensively working towards a technology named Virtual Testing (VT) (Cox et al. 2014). Conceptually, the VT involves the simulation of experimental tests through reliable numerical tools. Hence, VT entails the development and implementation of tools to model the physical behaviour of materials and structures. The aerospace industry, for example, is highly interested in this technology to reduce the number of experimental tests to certify generic specimens. According to the building block approach, which is summarised in Figure 1.1, the number of tests required in the certification process is very large. For instance, the *Composite Materials Handbook* (2017) lists more than 100 configurations and 700 tests to certificate a bolted joint. Therefore, the correct implementation of this technology could

encompass a significant reduction in the costs associated with FRP structural applications. In spite of the progress made up to now, VT of composites structures is still a developing technology due to its complexity.

Part of the complexity faced by the VT of FRP structures stems from the morphology of the composites materials. In particular, FRP composites have an intricate internal structure composed of continuous fibres embedded in a polymeric matrix. Thanks to this, FRPs can accumulate a substantial amount of damage before losing structural integrity. For instance, the initiation of the local failure in the matrix does not necessarily lead to the loss of the bearing capacities since the fibres can still sustain part of the load up to their breakage (Barbero 2017). This fact implies This feature to accumulate damage before the collapse implies that a damage initiation criterion may not be sufficient to provide accurate predictions of the withstand capacities of an composite structure. Therefore, a Progressive Damage Failure Analysis (PDFA) accounting for the onset and evolution of damage mechanisms is necessary to perform reliable simulations of composite structures.

One important aspect to consider when performing PDFA of composite materials is the length scale of the analysis. Their particular morphology makes them susceptible to be analysed on different length scales. As illustrated in Figure 1.2, each length scale is devoted to the study the mechanical response from a different point of view. Thus, each length scale needs a specific kind of information as input and returns a particular aspect of the mechanical behaviour as output. If the analysis focuses on generic specimens, i.e. coupon and subcomponent specimens, the intermediate length scale, so-called mesoscopic, is the most suitable to achieve a good trade-off between the local and global failure. The former is more related to the material collapse, while the latter to the structural one.

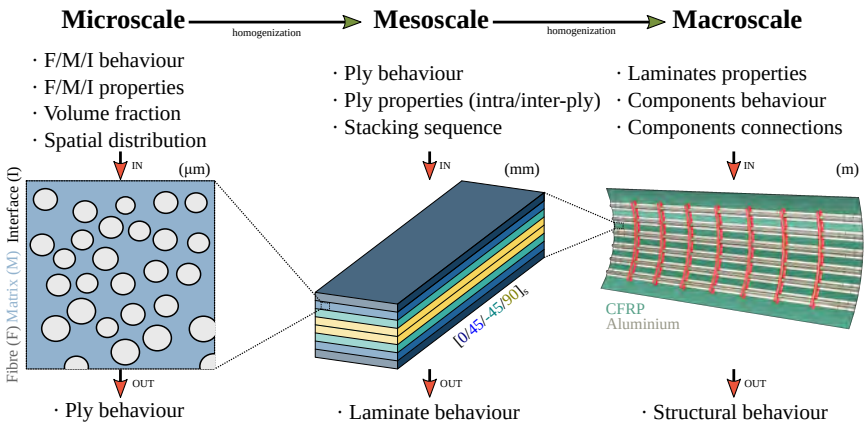

Figure 1.2: Schematic representation of the different length scales usually considered to study the behaviour of structural composite materials (Lopes et al. 2016; Tan et al. 2018).

The homogenization of the intra-ply structure mainly characterises the mesoscopic length scale. In this sense, the fibres and matrix of an FRP are considered as a homogeneous material with equivalent properties. These equivalent material properties are related to the fibre-matrix fraction volume, the spatial distribution, as well as other stochastic parameters associated with the constituents (Guerrero et al. 2018; Melro et al. 2008; Tavares et al. 2019). In turn, it is considered that the damage mechanisms that can develop on the mesoscopic length scale of an FRP are mainly four: (i) fibre breakage and kinking, (ii) matrix cracking, (iii) interface fibre-matrix debonding, and (iv) delamination failure between adjacent plies. The latter occurs in the interlaminar region, whereas the others in the intralaminar one, see Figure 1.3.

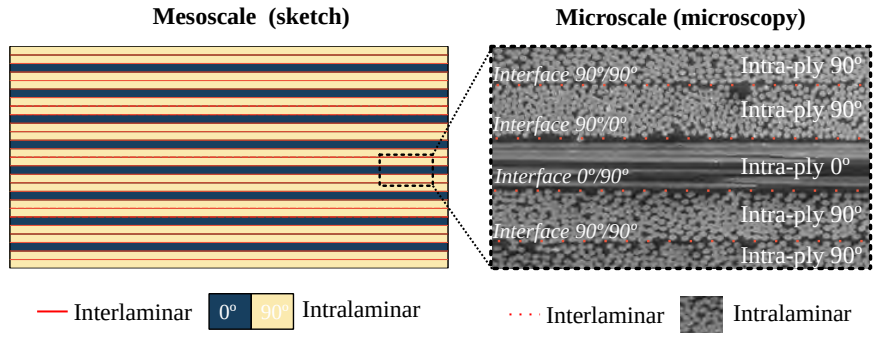

Figure 1.3: A schematic representation of a composite laminate from the mesoscopic length scale point of view with an optical micrography illustrating the intralaminar and interlaminar regions. (Micrography reproduced from Hayes and Gammon (2010))

Although the homogenisation assumptions mentioned above reduce the complexity of the analysis, the PDFA of composite structures on the mesoscopic scale is still a challenging problem. This is because of the four damage mechanisms previously listed can onset and interact during the failure process. For instance, a transverse crack can initiate its propagation in a ply cracking the matrix, then deflect across the interface provoking delamination, and finally penetrate in the other ply, continuing its propagation breaking fibres. Consequently, reliable physical theories and robust numerical methods are necessary to model with accuracy the possible failure sequence. Among the approaches for tackling such complex problem, the non-linear physical models based on solid mechanics in combination with the Finite Element Method (FEM) seems to be one of the most optimal options for performing high-fidelity PDFA of composite structures. The reason is that their combination conforms a numerical framework that has enough versatility to accommodate different modelling procedures.

Focusing on the standard FEM (O. Zienkiewicz et al. 2013), the continuity condition of the displacement field faces directly with the discontinuous nature of the principal source

of damage in FRP structures, namely, the cracks. This fact has resulted in a large number of formulations to model the onset and propagation of cracks using the FEM. In general, these formulations can be divided into continuous and discontinuous approaches (Forghani et al. 2015). In the former, the crack is smeared over the continuum modelling its effect through the degradation of the material properties, while in the latter, the crack is considered a geometric entity that induces a discontinuity in the displacement field.

Regardless of the approach, both aspect ratio and the tiny fracture process zone of FRPs imposes the use of fine meshes to reach proper levels of accuracy in the simulations. This implies an increase of the computational costs due to the increment of degrees of freedom which, if not managed efficiently, may hinder the simulation. One option to deal with this issue is to reduce the computational cost of the simulation by employing simplified models or coarse meshes. However, the accuracy of the numerical results can decrease drastically to the point of precluding the predictive capabilities of the simulation. Another option aimed at maintaining the level of accuracy is to increase the computational power. Even though this choice seems more natural and straightforward, the price of the hardware and the complexity of the programming models make it less attractive and some times prohibitive. Fortunately, the accessibility to parallel computing facilities (such as supercomputers or cloud-based platforms) has become nowadays more feasible and cheaper, opening a new horizon for engineers and researches.

Beyond access to parallel computing facilities, the simulation codes need to be programmed explicitly for exploiting the different levels of parallelism. As illustrated in Figure 1.4a, each level of parallelism is executed into a specific part of the hardware and therefore, has its characteristics and a particular programming model associated. In the context of FEM, a significant part of the parallelisation is achieved through the split of the computational domain using appropriate decomposition techniques. Generally speaking, the computational domain defined by the FE mesh is split into several subdomains, enabling the parallel execution of some tasks. In turn, this parallel execution increases the performance of the execution with respect to the sequential one. At the node level, the mesh is partitioned into several subdomains using a distributed memory programming model, such as MPI. Then, each partition is divided again at the chip level to parallelise large loops, such as the elemental loops. In contrast to the node level, a shared memory programming model can be used for this purpose, such as OpenMP. Finally, at the core level, vectorisation techniques are used to perform some tasks concurrently, either via compiler directives or programming models for Graphical Process Units (GPUs), such as OpenACC. This parallelisation strategy is summarized in Figure 1.4b.

In this sense, the simulation codes based on the FE method must include a High-Performance Computing (HPC) approach to maximise the performance of the executions. In other words,

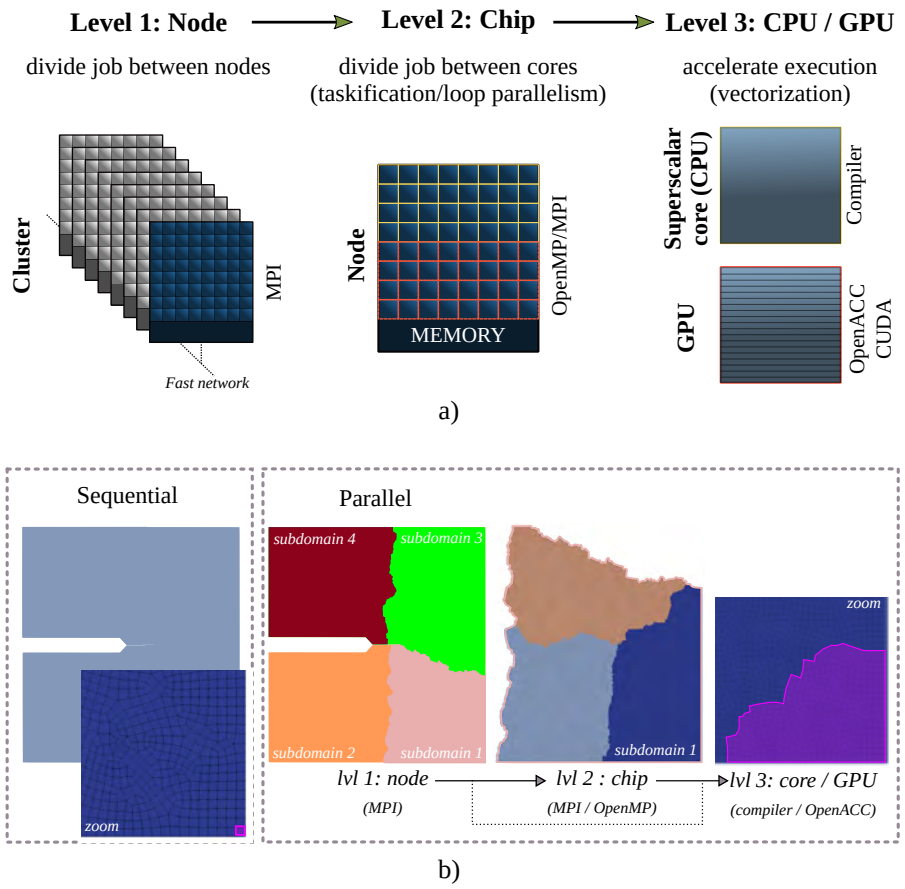

Figure 1.4: Schematic representation of a parallel computational environment applied to the numerical solution of the finite element problem. Part a) illustrates the hierarchy of the three levels of parallelisms that are usually offered by modern computing platforms. The node, chip and CPU/GPU referres to the hardware involved, while MPI, OpenMP and OpenCC the programming model used. Part b) shows a sequential versus parallel execution of the assembly process, relating the split of the domain with the different parallelism levels. The pink region represents the number of elements assembled concurrently.

the programmers of these codes should use highly efficient parallelisation techniques if they want to exploit the capabilities of the hardware. From this fact emerges the concept of HPC-based FE codes to designate those FE simulation codes capable of running efficiently in parallel computing platforms.

Based on the previous observations, the primary motivation of this dissertation is to explore what an HPC-based FE code can offer to the VT of FRP structures. Besides, the present work aims to develop a numerical framework to perform reliable simulations of the failure process of FRP structures in terms of the continuum damage mechanics in HPC facilities.

1.2 Objective and challenges

The principal objective of this dissertation is:

> **To develop and validate a high-performance computing numerical framework, based on the finite element method, for performing virtual testing of long fibre composite materials at a mesoscopic length scale through the use of novel fracture models.**

It is intended to reach the previous main objective by implementing new features in Alya code, the Barcelona Supercomputing Center in-house HPC-based FE code (Casoni et al. 2015; Vázquez et al. 2016). Considering the characteristics of Alya code and that, on the mesoscopic length scale, the structural failure of FRP is driven by intralaminar (fibre breaking and matrix cracking) and interlaminar (interface debonding) damage mechanisms, four challenges are postulated to achieve the main objective of the thesis:

1. **Formulation and implementation of a local continuum damage model for capturing the intralaminar failure mechanisms.**

   Local continuum damage models are the most conventional approach to model the intralaminar damage. Their formulation consists of the definition of a constitutive law to account for the degradation of the material properties ensuring a consistent thermodynamic formulation. Hence, their implementation in a standard FEM code is usually straightforward allowing to hold its scalability. Despite the extensive range of options available in the literature, not all of them are suitable for scalable HPC simulations, neither account for 3D stress states.

2. **Formulation and implementation of a non-local continuum damage model for capturing intralaminar failure mechanisms.**

   The key idea of the nonlocal continuum damage models is to account for the damage

evolution in a global way by defining a new primary field. As a consequence, extra degrees of freedom are introduced at the node level in the corresponding finite element formulation and implementation. Furthermore, the use of these models also implies the implementation of solution procedures to solve the coupled-field problem. Both facts usually hind the use of nonlocal continuum damage models in commercial FE codes because of their limited flexibility, even more, when parallel simulations are needed. Taking advantage of the flexibility of the Alya code, both questions are addressed in HPC simulations.

3. **Implementation of a local cohesive zone model for capturing the interlaminar failure mechanism.**

   The principal source of damage at the interfaces between plies is delamination. Considering that the interface is a predefined and known region, the most extended option for accounting its debonding is the binomial: cohesive zone model and the interface element technology. When this element technology is employed, the nodal quantities can be naturally interpolated to the mid-plane, hence allowing the computation of the displacement jump or crack opening needed by the cohesive zone model. Considering the element library available in the Alya code, the implementation of the interface element technology is also needed.

4. **Formulation and implementation of a strategy for coupling the nonlocal continuum damage model for the intralaminar failure and the cohesive zone model for the interlaminar failure.**

   The combination of local continuum damage and cohesive zone models does not imply an explicitly coupling between both mechanisms. The displacement field governs the relation between both damage mechanisms, which difficult the correct modelling of the interaction between intralaminar and interlaminar cracks. In some specific cases, such as delamination induced by matrix cracking, a formulation considering a coupling between the damage state of the intra-ply and interface regions could give more accurate results. Thus, a combination of nonlocal damage continuum and cohesive zone models seems a more suitable option.

All developments and implementations derived from the previous challenges are validated by performing VT of composites structures at coupon level. In this sense, analytical theories or experimental results are used to compare, verify and validate the numerical predictions of the implemented models.

1.3 Thesis layout

The present thesis is presented as a compendium of publications fulfilling the academic regulation of the doctoral studies of the Universitat de Girona. Accordingly, the document is divided into four parts. The first part consists of Chapters 2 and 3 and gives a general overview of the methodology employed. Chapter 2 introduces the framework for the models concerning the current state of the progressive damage modelling utilising the finite element method, while Chapter 3 presents the simulation code setting the basis of the computational framework. The second part describes the damage models developed and implemented in the context of this thesis and demonstrates their reliability through several virtual tests. In this sense, Chapter 4 describe the novelties regarding the formulation and implementation of the models, referring to the publications that support this thesis. In turn, Chapter 5 presents and discusses the main results concerning the numerical simulations. The third part consists of Chapter 6 and provides the principal conclusions and perspectives for future work. Finally, the fourth part gives the current version of the papers supporting the present thesis as a compendium of articles.

2 Progressive damage modeling for the virtual testing of composites

This chapter aims at providing the fundamental aspects concerning the HPC-based FE framework developed in the present thesis. Firstly, the damage morphology of composites at a mesoscopic length scale is described. Then, it is presented an overall classification of the existing approaches for modelling the damage of composite structures in the field of computational mechanics. Besides, for each of the contributions, there is a revision of the specific state-of-the-art in the journal versions presented in the appendices. Finally, the mathematical frameworks setting the basis for the formulation of the models is given.

2.1 Damage morphology of composite materials

Fibre-reinforced polymer composite (FRPs) are composed of at least two constituents, namely continuous fibres and matrix. Thanks to this combination, the resultant material, the FRP, has superior properties than those of the individual components acting independently (Daniel and Ishai 2006; Gay and Hoa 2007). The continuous fibres, usually made of glass or carbon, have an excellent performance for bearing tensile loads but they cannot efficiently sustain compression and transverse loads. For this reason, they are embedded into a matrix, which is usually made of a polymer. Besides to hold them together, the matrix also has the function to isolate the fibres of the environment, protecting them from hygrothermal effects and corrosion attacks (Barbero 2017).

Since the material properties of the fibres and the matrix are quite different, the mechanical response of FRPs possesses an anisotropic character. More specifically, FRPs behave as transversally-isotropic material on the mesoscopic level. The elastic and fracture properties along the direction of the fibre are higher than the properties in the isotropy plane defined by the transversal directions. As a consequence, the fibre orientation plays a crucial role in the mechanical response of composites. For instance, the bearing capacities of FRPs for structural applications can be improved by stacking several plies with different fibre orientations, resulting in the so-called composite laminate. However, the process of stacking separate plies creates interlaminar regions known as interfaces. As shown in Figure 2.1, the interfaces are characterised for having major content of matrix than fibre, which leads to a different elastic and failure behaviour compared to the one of the intralaminar region.

Therefore, on the mesoscopic level, two regions can be identified in laminates made of FRP plies: (i) intralaminar and (ii) interlaminar (interfaces).

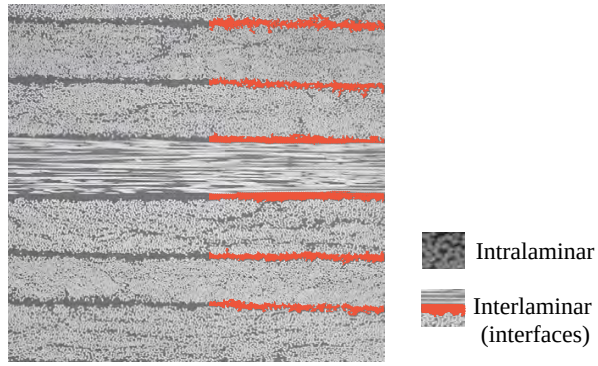

Figure 2.1: Optical micrograph of a fibre-reinforced polymer composite showing that between two intralaminar plies a region with less content of fibres is created denominated interlaminar (or interface). (Optical micrograph reproduced from Hayes and Gammon (2010))

Regarding the failure process of FRP laminates, it can be originated either in the intralaminar or interlaminar region. In other words, the failure can be onset in the fibres, matrix or interfaces, i.e anywhere of the laminate. In fact, this is one of the main reason because the prediction of the onset and damage evolution is a complicated task. In turn, the failure process may be a consequence of different physical phenomena, such as the onset and propagation of cracks, plasticity or creep. However, it is considered that the cracks are the primary source of damage in FRP and therefore, the phenomenon to model.

From a physical point of view, a crack is a discontinuity in the material due to its rupture, which tends to grow across the path that requires less energy. For instance, and in general terms, a crack originated in the matrix will tend to grow parallel to the fibres, because cracking matrix requires less energy than breaking or kinking fibres. Another example is a crack impinging an interface which, depending on the material properties and loading conditions, will penetrate the interface or deflected through it, inducing delamination (Pernice et al. 2015). Hence, the study of the onset and growth of cracks in heterogeneous materials with a complex microstructure, such as FRP, is complicated. Not only the material properties of the constituents and the loading conditions influence the failure process, but also other factors such as the statistical distribution of the fibre and the fibre-matrix volume ratio. Therefore, the morphology of the FRP failure is a complex physical phenomenon, which nowadays is still a topic of interest for researchers. See, for instance, the following recent experimental studies: Borstnar et al. (2015), Bull et al. (2014, 2015), García-Rodríguez et al. (2019, 2018a,b), and Wagih et al. (2016, 2019).

As can be appreciated in the failure sequences described in the previous paragraph, four dif-

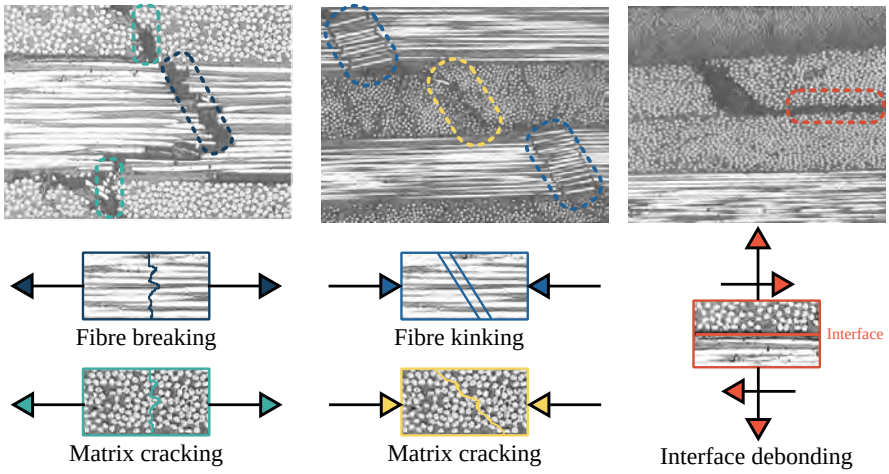

Figure 2.2: Optical micrographs of a fibre-reinforced polymer laminate illustrating the principal failure mechanics: fibre breaking and kinking, matrix cracking and interface debonding. Each mechanism is associated with a schematic representation of the loading state driving it. (Optical micrographs reproduced from the works of Camanho (1999) and Pinho (2005))

ferent damage mechanisms can lead to the failure of a composite laminate on the mesoscopic level, namely, breaking and kinking of the fibres, cracking of the matrix and debonding of the interface. Although all of these mechanisms provoke a rupture of the material through the formation of cracks, their particular morphology allows its differentiation. In general terms, each damage mechanism affects a specific constituent and tends to initiate and propagate for a particular state of loading. Figure 2.2 shows the morphology of the four main damage mechanisms on the microscopic level. Moreover, the same figure illustrates the loading state usually associated with the development of each damage mechanisms.

2.2 Solid mechanics computational framework

The modelling of the progressive damage modelling of composites mostly lies within the field of continuum solid mechanics. Hence, the conservation of the linear momentum for a continuous medium is the main governing principle of the corresponding initial-boundary value problem (IBVP). In the following, the equations setting the foundations of the computational problem are presented. For more details, the reader should refer to one of the following classical references: Hughes 2012, Belytschko et al. 2014 or O. Zienkiewicz et al. 2013.

2.2.1 Problem statement

Let us consider an arbitrary deformable body $\mathcal{B}$ in a N dimensional Euclidean space $\mathbb{R}^N$, which is illustrated in Figure 2.3. The position of a material point of the body at the reference

time $t = 0$ is described by the vector $\mathbf{X}$, while its position at the current time $t \in \mathbb{T} = [0, T]$ is given by the vector $\mathbf{x}$. Formally, the current position vector is the image of the regular map function $\chi(\mathbf{X}, t)$, which is denoted as motion. The displacement field is defined as:

$$\mathbf{u}(\mathbf{X}, t) := \chi(\mathbf{X}, t) - \mathbf{X}. \tag{2.1}$$

The outer boundary of the domain is denoted as $\partial\mathcal{B}$, whose normal outward vector is represented by $\boldsymbol{n}$. Henceforward, the dependency of the kinematic quantities with the time is omitted to alleviate the formulation. We assume that the body is subjected to body forces ($\boldsymbol{b}$ in $\mathcal{B}$) as well as prescribed displacements ($\bar{\mathbf{u}}$ on $\partial\mathcal{B}_u$) and tractions ($\bar{\boldsymbol{t}}$ on $\partial\mathcal{B}_t$) on the corresponding boundaries. Considering the Neumann-Dirichlet boundary conditions, $\partial\mathcal{B}$ is covered by two disjoint sets, $\partial\mathcal{B}_u$ and $\partial\mathcal{B}_t$, such that:

$$\partial\mathcal{B}_t \cup \partial\mathcal{B}_u = \partial\mathcal{B}, \tag{2.2}$$

$$\partial\mathcal{B}_t \cap \partial\mathcal{B}_u = \emptyset. \tag{2.3}$$

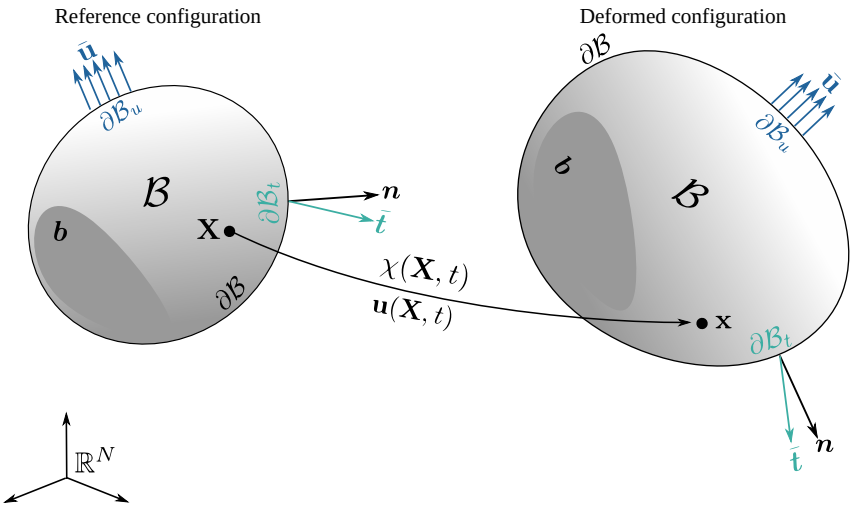

Figure 2.3: The initial (reference) and deformed (current) configuration of a body subjected to body forces $\boldsymbol{b}$, displacements $\bar{\mathbf{u}}$ and tractions $\bar{\boldsymbol{t}}$.

Assuming that the deformations in long fibre composite materials are not vey large (Reddy 2003), the infinitesimal deformation and the updated-Lagrangian description sets the basic framework for the motion and deformation. However, the formulation presented in the following can be expressed according to a total-Lagrangian description by using the appropriate

transformation operators.

The strong form (or derivative) governing the conservation of linear momentum of the solid mechanics problem consists of finding the displacement field $\mathbf{u}$ at each time t such that:

$$\nabla \cdot \boldsymbol{\sigma} + \boldsymbol{b} = \rho \ddot{\mathbf{u}} \quad \text{in} \quad \mathcal{B}, \tag{2.4}$$

subjected to the initial and boundary conditions:

$$\mathbf{u}|_{t=0} = \mathbf{u}_0 \quad \text{in} \quad \mathcal{B}_0, \tag{2.5}$$
$$\dot{\mathbf{u}}|_{t=0} = \dot{\mathbf{u}}_0 \quad \text{in} \quad \mathcal{B}_0, \tag{2.6}$$
$$\boldsymbol{\sigma} \cdot \boldsymbol{n} = \bar{\boldsymbol{t}} \quad \text{on} \quad \partial\mathcal{B}_t, \tag{2.7}$$
$$\mathbf{u} = \bar{\mathbf{u}} \quad \text{on} \quad \partial\mathcal{B}_u. \tag{2.8}$$

where $\boldsymbol{\sigma}$ is the Cauchy stress tensor, $\boldsymbol{b}$ is the body force per unit of the current volume, $\dot{\mathbf{u}}$ and $\ddot{\mathbf{u}}$ are the velocity and acceleration field, and ρ is the density. Here, the subscript 0 denotes the quantities at the reference configuration, i.e. at the beginning of the problem when $t = 0$. Note that the displacement field must be of the class C^2 continuously differentiable and must satisfy Eqs. (2.4) - (2.8) in the whole domain of the body $\mathcal{B}$. In the computational field, a weak form of the conservation of linear momentum is formulated which, in turn, alleviates the continuity conditions.

2.2.2 Weak form

The weak form (or integral) of the balance of linear momentum governing equation presented in the previous section leads to the well-known principle of the virtual work for a static systems or the virtual power for dynamic systems (Wriggers 2008). Following standard procedures, the weak form can be obtained from the strong form by multiplying the linear momentum governing equation by a test function and integrating over the current configuration. In this process, the spatial derivative of the stress tensor is eliminated and therefore, the continuity conditions of the displacement field are reduced.

Another way to conceive the weak form of the linear momentum problem is relating it with the calculus of infinitesimal energy variations. In this sense, an energy functional governing the conservation of linear momentum is stated and afterwards minimised to find the displacement field that corresponds to the given boundary conditions. The following presents the weak form of the solid mechanics problem through this last interpretation.

Let us define the energy functional Π of the body described in the above section, which is related with the balance of momentum equation (Wriggers 2008):

$$\Pi(\mathbf{u}) = \Pi_{ine}(\mathbf{u}) + \Pi_{int}(\mathbf{u}) - \Pi_{ext}(\mathbf{u}) \tag{2.9}$$

where Π_{ine}, Π_{int} and Π_{ext} are the inertial, internal and external contributions defined as:

$$\Pi_{ine}(\mathbf{u}) := \frac{1}{2} \int_{\mathcal{B}} \rho \dot{\mathbf{u}} \cdot \dot{\mathbf{u}} \, \mathrm{d}V, \tag{2.10}$$

$$\Pi_{int}(\mathbf{u}) := \int_{\mathcal{B}} \Psi(\boldsymbol{\varepsilon}(\mathbf{u})) \, \mathrm{d}V, \tag{2.11}$$

$$\Pi_{ext}(\mathbf{u}) := \int_{\mathcal{B}} \mathbf{u} \cdot \rho \boldsymbol{b} \, \mathrm{d}V + \int_{\partial \mathcal{B}_t} \mathbf{u} \cdot \bar{\boldsymbol{t}} \, \mathrm{d}S, \tag{2.12}$$

where Ψ is the internal elastic energy function. The infinitesimal strain tensor $\boldsymbol{\varepsilon}$ is defined as the symmetric gradient of the displacement field (Wriggers 2008):

$$\boldsymbol{\varepsilon} := \frac{1}{2} \left(\nabla \mathbf{u} + \nabla^{\mathbf{T}} \mathbf{u} \right), \tag{2.13}$$

which is introduced here because of Ψ is generally expressed respect to the strain state. Further, the Cauchy stress tensor can be derived from the specific elastic energy and strain tensor as (Wriggers 2008):

$$\boldsymbol{\sigma} := \frac{\partial \Psi}{\partial \boldsymbol{\varepsilon}}. \tag{2.14}$$

Recalling the continuous Galerkin-Bubnov method of weighted residuals, the trial solution of the displacement field $\mathbf{u}$ are extended with the corresponding admissible weigthening or test functions $\delta\mathbf{u}$. Formally, the trial solution $\mathbf{u}$ is the set of functions living in the subspace $\mathcal{U} \subset H^1$, which garentees the fulfilment of the Dirichlet boundary conditions on $\partial\mathcal{B}_u$. In turn, the tests functions $\delta\mathbf{u}$ are all the kinematically admisible displacement fields living in the subspace $\mathcal{V} \subset H^1$, which impose zero value on $\partial\mathcal{B}_u$. Here, H^1 denotes the Sobolev space vector, which ensures that these functions and their first partial derivatives are square integrables (Debnath and Mikusinski 2005).

Applying the standard procedure (Wriggers 2008), the weak form of Eq. (2.9) is:

$$\delta\Pi(\mathbf{u}, \delta\mathbf{u}) = \delta\Pi_{ine}(\mathbf{u}, \delta\mathbf{u}) + \delta\Pi_{int}(\mathbf{u}, \delta\mathbf{u}) - \delta\Pi_{ext}(\mathbf{u}, \delta\mathbf{u}) \tag{2.15}$$

where each term is defined as:

$$\delta\Pi_{ine}(\mathbf{u}, \delta\mathbf{u}) := \int_{\mathcal{B}} \delta\mathbf{u} \cdot \rho\ddot{\mathbf{u}} \, \mathrm{d}V, \tag{2.16}$$

$$\delta\Pi_{int}(\mathbf{u}, \delta\mathbf{u}) := \int_{\mathcal{B}} \boldsymbol{\sigma} : \delta\boldsymbol{\varepsilon} \, \mathrm{d}V, \tag{2.17}$$

$$\delta\Pi_{ext}(\mathbf{u}, \delta\mathbf{u}) := \int_{\mathcal{B}} \delta\mathbf{u} \cdot \rho\boldsymbol{b} \, \mathrm{d}V + \int_{\partial\mathcal{B}_t} \delta\mathbf{u} \cdot \bar{\boldsymbol{t}} \, \mathrm{d}S, \tag{2.18}$$

where $\delta\boldsymbol{\varepsilon} = \partial_{\mathbf{u}}\boldsymbol{\varepsilon}(\delta\mathbf{u})$ is the variation of the strain tensor with respect to the displacement field, so-called virtual strains.

The weak or integral form of the solid mechanics problem concerning the conservation of the linear momentum consists of finding the displacement field $\mathbf{u} \in \mathcal{U}$ at each time t such that for all $\delta\mathbf{u} \in \mathcal{V}$:

$$\delta\Pi(\mathbf{u}, \delta\mathbf{u}) = 0 \tag{2.19}$$

subjected to the initial conditions $\mathbf{u}_0$ and $\dot{\mathbf{u}}_0$ defined in $\mathcal{B}$ and the prescribed traction $\bar{\boldsymbol{t}}$ defined on $\partial\mathcal{B}_t$. In the following section is presented the discrete form resulting from the finite element spatial approximation.

2.2.3 Discrete form

The spatial discretisation of the weak form of the balance of linear momentum equation presented before is formulated using the finite element method. The basic idea behind this method is to approximate the infinite-dimensional function spaces, $\mathcal{U}$ and $\mathcal{V}$, by finite-dimensional ones, $\mathcal{U}^h$ and $\mathcal{V}^h$, imposing the same conditions on the boundaries, but in the approximated domain. As illustrated in Figure 2.4, this idea means that the continuous domain $\mathcal{B}$ of the body is approximated by a discrete domain Ω^h, which is built by a finite number of disjoints elements Ω_e, such that

$$\mathcal{B} \approx \Omega^h = \bigcup_{e}^{\mathrm{n}_e} \Omega_e, \tag{2.20}$$

where n_e is the total number of elements and e is the subscript denoting the element number. Hence, the continuum quantities are approximated within each finite element and then assembled with the so-called assembly procedure, here expressed with the operator $\mathcal{A}_{e=1}^{n_e}\{\bullet\} = \bigcup_{e}^{\mathrm{n}_e}\{\bullet\}$. Adopting an isoparametric formulation (Irons 1966), the continuum variables related to kinematics are approximated within each element as:

$$\boldsymbol{X} \approx \boldsymbol{X}^h = \boldsymbol{\mathcal{N}}(\xi)\hat{\boldsymbol{X}}, \tag{2.21}$$

$$\boldsymbol{x} \approx \boldsymbol{x}^h = \boldsymbol{\mathcal{N}}(\xi)\hat{\boldsymbol{x}}(t), \tag{2.22}$$

$$\tag{2.23}$$

where h is the superscript denoting the discretised quantity, $\hat{\boldsymbol{X}}$ and $\hat{\boldsymbol{x}}$ are the vectors arranging the nodal positions at the reference and spatial configurations, and ξ is the vector of natural coordinates. Similarly, the continuum displacement and admissible displacement field are approximated as:

$$\mathbf{u} \approx \mathbf{u}^h(\xi, t) = \boldsymbol{\mathcal{N}}(\xi)\mathbf{d}(t), \tag{2.24}$$

$$\delta\mathbf{u} \approx \delta\mathbf{u}^h(\xi) = \boldsymbol{\mathcal{N}}(\xi)\mathfrak{c}, \tag{2.25}$$

$$\tag{2.26}$$

where $\mathbf{d}$ and $\mathfrak{c}$ are the vectors arranging the nodal and weighted displacements, respectively. Further, $\boldsymbol{\mathcal{N}}$ is the interpolation operator, which is a matrix arranging the $\mathcal{C}^0$-continuous shape functions associated with the nodes supporting the element. Using the above approximations, the virtual strain is computed as $\delta\boldsymbol{\varepsilon} = \mathbf{B}\delta\mathbf{d}$, where $\mathbf{B}$ is the strain-displacement compatibility operator (Wriggers 2008). Finally, it is worth noting that the velocities and accelerations, $\dot{\mathbf{u}}$ and $\ddot{\mathbf{u}}$ are approximated using the same procedure, which defines $\dot{\mathbf{d}}$ and $\ddot{\mathbf{d}}$.

Following the continuous Galerkin-Bubnov method of weighted residuals and considering the arbitrariness of the test functions, the discrete form of the conservation of the linear momentum problem consist on finding the nodal values of the displacement field $\mathbf{u}^h \in \mathcal{U}^h$ at each time t such that:

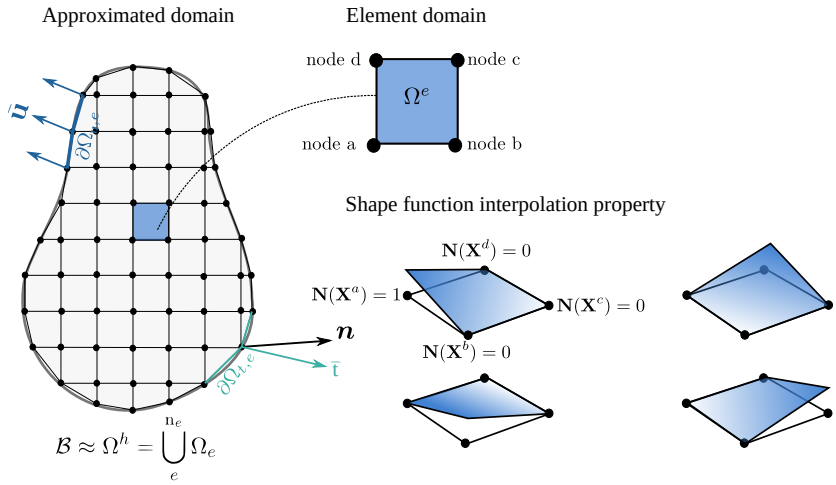

Figure 2.4: The deformed configuration of a body discretized using a FE mesh, which is subjected to displacements $\bar{\mathbf{u}}$ and tractions $\bar{\boldsymbol{t}}$.

$$\mathbf{F}_{ine}(\ddot{\mathbf{d}}) + \mathbf{F}_{int}(\mathbf{d}) - \mathbf{F}_{ext}(\mathbf{d}) = 0 \tag{2.27}$$

subjected to the initial and boundary conditions on the approximated domain Ω^h. In the above expression, $\mathbf{F}_{ine}$, $\mathbf{F}_{int}$ and $\mathbf{F}_{ext}$ are respectively the vectors defining the counterparts of Eqs. (2.16) - (2.18):

$$\mathbf{F}_{ine}(\ddot{\mathbf{d}}) := \mathcal{A}_{e=1}^{n_e} \left\{ \int_{\Omega_e} \rho \boldsymbol{\mathcal{N}}^{\mathrm{T}} \boldsymbol{\mathcal{N}} \ddot{\mathbf{d}} \, \mathrm{d}V \right\}, \tag{2.28}$$

$$\mathbf{F}_{int}(\mathbf{d}) := \mathcal{A}_{e=1}^{n_e} \left\{ \int_{\Omega_e} \mathbf{B}^{\mathrm{T}} \boldsymbol{\sigma} \, \mathrm{d}V \right\}, \tag{2.29}$$

$$\mathbf{F}_{ext}(\mathbf{d}) := \mathcal{A}_{e=1}^{n_e} \left\{ \int_{\Omega_e} \rho \boldsymbol{\mathcal{N}}^{\mathrm{T}} \boldsymbol{b} \, \mathrm{d}V + \int_{\partial\Omega_{t,e}} \boldsymbol{\mathcal{N}} \bar{\boldsymbol{t}} \, \mathrm{d}S \right\}, \tag{2.30}$$

where $\int_{\Omega_e} \rho \boldsymbol{\mathcal{N}}^{\mathrm{T}} \boldsymbol{\mathcal{N}} \mathrm{d}V$ defines the so-called elemental mass matrix. Finally, the volume and interface integrals can be computed exactly in the integration points using numerical methods such as the Newton-Cotes or the Gauss-quadrature (O. Zienkiewicz et al. 2013).

Note that the discrete form of the balance of momentum results in a system of ordinary differential equations of second order in time, which can be solved employing a temporal

integration scheme. Accordingly, the unknown of the displacement field ($\mathbf{d}$) and its temporal derivatives ($\dot{\mathbf{d}}$ and $\ddot{\mathbf{d}}$) must be computed at each time step. Thus, depending on the temporal integration scheme, the set of solutions ($\mathbf{d}$, $\dot{\mathbf{d}}$, $\ddot{\mathbf{d}}$) is obtained explicitly or implicitly.

In the field of solid mechanics, a common choice is to use a scheme of the Newmark's family (Katona and OC Zienkiewicz 1985). For example, following the β-Newmark scheme, the solution at a specific time step of the simulation is obtained by solving the following system of equations (Belytschko et al. 2014):

$$\mathbf{F}_{ine}(\ddot{\mathbf{d}}^{n+1}) = \mathbf{F}_{ext}(\mathbf{d}^{n+1}) - \mathbf{F}_{int}(\mathbf{d}^{n+1}), \tag{2.31}$$

$$\mathbf{d}^{n+1} = \mathbf{d}^{n} + \Delta t \dot{\mathbf{d}}^{n} + (\Delta t)^2 \left[\left(\frac{1}{2} - \beta \right) \ddot{\mathbf{d}}^{n} + \beta \ddot{\mathbf{d}}^{n+1} \right], \tag{2.32}$$

$$\dot{\mathbf{d}}^{n+1} = \dot{\mathbf{d}}^{n} + \Delta t \left[(1-\gamma) \ddot{\mathbf{d}}^{n} + \gamma \ddot{\mathbf{d}}^{n+1} \right] \tag{2.33}$$

where superscripts n and $n+1$ denotes that the variables are evaluated at time t^n and t^{n+1}, while β and γ are numerical parameters associated with the temporal integration. For $\beta = 0$ the scheme is explicit, whereas for $0 < \beta < 0.5$ the scheme is implicit. In turn, for $\gamma = 0.5$ no artificial damping is added, whereas $\gamma > 0.5$ artificial damping proportional to $\gamma - 0.5$ is added by the Newmark integrator (Belytschko et al. 2014). When dealing with an implicit scheme, a full Newton-Raphson method is usually employed to compute the displacement at t^{n+1}.Thus, a sequence of linear models is constructed and solved iteratively to approximate the solution until achieving the desired tolerance. This procedure can be generally expressed as:

$$\mathbf{K}^{(k)} \Delta \mathbf{d}^{(k)} = -\mathbf{R}^{(k)}, \tag{2.34}$$

$$\mathbf{d}^{(k+1)} = \mathbf{d}^{(k)} + \Delta \mathbf{d}^{(k)} \tag{2.35}$$

where the superscript k indicates the inner iteration of the Newton-Rhapson loop. Here, $\mathbf{K}$ and $\mathbf{R}$ are respectively the matrix and right-hand side vector resulting from the linearization process of Eq. (2.27) (Belytschko et al. 2014). In the field of solid mechanics, $\mathbf{K}$ is commonly known as the stiffness matrix, while $\mathbf{R}$ is the residual force vector. Finally, it is worth mentioning that the algebraic system of equations given in Eq. (2.34) can be solved employing direct or iterative solvers (Langer and Neumüller 2018).

2.3 Progressive damage modelling

The principal reason because the modelling of progressive failure analysis of composites is a challenging computational problem stems from the previous two sections. The discretisation of the balance of linear momentum in terms of the FEM requires continuity on the displacement field, whereas the physical mechanisms driving the failure of FRP mainly violates the continuity of the displacement field. To overcome this issue, a huge number of models, approaches and techniques has been proposed in the context of the FEM (Tay et al. 2008; Van der Meer et al. 2012). In the following, the most suitable methods for the aims of this thesis are presented and contextualised between the other techniques. For this purpose, firstly is presented those models to lying in the so-called continuous approach and then, those in the discontinuous one.

2.3.1 Continuous approach

The continuous approach models the structural failure provoked by cracks without considering strong discontinuities in the displacement field. For this purpose, it is employed constitutive relationships formulated within the thermodynamic principles of the continuum damage mechanics theory (CDM), which is also known as damage mechanics.

The CDM, initiated by L.M. Kachanov and Y.N. Rabotnov, aims the modelling of failure mechanisms by making assumptions about its morphology and how it affects the mechanical response (Murakami 2012). In this sense, the models within the CDM formulate hypotheses about the nature of the failure and define its influence within the different length scales. For instance, the progressive degradation of the material properties occurring before the macroscopic initiation of a crack can be understood as the loss of active area due to the nucleation of micro-cracks along the fracture process zone (FPZ). In the context of CDM, the degradation phenomenon of the material properties is the so-called damage (Murakami 2012).

The concept of the damage permits the modelisation of the rupture of the continuum through the stress-strain law by assuming how it affects the loading capacities. This methodology leads to a smeared representation of the crack. Accordingly, the stress-strain law has a softening part that describes the loss of the rigidity of a material point due to the nucleation of a crack. This softening part is not only governed by the strain state but also by a set of internal state variables, which accounts for the thermodynamic history state. Therefore, CDM formulations employ the internal state variable theory for describing the state of damage of a material point (Coleman and Gurtin 1967; Horstemeyer and Bammann 2010).

The main drawback of the CDM models is the dependency of the predictions with the spatial discretisation, i.e. the results depends on the characteristics of the FE mesh. The reasons for

this dependency principally arise from the loss of the positive-definiteness of the material tangent tensor in the softening part of the stress-strain law (Bažant and Cedolin 1979, 1983; Crisfield 1988). This loss induces material instabilities that may provoke the loss of ellipticity of the equations that govern the IBVP (De Borst et al. 1993; Peerlings et al. 2002). As a consequence, the solution is no longer unique, and therefore, the IBVP may admit multiple correct solutions (Benallal et al. 2001). In addition, the loss of positive-definiteness also provokes the localisation of the damage into a finite band with the minimum possible width. Commonly, these numerical problems are denominated localisation issues because they are triggered after the localisation of the strains, i.e. when the damage initiates at the very beginning of the softening region starts.

The damage localisation issue results in a wrong prediction of the strain energy that is dissipated during the nucleation of a crack. From a physical point of view, the strain energy consumed by the nucleation is expected to be equal to the fracture toughness of the material multiplied by the cracked surface area. However, since the fracture toughness is a material property independent of the spatial discretisation, the energy dissipated during the formation of a crack decreases as finner is the mesh. In the limit case of infinitesimal element size, this energy tends to zero leading to non-consistent physical solution (Pineda et al. 2012). Besides this inconsistency, the localisation of the damage into a finite band also induces the alignment of the failure pattern with the mesh orientation (De Borst et al. 1993). Depending on the failure mechanism, a wrong representation of the failure pattern could have associated an incorrect prediction of the ultimate failure. For instance, this issue can be especially critical in failure scenarios dominated by matrix splits.

During the last three decades, the mitigation of mesh dependency of the continuous damage models has been an extense topic of research. These investigations have resulted in a large variety of continuous models, which can be mainly classified into two types: local and nonlocal damage models. However, other approaches have also been proposed to alleviate the mesh dependency, such as the meshless methods or the viscous regularisation techniques (Needleman 1988; Rabczuk 2013). According to the objectives of the present thesis, the following sections briefly presents the local and nonlocal damage models.

2.3.1.1 Local damage models

Local damage models describe the mechanical response of a material point employing only its thermodynamic state. In other words, the local damage models assume that the constitutive behaviour of a material point solely depends on its loading state and the history of its internal state variables. This hypothesis simplifies their formulation and implementation, giving one of their principal advantages, namely: the straightforward use in a standard finite element code. Local damage models are, in essence, stress-strain constitutive relationships acting at

the integration point level. Hence, these models do not require any significant modification of the formulation presented in Section 2.2. However, to achieve good accuracy in the numerical predictions, the usage of local damage models requires very thin meshes in conjunction with energy regularisation techniques. Otherwise, the results have a mesh dependency induced by the localisation issues mentioned previously. It is worth mentioning that, besides those issues, the damage representation in the local damage models is not strictly continuous due to the strain localisation in a band of elements. Then, the damage is continuous inside the element, but not between elements.

The crack band theory is one of the most extended methodologies to mitigate the localisation issues. Hence, it does not attempt to solve the issues related to the alignment of the failure pattern with the mesh orientation. Specifically, this theory aims to guarantee the correct amount of energy dissipated during the nucleation of a crack with independency of the mesh size. Firstly proposed by Bažant and Oh (1983), the crack band theory modifies the energy consumed through the dissipation process as a function of the initial characteristic length of the element. Here, it is worth to remember that the energy consumed in the softening part of the stress-strain law, i.e. after the strain localisation, is related to the fracture toughness of the material, in a similar way to the fictitious crack theory of Hillerborg et al. (1976) (Maimí 2007). Despite the implementation of a local damage model using the crack band theory is straightforward, the evaluation of the characteristic element length can be challenging, or even not clear. The reason is that the length required by the crack band theory depends on several aspects: element type, element shape, and the orientation of the fracture plane (Bažant and Cedolin 1983; Maimí et al. 2007b). For these reasons, the crack band models usually proportionate more accurate results when the mesh is structured and oriented according to the expected damage pattern.

2.3.1.2 Nonlocal damage models

Nonlocal damage models describe the mechanical response of a material point utilising not only its thermodynamical state but also the state of the points in the surrounding region. For this purpose, nonlocal damage models incorporate procedures in the formulation of the IBVP that average or regularise the internal variables that govern the damage evolution. These procedures, known as localisation limiters, are in charge of accounting the thermodynamical state of the surrounding region, giving the nonlocal character of the formulation. In general terms, the localisations limiters enforce the localisation of the strain in a finite region independently of the spatial discretisation, preventing its localisation into an arbitrarily small volume. This enforcement mitigates the dependency of the solution with the size and alignment of the mesh (Azinpour et al. 2018; Forghani et al. 2015; Mediavilla et al. 2006; Rodríguez-Ferran et al. 2004). In addition, the variation of the damage state inside the regularisation zone is smooth, recovering the continuity hypothesis stated in the continuum

damage mechanics theory (Peerlings et al. 2002). Regarding their implementation, nonlocal damage models require substantial modifications of the standard FE formulation presented in Section 2.2. For instance, the localisation limiters usually calculate some variables in a nonlocal sense and need to manage with extra degrees of freedom.

Most of the nonlocal damage models can be classified into two types: integrative and enhanced-gradient formulations. The former type uses integrals for averaging the nonlocal variables to represent the spatial interaction between the material points of the domain, whereas the latter one incorporates spatial gradients of the nonlocal variables for modelling the interaction (Jirásek 2007). Further, the enhanced-gradient models can be classified according to the method used to computed the nonlocal strain variable driving the damage growth, namely: implicit and explicit gradient formulations. The implicit formulations compute the nonlocal variable by solving the differential equation that results from the incorporation of the spatial gradients in the formulation. In turn, the explicit formulations obtain the nonlocal variable by adding the spatial information giving by the derivatives in its local counterpart. A detailed and comprehensive comparison between both types of nonlocal damage models can be found in the study carried by Peerlings et al. (2001).

Beyond the models lying in the previous classification, a new type of nonlocal damage model known as Phase Field (PF) has been recently established as a reliable alternative for modelling brittle fracture problems. Seminally proposed by (Bourdin et al. 2000, 2008), the PF is a regularisation technique for the variational fracture problem formulated by Francfort and Marigo (1998). This technique consists of smearing the discrete representation of a crack within the continuum, maintaining the spirit of Griffith regarding the brittle fracture problem. For this purpose, Bourdin and co-workers employed the work in image-segmentation performed by Mumford and Shah to regularise the discrete internal boundary associated with a crack, exploiting the Γ-convergence concept (Ambrosio and Tortorelli 1990). Thanks to this, the PF approach preserves the continuity of the displacement field and precludes the necessity of algorithms for tracking the crack evolution. After their pioneering work, Miehe et al. (2010b) presented a thermodynamically consistent formulation based on the PF approach, which emphasises the differences between the energetic and dissipative mechanisms as well as accounts for the irreversibility condition of the damage.

2.3.2 Discontinuous approach

The discontinuous approach models the structural failure provoked by cracks through the modelling of the strong discontinuities in the displacement field, known as displacement jumps. This displacement jump governs the softening region of the constitutive model through a definition of a traction-separation law or cohesive law. Hence, the discontinuous approach has to deal with the constitutive modelling and the kinematics of the displacement jump.

The constitutive basis of the discontinuous models is the cohesive zone model (CZM) stemming from the early work of Dugdale (1960) and Barenblatt (1962) for elastic-plastic materials, and Hillerborg et al. (1976) for quasi-brittle materials. From their studies, it is postulated the existence of a fracture process zone (FPZ) that extends from the crack tip. Along the FPZ, the rupture of the material is considered as a gradual phenomenon resisted by cohesive tractions. In this sense, the CZM models the nucleation and propagation of cracks by lumping their effect into a discrete plane (or fictitious crack), which extension and orientation are associated with the FPZ (Soto et al. 2016). Accordingly, the constitutive response of the material is governed by the cohesive law that relates the displacement jump across the fictitious crack with the cohesive tractions (Ortiz and Pandolfi 1999). Further, this law can be formulated within plasticity or damage mechanics theories (Van der Meer 2010).

Regarding the evaluation of the displacement jump across the FPZ, there are different methodologies in the context of an FE spatial discretisation. Essentially, these methodologies are aimed at describing the displacement jump induced by a crack. On the one hand, some of these methodologies act at the element level. The most widely used are: (i) the Interface Element Method (IEM) (Alfano and Crisfield 2001; De Borst 2003; Goyal et al. 2004), (ii) the eXtended Finite Element Method (X-FEM) (Fries and Belytschko 2010; Moës et al. 1999), which is based on the partition-of-unity property stated by Melenk and Babuška (1996), and (iii) the Phantom Node Method (PNM) (Mergheim et al. 2005; Song et al. 2006), the Floating Point Method (FPM) (Chen et al. 2014) and the Augmented Finite Element Method (A-FEM) (Ling et al. 2009), all based on the Hansbo and Hansbo approach (A. Hansbo and P. Hansbo 2004). On the other hand, other interesting techniques enabling the modelling of strong discontinuities are based, for instance, in re-meshing procedures (Bouchard et al. 2000).

Excepting the IEM, the previously mentioned technologies acting at the elemental level (X-FEM, PNM, FPM, and A-FEM) enrich the displacement field with extra degrees of freedom. Furthermore, these technologies usually require algorithms for computing and tracking the orientation of the crack propagation. Therefore, the complexity of their implementation and the computational costs of the simulation are generally higher than the models of the continuous approach. On the contrary, the IEM does not require tracking algorithms, and its implementation in the standard formulation presented in Section 2.2 is straightforward.Specifically, IEM defines a new type of element, called interface element, that enables a simple evaluation of the displacement jumps across a virtual interface assumed in its mid-plane. When modelling fracture processes, this virtual interface is associated with the mid-plane of a fictitious crack. Hence, the interface elements must be defined along the expected crack path with the correct orientation, which reduces the performance of the technique for unknown failure patterns. Otherwise, IEM is especially suited for modelling the debonding of an interface because the potential crack path is well-defined from the very

beginning of the analysis.

2.4 Frameworks for the applied methods

This final section is devoted to present the basic principles of the frameworks used to formulate the damage models concerning this thesis. Specifically, it is intended to highlight how each framework modifies or not the finite element formulation of the balance of momentum law governing the solid mechanics problem stated in Section 2.2. Firstly, it is summarised the thermodynamical bases of the continuum damage mechanics theory, which are basically used in the formulation of the local damage model for the intralaminar region. Then, the phase field approach, which set the bases for the nonlocal damage model also formulated for the intralaminar material, are presented. Finally, the cohesive zone model concept applied to the intralaminar region is described.

In the following, the internal energy functional for the uncracked homogeneous body, which is described in Section 2.2 and illustrated in Figure 2.3, is herein employed to show the implications of each technique in the standard finite element formulation. For this purposes, let us recall the energy functional Eq. (2.9) that governs the deformation problem, which for a quasi-static condition reads as:

$$\Pi(\mathbf{u}) = \Pi_{int}(\mathbf{u}) - \Pi_{ext}(\mathbf{u}), \tag{2.36}$$

where the internal energy contribution is defined in Eq. (2.11), while the external energy contribution in Eq. (2.12).

2.4.1 Continuum Damage Mechanics

The continuum damage mechanics (CDM) sets the principles for modelling the progressive failure of materials within the continuum mechanics theory (Lemaitre and Chaboche 1990; Murakami 2012). According to CDM, nucleation and propagation of cracks and voids can be interpreted as a deteriorating process of the material properties. In turn, this damaging process is governed by the thermodynamical state of a material point through a set of internal state variables, denoted in the following as $\boldsymbol{\mathcal{D}}$. Hence, the CDM postulates that the damage induced by cracks can be modelled in the continuum by assuming how it affects the material properties. The following gives the basic thermodynamic principles establishing the basis for the damage models formulated and implemented in the context of this thesis.

Let us assume that, during the failure process of the body described in Section 2.2.1, the variation of density is negligible and the evolution of damage occurs in an adiabatic manner. Considering those assumptions, the Clasius-Duhem inequality for the balance of momentum

and energy postulates that the process is thermodynamical consistent if the mechanical energy dissipation is positive, i.e. $\Xi \geq 0$. For a system only subjected to mechanical loads, it can be expressed as:

$$\Xi := \boldsymbol{\sigma} : \dot{\boldsymbol{\varepsilon}} - \dot{\Psi} \geq 0 \tag{2.37}$$

where $\boldsymbol{\sigma} : \dot{\boldsymbol{\varepsilon}}$ is the mechanical power supplied by external agents and $\dot{\Psi}$ is the rate of change of the internal elastic energy of the system. In turn, $\boldsymbol{\sigma}$ is the stress tensor, $\boldsymbol{\varepsilon}$ is the strain or deformation tensor, and Ψ is the Helmholtz energy. By definition, Ψ represents the free elastic energy available for the solid to undergo the deformation process. Hence, according to CDM, the damage state of the solid must directly affect its value. Accordingly, the rate of change of the Helmholtz for a constant absolute tempreature can be expressed as:

$$\dot{\Psi}(\boldsymbol{\varepsilon}, \boldsymbol{\mathcal{D}}) = \frac{\partial \Psi}{\partial \boldsymbol{\varepsilon}} : \dot{\boldsymbol{\varepsilon}} + \frac{\partial \Psi}{\partial \boldsymbol{\mathcal{D}}} : \dot{\boldsymbol{\mathcal{D}}}, \tag{2.38}$$

By substituting Eq. (2.38) into Eq. (2.37) and operating, the Clausius-Duhem inequality reads as:

$$(\boldsymbol{\sigma} - \frac{\partial \Psi}{\partial \boldsymbol{\varepsilon}}) : \dot{\boldsymbol{\varepsilon}} - \frac{\partial \Psi}{\partial \boldsymbol{\mathcal{D}}} : \dot{\boldsymbol{\mathcal{D}}} \geq 0, \tag{2.39}$$

where $-\partial_{\boldsymbol{\mathcal{D}}} \Psi = \boldsymbol{Y}$ are the thermodynamical forces, which define the variation of the internal free energy when the internal state variables evolve. Taking into account that the strain tensor can vary freely, the expression inside the parenthesis must be equal to zero leading to the definition given in Eq. (2.14). Therefore, the thermodynamic consistency is ensured when:

$$\boldsymbol{Y} : \dot{\boldsymbol{\mathcal{D}}} \geq 0. \tag{2.40}$$

At this point, considering positive thermodynamical forces, the consistency of the damage falls on a positive evolution of the damage variable. For this purpose, the framework of Maimí et al. (2007a,b) can be employed to define damage evolution laws fulfilling the thermodynamical consistency. Accordingly, a variable change is performed, and a historical damage threshold variable r is defined, which governs the damage evolution law and considers the past states. Then, the onset and growth of the damage state can be associated with a failure criterion F, such that:

$$F = \phi - r \leq 0 \tag{2.41}$$

where ϕ is the loading function defining the shape of the failure surface. On one hand, ϕ is computed through the independent variable ($\boldsymbol{\varepsilon}$ or $\boldsymbol{\sigma}$) and some constant parameters, which are usually related to the material properties. On the other hand, r can be explicitly integrated over the time as:

$$r = \max_{s \in \mathbb{T}} (1, \phi^{s}) \tag{2.42}$$

where $s \in \mathbb{T} = [0, T]$ represents the full history process. Then, the material response state is determined by means of the appropriate form of the Kuhn-Tucker conditions (Simo and Hugues 2003):

$$\dot{r} \geq 0, \quad F \leq 0, \quad \dot{r}F = 0. \tag{2.43}$$

If $F < 0$ the material is in the elastic regime, the damage criterion is not satisfied and $\dot{r} = 0$. Otherwise, if $F = 0$ the damage criterion is satisfied and the material response state is determined from the loading function gradient $\dot{\phi}$ as:

$$\dot{\phi} < 0 \quad \rightarrow \quad \text{unloading}, \tag{2.44}$$

$$\dot{\phi} = 0 \quad \rightarrow \quad \text{neutral loading}, \tag{2.45}$$

$$\dot{\phi} > 0 \quad \rightarrow \quad \text{loading}. \tag{2.46}$$

Under loading state, further damage takes place and the damage threshold r must be updated. Taken into account Eq. (2.41) and (2.43),

$$\dot{r}\dot{F} = 0 \Rightarrow \dot{\phi} - \dot{r} = 0 \Rightarrow \dot{\phi} = \dot{r}. \tag{2.47}$$

Here, it is worth remembering that r is used to computed the current state of the internal damage variable representing the damage, i.e. $\mathcal{D}(r)$.

According to the above formulation, the local continuum damage model should define a suitable expression for the free energy density and a set of damage state variables degrading

the elastic properties, $d := \mathcal{D}(r, ...)$. Further, these damage state variables should be computed through the damage evolution law depending on a set of damage threshold variables r. In turn, these threshold variables must be defined as monotonic growing continuous variables associated with the loading functions ϕ. Hence, the local model should also propose the loading functions setting the limit between the elastic and inelastic regimes.

Therefore, the implementation of the continuum damage mechanics based consititutive models does not require any substantial modification of the standard finite element approximation of the balance of momentum problem. It only needs the definition and management of the state variables at the integration points. In this sense, the counterpart of the internal energy contribution stated previously is:

$$\Pi_{int}(\mathbf{u}, \boldsymbol{\mathcal{D}}) := \int_{\mathcal{B}} \Psi\left(\boldsymbol{\varepsilon}(\mathbf{u}), \boldsymbol{\mathcal{D}}\right) \mathrm{d}V. \tag{2.48}$$

Therefore, the implementation of a local continuum damage model in a standard FE-code should be straightforward because only the computation of the stress tensor defined in Eq. (2.14) is modified. The expressions for the discrete problem are also the same presented before. More details about the CDM theory and its implementation in a IBVP can be found in the works of Camanho et al. (2007), Maimí (2007), Murakami (2012), and Van der Meer (2010).

2.4.2 Phase field approach to brittle fracture

The phase field (PF) approach is a regularisation technique of the variational problem of brittle fracture proposed in the sense of the Griffith theory by Marigo et al. (2016). Following the PF, the discrete representation of a crack is smeared within the continuum by the definition of a functional representing the crack energy density (Bourdin et al. 2000, 2008; Miehe et al. 2010a,b). In turn, the crack energy density functional depends on the PF represented by a scalar variable and its spatial gradient, in line of the enhanced-gradient models. Therefore, the PF approach is a nonlocal approach that requires the solution of a coupled-field problem, namely: the displacement and phase fields. In the following, the basic principles fo the PF approach to brittle fracture are presented.

Let us postulate that the body described in Section 2.2.1 has an interior boundary Γ_{c} that represents a fully developed crack, see Figure 2.5. Further, let us remark the body forces $\boldsymbol{b}$ and external boundary conditions, $\bar{\boldsymbol{t}}$ and $\bar{\mathbf{u}}$, are the ones prescribed for the uncracked body. According to the Griffith theory of fracture and assuming static crack growth conditions, the internal energy functional governing the solution of the problem is:

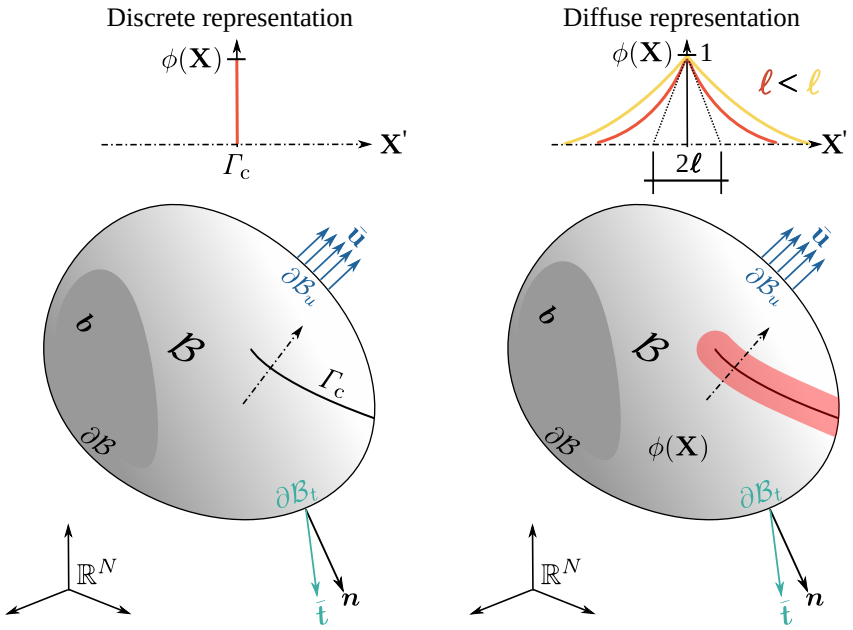

Figure 2.5: A cracked body subjected to body forces $\boldsymbol{b}$, displacements $\bar{\mathbf{u}}$ and tractions $\bar{\boldsymbol{t}}$, illustrating the discrete and diffuse (according to the phase field) representation of the crack.

$$\Pi_{int}(\mathbf{u}, \Gamma_c) = \int_{\mathcal{B}\setminus\Gamma_c} \Psi_e(\boldsymbol{\varepsilon}(\mathbf{u}))\, \mathrm{d}V + \int_{\Gamma_c} \mathcal{G}_c\, \mathrm{d}S, \tag{2.49}$$

where Ψ_e is the free elastic energy available in the solid, $\boldsymbol{\varepsilon}$ is the infinitessimal strain tensor defined in Eq. (2.13), and $\mathcal{G}_c$ is the critical energy release rate. Recalling the phase field approach, the crack boundary Γ_c is approximated over $\mathcal{B}$ through a functional representing the crack surface density $\gamma(\phi, \nabla\phi)$, such that:

$$\int_{\Gamma_c} \mathcal{G}_c\, \mathrm{d}S \approx \int_{\mathcal{B}} \mathcal{G}_c \gamma(\phi, \nabla\phi)\, \mathrm{d}V. \tag{2.50}$$

The arguments of the crack surface density functional are the phase field variable ϕ and its spatial gradient $\nabla\phi$. By definition, the phase field is a scalar field describing for the amount of equivalent crack surface at a material point and therefore, it can be related to the damaged state of the material point. Moreover, note that the later argument endows the aforementioned nonlocal character in the spirit of gradient enhanced models (Marigo et al. 2016). Here, following the notation used by Miehe et al. (2010b), the crack surface density

defined through the Ambrosio-Tortorelli functional (Ambrosio and Tortorelli 1990) is given by:

$$\gamma(\phi, \nabla\phi) = \frac{1}{2\ell}\left(\phi^2 + \ell^2 \nabla\phi \cdot \nabla\phi\right), \tag{2.51}$$

where ℓ is the so-called length scale parameter, which controls the size of the damage diffusion around the process region as depicted in Figure 2.5. Using Eq. (2.51) and (2.50), the internal energy contribution defined in Eq. (2.49) is approximated as:

$$\Pi_{int}(\mathbf{u}, \mathit{\Gamma}_{\mathrm{c}}) \approx \Pi_{int}(\mathbf{u}, \phi), \tag{2.52}$$

where the rigth hand term is defined as:

$$\Pi_{int}(\mathbf{u}, \phi) := \int_{\mathcal{B}} \Psi(\boldsymbol{\varepsilon}(\mathbf{u}), \phi)\, \mathrm{d}V + \int_{\mathcal{B}} \frac{\mathcal{G}_{\mathrm{c}}}{2\ell}\left(\phi^2 + \ell^2 \nabla\phi \cdot \nabla\phi\right)\, \mathrm{d}V. \tag{2.53}$$

In the previous expression, Ψ is the free energy functional modelling the degradation of elastic energy within the smearing transition zone that is characterised by ℓ, i.e. between a pristine ($\phi = 0$) and a fully-damaged ($\phi = 1$) state. Note that such representation is related to the CDM, where the internal state variables describe the thermodynamic state of a material point due to the development of micro-cracks and micro-voids. Let us assume in the following the most simple expression for the free energy density:

$$\Psi(\phi, \mathbf{u}) = (1 - \phi)^2 \Psi_{\mathrm{e}}(\varepsilon(\mathbf{u})) \tag{2.54}$$

Next, recalling the standard Galerkin-Bubnov method for the approximation of the two primary field variables ($\mathbf{u}$ and ϕ) and their spatial gradients, the semi-discrete form of the internal force vector of the stress equilibrium problem, which is the counterpart of Eq. (2.29), is given by:

$$\mathbf{F}^{u}_{int}(\mathbf{d}, \mathfrak{d}) = \mathcal{A}_{e=1}^{n_e}\left\{\int_{\Omega_e} (1 - \mathfrak{d})^2 \mathbf{B}^{\mathrm{T}} \boldsymbol{\sigma}\, \mathrm{d}V\right\}, \tag{2.55}$$

where $\mathfrak{d}$ is the vector arranging the nodal values of the phase field. In turn, the residual

corresponding to the evolution of the crack evolution problem governed by the PF is given by:

$$\mathbf{F}_{int}^{\phi}(\mathbf{d},\mathfrak{d}) = \mathcal{A}_{e=1}^{n_e}\left\{\int_{\Omega_e}\left[(\mathfrak{d}-2(1-\mathfrak{d})\mathcal{H})\,\boldsymbol{\mathcal{N}}_{\mathfrak{d}}+\ell^2\mathbf{B}_{\mathfrak{d}}^{\mathrm{T}}\nabla\mathfrak{d}\right]\,\mathrm{d}V\right\} \tag{2.56}$$

where $\boldsymbol{\mathcal{N}}_{\mathfrak{d}}$ is the interpolation operator for the relative displacements and $\mathbf{B}_{\mathfrak{d}}$ is the kinematic operator that approximates the spatial gradient of the phase field. Their specific expressions can be found in the works of Carollo et al. (2018), Molnár and Gravouil (2017), and Msekh et al. (2015). In turn, $\mathcal{H}$ is a field variable that accounts for the historical value of the crack driving state function $\tilde{\mathcal{D}}$ by setting:

$$\mathcal{H} = \max_{s\in\mathbb{T}}\left(\tilde{\mathcal{D}}^s\right) \quad \text{with} \quad \tilde{\mathcal{D}}^s = \frac{\Psi_{\mathrm{e}}^s}{\mathcal{G}_c/\ell} \tag{2.57}$$

where $s \in \mathbb{T} = [0, T]$ represents the full history process. Thus, this history field ensures two conconditions required to correctly model the evolution of a crack: (i) the irreversible condition preventing healing effects and (ii) the positiveness of the crack driving force enforcing for fracture growth.

Note that the phase field approach leads to a coupled-field problem in which the displacement field governs the balance of momentum and the phase field governs the evolution of the crack (or damage). Therefore, the solution of the two primary fields ($\mathbf{u}$, ϕ) must be computed at each time step. In the literature different approaches has been used for this purpose, monolithic, alternte minimization and staggered schemes. More details about the implementation of PF approach in the IBVP can be found, for instance, in Molnár and Gravouil (2017) and Msekh et al. (2015).

2.4.3 Cohesive zone model

The cohesive zone model (CZM) is a framework conceived to analyse the onset and propagation of cracks when the fracture process zone is non-negligible. Even though CZMs can be used to model the intralaminar failure, they are well suited to describe the interlaminar failure affecting laminated composites. The delamination is essentially a crack propagating within the region confined between two adjacent plies known as the interface. Therefore, the potential crack path where the delamination can occurs is known a priori. This fact brings the perfect scenario for a discontinuous modelling strategy using the interface element method (IEM) in conjunction with a CZM. The following describes the basis of the IEM - CZM strategy, emphasising how it can be justified in the balance of momentum equation.

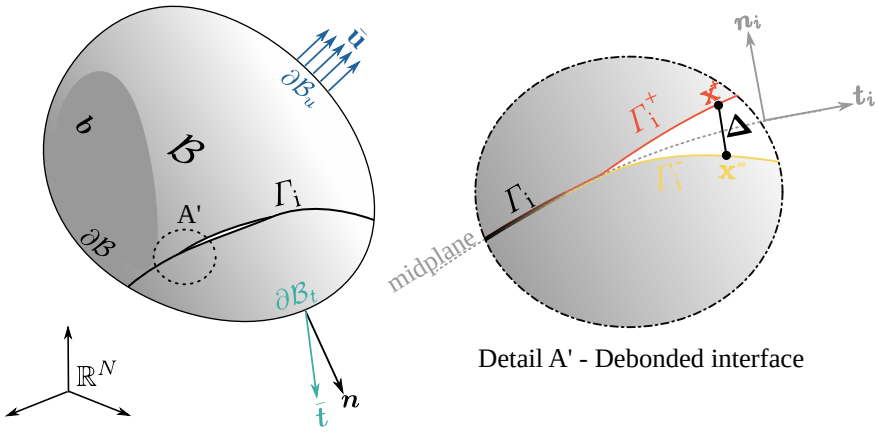

Figure 2.6: A body with a damaged interface subjected to prescribed body forces $\boldsymbol{b}$, displacements $\bar{\mathbf{u}}$ and tractions $\bar{\boldsymbol{t}}$, showing the kinematic representation of the displacement jump across the interface.

Let us postulate that the body described in Section 2.2.1 has an interface represented by an interior boundary Γ_i, as illustrated in Figure 2.6. Let us, for convenience, postulate that the displacement jumps field across the interface describes the configuration of the system at the interface itself. These jumps represent the crack opening and sliding of the interface. Mathematically, they are computed as the projection of the relative displacement of two homologous points, $\boldsymbol{X}^+ \in \Gamma_\mathrm{i}^+$ and $\boldsymbol{X}^- \in \Gamma_\mathrm{i}^-$, onto the mid-plane defined by the unit vectors $\boldsymbol{n}_i$ and $\boldsymbol{t}_i$, such that:

$$\boldsymbol{\Delta}(\mathbf{u}) = \boldsymbol{R}\left[\mathbf{u}(\boldsymbol{X}^+, t) - \mathbf{u}(\boldsymbol{X}^-, t)\right], \tag{2.58}$$

where $\boldsymbol{R}$ is the rotation operator from the global to the mid-plane coordinate system. Formally, it depends on the displacement field (Reinoso and Paggi 2014); however, for an infinitesimal rotation case, this dependency can be neglected. Finally, let us remark that the body forces $\boldsymbol{b}$ and external boundary conditions, $\bar{\boldsymbol{t}}$ and $\bar{\mathbf{u}}$, are the ones prescribed for the uncracked body. Considering those modifications, the internal energy functional governing the deformation of the solid can be expressed as:

$$\Pi(\mathbf{u}, \Gamma_\mathrm{i}) = \Pi_{\mathcal{B}}(\mathbf{u}) + \Pi_{\Gamma_\mathrm{i}}(\Gamma_\mathrm{i}), \tag{2.59}$$

where $\Pi_{\mathcal{B}}$ and Π_{Γ_i} are the energy contributions associated with the deformation process of

bulk (intralmainar) and interface (interlaminar) regions, respectively. On the one hand, $\Pi_{\mathcal{B}}$ is the same expression used for a body without an interface, i.e. Eq. (2.11). On the other hand, assuming that the interface has a negligible thickness and the unique dissipative mechanism is the debonding induced by cracks, Π_{Γ_i} is:

$$\Pi_{\Gamma_\mathrm{i}}(\Gamma_\mathrm{i}) \approx \Pi_{\Gamma_\mathrm{i}}(\mathbf{u}, \boldsymbol{\mathcal{D}}) = \int_{\Gamma_\mathrm{i}} \Psi_\mathrm{i}(\boldsymbol{\Delta}(\mathbf{u}), \boldsymbol{\mathcal{D}}) \, \mathrm{d}S, \tag{2.60}$$

where Ψ_i is the specific energy functional of the interface. As can be appreciated, Ψ_i not only depends on the displacement jump but also to a set of internal state variables $\boldsymbol{\mathcal{D}}$ in the sense of a damage mechanics framework. Accordingly, the work-conjugated variable stemming from the specific energy of the interface and the relative displacement jumps are cohesive tractions, which are defined as:

$$\boldsymbol{\tau} := \frac{\partial \Psi_\mathrm{i}}{\partial \boldsymbol{\Delta}} \tag{2.61}$$

At this point, the counterpart of the internal energy contribution of a body with interfaces considering a CZM is:

$$\Pi_{int}(\mathbf{u}, \boldsymbol{\mathcal{D}}) = \int_{\mathcal{B}} \Psi_\mathrm{e}(\mathbf{u}) \, \mathrm{d}V + \int_{\Gamma_\mathrm{i}} \Psi_\mathrm{i}(\boldsymbol{\Delta}(\mathbf{u}), \boldsymbol{\mathcal{D}}) \, \mathrm{d}S. \tag{2.62}$$

Next, recalling the standard Galerkin-Bubnov method and considering an interface element formulation for the interface region, the semi-discrete form of the internal force vector, which is the counterpart of Eq. (2.29), reads:

$$\mathbf{F}_{int}(\mathbf{d}) = \mathcal{A}_{e=1}^{n_e} \left\{ \int_{\Omega_e} \mathbf{B}^\mathrm{T} \boldsymbol{\sigma} \, \mathrm{d}V + \int_{\Gamma_{\mathrm{i,e}}} \mathbf{B}_\Delta^\mathrm{T} \boldsymbol{\tau} \, \mathrm{d}S \right\}, \tag{2.63}$$

where $\mathbf{B}_\Delta = \mathbf{R}\boldsymbol{\mathcal{N}}_\Delta\mathbf{L}$ is the kinematic jump-displacement operator that approximates the nodal dispacement jump into the integration points of the middle plane of the interface. Here, $\boldsymbol{\mathcal{N}}_\Delta$ is the interpolation operator for the relative displacements and $\mathbf{L}$ provides the difference between the displacements of the upper and the lower interface points. The specific form of these operators can be found in the works of Paggi and Reinoso (2015), Reinoso and Paggi (2014), and Reinoso et al. (2017b). Further, to alleviate the notation, the dependency with

the internal state variables is omitted in the previous expression.

As can be appreciated through the formulation presented above, CZM requires a new typology of elements to capture the displacement jump across the interface. Therefore, the main modification in the standard finite element approximation of the deformation problem is the definition of the so-called interface element technology. Besides this modification, the management of the internal state variables is also required. However, the flow of the numerical scheme is the same as the standard formulation. Finally, note in Eq. (2.62) that the bulk region can be modelled using different approaches, even the local or nonlocal continuum damage model. More details about the modelling using CZM and its implementation in the IBVP can be found in the works of Camanho et al. (2003), Goyal et al. (2004), and Turon et al. (2006).

3 Computational framework: Alya High-Performance simulation code

This chapter presents Alya, a simulation code designed to solve complex multi-physical problems in large-scale supercomputing facilities. A key aspect of Alya is that it is not a sequential simulation code, afterwards parallelised. It was conceived from scratch as a parallel code aimed to exploit the features of parallel programming models and the characteristics of the hardware to run with the highest efficiency standards. For instance, Alya has been used to perform large numerical simulations related to non-linear solid mechanics (Casoni et al. 2015; Vigueras et al. 2015), compressible and incompressible flow (Eguzkitza et al. 2013; G. Houzeaux et al. 2009; Guillaume Houzeaux et al. 2014), heat transfer (Gövert et al. 2018; Rodriguez et al. 2019), turbulence modelling (Lehmkuhl et al. 2019; Pastrana et al. 2018), electrical propagation (Santiago et al. 2018; Vázquez et al. 2011), particle transport (Calmet et al. 2018a,b) and chemistry (Mira et al. 2016), among other (Cajas et al. 2018). Concerning the development and maintenance of Alya, it is principally done by at the Department of Computer Applications for Science and Engineering (CASE) of the Barcelona Supercomputing Center – Centro Nacional de Supercomputación (BSC - CNS).

The following gives the main features of Alya, highlighting the most relevant for the context of the current thesis, namely: (i) structure of the code, (ii) parallel hierarchy, and (iii) parallel performance.

3.1 Code structure

The architecture of Alya is composed of several parts grouped in three blocks according to the performed task: kernel, modules and services. The kernel controls de work-flow of the execution including the reading of the input files and the writing of the solution, the management of the data structures related to the mesh and geometry, and the resolution of the algebraic system managing the linear and nonlinear solvers. Further, it is responsible of the communication between the other blocks and itself through well-defined interfaces. In turn, the modules are responsible of the solution of a particular physics and therefore, they contain the workflow and the information necessary to solve a set of partial differential equations, including the constitutive mathematical models and boundary conditions. Finally, the services are third-party libraries and tools related with code optimization (Garcia-Gasulla

et al. 2019), parallel performance (G. Houzeaux et al. 2010), mesh divisors (G. Houzeaux et al. 2013) and format writers (Artigues et al. 2017).

The solid mechanics constitutive equations are implemented in Alya using a discretization with the standard Galerkin method for a finite strain framework, considering a total-Lagrangian formulation (Casoni et al. 2015). Push-forward and pull-back relations between the different configurations are used for the stress measures conveniently depending on the material model selected. Regarding the nonlinearities arising from the governing equations (balance of linear momentum), explicit and implicit solution schemes can be used indistinctly within the solid mechanics' module by means of the generalised β-Newmark scheme. For the implicit scheme, a full Newton-Raphson method is used.

3.2 Parallel hierarchy

Alya exploits the three levels of parallelism mainly offer by modern supercomputers. At the node and chip levels, Alya splits the computational problem between different processes using a Master-Slave strategy (Vázquez et al. 2016). Firstly, the Master reads the information about the problem and divides it among the Slaves. In the context of the finite element problem, this division is the so-called domain decomposition which, in Alya, can be performed in sequential using the METIS (Karypis and Kumar 2009) or in parallel using a novel built-in method based on space-filling curves (Borrell et al. 2018). Once the partitioning finishes, each Slave stores all the necessary data to operate over the assigned subdomain. Afterwards, during the execution of the simulation, the Master executes and controls the global operations associated with the flow of the solution process, while the Slaves perform the local ones related to the subdomains. For instance, the Master is in charge of executing the algebraic solver, whereas the Slaves performs the assembly of the linearised system of equations, i.e. the construction of the local Jacobian matrix and the local right-hand side vector. This process is illsutrated in Figure 3.1.

The principal characteristic of the Master-Slave strategy in the context of the FEM is the communication between the different computational processes. The assembly procedure requires a few numbers of communications, whereas the algebraic solver usually requires a more significant quantity. This is because of the matrix-vector and vector-vector (dot) products operations, which are graphically represented in Figure 3.2 (Casoni et al. 2015; Eguzkitza et al. 2013). In Alya, this communication is performed using the programming model for distributed memories denominated message passing. Thus, each processor performs the assigned task assuming a local and private memory that can only be accessed by itself. Then, the processors communicate between them by sending and receiving messages with data. Due to these characteristics, this programming model is well-suited for parallelism at the node level. However, it can be also used at the chip level. In Alya, the communication uses

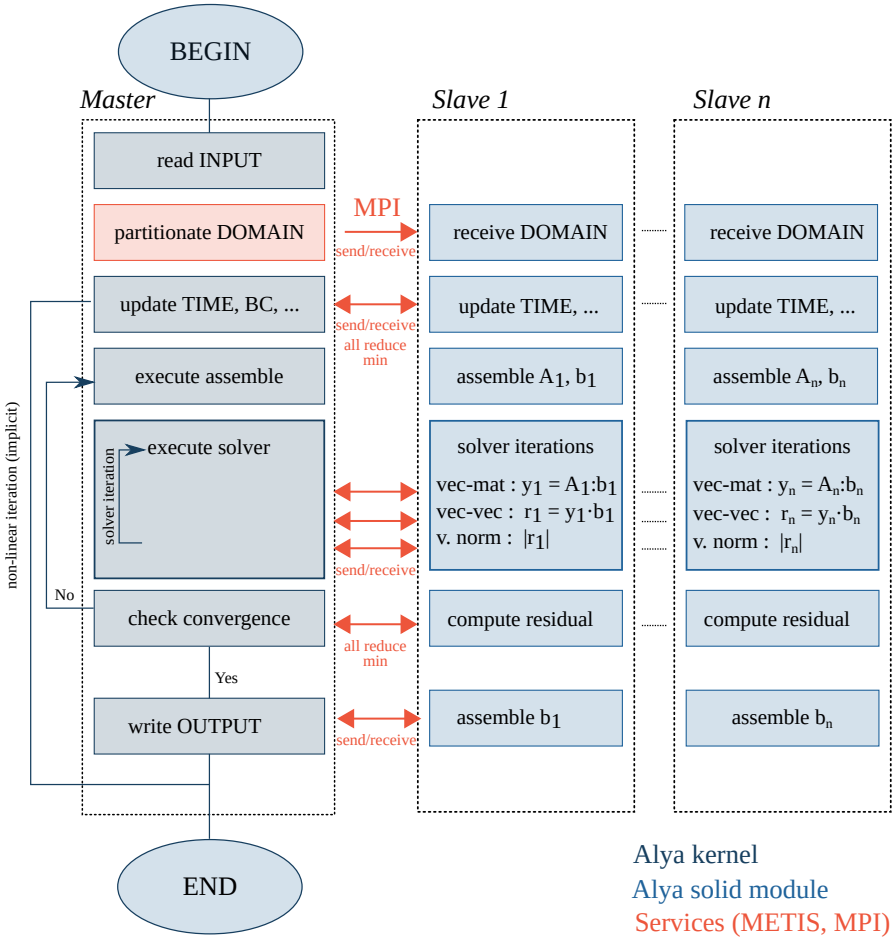

Figure 3.1: Work-flow of the parallel execution of a finite element simulation in Alya according to the master-slave strategy (Redrawn from (G. Houzeaux et al. 2009)).

the data types and functions defined in the standardized Message-Passing Interface (MPI) library (Gropp et al. 1999).

Beyond the Master-Slave strategy, Alya also considers other programming models, which exploits the second and third levels of parallelism. On the one hand, Alya offers the option to parallelise the most expensive nodal and elemental loops by opening threads. This parallelisation at the chip level makes use of of the directives defined in the OpenMP library (Dagum and Menon 1998). Contrary to the MPI, OpenMP is a multiprocessing programming model, which divides the work in different threads and assumes a shared memory among them. Hence, communication between processes is implicit by accessing the same data structure.

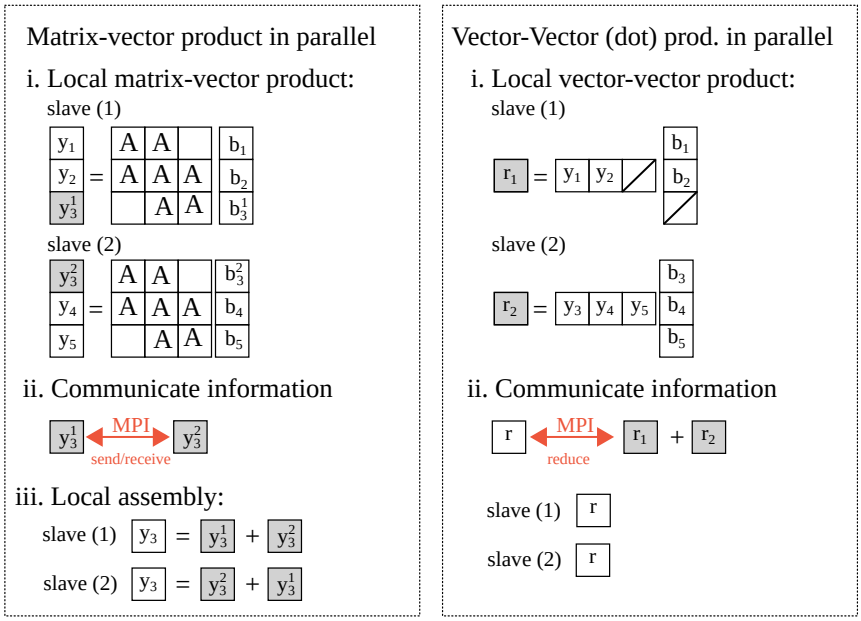

Figure 3.2: Matrix-Vector and Vector-Vector (dot) product in parallel according to the message pass programming model. The squares represent an item of the matrix or vector. The white ones are those having the final value, whereas the grey ones are those items having a partial value and therefore, are the ones that communicate. (Casoni et al. 2015; Eguzkitza et al. 2013).

On the other hand, Alya includes vectorisation techniques in some functions of the kernel exploiting the concurrency capacities of the third level of parallelism (García-Rodríguez et al. 2018b). These techniques accelerate the execution of the processes by maximising the potential of the hardware guiding the compiler with some specific directives. Finally, the third level of parallelism is used to accelerate some algebraic solvers. Thus, Alya has some built-in solvers programmed to run in Graphical Processing Units (GPU), using for instance the capabilities given by the OpenACC (Wienke et al. 2012).

3.3 Parallel performance

The parallel performance of a simulation code is obtained by performing some benchmark tests. In these tests, the same computational problem with a different number of processors (np) is executed to obtain quantitative values of efficiency in terms of the execution time. Formally, the parallel efficiency (E_{np}) is the ratio between the achievable (S_{np}) and the maximum (S_{max}) speedups of the parallelisation (Magoulès et al. 2016). Considering that the ideal speed up is the number of processors, i.e. $S_{max} = np$, it is postulated that:

$$E_{np} = \frac{S_{np}}{S_{max}} \tag{3.1}$$

where S_{np} is defined as the ratio between the execution time on one processor (T) and on np processors (T_{np}):

$$S_{np} = \frac{T_{np}}{T} \tag{3.2}$$

Concerning the parallel performance of Alya, it has been demonstrated their efficiency and scalability up to several thousands of processors for different physical problems and different hardware architectures, see previous references and Figure 3.3. It is noteworthy the parallel performance obtained in the Blue Waters supercomputer hosted in the National Center for Supercomputing Applications (NCSA), located at the University of Illinois at Urbana-Champaign (Vázquez et al. 2016). In this case, Alya achieved a parallel efficiency of 85% running into 100,000 cores using a mesh of 3.416B of elements.

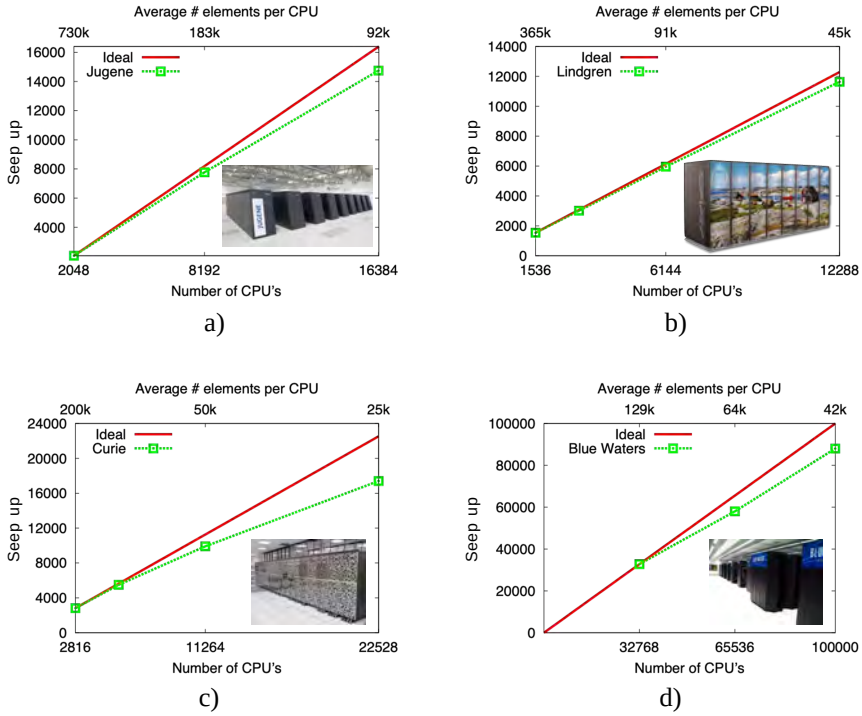

Figure 3.3: Speed-up of Alya code in different supercomputers: a) Jugene - Blue Gene/P (Germany), b) Lindgren - Cray XE6 (Sweden), c) Curie - BullX (France), and d) Blue Waters - Cray XE6 (USA).

Part II

Scope of the Publications, Results and Discussion

4 A high-performance computational framework for virtual testing of composite structures (ALYA-VITECOST)

This chapter highlights the novelties of the models developed and used in the context of this thesis. In this sense, the following sections address the main characteristics of the models, whereas the specific details can be found in the articles supporting this thesis. Regarding the structure of this chapter, the first and second sections present, respectively, the local and nonlocal continuum damage models, both aimed for modelling the intralaminar failure. Then, the third section describes the cohesive zone model used to model the interlaminar failure. Finally, the fourth section presents the formulation proposed for coupling between the nonlocal continuum damage model and the cohesive zone model.

4.1 Local continuum damage model for the intralaminar failure

A local continuum damage model formulated and implemented in the context of the current dissertation has been published in the paper entitled **"3D transversally isotropic constitutive model for advanced composites implemented in a high-performance computing code"** (Quintanas-Corominas et al. 2018). Paper A presents its manuscript version.

The formulation of the local damage model is rooted in the continuum damage mechanics and follows the framework used by Maimí et al. (2007a,b). It has a novel formulation conceived for modelling the onset and evolution of the intralaminar damage mechanisms arising from a 3-dimensional stress state, especially the mechanisms related to the matrix failure. In this sense, three loading functions are defined to predict the breakage and kinking of the fibres and the cracking of the matrix. As illustrated in Figure 4.1, the proposed loading functions match the uniaxial strengths, but at the same time, proportionate enough flexibility to describe a wide range of FRP. Regarding the degradation of the elastic properties, five laws are defined to govern the evolution of the damage state variables. Each law is formulated as a piecewise linear function aimed at representing the arbitrary shape of the uniaxial cohesive law. Hence, the proposed formulation assumes that the cohesive law is a physical property

of the material, which can be obtained experimentally (Ortega et al. 2016). In addition, the expressions of the damage evolution laws make use of the crack band theory proposed by Bažant and Oh (1983), intending to ensure the energy objectivity with regards to the mesh size.

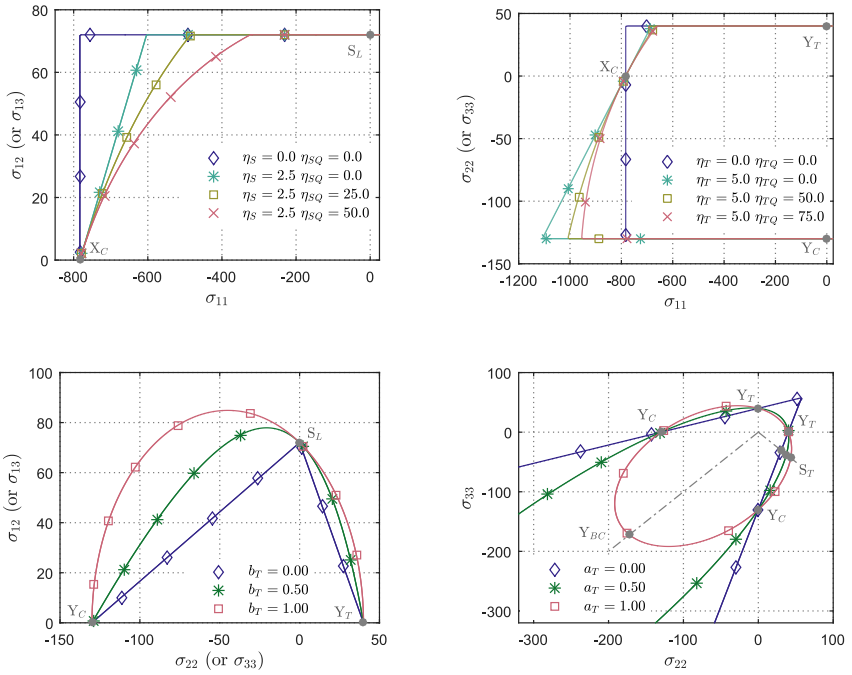

Figure 4.1: Influence of the shape parameters on the loading functions concerning the local continuum damage model at the onset of damage (Quintanas-Corominas et al. 2018).

4.2 Nonlocal continuum damage model for intralminar failure

The nonlocal continuum damage model formulated and implemented in the context of this thesis has been published in the paper entitled "**A phase field approach to simulate intralaminar and translaminar fracture in long fiber composite materials**" (Quintanas-Corominas et al. 2019a). In Paper B can be found its manuscript version.

The formulation of the nonlocal continuum damage model is rooted in the phase field approach to the brittle fracture problem presented by (Bourdin et al. 2000), whose basics principles are presented in Section 2.4.2. The novelty of the presented formulation is the capability to model the anisotropic response that characterises FRP composites. For this

purpose, the functionals defining the elastic energy density and the crack surface density are modified. It is proposed to use the expression of the free energy density of the local continuum damage model presented in Paper A as the functional of elastic energy density. In turn, a structural tensor is introduced in the definition of the crack surface density functional in order to account for different regularisation lengths (Gültekin et al. 2018, 2016). Besides these modifications, the energetic force that drives the phase field evolution is divided into several contributions, one for each damage mechanism. This strategy enables to model independently the initiation of each damage mechanisms but not their growth. The fact of using only one phase field and therefore a single damage-like variable imposes a simultaneous degradation of the elastic properties. For this reason, it is considered that the proposed formulation is between the mesoscopic and macroscopic modelling assumptions.

The numerical scheme implemented to solve the coupled-field problem is a modified version of the alternate minimisation scheme used by Bourdin et al. (2008). The principal objective of this modified version is to preclude the necessity of using a bound-constrained optimisation solver. This necessity is, in part, imposed by the irreversibility evolution condition of the damage represented by the phase field. On the one hand, it is used the strategy based on the posterior projection of the solution, which was proposed by Lancioni and Royer-Carfagni (2009). On the other hand, the phase field value is fixed when its value is close to one, i.e. when the material points are almost completely damaged. Thanks to this strategy, a standard Netwon Raphson method can be used to obtain the solution of the phase field problem.

4.3 Cohesive zone model for interlaminar failure

The cohesive zone model implemented in the context of this thesis is the recent formulation presented by Turon et al. (2018). In turn, the formulation implemented for the interface element techonology is the one presented by Reinoso and Paggi (2014).

The new formulation implemented improves the accuracy of the original one (Turon et al. 2006, 2007) with regards the behaviour under mixed-mode loading conditions. For this purpose, the expression for the penalty stiffness is modified to make it dependent on the current mixed-mode ratio. Regarding the constitutive law, a bi-linear traction-separation law governs the response of the interface as in the original formulation, see Figure 4.2. The first part of the law models a fictitious elastic response ensuring the connection between the crack flanks before the onset of the damage, while the second part models the linear softening up to the propagation of the delamination. The onset and propagation criterion are those proposed by Benzeggagh and Kenane (1996) and González et al. (2014), respectively. Further, the formulation ensures the thermodynamic consistency of the debonding process, even under a variation of the mixed-mode ratio.

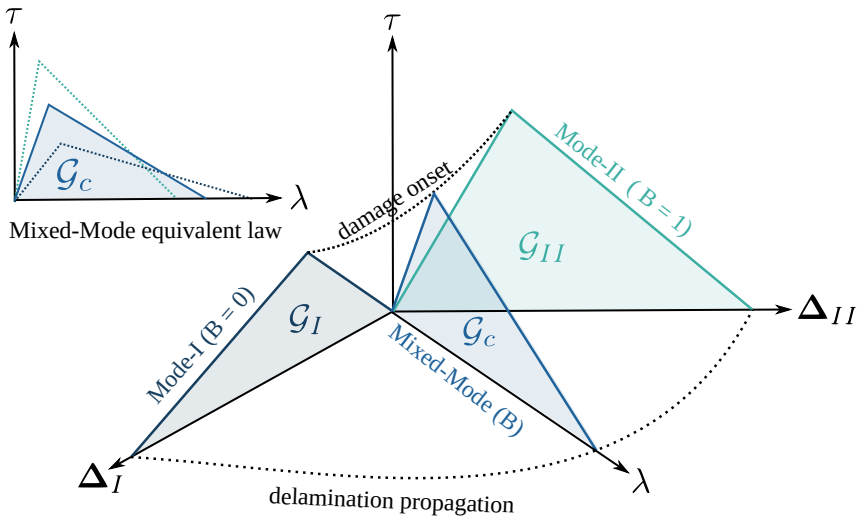

Figure 4.2: Schematic representation of the equivalent cohesive law for given local mode mix ratio B according to the (Turon et al. 2018).

Although the formulation of the cohesive zone model and the interface element technology are not new, some of the aspects of their implementation are novel. In this sense, their implementation is aimed to run efficiently in a high-performance computing environment. For instance, the computation of the material tangent tensor is performed using a different method to the one used by Turon et al. (2018). In their work, they use a numerical method based on small perturbations of the displacement jump to approximate the material tangent tensor as done by Martínez et al. (2008). On the contrary, the implementation in the context of this thesis evaluates the material tangent tensor using the complex step derivative approximation (CSDA) (Martins et al. 2003).

4.4 Strategy for coupling the intralaminar and interlaminar failure

The strategy for coupling the nonlocal damage model for the intralminar failure and the cohesive zone model for the interlaminar one is presented in the paper entitled "**A phase field approach enhanced with a cohesive zone model for modelling delamination induced by matrix cracking**" (Quintanas-Corominas et al. 2019b). In Paper C can be found the submitted version of the article.

The strategy for coupling the intralaminar and interlaminar failure is based on the framework presented by Paggi and Reinoso (Paggi et al. 2018; Paggi and Reinoso 2017). According to their framework, the cracking of a body with interfaces can be modelled using a nonlocal damage model based on the phase field approach for the bulk region and a cohesive zone

model for the interface region. The novelty of the proposed formulation is in both the constitutive models and how the coupling strategy. On the one hand, the constitutive models are the nonlocal damage model and cohesive zone model presented in Sections 4.2 and 4.3, respectively. On the other hand, the strategy to couple both models exploits the physical meaning of the damage and phase field variables. In general terms, both variables represent the ratio of the cracked area of a material point. Based on this interpretation, the damage evolution law of the cohesive zone model is redefined to include not only the dependence with the displacement jump but also with the phase field. Hence, the intralaminar and interlaminar failures are coupled through the phase field variable. The traction-separation law of the cohesive zone model resulting from this coupling strategy is illustrated in Figure 4.3. Finally, it is worth mentioning that the proposed approach retains the qualities of both models, such as the accuracy of the mixed-mode loading of the cohesive zone model.

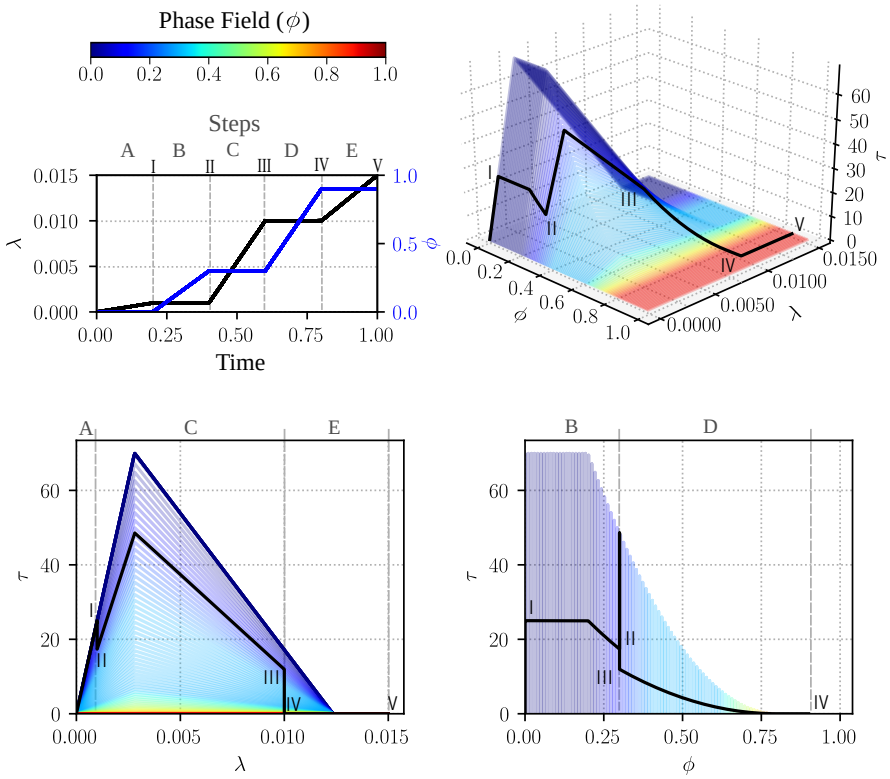

Figure 4.3: Cohesive law response according to the coupling strategy proposed in Quintanas-Corominas et al. 2019b. Rainbow coloured map represents the cohesive law for a fixed initial phase field value, while the black line illustrates a loading cycle combining phase field and equivalent opening.

5 Results and discussion

This chapter presents and discusses the main results, showing the capabilities of the models developed and demonstrating the fulfilment of the objective of the present thesis, namely, the implementation of a framework for performing virtual testing of composites structures on the mesoscopic length scale. The results are grouped according to the virtual test to facilitate the discussion. The acronyms used through this chapter to refer the models are listed in Table 5.1, while the numerical tests herein presented are summarised in Table 5.2.

Acronym	Description	Section
CDM	Local continuum damage model	4.1
PFM	Phase field model (nonlocal model)	4.2
CZM	Cohesive zone model	4.3
PFM-CZM	Coupling model between PFM and CZM	4.4

Table 5.1: Acronyms used for referring the damage models implemented in the context of the thesis.

Virtual Test	Failure mode	Model	Section
Open hole	Intralaminar	CDM	5.1
Transverse cracking	Intralaminar	CDM / PFM	5.2
Out-off-axis	Intralaminar	PFM	5.3
Mode-I/II delamination	Interlaminar	CZM	5.4
4-point bending	Intralaminar & Interlaminar	CZM-PF	5.5
Compact tension	Translaminar	PFM / PFM	5.6

Table 5.2: Virtual tests simulated in the context of the thesis.

5.1 Open hole

The virtual test consists of an open hole specimen subjected to tensile loads. The principal objective is to demonstrate that the formulation of the CDM predicts both the ultimate strength and failure pattern with reasonable accuracy. In this sense, it is intended to examine whether the use of very refined meshes reduces the dependency of the failure pattern with the orientation of mesh. The following presents the main results and discussions regarding the numerical predictions, while more specific details can be found in Paper A.

The open hole specimen is a laminate of IM7/8552 unidirectional plies stacked according to the following sequence: $[90/0/+45/-45]_{3s}$. Figure 5.1 shows a sketch of the geometry and loading conditions. Regarding the computational model, three meshes with different levels of refinement are considered, namely: n = 1, 2 and 4. Here, n indicates the number of elements defined per ply in the direction of the thickness. More specific details regarding material properties, mesh characteristics, and boundary conditions are given in Paper A.

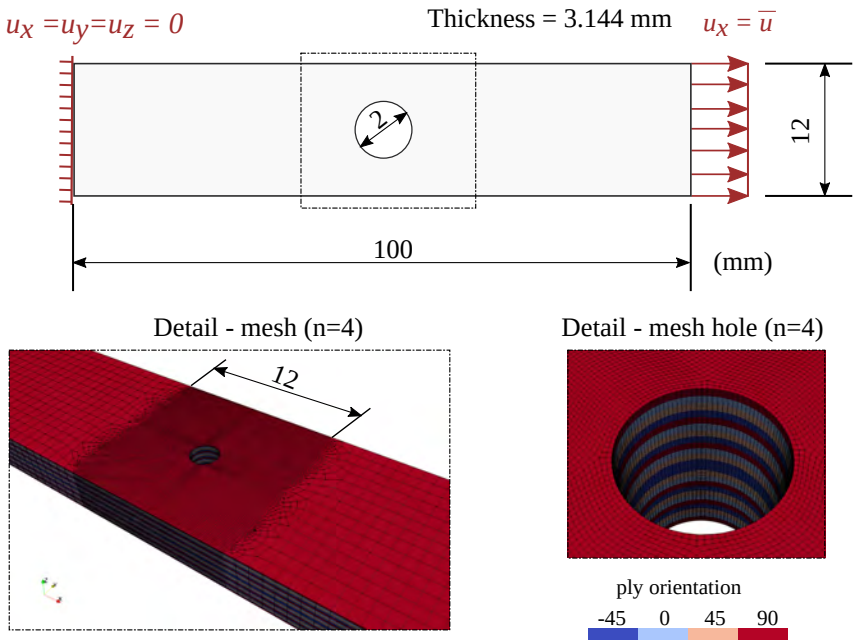

Figure 5.1: Sketch of the open hole specimen loaded in tension, illustrating the boundary conditions and a detail of the FE mesh.

The numerical predictions of the stress-strain curve are shown in Figure 5.2. The curves demonstrate that the model predicts with reasonable accuracy the experimental strength when the level of refinement is n = 2 or n = 4. Moreover, for these levels of discretisation, the results

also demonstrate that the model captures the initiation of the damage correctly. The initiation of the damage occurs around the 200 MPa as can be identified by the change of the slope in the stress-strain curve (Reinoso et al. 2017a). On the other hand, the underestimation of the ultimate strength predicted by the coarse refinement level, n = 1, is because, after the damage localisation, the kinematics of the deformation is not described with enough precision. As a consequence, the stress field is overestimated, which accelerates the localisation of the damage and provokes a premature collapse of the specimen.

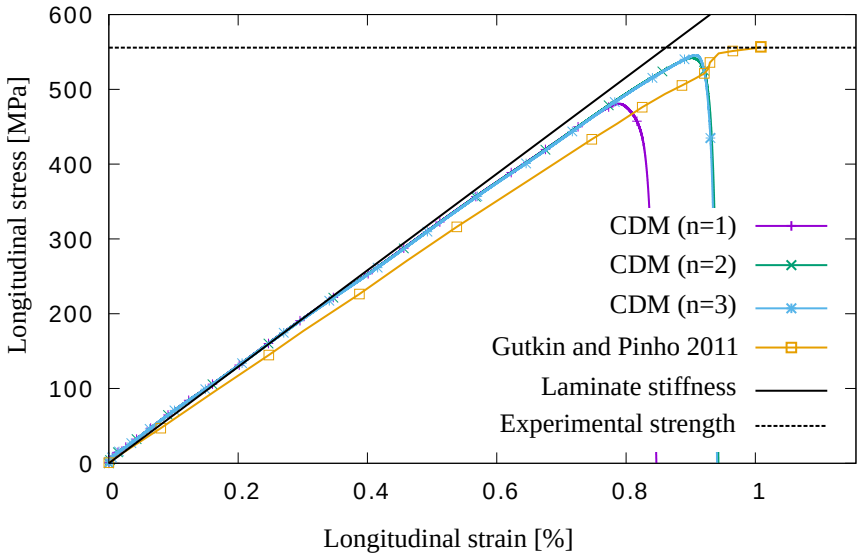

Figure 5.2: Mechanical response numerically predicted using the local continuum damage model (CDM) for the open hole test considering three levels of discretisation.

The failure pattern just before the ultima strength is illustrated for the level of refinement n = 4 in Figure 5.3. Considering that the predicted failure pattern is almost symmetric, the figure only shows the plies of the top half part of the specimen grouped according to the ply orientation. A global perspective of the results indicates that the failure pattern is in agreement with the expected failure mode observed in experiments: (i) 90º plies mostly have matrix failure under tension (d_K), (ii) ± 45° plies have matrix failure under shear (d_G) as the most predominant, and (iii) 0º plies have fibre failure (d_1). However, a closer look reveals that, despite using a fine mesh, the damage localises in a band of elements aligned along with the mesh. This is a well-known issue of the local continuum damage models. This alignment is partly caused because the information regarding the damage state is local. When the damage initiates in one material point, the surrounding ones do not notice the damage because, in a standard FE formulation, the unique information shared between two elements is the displacement field on the nodes that they have in common. Then, the usage of thin

meshes only alleviate the issue related to the localisation but does not solve it completely.

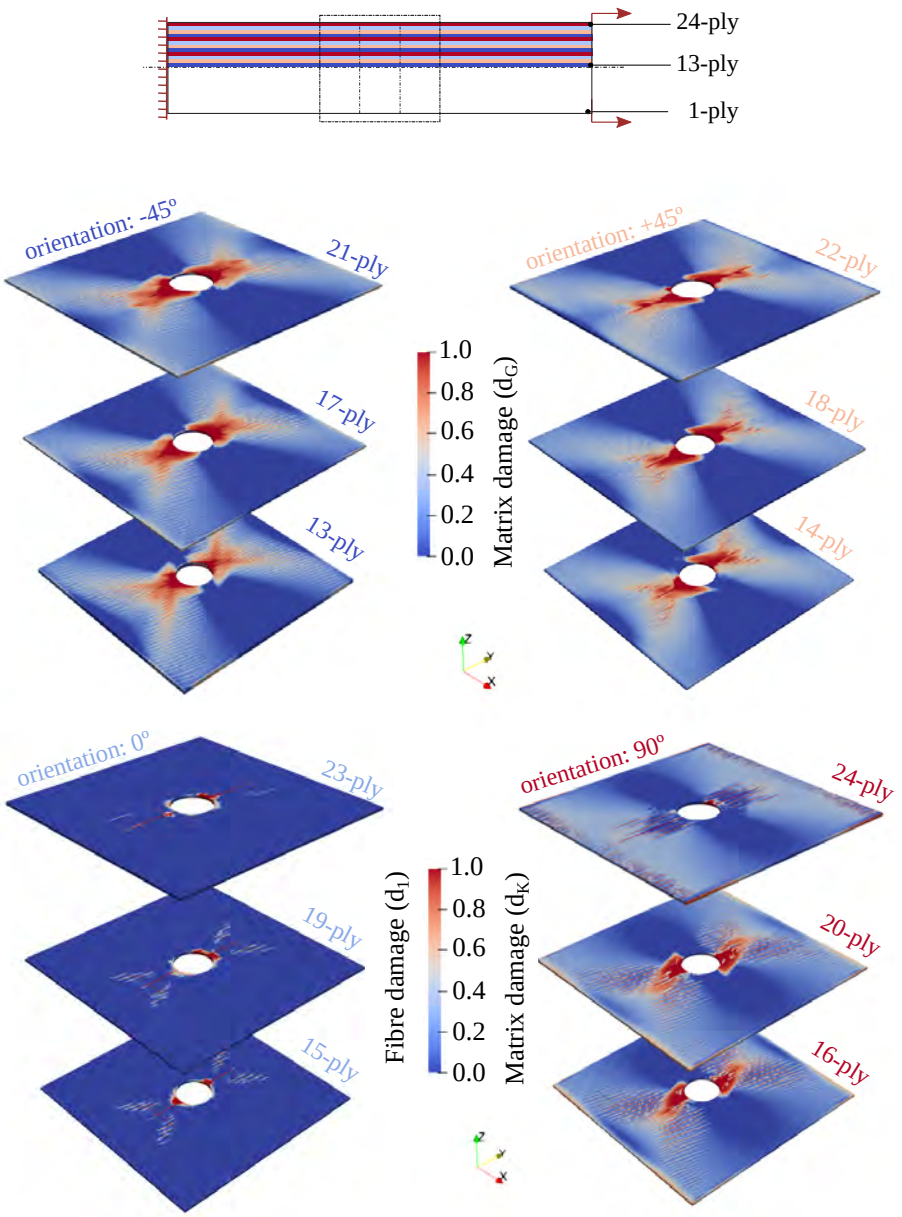

Figure 5.3: View of the damage pattern predicted by the local continuum damage model (CDM) for the open hole test.

5.2 Transverse cracking

The virtual test consists of a cross-ply laminate subjected to tensile loads. The main objective of this test is to demonstrate the reliability of the PFM for modelling the intralaminar failure. For this purpose, the results concerning the cracking of the central plies and ultimate strength predicted by the PFM are compared with the predictions of the CDM. The following presents the principal results and discussion supporting the comparison. Further details of the comparison can be found in Paper B, while specific information of the simulations using the CDM are given in Paper A.

The specimen used for the comparison is a cross-ply laminate made of IM7/8552 unidirectional plies with the following stacking sequence: $[0_2/90_n]_s$. The comparison is performed for two different number of central plies: $n = 1$ and $n = 4$. Figure 5.4 shows a sketch of the geometry and loading conditions. The figure also illustrates the strategy used for defining an initial defect in the computational models that employ the PFM. The specific details regarding material properties, mesh characteristics, and boundary conditions can be found in the corresponding articles, Paper A and Paper B. Finally, it is worth mentioning that an implicit scheme considering quasi-static conditions are used to run the simulations.

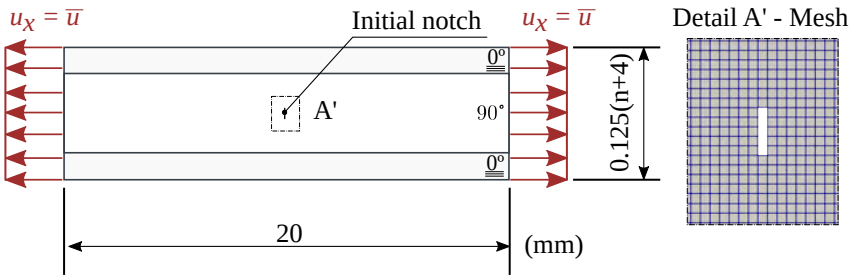

Figure 5.4: Sketch of the transverse cracking specimen loaded in tension, illustrating the boundary conditions and a detail of the FE mesh around the initial defect.

The stress-strain responses predicted by both approaches are depicted in Figure 5.5. A comparison of the curves shows that the predictions regarding the mechanical response of the specimen until the ultimate failure are very similar. Further, the failure stress is in reasonable agreement with the one predicted by the maximum stress criterion of the fibre (Maimí et al. 2011, 2008). In the current configuration, this criterion gives consistent predictions because of the 0º plies are supporting almost all the load. Despite this good agreement between both methods, the PFM predicts a more substantial loss of longitudinal stiffness after the onset of the first transverse crack. This is because the damage field in the PFM extends through the interfaces between the 0º and 90º plies, damaging the 0º plies and inducing a significant loss of their bearing capacities. Note that, for the simulated configuration, this issue is magnified

due to the 0º plies are bearing almost all the load. Otherwise, the loss of bearing capacities would be less relevant.

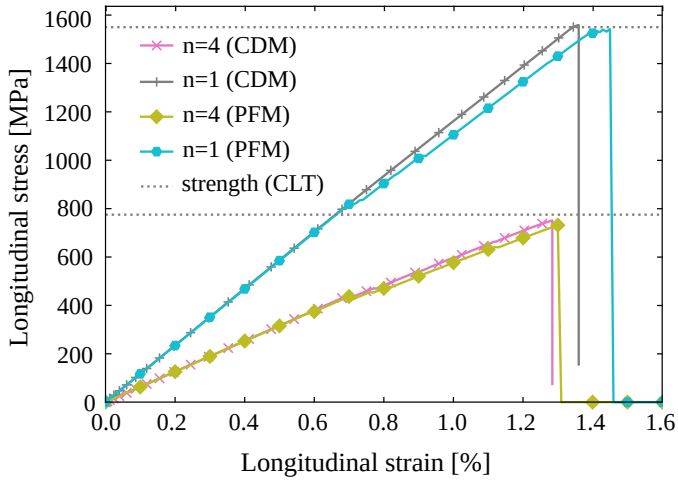

Figure 5.5: Comparison of the mechanical response numerically predicted using the local and nonlocal continuum damage model (CDM and PFM) for the transverse cracking test considering two different thickness.

The failure patterns at 1% of longitudinal strain predicted by the PFM and CDM are shown in Figure 5.6. The crack density increases as the thickness of the 90º plies decreases, which is consistent with the experimental observations reported in literature (Varna and Berglund 1991). Further, for $n = 4$, both models predict similar crack density, whereas, for $n = 1$, the crack density is higher in the CDM. Considering that the stress relaxation precludes the localisation of new crack inside the regularisation zone of the PF, the crack density of the simulation using the PFM seems to be ruled by the regularisation length. Therefore, the crack density should increase by reducing the PF length. Then, it would be possible to have similar predictions to the ones of the CDM. However, it would not be useful for the comparison objective of this test. In that case, the PFM would impose a finer mesh, and therefore, both models would not use a similar mesh size.

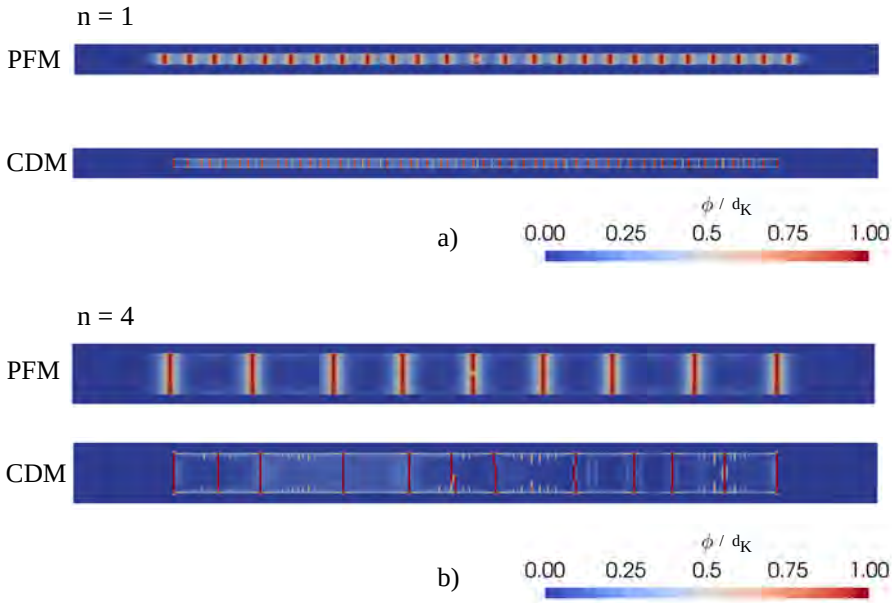

Figure 5.6: Comparative view of the failure pattern predicted using the local and nonlocal continuum damage model (CDM and PFM) for the transverse cracking test.

5.3 Out-off-axis

The virtual test consists of a unidirectional specimen subjected to tensile loads, whose fibres are oriented 10º respect to the direction of the loading. This type of specimen is so-called out-off-axis tests, and here it is used to demonstrate one of the virtues of the nonlocal formulation of the PFM. That is the capacity of predicting the failure pattern in a case which the crack path is governed by the fibre orientation governs rather than the stress field. According to Van der Meer and Sluys (2009), in such situations, the homogenization of the internal structure assumed on the mesoscopic and macroscopic scale precludes the capacity of the continuum damage for providing accurate prediction regarding the crack path. The reason is that the constraining effect of the fibres, which guides the orientation of the crack propagation, is not modelled. However, the nonlocal formulation proposed for the PFM can deal with this situation. The following presents the results concerning this virtual test, while more specific details can be found in Paper B.

The out-off-axis specimen is a unidirectional tape made of a generic glass/epoxy material with the fibres oriented 10º respect to the longitudinal axis. Figure 5.7 depicts the sketch and loading conditions of the test, and shows a detail of the FE mesh. Following the experimental setup, the specimen has oblique ends with an angle of 54º respect to the loading direction in

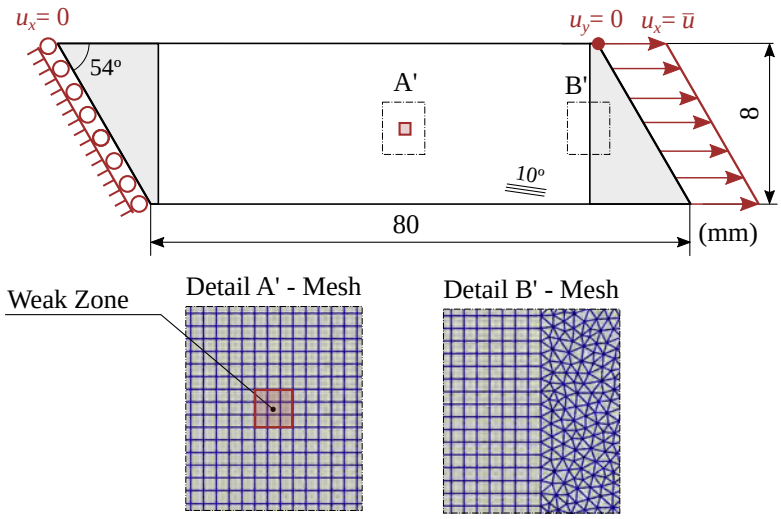

Figure 5.7: Sketch of the out-off-axis specimen loaded in tension, illustrating the boundary conditions and a detail of the FE mesh.

order to generate an homogeneous in-plane shear stress state. For this test, the PFM uses the elastic threshold in the whole model, except for a zone in the centre of the specimen. This strategy is used to define an area containing a defect that, from a numerical point of view, is something required by the numerical problem due to the homogeneous stress state. Without this defect, the localisation of the damage would be erroneous. More specific details about the material properties and computational model can be found in the Paper B.

The numerical prediction regarding the mechanical response is depicted in Figure 5.8. The ultimate in-plane shear stress predicted by the PFM is in close agreement with the shear strength obtained experimentally. Moreover, no significant loss of the stiffness priory to the catastrophic failure is observed in the mechanical response, which is thanks to the definition of the elastic threshold.

Figure 5.9 illustrates the failure pattern at the end of the simulation, i.e. after the catastrophic collapse. The numerical crack path is in agreement with the experimental observation. Thus, the direction of the crack predicted by the PFM is reasonably close to the orientation of the fibres, i.e. 10º. Note that, close to the free edge, the path is slightly curved due to the normality condition, $\nabla\phi \cdot \boldsymbol{n} = 0$, which is a natural condition stemming from the phase field formulation (Molnár and Gravouil 2017). Despite this misprediction, the accuracy of the crack direction is significantly better to the one predicted using a local continuum damage model, see the simulations reported by Van der Meer and Sluys (2009). Hence, this test demonstrates not only that the PFM is not dependent on the mesh orientation but also the potential of the formulation in problems governed by the fibre orientation instead of the

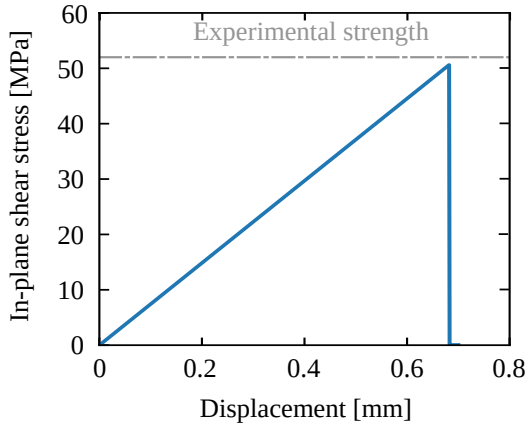

Figure 5.8: Mechanical response numerically predicted using the nonlocal continuum damage model (PFM) for the out-off-axis tensile test.

stress field.

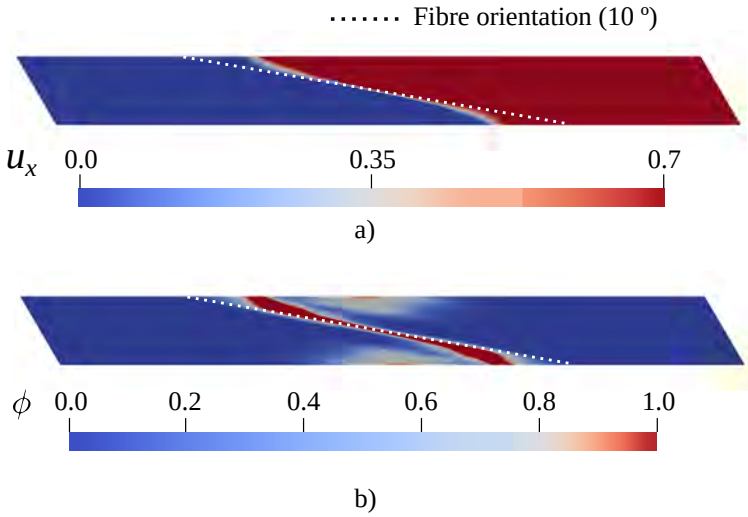

Figure 5.9: View of the final patterns predicted by the nonlocal continuum damage model (PFM) for the out-off-axis tensile test: a) displacement field and b) phase field (damage).

5.4 Mode-I/II delamination

This simulations concerns the virtual tests of two standardized mode delamination tests, which are typically utilised to characterise the interface mode-I and mode-II fracture toughness, namely Double Cantilever Beam (DCB) and End-Notched Flexural Test (ENF). The objective of these simulations is twofold. On the one hand, it is intended to validate the correct implementation of the CZM and interface elements in Alya. On the other hand, these tests are also used to show that the coupling strategy proposed for the PFM-CZM retains the qualities of the original formulation concerning the modelling of pure delamination failure. In the following, the numerical predictions presented in Paper C are summarized.

The geometry and loading conditions of the specimen considered in each configuration (DCB and ENF) are shown in Figure 5.10. In both cases, the laminate of the specimen is made of unidirectional carbon fibre reinforced plies, which material properties are given by Turon et al. 2018. Regarding the numerical model, a structured mesh conformed of 4-node quadrilateral elements is used, whereas the boundary conditions are those illustrated in Figure 5.10. Finally, the PFM is used for the bulk region.

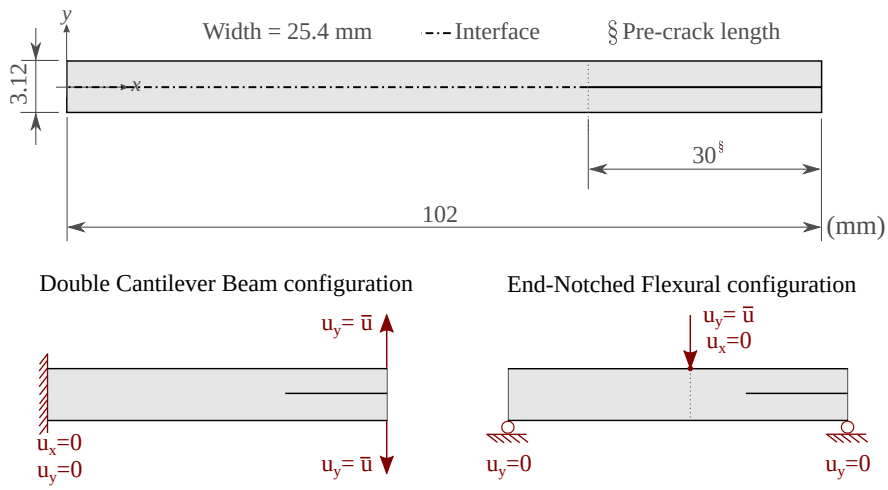

Figure 5.10: Sketch of the specimen representing the boundary conditions corresponding to a Double Cantilever (DCB) and End-Notched Flexural (ENF) tests.

The load versus displacement curve for the DCB and ENF predicted by the current framework, and the Linear Elastic Fracture Mechanics (LEFM) curves (González 2011) are shown in Figure 5.11. As can be appreciated, the predictions display an excellent agreement with respect LEFM results in both cases. As expected, in this analysis the bulk region is not affected by the opening of the interface thanks to in the proposed formulation the driving force that governs the increase of the PF is not affected when the failure is driven purely by a

delamination mechanism. For this reason, it is expected that the current framework can be used in those cases previously analysed with the cohesive zone model.

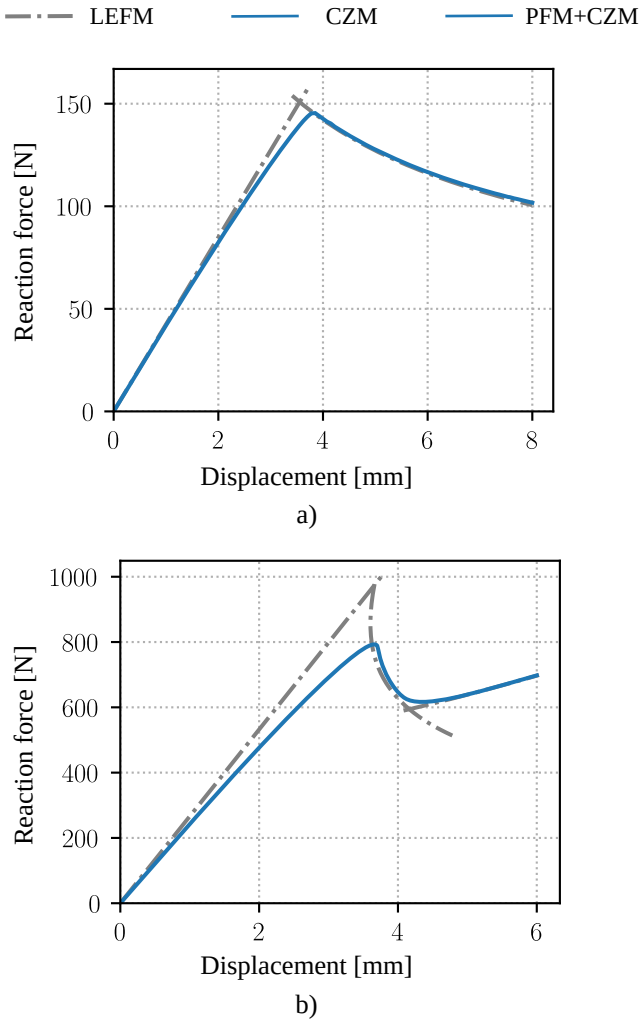

Figure 5.11: Mechanical response numerically predicted using the cohesive zone model (CZM) and the enhanced formulation with the nonlocal continuum damage model (PFM-CZM) concerning: a) Double Cantilever Beam (DCB) and b) End-Notched Flexural (ENF) configurations.

5.5 4-points bending

The virtual test consists of a specimen subjected to a 4-point bending loading configuration. The principal objective of this test is to show the capabilities of PFM-CZM for predicting the behaviour of delamination induced by matrix cracking correctly. The more representative results are summarised in the following, while specific details of the study can be found in Paper C.

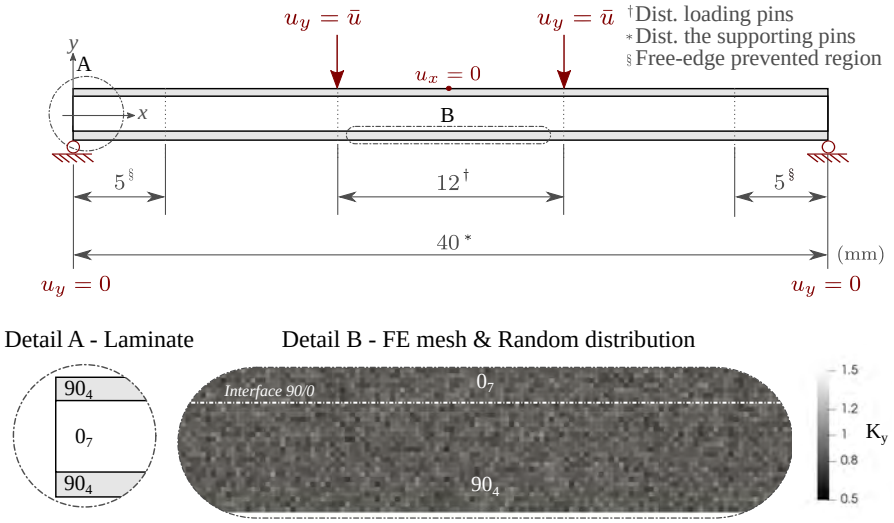

Figure 5.12: Sketch of the 4-point bending test showing the boundary conditions and a detail of the laminate as well as the random distribution applied to the strengths at the mesh level.

The simulated specimen is a cross-ply laminate made of HTA/6376 unidirectional plies, which stacking sequence is $[90_4/0_7/90_4]$. The sketch of the specimen with the dimensions and loading conditions is depicted in Figure 5.12. As shown in the same figure, a random field for the transverse strength value is defined to mitigate the issues related to the correct localisation of the damage in the zone of constant bending, i.e. the region between the loading pins. More details about the material properties, mesh characteristics, and loading conditions are given in Paper C.

Observation	Exp.	PFM-CZM	Units
Onset transverse cracks	62	67.5	MPa
Crack saturation	0.7	0.5	cr/mm
Total number of cracks	15	14	-
Average space between cracks	2	2.25	mm

Table 5.3: Comparison of the experimental and numerical observations concerning the 4-point bending test (Mortell et al. 2014).

The experimental observations reported by Mortell et al. (2014) and the ones predicted by the simulation are listed in Table 5.3. Direct comparison of both observations reveals that the predictions of PFM-CZM are in close agreement with the experimental findings. Despite the good results, it seems that the size effect reported by Mortell and coworkers is not captured correctly. They reported that as thicker is the outer ply clustering, lower is the stress level at which the first transverse crack appears. In turn, the stress level predicted by the PFM-CZM is close to the nominal transverse strength and therefore, slightly higher than the experimental stress. This overestimation of the onset stress can in part be attributed by an unfit definition of the random field.

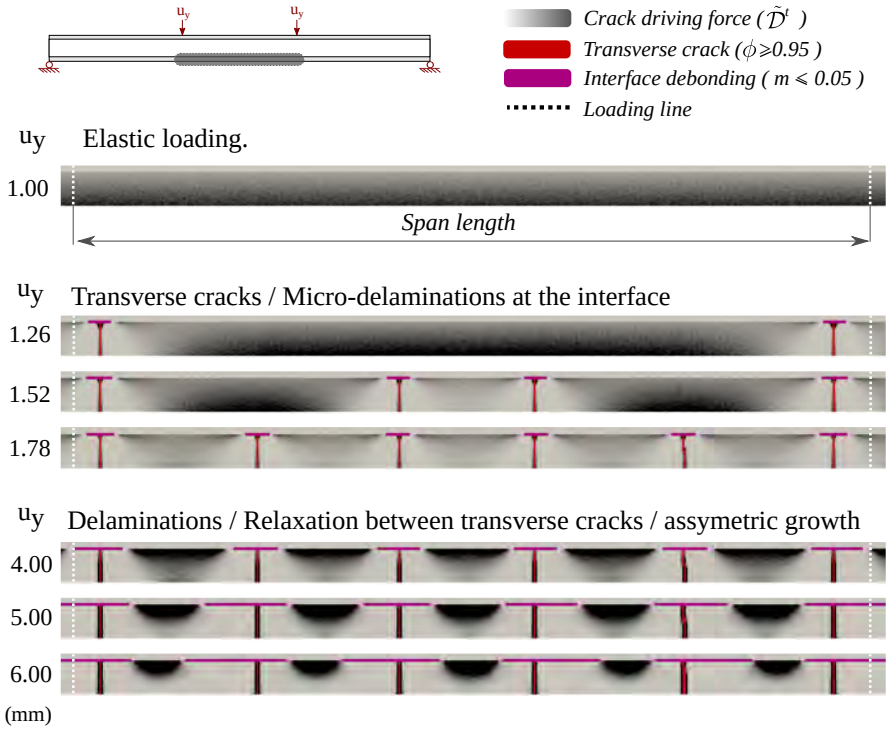

Figure 5.13: View of the fracture pattern of the bottom 90 plies in the span-length region of the 4-point bending test for different applied vertical displacements numerically predicted using cohesive zone model enhanced with the nonlocal model (PFM-CZM). The grey-scale colour palette illustrates the crack driving force of the transverse cracks, the purple colour represents the interface debonding, and the red colour represents the transverse cracks (warping scale = 0).

Figure 5.13 shows the failure sequence numerical predicted by PFM-CZM. Compared to the findings reported by Mortell and coworkers, the failure sequence obtained numerically is in perfect agreement to the experimental one. Three phases composes the failure sequence. The elastic loading of the specimen governs the first phase. Then, the second phase is

characterised by the onset of transverse cracks along the span length of the bottom clustering of 90º plies. These crack growth from the bottommost edge to the 90/0 interface, inducing a micro-delamination at the intersection point. Finally, the third phase begins after reaching the crack saturation in the bottom clustering of 90º plies. This last phase is characterised by the debonding of the 90/0 interface, which is initiates from the micro-delaminations provoked by the transverse cracks in the previous stage.

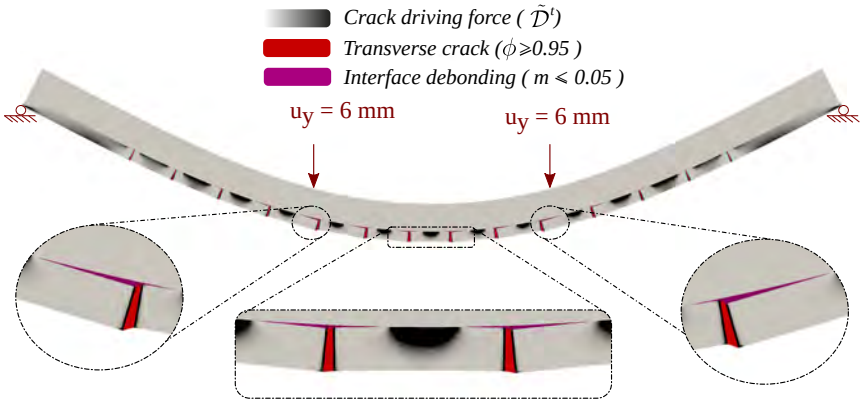

Figure 5.14: A view of the fracture pattern in the span-length region at the final applied vertical displacements numerically predicted using cohesive zone model enhanced with the nonlocal model (PFM-CZM). The grey-scale colour palette illustrates the crack driving force of the transverse cracks, the purple colour represents the interface debonding, and the red colour represents the transverse cracks (warping scale = 1).

Related to the third phase previously described, Mortell and coworkers observed an asymmetrical growth of the delamination. They reported that the debonding initiated in transverse cracks that are far from the centre of the specimen is more asymmetrical than those close to it. Further, they observed that the direction of the propagation is moving away from the centre of the specimen. Figure 5.14 shows the failure pattern at the end of the simulation, which in turn demonstrates that the PFM-CZM captures the asymmetrical growth correctly.

5.6 Compact tension

The virtual test consists of two compact tension specimens subjected to tensile loads. The specimens herein simulated were previously studied by González et al. (2014) and Ortega et al. (2017, 2016). The main objective of this test is to demonstrate that the translaminar failure of quasi-isotropic laminates can be numerically predicted using the PFM. For this purpose, the numerical predictions regarding the mechanical response are compared with: (i) experimental data, (ii) analytical curves (LEFM), and (iii) numerical predictions using a cohesive zone model (CZM). The following presents the principal results supporting the comparison, while the details can be found in Paper B.

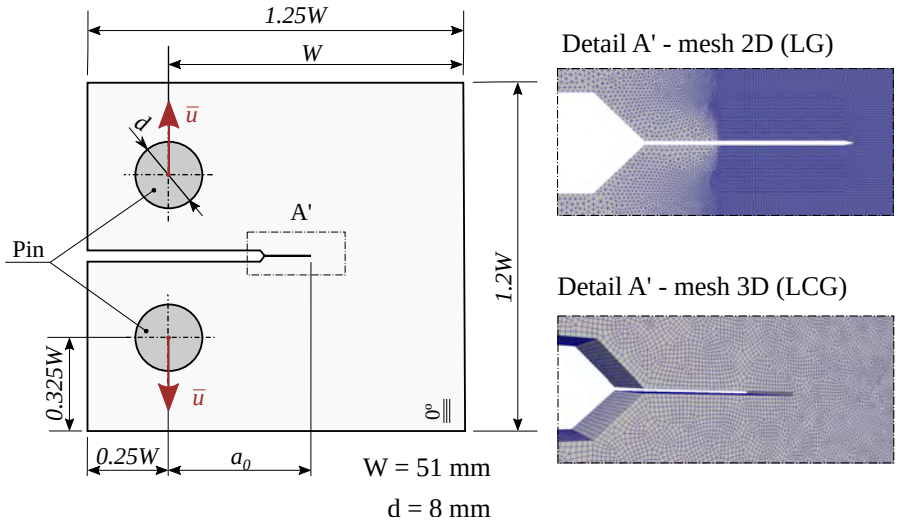

Figure 5.15: Sketch of the compact tension test, showing the boundary conditions and a detail of the 2D and 3D FE meshes.

The two simulated specimens have the same geometry and loading conditions, which are shown in Figure 5.15. The main difference between them stems from the material and laminate. Although both have a quasi-isotropic laminate, the first specimen labelled as LCG is made of carbon/glass woven fabric plies, while the second one labelled as LG is made of glass woven fabric plies. Regarding the computational model, it is worth mentioning that each specimen is discretised with a different mesh, see Figure 5.15. More details about the material properties and the computational models are given in the corresponding article.

The load-displacement curves for both specimens are plotted in Figure 5.16. The mechanical responses predicted by both numerical models, PFM and CZM, are in good agreement with

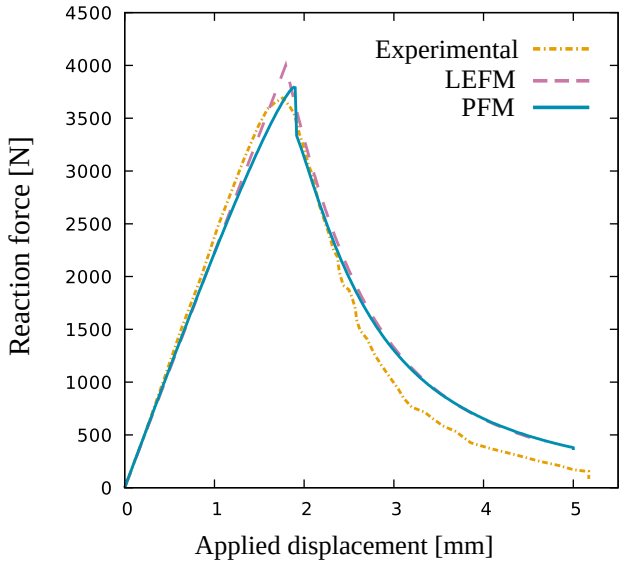

a) LG

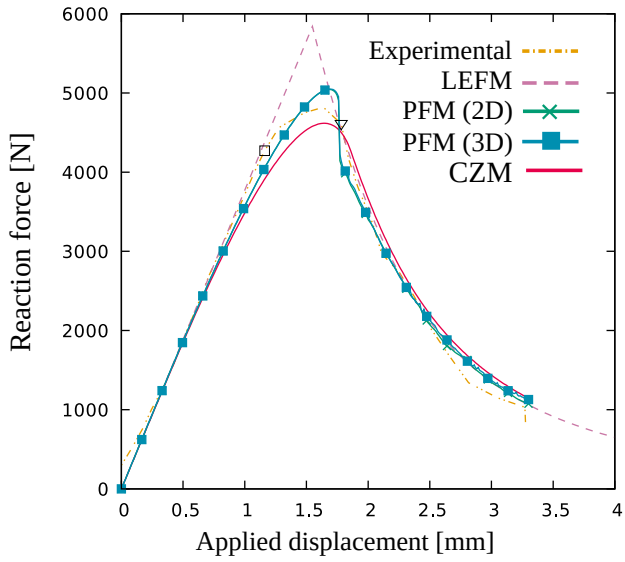

b) LCG

Figure 5.16: Mechanical response numerically predicted using the nonlocal continuum damage model (PFM) and the cohesive zone model (CZM) for the compact tension test.

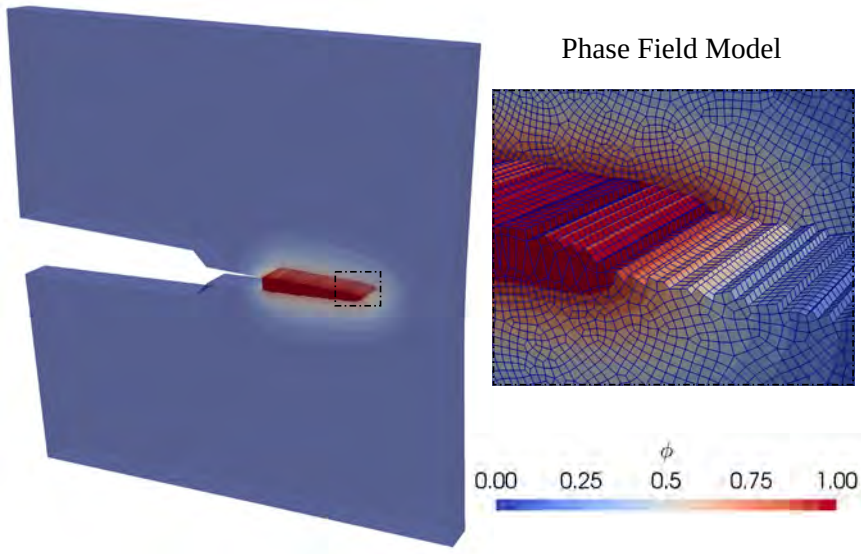

a)

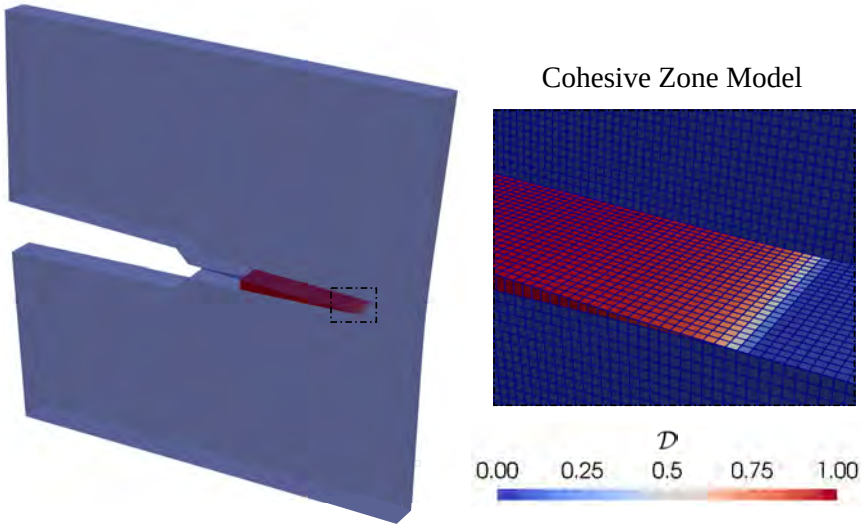

b)

Figure 5.17: A comparative view of the fracture pattern numerically predicted using the nonlocal continuum damage model (PFM) and the cohesive zone model (PFM) for the compact tension test at the end of the simulation.

the experimental and analytical curve. The comparison of the peak forces reveals that the PFM slightly overestimates the experimental values, whereas the CZM underestimates them. However, the relative error for both models is quite similar and below 5%. A closer look into the results shows that the PFM predicts of a sharp fall just before the softening region, which coincides with the moment identified in the experimental curves as the initiation of the crack propagation. Considering the numerical study done by Mesgarnejad et al. (2015), a feasible explanation for the overestimation of the energy and force previous to the force drop is because of the solution found for the phase field problem is a local minimiser instead of the global one. To mitigate this kind of issues, they propose the usage of backtracking techniques. However, the implementation and usage of this kind of methods are out of the scope of the current investigation.

The crack path for the LCG laminate predicted by both PFM and CZM at the end of the simulation is shown in Figure 5.17. In both cases, the crack extends from the tip of the pre-crack along a plane that is perpendicular to the loading direction. Moreover, it can be observed that the path predicted by the PFM is independent of the mesh orientation. However, compared to the crack path of the CZM, the damage extends perpendicularly to the growth direction due to the nonlocal formulation. As a consequence, the softening part of the curve predicted by PFM is slightly under to the one of the CZM.

Part III

Concluding remarks

Concluding remarks

6

This chapter presents the main conclusions of the work carried out in this thesis and proposes some topics that should be subject to further development to understand the true potential of the high-performance computing concerning the virtual testing of composite materials.

6.1 Conclusions

This thesis has been focused on the formulation, implementation and validation of several progressive damage models for virtual testing of composites structures in a high-performance computing finite element code. Two novel formulations within the continuum damage mechanics theory aiming at modelling the intralaminar failure have been formulated and implemented. The former one is a local damage model specially conceived for complex three-dimensional loading cases (Paper A, Quintanas-Corominas et al. (2018)), while the latter one is a nonlocal damage model based on the phase field approach for brittle fracture (Paper B, Quintanas-Corominas et al. (2019a)). In turn, the cohesive zone model proposed by Turon et al. (2018), aimed at modelling the interlaminar failure, has been implemented, employing the complex step derivation approximation for the evaluation of the material tangent tensor. Finally, a new coupling strategy between the nonlocal damage model and the cohesive zone model has been developed to simulate the interaction between the intralaminar and interlaminar failures (Paper C, Quintanas-Corominas et al. (2019b)). The accuracy of the models and their proper implementation in the Alya code have been demonstrated by performing virtual testing of different specimens at coupon level. Therefore, the principal objective of the thesis, i.e. the implementation of a HPC-based FE simulation framework for virtual testing of unidirectional fibre-reinforced polymer composites, has been satisfactorily achieved. Hence, the principal output of this thesis is not only the novel formulation of the models, but also the virtual testing framework so-called Alya-VITECOST.

For each of the models conforming Alya-VITECOST, the following conclusions are drawn:

- The fully three-dimensional formulation of the local continuum damage model provides reliable numerical predictions concerning the onset and progression of the intralaminar damage. The virtual tests performed using a very fine spatial discretisation through the ply thickness has revealed that a proper definition of the loading functions precludes the necessity of defining in-situ properties for predicting the ultimate strength of the laminate. Also, the simulations have demonstrated that it is possible to capture the free-edge effect, opening the possibility of modelling damage near the interface employing the same continuum damage model. Regarding the failure

pattern, the results have shown that the use of thin meshes mitigates the dependency with the mesh orientation, but not entirely resolves it.

- The nonlocal continuum damage model based on the phase field approach provides reliable predictions of the intralaminar failure. The virtual tests have demonstrated that the proposed formulation is not only capable of predicting the onset of different damage mechanisms but also the failure pattern. Further, the simulations have shown that the failure pattern is predicted with a minimum dependency on the mesh characteristics. Despite these excellent features, the results have revealed that special care must be taken when modelling systems with material discontinuities, such as composite laminates. The nonlocal nature of the phase field formulation may provoke that the damage field extends through several plies with independency of the interfaces. As a consequence, the prediction of the bearing capacity of the structure can be wrong in some configurations due to a premature loss of stiffness. In addition, it must be mentioned that the formulation herein proposed assumes simultaneously degradation of the material properties. For complex loading scenarios, the approach from Bleyer and Alessi (2018), which considers two phase field variables, one for the fibre breaking and other for a matrix cracking, may be more appropriate. It is worth mentioning that their strategy can be used in conjunction with the formulation herein proposed. Finally, the numerical tests have illustrated that the power offered by the HPC environment is essential for dealing with the strict mesh requirements imposed by the regularisation parameter.

- The virtual tests concerning the onset and propagation of the interlaminar damage have verified not only the implementation of the cohesive zone model but also the robustness of the complex-step derivative approximation. Thanks to the efficient management of the computational resource provided by the HPC environment, a noticeable loss of performance due to the use of complex-type variables has not been detected.

- The coupling strategy between the nonlocal damage model and the cohesive zone model provides a reliable framework for modelling the interaction between the intralaminar and interlaminar failure mechanisms. The virtual tests have illustrated the necessity of a coupling strategy to correctly model the delamination induced by transverse cracking. In addition, the numerical predictions have demonstrated that, with a statistically random strength distribution, it is possible to predict the onset of the transverse cracks without defining initial flaws. Finally, the simulations have also shown that the proposed framework provides a correct prediction of the mechanisms that initiate the delamination as well as the direction along the delamination propagates.

- The nonlocal damage model requires the use of a numerical strategy to deal with the

coupled field problem. The virtual tests presented in the context of this thesis have been performed using a modified alternate minimisation scheme. The simulations revealed that a large number of iterations is necessary when the damage field is growing, especially if the crack growth is unstable. Hence, the HPC environment is necessary for dealing with both the costs associated with the mesh size and the ones related to the solution scheme.

Beyond the previous conclusions, the implementation of the constitutive models has shown the flexibility of the Alya code to be updated with state of the art of the progressive damage modelling. For instance, the development of the Alya-VITECOST framework has not exclusively faced with the implementation of the material models but also with several auxiliary aspects: element technologies, material coordinate systems, internal state variables, solution procedures, pre- and post-processing, among others. Thanks to the structure and work-flow of Alya code, these features have been implemented for both sequential and parallel executions, without a substantial additional effort.

Finally, a general conclusion can be stated answering the main research question of this thesis: what an HPC-based FE code can offer to the virtual testing of composite structures? That is the efficient management of the computational resources enables the use of very spatial and temporal discretisation. Thus, the computational power permits to exploit the maximum potential of the constitutive formulations, illustrating their virtues and flaws. In addition, this power also allows the possibility of dealing with the costs associated with the nonlinearities that stem from complex problems. In that sense, despite many solvers are adapted and designed to be run in parallel executions, there is still a lot of investigation to be done in this direction.

6.2 Perspectives and future work

The potential of Alya-VTIECOST framework can be extended with the objective of performing virtual testing of more complex specimens. In terms of the building block approach, the next level of complexity regards to detail and sub-component specimens. For this purpose, different technologies and techniques, which were out of the scope of this thesis, need to be considered for their implementation. The two features considered mandatory are the implementation of (i) shell elements and (ii) contact formulations. Despite the computational power offered by the HPC environment, the combination of the small fracture zone and tiny aspect ratio of the composite laminate structure makes necessary the use of shell elements for simulating medium and large size structural components. Regarding the contact formulation, Rivero (2018) has recently presented a novel algorithm suitable for HPC simulations using Alya. Thanks to Rivero's algorithm, Alya-VITECOST can be used to simulate, for instance, impact and compression after impact tests. For such virtual tests, the local damage model for

the intralaminar failure and the cohesive zone model for the interlaminar seems a suitable modelling strategy to explore more deeply the potential of Alya-VITECOST.

Another immediate work is related to the improvement of not only the formulation of nonlocal damage model but also the scheme to solve the resulting coupled-field problem. Regarding the model formulation, more numerical tests are necessary to understand the influence of the nonlocal character in the numerical predictions. For instance, the influence of the crack density with the regularisation length should be more studied. Moreover, it is also essential to search for a strategy to mitigate the numerical issue related to the extension of the damage field through the different plies. Apart from this issue, one possibility to extend the formulation is the definition of a physically-based criterion for modelling the initiation of the damage under a complex stress state. In turn, the numerical scheme aimed to solve the coupled-field problem may be improved. Two promising alternatives for its improvement are (i) the use of local re-meshing algorithms in line with the methodology presented by Areias et al. (2016) and (ii) the use of Schur complements to increase the performance of the solution scheme as done by G. Houzeaux et al. (2011).

Besides the aspects regarding the formulation, the implementation of the models in Alya-VITECOST can be refactored to maximise the performance of the HPC technology. For example, large loops can be optimised using OpenMP and some functions can be vectorised. After the refactoring, the numerical efficiency in terms of scalability and computational time should be explored by making, for instance, a comparison between the local and nonlocal damage models. This future work is in line with the exploration of the other capability offered by the high-performance computing environment, namely: the reduction of the simulation times. It is worth remembering that this thesis has focused only on the exploration of what the HPC-based simulation codes can offer in terms of the management of a large number of degrees of freedom, not in terms of efficiency.

Finally, the combination of reliable progressive damage models and efficient scalability opens the possibility of using Alya-VITECOST in optimisation processes, opening a vast topic for future research. For example, thanks to the power of the high-performance computing, it would be feasible to use Alya-VITECOST to create a set of reliable numerical results for training a neural network using a supervised learning algorithm.Another example could be the usage of Alya-VITECOST in numerical laminate design techniques with the aim to improve the damage tolerance as presented by Sasikumar (2019).

Bibliography

Alfano, G. and M.A. Crisfield (2001). *Finite element interface models for the delamination analysis of laminated composites: mechanical and computational issues*. In: *International Journal for Numerical Methods in Engineering* 50.7, pp. 1701–1736.

Ambrosio, L. and V.M. Tortorelli (1990). *Approximation of functional depending on jumps by elliptic functional via t-convergence*. In: *Communications on Pure and Applied Mathematics* 43.8, pp. 999–1036.

Areias, P., T. Rabczuk, and M.A. Msekh (2016). *Phase-field analysis of finite-strain plates and shells including element subdivision*. In: *Computer Methods in Applied Mechanics and Engineering* 312, pp. 322–350.

Artigues, A., C. Cugnasco, Y. Becerra, F. Cucchietti, G. Houzeaux, M. Vázquez, J. Torres, E. Ayguadé, and J. Labarta (2017). *ParaView + Alya + D8tree: Integrating High Performance Computing and High Performance Data Analytics*. In: *Procedia Computer Science* 108, pp. 465–474.

Azinpour, E., J.P.S Ferreira, M.P.L. Parente, and J. Cesar de Sa (2018). *A simple and unified implementation of phase field and gradient damage models*. In: *Advanced Modeling and Simulation in Engineering Sciences* 5.1, p. 15.

Barbero, E.J. (2017). *Introduction to composite materials design*. 3rd ed. Taylor & Francis, CRC Press.

Barenblatt, G.I. (1962). *The Mathematical Theory of Equilibrium Cracks in Brittle Fracture*. In: 7, pp. 55–129.

Bažant, Z.P. and L. Cedolin (1979). *Blunt crack band propagation in finite element analysis*. In: *ASCE Journal Engineering Mechanical Division* 105.2, pp. 297–315.

– (1983). *Finite Element Modeling of Crack Band Propagation*. In: *Journal of Structural Engineering* 109.1, pp. 69–92.

Bažant, Z.P. and B.H. Oh (1983). *Crack band theory for fracture of concrete*. In: *Matériaux et Construction* 16.3, pp. 155–177.

Belytschko, T., W.K. Liu, B. Moran, and K. Elkhodary (2014). *Nonlinear Finite Elements for Continua and Structures*. 2nd ed. Wiley.

Benallal, A., T. Berstad, T. Borvik, and O.S. Hopperstad (2001). *Uniqueness, loss of ellipticity and localization for the time-discretized, rate-dependent boundary value problem with softening*. In: *International Journal for Numerical Methods in Engineering* 84.7, pp. 864–882.

Benzeggagh, M.L. and M. Kenane (1996). *Measurement of mixed-mode delamination fracture toughness of unidirectional glass/epoxy composites with mixed-mode bending apparatus*. In: *Composites Science and Technology* 56.4, pp. 439–449.

Bleyer, J. and R. Alessi (2018). *Phase-field modeling of anisotropic brittle fracture including several damage mechanisms*. In: *Computer Methods in Applied Mechanics and Engineering* 336, pp. 213–236.

Borrell, R., J.C. Cajas, D. Mira, A. Taha, S. Koric, M. Vázquez, and G. Houzeaux (2018). *Parallel mesh partitioning based on space filling curves*. In: *Computers & Fluids* 173, pp. 264–272.

Borstnar, G., M.N. Mavrogordato, L. Helfen, I. Sinclair, and S.M. Spearing (2015). *Interlaminar fracture micro-mechanisms in toughened carbon fibre reinforced plastics investigated via synchrotron radiation computed tomography and laminography*. In: *Composites Part A: Applied Science and Manufacturing* 71, pp. 176–183.

Bouchard, P.O., F. Bay, Y. Chastel, and I. Tovena (2000). *Crack propagation modelling using an advanced remeshing technique*. In: *Computer Methods in Applied Mechanics and Engineering* 189.3, pp. 723–742.

Bourdin, B., G.A. Francfort, and J.J. Marigo (2000). *Numerical experiments in revisited brittle fracture*. In: *Journal of the Mechanics and Physics of Solids* 48.4, pp. 797–826.

– (2008). *The Variational Approach to Fracture*. In: *Journal of Elasticity* 91.1, pp. 5–148.

Bull, D.J., S.M. Spearing, and I. Sinclair (2014). *Observations of damage development from compression-after-impact experiments using ex situ micro-focus computed tomography*. In: *Composites Science and Technology* 97, pp. 106–114.

– (2015). *Investigation of the response to low velocity impact and quasi-static indentation loading of particle-toughened carbon-fibre composite materials*. In: *Composites Part A: Applied Science and Manufacturing* 74, pp. 38–46.

Cajas, J., G. Houzeaux, M. Vázquez, M. García, E. Casoni, H. Calmet, A. Artigues, R. Borrell, O. Lehmkuhl, D. Pastrana, D. Yáñez, R. Pons, and J. Martorell (2018). *Fluid-Structure Interaction Based on HPC Multicode Coupling*. In: *SIAM Journal on Scientific Computing* 40.6, pp. 677–703.

Calmet, H., G. Houzeaux, M. Vázquez, B. Eguzkitza, A.M. Gambaruto, A.J. Bates, and D.J. Doorly (2018a). *Flow features and micro-particle deposition in a human respiratory system during sniffing*. In: *Journal of Aerosol Science* 123, pp. 171–184.

Calmet, H., C. Kleinstreuer, G. Houzeaux, A.V. Kolanjiyil, O. Lehmkuhl, E. Olivares, and M. Vázquez (2018b). *Subject-variability effects on micron particle deposition in human nasal cavities*. In: *Journal of Aerosol Science* 115, pp. 12–28.

Camanho, P.P. (1999). *Application of Numerical Methods to the Strength Prediction of Mechanically Fastened Joints in Composite Laminates*. PhD thesis, Imperial College London.

Camanho, P.P., C.G. Dávila, and M.F. de Moura (2003). *Numerical Simulation of Mixed-Mode Progressive Delamination in Composite Materials*. In: *Journal of Composite Materials* 37.16, pp. 1415–1438.

Camanho, P.P., P. Maimí, and C.G. Dávila (2007). *Prediction of size effects in notched laminates using continuum damage mechanics*. In: *Composites Science and Technology* 67.13, pp. 2715–2727.

Carollo, V., J. Reinoso, and M. Paggi (2018). *Modeling complex crack paths in ceramic laminates: a novel variational framework combining the phase field method of fracture and the cohesive zone model*. In: *Journal of the European Ceramic Society* 38.8, pp. 2994–3003.

Casoni, E., A. Jérusalem, C. Samaniego, B. Eguzkitza, P. Lafortune, D.D. Tjahjanto, X. Sáez, G. Houzeaux, and M. Vázquez (2015). *Alya: Computational Solid Mechanics for Supercomputers*. In: *Archives of Computational Methods in Engineering* 22, pp. 557–576.

Chen, B.Y., S.T. Pinho, N.V. De Carvalho, P.M. Baiz, and T.E. Tay (2014). *A floating node method for the modelling of discontinuities in composites*. In: *Engineering Fracture Mechanics* 127, pp. 104–134.

Coleman, B.D. and E.M. Gurtin (1967). *Thermodynamics with Internal State Variables*. In: *The Journal of Chemical Physics* 47.2, pp. 597–613.

Composite Materials Handbook (2017). SAE International.

Cox, B.N., H.A. Bale, M. Begley, M. Blacklock, B.C. Do, T. Fast, M. Naderi, M. Novak, V.P. Rajan, R.G. Rinaldi, R.O. Ritchie, M.N. Rossol, J.H. Shaw, O. Sudre, Q. Yang, F.W. Zok, and D.B. Marshall (2014). *Stochastic Virtual Tests for High-Temperature Ceramic Matrix Composites*. In: *Annual Review of Materials Research* 44.1, pp. 479–529.

Crisfield, M.A. (1988). *Snap-through and snap-back response in concrete structures and the dangers of under-integration*. In: *International Journal for Numerical Methods in Engineering* 22.3, pp. 751–767.

Dagum, L. and R. Menon (1998). *OpenMP: An industry-standard API for shared-memory programming*. In: *Computing in Science & Engineering* 1, pp. 46–55.

Daniel, I.M. and O. Ishai (2006). *Engineering mechanics of composite materials*. 2nd ed. Oxford University Press.

De Borst, R. (2003). *Numerical aspects of cohesive-zone models*. In: *Engineering Fracture Mechanics* 70.14, pp. 1743–1757.

De Borst, R., L.J. Sluys, H.B. Muhlhaus, and J. Pamin (1993). *Fundamental issues in the finite element analyses of localization of deformation*. In: *Engineering Computations* 10.2, pp. 99–121.

Debnath, L. and P. Mikusinski (2005). *Introduction to Hilbert spaces with applications*. 3rd ed. Academic press.

Dugdale, D.S. (1960). *Yielding of steel sheets containing slits*. In: *Journal of the Mechanics and Physics of Solids* 8.2, pp. 100–104.

Eguzkitza, B., G. Houzeaux, R. Aubry, H. Owen, and M. Vázquez (2013). *A parallel coupling strategy for the Chimera and domain decomposition methods in computational mechanics*. In: *Computers & Fluids* 80, pp. 128–141.

Forghani, A., M. Shahbazi, N. Zobeiry, A. Poursartip, and R. Vaziri (2015). *An overview of continuum damage models used to simulate intralaminar failure mechanisms in advanced composite materials*. In: *Numerical Modelling of Failure in Advanced Composite Materials*. Ed. by P.P. Camanho and Stephen R. Hallett. Woodhead Publishing Series in Composites Science and Engineering. Woodhead Publishing, pp. 151–173.

Francfort, G.A. and J.J. Marigo (1998). *Revisiting brittle fracture as an energy minimization problem*. In: *Journal of the Mechanics and Physics of Solids* 46.8, pp. 1319–1342.

Fries, T.P. and T. Belytschko (2010). *The extended/generalized finite element method: An overview of the method and its applications*. In: *International Journal for Numerical Methods in Engineering* 84.3, pp. 253–304.

Garcia-Gasulla, M., G. Houzeaux, R. Ferrer, A. Artigues, V. López, J. Labarta, and M. Vá'zquez (2019). *MPI+X: task-based parallelisation and dynamic load balance of finite element assembly*. In: *International Journal of Computational Fluid Dynamics* 0.0, pp. 1–22.

García-Rodríguez, S.M., J. Costa, P. Maimí, V. Singery, and A. Sasikumar (2019). *On how matrix cracks induce delamination under out-of-plane shear and the associated in-situ effect*. In: *Submitted to Composites Science and Technology*.

García-Rodríguez, S.M., J. Costa, V. Singery, I. Boada, and J.A. Mayugo (2018a). *A 3D tomographic investigation to elucidate the low-velocity impact resistance and tolerance of thin non-crimp fabric laminates: effect of ply-thickness*. In: *Composites Part A: Applied Science and Manufacturing* 113, pp. 53–65.

– (2018b). *The effect interleaving has on thin-ply non-crimp fabric laminate impact response: X-ray tomography investigation*. In: *Composites Part A: Applied Science and Manufacturing* 107, pp. 409–420.

Gay, D. and S.V. Hoa (2007). *Composite materials: design and applications*. 2nd ed. Taylor & Francis, CRC Press.

González, E.V. (2011). *Simulation of interlaminar and intralaminar damage in polymer-based composites for aeronautical applications under impact loading*. PhD thesis, Universitat de Girona.

González, E.V., P. Maimí, J.R. Sainz de Aja, P. Cruz, and P.P. Camanho (2014). *Effects of interply hybridization on the damage resistance and tolerance of composite laminates*. In: *Composite Structures* 108, pp. 319–331.

Gövert, S., D. Mira, J.B.W. Kok, M. Vázquez, and G. Houzeaux (2018). *The Effect of Partial Premixing and Heat Loss on the Reacting Flow Field Prediction of a Swirl Stabilized Gas Turbine Model Combustor*. In: *Flow, Turbulence and Combustion* 100.2, pp. 503–534.

Goyal, V.K., E.R. Johnson, and C.G. Dávila (2004). *Irreversible constitutive law for modeling the delamination process using interfacial surface discontinuities*. In: *Composite Structures* 65.3, pp. 289–305.

Gropp, W.D., E. Lusk, and A. Skjellum (1999). *Using MPI: portable parallel programming with the message-passing interface*. Vol. 1. MIT press.

Guerrero, J.M., J.A. Mayugo, J. Costa, and A. Turon (2018). *A 3D Progressive Failure Model for predicting pseudo-ductility in hybrid unidirectional composite materials under fibre tensile loading*. In: *Composites Part A: Applied Science and Manufacturing* 107, pp. 579–591.

Gültekin, O., H. Dal, and G. A. Holzapfel (2018). *Numerical aspects of anisotropic failure in soft biological tissues favor energy-based criteria: A rate-dependent anisotropic crack phase-field model*. In: *Computer Methods in Applied Mechanics and Engineering* 331, pp. 23–52.

– (2016). *A phase-field approach to model fracture of arterial walls: Theory and finite element analysis*. In: *Computer Methods in Applied Mechanics and Engineering* 312, pp. 542–566.

Hansbo, Anita and Peter Hansbo (2004). *A finite element method for the simulation of strong and weak discontinuities in solid mechanics*. In: *Computer Methods in Applied Mechanics and Engineering* 193.33, pp. 3523–3540.

Hayes, B.S. and L.M. Gammon (2010). *Optical Microscopy of Fiber-Reinforced Composites*. ASM International.

Hillerborg, A., M. Modéer, and P.E. Petersson (1976). *Analysis of crack formation and crack growth in concrete by means of fracture mechanics and finite elements*. In: *Cement and Concrete Research* 6.6, pp. 773–781.

Horstemeyer, M.F. and D.J. Bammann (2010). *Historical review of internal state variable theory for inelasticity*. In: *International Journal of Plasticity* 26.9, pp. 1310–1334.

Houzeaux, G., R. Aubry, and M. Vázquez (2011). *Extension of fractional step techniques for incompressible flows: The preconditioned Orthomin(1) for the pressure Schur complement*. In: *Computers & Fluids* 44.1, pp. 297–313.

Houzeaux, G., R. Cruz, H. Owen, and M. Vázquez (2013). *Parallel uniform mesh multiplication applied to a Navier–Stokes solver*. In: *Computers & Fluids* 80, pp. 142–151.

Houzeaux, G., M. Vázquez, R. Aubry, and J.M. Cela (2009). *A massively parallel fractional step solver for incompressible flows*. In: *Journal of Computational Physics* 228.17, pp. 6316–6332.

Houzeaux, G., M. Vázquez, X. Sáez, and J.M. Cela (2010). *Hybrid MPI-OpenMP performance in massively parallel computational fluid dynamics*. In: *Parallel Computational Fluid Dynamics 2008*. Ed. by D. Tromeur-Dervout, G. Brenner, D.R. Emerson, and J. Erhel. Berlin, Heidelberg: Springer Berlin Heidelberg, pp. 293–297.

Houzeaux, Guillaume, Beatriz Eguzkitza, Romain Aubry, Herbert Owen, and Mariano Vázquez (2014). *A Chimera method for the incompressible Navier–Stokes equations*. In: *International Journal for Numerical Methods in Fluids* 75.3, pp. 155–183.

Hughes, J.R.T. (2012). *The finite element method: linear static and dynamic finite element analysis*. Courier Corporation.

Irons, B.M. (1966). *Engineering applications of numerical integration in stiffness methods*. In: *AIAA Journal* 4.11, pp. 2035–2037.

Jirásek, M. (2007). *Nonlocal damage mechanics*. In: *Revue Européenne de Génie Civil* 11.7-8, pp. 993–1021.

Karypis, George and Vipin Kumar (2009). *MeTis: Unstructured Graph Partitioning and Sparse Matrix Ordering System, Version 4.0*. `http://www.cs.umn.edu/~metis`. University of Minnesota, Minneapolis, MN.

Katona, Michael C and OC Zienkiewicz (1985). *A unified set of single step algorithms part 3: The beta-m method, a generalization of the Newmark scheme*. In: *International Journal for Numerical Methods in Engineering* 21.7, pp. 1345–1359.

Lancioni, G. and G. Royer-Carfagni (2009). *The Variational Approach to Fracture Mechanics. A Practical Application to the French Panthéon in Paris*. In: *Journal of Elasticity* 95.1, pp. 1–30.

Langer, U. and M. Neumüller (2018). *Direct and Iterative Solvers*. In: *Computational Acoustics*. Ed. by Manfred Kaltenbacher. Springer International Publishing, pp. 205–251.

Lehmkuhl, O., G. Houzeaux, H. Owen, G. Chrysokentis, and I. Rodriguez (2019). *A low-dissipation finite element scheme for scale resolving simulations of turbulent flows*. In: *Journal of Computational Physics* 390, pp. 51–65.

Lemaitre, J. and J.L. Chaboche (1990). *Mechanics of Solid Materials*. Cambridge University Press, 1990.

Ling, D., Q. Yang, and B. Cox (2009). *An augmented finite element method for modeling arbitrary discontinuities in composite materials*. In: *International Journal of Fracture* 156.1, pp. 53–73.

Lopes, C.S., C. González, O. Falcó, F. Naya, J. LLorca, and B. Tijs (2016). *Multiscale virtual testing: the roadmap to efficient design of composites for damage resistance and tolerance*. In: *CEAS Aeronautical Journal* 7.4, pp. 607–619.

Magoulès, F., F. Roux, and G. Houzeaux (2016). *Parallel scientific computing*. Wiley Online Library.

Maimí, P. (2007). *Modelización constitutiva y compuntacional del daño y fractura de materiales compuestos*. PhD thesis, Universitat de Girona.

Maimí, P., P.P. Camanho, J.A. Mayugo, and C.G. Dávila (2007a). *A continuum damage model for composite laminates: Part I – Constitutive model*. In: *Mechanics of Materials* 39.10, pp. 897–908.

– (2007b). *A continuum damage model for composite laminates: Part II – Computational implementation and validation*. In: *Mechanics of Materials* 39.10, pp. 909–919.

Maimí, P., P.P. Camanho, J.A. Mayugo, and A. Turon (2011). *Matrix cracking and delamination in laminated composites. Part I: Ply constitutive law, first ply failure and onset of delamination*. In: *Mechanics of Materials* 43.4, pp. 169–185.

Maimí, P., J.A. Mayugo, and P.P. Camanho (2008). *A Three-dimensional Damage Model for Transversely Isotropic Composite Laminates*. In: *Journal of Composite Materials* 42.25, pp. 2717–2745.

Marigo, J.J., M. Corrado, and K. Pahm (2016). *An overview of the modelling of fracture by gradient damage models*. In: *Meccanica* 51.12, pp. 3107–3128.

Martínez, X., S. Oller, F. Rastellini, and A.H. Barbat (2008). *A numerical procedure simulating $\{RC\}$ structures reinforced with $\{FRP\}$ using the serialparallel mixing theory*. In: *Computers & Structures* 86, pp. 1604–1618.

Martins, J.R.R.A., P. Sturdza, and J.J. Alonso (2003). *The Complex-step Derivative Approximation*. In: *ACM Trans. Math. Softw.* 29.3, pp. 245–262.

Mediavilla, J., R.H.J. Peerlings, and M.G.D. Geers (2006). *Discrete crack modelling of ductile fracture driven by non-local softening plasticity*. In: *International Journal for Numerical Methods in Engineering* 66.4, pp. 661–688.

Melenk, J.M. and I. Babuška (1996). *The partition of unity finite element method: Basic theory and applications*. In: *Computer Methods in Applied Mechanics and Engineering* 139.1, pp. 289–314.

Melro, A.R., P.P. Camanho, and S.T. Pinho (2008). *Generation of random distribution of fibres in long-fibre reinforced composites*. In: *Composites Science and Technology* 68.9, pp. 2092–2102.

Mergheim, J., E. Kuhl, and P. Steinmann (2005). *A finite element method for the computational modelling of cohesive cracks*. In: *International Journal for Numerical Methods in Engineering* 63.2, pp. 276–289.

Mesgarnejad, A., B. Bourdin, and M.M. Khonsari (2015). *Validation simulations for the variational approach to fracture*. In: *Computer Methods in Applied Mechanics and Engineering* 290, pp. 420–437.

Miehe, C., M. Hofacker, and F. Welschinger (2010a). *A phase field model for rate-independent crack propagation: Robust algorithmic implementation based on operator splits*. In: *Computer Methods in Applied Mechanics and Engineering* 199.45, pp. 2765–2778.

Miehe, C., F. Welschinger, and M. Hofacker (2010b). *Thermodynamically consistent phase-field models of fracture: Variational principles and multi-field FE implementations*. In: *International Journal for Numerical Methods in Engineering* 83.10, pp. 1273–1311.

Mira, D., M. Zavala-Aké, M. Avila, H. Owen, J.C. Cajas, M. Vázquez, and G. Houzeaux (2016). *Heat Transfer Effects on a Fully Premixed Methane Impinging Flame*. In: *Flow, Turbulence and Combustion* 97.1, pp. 339–361.

Moës, N., J. Dolbow, and T. Belytschko (1999). *A finite element method for crack growth without remeshing*. In: *International Journal for Numerical Methods in Engineering* 46.1, pp. 131–150.

Molnár, G. and A. Gravouil (2017). *2D and 3D Abaqus implementation of a robust staggered phase-field solution for modeling brittle fracture*. In: *Finite Elements in Analysis and Design* 130, pp. 27–38.

Mortell, D.J., D.A. Tanner, and C.T. McCarthy (2014). *In-situ SEM study of transverse cracking and delamination in laminated composite materials*. In: *Composites Science and Technology* 105, pp. 118–126.

Msekh, M., J.M. Sargado, M. Jamshidian, P. Areias, and T. Rabczuk (2015). *Abaqus implementation of phase-field model for brittle fracture*. In: *Computational Materials Science* 96.12, pp. 472–484.

Murakami, S. (2012). *Continuum Damage Mechanics*. 1st ed. Springer Netherlands.

Needleman, A. (1988). *Material rate dependence and mesh sensitivity in localization problems*. In: *Computer Methods in Applied Mechanics and Engineering* 67.1, pp. 69–85.

Ortega, A., P. Maimí, E.V. González, J.R. Sainz de Aja, F.M. de la Escalera, and P. Cruz (2017). *Translaminar fracture toughness of interply hybrid laminates under tensile and compressive loads*. In: *Composites Science and Technology* 143, pp. 1–12.

Ortega, A., P. Maimí, E.V. González, and D. Trias (2016). *Characterization of the translaminar fracture Cohesive Law*. In: *Composites Part A: Applied Science and Manufacturing* 91, Part 2. CompTest 2015, pp. 501–509.

Ortiz, M. and A. Pandolfi (1999). *Finite-deformation irreversible cohesive elements for three-dimensional crack-propagation analysis*. In: *International Journal for Numerical Methods in Engineering* 44.9, pp. 1267–1282.

Paggi, M., M. Corrado, and J. Reinoso (2018). *Fracture of solar-grade anisotropic polycrystalline Silicon: A combined phase field–cohesive zone model approach*. In: *Computer Methods in Applied Mechanics and Engineering* 330, pp. 123–148.

Paggi, M. and J. Reinoso (2015). *An anisotropic large displacement cohesive zone model for fibrillar and crazing interfaces*. In: *International Journal of Solids and Structures* 69, pp. 106–120.

– (2017). *Revisiting the problem of a crack impinging on an interface:A modeling framework for the interaction between the phase field approach for brittle fracture and the interface cohesive zone model*. In: *Computer Methods in Applied Mechanics and Engineering* 321, pp. 145–172.

Pastrana, D., J.C. Cajas, O. Lehmkuhl, I. Rodríguez, and G. Houzeaux (2018). *Large-eddy simulations of the vortex-induced vibration of a low mass ratio two-degree-of-freedom circular cylinder at subcritical Reynolds numbers*. In: *Computers & Fluids* 173, pp. 118–132.

Peerlings, R.H.J., R. de Borst, W.A.M. Brekelmans, and M.G.D. Geers (2002). *Localisation issues in local and nonlocal continuum approaches to fracture*. In: *European Journal of Mechanics - A/Solids* 21.2, pp. 175–189.

Peerlings, R.H.J., M.G.D. Geers, R. de Borst, and W.A.M. Brekelmans (2001). *A critical comparison of nonlocal and gradient-enhanced softening continua*. In: *International Journal of Solids and Structures* 38.44, pp. 7723–7746.

Pernice, M.F., N.V. De Carvalho, J.G. Ratcliffe, and S.R. Hallett (2015). *Experimental study on delamination migration in composite laminates*. In: *Composites Part A: Applied Science and Manufacturing* 73, pp. 20–34.

Pineda, E.J., B.A. Bednarcyk, A.M. Waas, and S.M. Arnold (2012). *Implementation of a smeared crack band model in a micromechanics framework*. Tech. rep. TM 2012–217603. NASA.

Pinho, S.T. (2005). *Modelling failure of laminated composites using physically-based failure models*. PhD thesis, Imperial College London.

Quintanas-Corominas, A., P. Maimí, E. Casoni, A. Turon, J.A. Mayugo, G. Guillamet, and M. Vázquez (2018). *A 3D transversally isotropic constitutive model for advanced composites implemented in a high performance computing code*. In: *European Journal of Mechanics - A/Solids* 71, pp. 278–291.

Quintanas-Corominas, A., J. Reinoso, E. Casoni, A. Turon, and J.A. Mayugo (2019a). *A phase field approach to simulate intralaminar and translaminar fracture in long fiber composite materials*. In: *Composite Structures* 220, pp. 899–911.

Quintanas-Corominas, A., J. Reinoso, E. Casoni, A. Turon, M. Paggi, and J.A. Mayugo (2019b). *A phase field approach enhanced with a cohesive zone model for modelling delamination induced by matrix cracking*. In: *Computer Methods in Applied Mechanics and Engineering*.

Rabczuk, T. (2013). *Computational Methods for Fracture in Brittle and Quasi-Brittle Solids: State-of-the-Art Review and Future Perspectives*. In: *ISRN Applied Mathematics* 2013, p. 38.

Reddy, J.N. (2003). *Mechanics of Laminated Composite Plates and Shells*. 2nd ed. CRC Press.

Reinoso, J., G. Catalanotti, A. Blázquez, P. Areias, P.P. Camanho, and F. París (2017a). *A consistent anisotropic damage model for laminated fiber-reinforced composites using the 3D-version of the Puck failure criterion*. In: *International Journal of Solids and Structures*, pp. 37–53.

Reinoso, J. and M. Paggi (2014). *A consistent interface element formulation for geometrical and material nonlinearities*. In: *Computational Mechanics* 54, pp. 1569–1581.

Reinoso, J., M. Paggi, and A. Blázquez (2017b). *A nonlinear finite thickness cohesive interface element for modeling delamination in fibre-reinforced composite laminates*. In: *Composites Part B: Engineering*, pp. 116–128.

Rivero, M.I. (2018). *A Parallel Algorithm for Deformable Contact Problems*. PhD thesis, Universitat Politécnica de Catalunya.

Rodríguez-Ferran, A., I. Morata, and A. Huerta (2004). *Efficient and reliable nonlocal damage models*. In: *Computer Methods in Applied Mechanics and Engineering* 193.30, pp. 3431–3455.

Rodriguez, I., O. Lehmkuhl, M. Soria, S. Gómez, M. Domínguez-Pumar, and L. Kowalski (2019). *Fluid dynamics and heat transfer in the wake of a sphere*. In: *International Journal of Heat and Fluid Flow* 76, pp. 141–153.

Santiago, A., J. Aguado-Sierra, M. Zavala-Aké, R. Doste-Beltran, S. Gómez, R. Arís, J.C. Cajas, E. Casoni, and M. Vázquez (2018). *Fully coupled fluid-electro-mechanical model of the human heart for supercomputers*. In: *International Journal for Numerical Methods in Biomedical Engineering* 34.12, e3140.

Sasikumar, A. (2019). *Improving compression after impact response of composite laminates through ply level hybridization with thin plies and unsymmetrical designs*. PhD thesis, Universitat de Girona.

Simo, J.C. and T.J.R. Hugues (2003). *Computational inelasticity*. 2nd ed. Springer Science & Business Media.

Song, J.H., P.M.A. Areias, and T. Belytschko (2006). *A method for dynamic crack and shear band propagation with phantom nodes*. In: *International Journal for Numerical Methods in Engineering* 67.6, pp. 868–893.

Soto, A., E.V. González, P. Maimí, A. Turon, J.R. Sainz de Aja, and F.M. de la Escalera (2016). *Cohesive zone length of orthotropic materials undergoing delamination*. In: *Engineering Fracture Mechanics* 159, pp. 174–188.

Tan, W., F. Naya, L. Yang, T. Chang, B.G. Falzon, L. Zhan, J.M. Molina-Aldareguía, C. González, and J. Llorca (2018). *The role of interfacial properties on the intralaminar and interlaminar damage behaviour of unidirectional composite laminates: Experimental characterization and multiscale modelling*. In: *Composites Part B: Engineering* 138, pp. 206–221.

Tavares, R.P., J.M. Guerrero, F. Otero, A. Turon, J.A. Mayugo, J. Costa, and P.P. Camanho (2019). *Effects of local stress fields around broken fibres on the longitudinal failure of composite materials*. In: *International Journal of Solids and Structures* 156-157, pp. 294–305.

Tay, T.E., G. Liu, V.B.C. Tan, X.S. Sun, and D.C. Pham (2008). *Progressive Failure Analysis of Composites*. In: *Journal of Composite Materials* 42.18, pp. 1921–1966.

Turon, A., P.P. Camanho, J. Costa, and C.G. Dávila (2006). *A damage model for the simulation of delamination in advanced composites under variable-mode loading*. In: *Mechanics of Materials* 38.11, pp. 1072–1089.

Turon, A., C.G. Dávila, P.P. Camanho, and J. Costa (2007). *An engineering solution for mesh size effects in the simulation of delamination using cohesive zone models*. In: *Engineering Fracture Mechanics* 74.10, pp. 1665–1682.

Turon, A., E.V. González, C. Sarrado, G. Guillamet, and P. Maimí (2018). *Accurate simulation of delamination under mixed-mode loading using a cohesive model with a mode-dependent penalty stiffness*. In: *Composite Structures* 184.10–11, pp. 506–511.

Van der Meer, F.P. (2010). *Computational Modeling of Failure in Composite Laminates*. PhD thesis, Technische Universiteit Delft.

Van der Meer, F.P. and L.J. Sluys (2009). *Continuum Models for the Analysis of Progressive Failure in Composite Laminates*. In: *Journal of Composite Materials* 43.20, pp. 2131–2156.

Van der Meer, F.P., L.J. Sluys, S.R. Hallett, and M.R. Wisnom (2012). *Computational modeling of complex failure mechanisms in laminates*. In: *Journal of Composite Materials* 46.5, pp. 603–623.

Varna, J. and L. Berglund (1991). *Multiple transverse cracking and stiffness reduction in cross-ply laminates*. In: *Journal of Composites, Technology and Research* 13.2, pp. 97–106.

Vázquez, M., R. Arís, G. Houzeaux, R. Aubry, P. Villar, J. Garcia-Barnés, D. Gil, and F. Carreras (2011). *A massively parallel computational electrophysiology model of the heart*. In: *International journal for numerical methods in biomedical engineering* 27.12, pp. 1911–1929.

Vázquez, M., G. Houzeaux, S. Koric, A. Artigues, J. Aguado-Sierra, R. Arís, D. Mira, H. Calmet, F. Cucchietti, H. Owen, A. Taha, E.D. Burness, J.M. Cela, and M. Valero (2016). *Alya: Multiphysics engineering simulation toward exascale*. In: *Journal of Computational Science* 14, pp. 15–27.

Vigueras, G., F. Sket, C. Samaniego, L. Wu, L. Noels, D. Tjahjanto, E. Casoni, G. Houzeaux, A. Makradi, J.M. Molina-Aldareguia, M. Vázquez, and A. Jérusalem (2015). *An XFEM/CZM implementation for massively parallel simulations of composites fracture*. In: *Composite Structures* 125, pp. 542–557.

Wagih, A., P. Maimí, N. Blanco, and J. Costa (2016). *A quasi-static indentation test to elucidate the sequence of damage events in low velocity impacts on composite laminates*. In: *Composites Part A: Applied Science and Manufacturing* 82, pp. 180–189.

Wagih, A., P. Maimí, N. Blanco, S.M. García-Rodríguez, G. Guillamet, R.P. Issac, A. Turon, and J. Costa (2019). *Improving damage resistance and load capacity of thin-ply laminates using ply clustering and small mismatch angles*. In: *Composites Part A: Applied Science and Manufacturing* 117, pp. 76–91.

Wienke, S., P. Springer, C. Terboven, and D. Mey (2012). *OpenACC—first experiences with real-world applications*. In: *European Conference on Parallel Processing*. Springer, pp. 859–870.

Wriggers, P. (2008). *Nonlinear Finite Element Methods*. 1st ed. Springer-Verlag Berlin Heidelberg.

Zienkiewicz, O., R. Taylor, and J.Z. Zhu (2013). *The Finite Element Method: Its Basis and Fundamentals*. 7th ed. Butterworth-Heinemann.

Part IV

Annexes. Publications.

Paper A

A 3D transversally isotropic constitutive model for advanced composites implemented in a high performance computing code

Published in *European Journal of Mechanics / A Solids* (ISSN: 0997-7538)
Impact factors according to the 2017 Journal Citation Reports: 2.881, ranked 17/134 in category *Mechanics* (1st quartile)

European Journal of Mechanics / A Solids 71 (2018) 278–291

Contents lists available at ScienceDirect

European Journal of Mechanics / A Solids

journal homepage: www.elsevier.com/locate/ejmsol

A 3D transversally isotropic constitutive model for advanced composites implemented in a high performance computing code

Adrià Quintanas-Corominas[a,*], Pere Maimí[a], Eva Casoni[b], Albert Turon[a], Joan Andreu Mayugo[a], Gerard Guillamet[b], Mariano Vázquez[b,c]

[a] AMADE, Polytechnic School, Universitat de Girona, Campus Montilivi s/n, 17071 Girona, Spain
[b] Barcelona Supercomputing Center (BSC-CNS), Edificio NEXUS I, Campus Nord UPC, Gran Capitán 2–4, 08034, Barcelona, Spain
[c] Artificial Intelligence Research Institute CSIC (IIIA-CSIC), Campus de la UAB, 08193 Bellaterra, Spain

ARTICLE INFO

Keywords:
High performance computing
Fracture
Laminated composites
Damage model
Constitutive modelling
Finite elements

ABSTRACT

A 3D constitutive damage model is proposed for predicting the progressive failure of laminated composite materials at mesoscopic length scale. The damage initiation and growth functions are based on the experimental phenomenology. The damage evolution laws are defined ensuring the energy regularization thanks to the crack band model. The crack closure effect under load reversal is also considered. The model is specifically formulated to be implemented in a high-performance computing platform, Alya, that enables the use of very fine meshes, ensuring an accurate prediction of the onset and propagation of damage. The reliability and the performance of the proposed formulation are examined simulating a cross-ply laminate and open hole tests under tensile loading.

1. Introduction

One of the main difficulties that prevail the use of laminated composite materials in structural applications is the inability to predict accurately their strength and damage tolerance. Its heterogeneous nature accounts for the structural failure to be driven by several damage mechanisms. These damage mechanisms can be studied from different length scales including the multi-scale point of view. Moreover, laminated composite materials have the capacity to accumulate damage before the structural collapse, which means that the initial local failure does not necessarily lead to the loss of its structural integrity. As a consequence, the prediction of the onset of the failure process is not enough and a Progressive Damage Failure Analysis (PDFA) is necessary to predict accurately their strength and damage tolerance.

PDFA of composite laminates can be performed at different length scales, considering that the mesoscopic length scale is the most suitable to predict the material degradation and the structural behaviour. Even in this length scale, PDFA is a complex problem due to the interaction of several damage mechanisms that may occur during the failure process. For this reason, the use of numerical methods is necessary, with the Finite Element Method (FEM) being the most extended option.

When the FEM is used to perform computational failure analysis, modelling the cracks is the key-point as they are the principal source of damage in laminated composite structures. The different available methods can be divided in two main approaches: continuous and discontinuous (Van Der Meer et al., 2012). In the continuous approaches, the damage is modelled as a material constitutive relation that describes the degradation of the elastic properties. In discontinuous ones, the damage is modelled by inserting discontinuities in the displacement field with the aim of describing the kinematics of the interior boundaries accurately. Regarding their implementation, the continuous approach is suitable to be implemented in a standard FEM code without modifying its structure, whereas the discontinuous one usually requires a modification of the standard FEM code structure. For this reason, the continuous approach should be a priori less computationally expensive.

Regardless of the approach adopted, it is necessary to formulate a material model to describe the constitutive relationships. A good practice is to formulate the model within the framework of thermodynamics of irreversible process (Lemaitre and Chaboche, 1990; Hill, 1998). Early works in the context of laminated composite materials was performed by Ladevèze and Dantec (1992), Matzenmiller et al. (1995), and Sun and Chen (1989). After their pioneering works, several models have been formulated considering separately the continuous damage mechanics theory (see e.g. (Barbero and de Vivo, 2001; Williams et al., 2003; Maimí et al., 2007a, 2008; Martín-Santos et al., 2014; Reinoso et al., 2017)) and the plasticity theory (see e.g. (Oller et al., 1995; Weeks and Sun, 1998; Tsai and Sun, 2002; Yokozeki et al., 2007; Van

* Corresponding author.
E-mail address: adria.quintanas@udg.edu (A. Quintanas-Corominas).

https://doi.org/10.1016/j.euromechsol.2018.03.021
Received 19 May 2017; Received in revised form 7 March 2018; Accepted 27 March 2018
Available online 29 March 2018
0997-7538/

Der Meer, 2016)), but also some works that coupled both theories (see e.g. (Maimí et al., 2011; Vasiukov et al., 2015)).

Although the continuous approach has in general a good computational performance, the aspect ratio of the structures made of laminated composites, together with the small fracture process zone, involves the necessity of using fine meshes. One option to alleviate the mesh requirements is the use of continuum shells elements. This elements, which are intermediate elements between conventional shells and solid elements, are formulated to circumvent the different locking pathologies and also to avoid the use of simplificated hypothesis for the out-of-plane stress state, see Reinoso and Blázquez (2016). However, despite the use of continuum shell elements, the computational requirements in large models can increase up to the point that can preclude the simulation, if they are not managed efficiently. Thus highlighting the necessity of an efficient parallel computational code and constitutive models suitable for large simulations.

With the increasing necessity of High Performance Computing (HPC) resources for doing reliable simulations of laminated composite materials, several 3D continuum damage models may be adapted. Abisset et al. (2011) proposed a smeared crack model that considers distributed transversal damage depending on the crack density and the ply thickness. Despite the obtained results being in good agreement with the experimental data, their approach lacks consistency when a sufficient refined mesh is used. Later, Vogler et al. (2013) and Camanho et al. (2013) proposed another smeared crack model that includes plasticity and softening behaviour. Their model is formulated in a modular way, which makes it suitable for being adapted to new technologies and codes. However, their formulation uses an iterative procedure to find internal equilibrium at each integration point compromising the computational performance in large simulations. Finally, Cho et al. (2013) presented an improved version of the smeared crack model formulated by Pinho et al. (2006). They observed that without a correct modelling of the inter-ply damage an over-prediction of the ultimate strength is obtained. In order to overcome this undesirable mesh-dependence, they introduced the cohesive elements to account for the inter-ply damage, which increased the computational resources, but with good numerical predictions of the laminate strength. However, it should be pointed out that the use of cohesive elements may not be necessary if a proper definition of the matrix damage is combined with the accurate description of the complex stress states at the interface, using for instance, several elements through the ply thickness.

Based on the previous observations, a new continuum damage model for progressive damage failure analysis of composite structures at mesoscopic length scale is presented. The model is implemented in the Alya high performance computational code (Casoni et al., 2014) with the aim to perform large scale simulations.

The proposed model is an extension of the continuum damage model formulated by Maimí et al. (2007a, b) to a 3D space in order to capture the damage state arising from complex stress states. The current formulation improves the description of the transversal shear strength presented in (Maimí et al., 2008) with the aim to better capture the matrix damage. Thereby, the model is formulated by means of stress invariants with respect to the rotations in the transversal plane. Moreover, three new loading functions are presented in a closed form allowing to model the onset of failure for a wide range of materials. Each loading function is related to one of the three damage mechanisms considered: breakage and kinking of the fibers and cracking of the matrix. The damage laws are defined as piecewise functions composed by n-segments. The energy objectivity has been ensured through the crack band model proposed by Bažant and Oh (1983). Finally, the majority of model inputs are material properties of a unidirectional ply, whose can be obtained experimentally with standard and non-standard experimental procedures (Ortega et al., 2016, 2017).

In turn, Alya is a multi-physics parallel code developed at Barcelona Supercomputing Center aimed at solving partial differential equations in non-structured meshes (Casoni et al., 2014). On contrary to other codes, Alya has been conceived from the beginning for running in parallel with the highest efficiency for any physic and multi-physic application and is designed in a modular way (Vázquez et al., 2016). Therefore, it is easier to then enhance the code with new features. This will allow to use not only explicit time integration schemes, but also implicit ones with iterative solvers. Moreover, the parallelization is hidden behind a common solver that assembles matrices and residuals as well as carries out the solution scheme (Houzeaux et al., 2009, 2013). Finally, the material models can be implemented so as to conserve the extreme scalability while ensuring an accurate physical description of the material deformation and the onset and propagation of the damage up to failure. For this reason, the constitutive model presented in this work has an explicit form, which makes it computationally efficient and suitable to be used in large scale computations.

This paper is organized as follows: a full description of the model is presented in Section 2, describing the damage activation functions and the damage evolution laws. The numerical implementation is given in Section 3 and two demonstration cases in Section 4. Finally, the conclusions are presented in Section 5.

2. Constitutive model

It is assumed that, at mesoscopic scale and under small strains, a fibrous polymer composite material behaves as a homogeneous elastic transversely-isotropic material up to the onset of damage (Maimí et al., 2007a; b). Following the continuum damage mechanics framework, the first and second principle of thermodynamics must be fulfilled in order to ensure a consistent material response when a dissipative process occurs. Considering a constant density, an isothermal state and that the damage evolves in an adiabatic manner, the Clasius-Duhem inequality can be postulated such that the externally supplied mechanical power, $\boldsymbol{\sigma}: \dot{\boldsymbol{\varepsilon}}$, minus the rate of change of the Helmholtz free-energy, $\dot{\Psi}$, must be positive, i.e.

$$\boldsymbol{\sigma}: \dot{\boldsymbol{\varepsilon}} - \dot{\Psi} \geq 0 \tag{1}$$

where $\boldsymbol{\sigma}$ and $\boldsymbol{\varepsilon}$ are the stress and strain tensor, respectively. The dot notation for differentiation is adopted. Then, following the Coleman's method and the Legendre transformation rules (Houlsby and Puzrin, 2000), the rate of mechanical energy dissipation, $\dot{\Xi}$, can be expressed in terms of the complementary Gibbs free-energy per unit of volume, W, as:

$$\dot{\Xi} = \dot{W} - \dot{\boldsymbol{\sigma}}: \boldsymbol{\varepsilon} = \left(\frac{\partial W}{\partial \boldsymbol{\sigma}} - \boldsymbol{\varepsilon}\right): \dot{\boldsymbol{\sigma}} + \frac{\partial W}{\partial \boldsymbol{d}}: \dot{\boldsymbol{d}} \geq 0 \tag{2}$$

from which it is possible to define the deformation tensor as:

$$\boldsymbol{\varepsilon} = \frac{\partial W}{\partial \boldsymbol{\sigma}} \tag{3}$$

where $\boldsymbol{d}$ is a set of damage state variables.

The thermodynamic irreversibility of the damage process is ensured if the rate of dissipation is positive, i.e.

$$\boldsymbol{Y}: \dot{\boldsymbol{d}} \geq 0 \tag{4}$$

where $\boldsymbol{Y}$ are the conjugated thermodynamic forces defined as:

$$\boldsymbol{Y} = \frac{\partial W}{\partial \boldsymbol{d}} \tag{5}$$

In turn, a damage evolution law, which describes the onset and growth of a damage state variables, can be associated to a failure criterion, F. Following Maimí et al. (2007a), this criterion can be expressed as:

$$F = \phi - r \leq 0 \tag{6}$$

where ϕ is the loading function that defines the shape of the failure surface and r is the damage threshold variable that accounts for the past history of the damage process, also called the internal state variable. At

this point, the material response state is determined by means of the appropriate form of the complementary Kuhn-Tucker relations (Simo and Ju, 1987):

$$\dot{r} \geq 0, \quad F \leq 0, \quad \dot{r}F = 0 \tag{7}$$

If $F < 0$ the material is in the elastic regime, i.e. the damage criterion is not satisfied and therefore, $\dot{r} = 0$. On contrary, if $F = 0$ the damage criterion is fulfilled and the material response state is determined through the loading function gradient, $\dot{\phi}$, as:

$$\dot{\phi} < 0 \Leftrightarrow \text{Unloading} \tag{8}$$

$$\dot{\phi} = 0 \Leftrightarrow \text{Neutral loading} \tag{9}$$

$$\dot{\phi} > 0 \Leftrightarrow \text{Loading} \tag{10}$$

Under loading state, further damage takes place and the damage threshold, r, must be updated. Considering Eq. (6) and Eq. (7), it is possible to relate the rate of change of the loading state and the internal damage variable through the consistency condition as:

$$\dot{r}\dot{F} = 0 \Rightarrow \dot{\phi} = \dot{r} \tag{11}$$

Hence, the damage threshold variable is computed by integrating the loading function along its history. If ϕ depends exclusively on the strain tensor, Eq. (11) can be integrated explicitly as:

$$r = \max_{s\in[0,t]}(1, \phi^s) \tag{12}$$

where t is the current time. It is worth mentioning that when the material is undamaged, $\phi < 1$, the internal state variable is equal to one, $r = 1$.

2.1. Complementary Gibbs free-energy

The complementary Gibbs free-energy, W, which defines the total stored energy function per unit volume of material, is formulated by means of four stress measures: σ_L, τ_{LT}, p_T and τ_T, which have rotational invariance with respect to the longitudinal axis, i.e. the fiber direction. On one hand, σ_L describes the longitudinal stress and τ_{LT} describes the shear stress between the longitudinal and transversal directions, while on the other hand p_T and τ_T account for the transverse hydrostatic pressure and transverse shear stress, respectively. These two transverse invariants, p_T and τ_T, are inspired by the elasto-plasticity models for metals in which the strain tensor is additive split into the hydrostatic and the deviatoric contribution, as done by Simo and Ju (1987). Thanks to this invariant formulation, it is easier to define the damage modes associated to the matrix as well as the crack closure effect under reversal loading.

In the current formulation, it is considered that the stored energy function is a composition of the purely mechanical, W^{mech}, and the hygrothermal, W^{hygr}, energy such that:

$$W = W^{mech} + W^{hygr} \tag{13}$$

with:

$$W^{mech} = \frac{(\sigma_L)^2}{2(1-d_1)E_{11}} - \frac{2\nu_{12}\sigma_L p_T}{E_{11}} + \frac{(p_T)^2}{2(1-d_K)E_T} + \frac{(\tau_T)^2}{2(1-d_G)G_T} + \frac{(\tau_{LT})^2}{2(1-d_6)G_{12}} \tag{14}$$

$$W^{hygr} = (\alpha_L\sigma_L + \alpha_T p_T)\Delta T + (\beta_L\sigma_L + \beta_T p_T)\Delta M \tag{15}$$

where the aforementioned stress invariants are defined as:

$$\sigma_L = \sigma_{11} \tag{16}$$

$$p_T = \frac{\sigma_{22} + \sigma_{33}}{2} \tag{17}$$

$$\tau_T = \frac{\sqrt{(\sigma_{22} - \sigma_{33})^2 + 4(\sigma_{23})^2}}{2} \tag{18}$$

$$\tau_{LT} = \sqrt{(\sigma_{12})^2 + (\sigma_{13})^2} \tag{19}$$

and where ΔT and ΔM defines the increment of temperature and moisture contents with respect to the reference values, respectively. In turn, d_M (where M = 1, G, K, and 6) is a set of scalar variables that describe the damage state: for $d_M = 0$ the material is undamaged, for $0 < d_M < 1$ it is damaged and for $d_M = 1$ it is fully damaged. It should be pointed out that, regardless of the damage state, the original material symmetry planes are ensured. Then, E_T and G_T are, respectively, the bulk and shear stiffness in the transverse isotropy plane, which are defined as:

$$E_T = \frac{E_{22}}{2(1-\nu_{23})} \tag{20}$$

$$G_T = \frac{E_{22}}{2(1+\nu_{23})} \tag{21}$$

At this point, it is worth mentioning that rest of material properties are the elastic modulus and coefficients, which are: the longitudinal E_{11} and transversal E_{22} Young's modulus, the longitudinal ν_{12} and transversal ν_{23} Poisson's ratios, the longitudinal shear moduli G_{12}, the longitudinal α_L and transversal α_T thermal expansion coefficients, and the longitudinal β_L and transversal β_T moisture expansion coefficients.

2.2. Conjugated thermodynamic forces

The conjugated thermodynamic forces, $\boldsymbol{Y}$, relate the variation of stored energy with respect to the damage state variables. Using Eqs. (5) and (13), they are defined as:

$$Y_1 = \frac{\partial W}{\partial d_1} = \frac{(\sigma_L)^2}{2(1-d_1)^2E_{11}} \tag{22}$$

$$Y_K = \frac{\partial W}{\partial d_K} = \frac{(p_T)^2}{2(1-d_K)^2E_T} \tag{23}$$

$$Y_G = \frac{\partial W}{\partial d_G} = \frac{(\tau_T)^2}{2(1-d_G)^2G_T} \tag{24}$$

$$Y_6 = \frac{\partial W}{\partial d_6} = \frac{(\tau_{LT})^2}{2(1-d_6)^2G_{12}} \tag{25}$$

It should be pointed out that $\boldsymbol{Y}$ are always positive and therefore, the rate of dissipation energy, Eq. (4), is ensured if $\dot{\boldsymbol{d}} \geq 0$. In turn, it also denotes that the irreversibility of the degradation process is not possible, i.e. when a damage state is reached it cannot be healed.

2.3. Strain-stress relationship

The strain−stress relationship is the core part of a material model. In the current model, it is obtained by means of the variation of the stored energy with respect to the mechanical stresses, Eq. (3), as:

$$\boldsymbol{\varepsilon} = \frac{\partial W}{\partial \boldsymbol{\sigma}} = \mathbf{H}\colon\boldsymbol{\sigma} + \boldsymbol{\alpha}\Delta T + \boldsymbol{\beta}\Delta M \tag{26}$$

where $\mathbf{H}$ is the compliance tensor, and $\boldsymbol{\alpha}$ and $\boldsymbol{\beta}$ are the thermal and the moisture dilatations tensors, respectively. Due to the major symmetries of the material, the above tensors can be expressed using the standard Voigt notation as:

$$[\boldsymbol{\alpha}]^T = [\alpha_L, \alpha_T, \alpha_T, 0,0,0] \tag{27}$$

$$[\boldsymbol{\beta}]^T = [\beta_L, \beta_T, \beta_T, 0,0,0] \tag{28}$$

$$[\mathbf{H}] = \begin{bmatrix} H_{11} & H_{12} & H_{12} & 0 & 0 & 0 \\ H_{12} & H_{22} & H_{23} & 0 & 0 & 0 \\ H_{12} & H_{23} & H_{22} & 0 & 0 & 0 \\ 0 & 0 & 0 & H_{44} & 0 & 0 \\ 0 & 0 & 0 & 0 & H_{55} & 0 \\ 0 & 0 & 0 & 0 & 0 & H_{55} \end{bmatrix} \tag{29}$$

with:

$$H_{11} = \frac{1}{(1-d_1)E_{11}}$$

$$H_{12} = -\frac{\nu_{12}}{E_{11}}$$

$$H_{22} = \frac{1}{4(1-d_K)E_T} + \frac{1}{4(1-d_G)G_T}$$

$$H_{23} = \frac{1}{4(1-d_K)E_T} - \frac{1}{4(1-d_G)G_T}$$

$$H_{44} = \frac{1}{(1-d_G)G_T}$$

$$H_{55} = \frac{1}{(1-d_6)G_{12}}$$

At this point, it is important to define the crack closure effect under reversal loads, which can has an important role in those structures subjected to multi-axial loading. In the proposed formulation, it is assumed that the crack closure effect on the longitudinal direction is induced by the longitudinal stress, σ_L, whereas on the transverse direction by the transverse pressure, p_T. On the contrary, it is considered that shear stresses, τ_T and τ_{LT}, do not have any contribution (Maimí et al., 2007a). Taking advantage of the proposed invariant formulation, the aforementioned assumptions are accounted tracking the tensile, d_+, and compressive, d_-, damage state variables of the longitudinal, 1, and transversal, K, cases separately, i.e.:

$$d_1 = d_{1+}\frac{\langle \sigma_L \rangle}{|\sigma_L|} + d_{1-}\frac{\langle -\sigma_L \rangle}{|\sigma_L|} \tag{30}$$

$$d_K = d_{K+}\frac{\langle p_T \rangle}{|p_T|} \tag{31}$$

where $\langle \bullet \rangle$ is an operator defined as $\langle x \rangle = (x + |x|)/2$. Note that depending on the sign of stress invariant, a damage variable can be either active or passive.

2.4. Loading functions

Three loading functions are considered, one for each damage mechanism. These independent damage mechanisms, which are denoted with *N*, are: the longitudinal tensile fibre failure, L+; the longitudinal compressive failure, L-, that is related to the formation of the kink-band; and the transverse failure, T, is related to the formation of cracks in the matrix. The proposed definitions for the loading functions associated to the above mechanisms are:

$$\phi_{L+} = \frac{\tilde{\sigma}_L - 2\nu_{12}\tilde{p}_T}{X_T} = \frac{E_{11}}{X_T}\varepsilon_{11} \tag{32}$$

$$\phi_{L-} = \frac{1}{X_C}\left(\sqrt{(\tilde{\sigma}_L)^2 + \eta_T^q(\tilde{p}_T)^2 + \eta_S^q(\tilde{\tau}_{LT})^2} + \eta_T\tilde{p}_T + \eta_S\tilde{\tau}_{LT}\right) \tag{33}$$

$$\phi_T = \sqrt{\left(\frac{Y_T+Y_C}{Y_TY_C}\right)^2\frac{(\tilde{\tau}_T)^2+\mu_T(\tilde{p}_T)^2}{1+\mu_T} + \left(\frac{\mu_{LT}\tilde{\tau}_{LT}}{S_L}\right)^2} + \frac{Y_C-Y_T}{Y_TY_C}\tilde{p}_T + (1-\mu_{LT})\frac{\tilde{\tau}_{LT}}{S_L} \tag{34}$$

where X_T and X_C are the longitudinal tensile and compressive strengths; Y_T and Y_C are the transverse tensile and compressive strengths; S_L is the in-plane shear strength; η_S and η_S^q are the curvature parameters that govern the influence of the longitudinal shear stress, whereas η_T and η_T^q the influence of the transverse pressure; μ_T is either related to the transverse shear strength, S_T, or to the biaxial compression strength, Y_{BC}, through the following expressions:

$$\mu_T(S_T) = \left(\frac{S_T(Y_C+Y_T)}{Y_CY_T}\right)^2 - 1 \tag{35}$$

$$\mu_T(Y_{BC}) = \left(\frac{Y_{BC}(Y_C-Y_T)+Y_CY_T}{Y_CY_T(2Y_{BC}-Y_C)(2Y_{BC}+Y_T)}\right)^2 \tag{36}$$

μ_{LT} is a parameter related to the slope η_L at ordinate axis in the $\sigma_{22}-\sigma_{12}$ stress space through:

$$\mu_{LT} = \frac{1}{4}\left(2 + \frac{S_L}{\eta_L}\left(\frac{Y_C-Y_T}{Y_CY_T}\right)\right) \tag{37}$$

and, finally, $\tilde{p}_T$, $\tilde{\tau}_T$ and $\tilde{\tau}_{LT}$ are the effective invariants that are computed using the effective stresses, $\tilde{\boldsymbol{\sigma}}$, that are obtained as $\tilde{\boldsymbol{\sigma}} = \mathbf{H}_0^{-1}$: $\boldsymbol{\varepsilon}$ in where $\mathbf{H}_0$ is the undamaged compliance tensor defined by Eq. (29) with $d_M = 0$.

The envelopes of the loading functions in different stress spaces at the onset of damage, i.e. when $\phi_M = 1$, are shown in Fig. 1. They are obtained considering the material properties of a E-Glass/LY556 unidirectional ply, which are listed in Table 1. It is worth mentioning that a validation of the loading functions is performed in Section 4.1.

The model intrinsically accounts for the kink-band formation by means of the modification of X_C. Two main hypotheses are usually considered to define the kink-band formation: Rosen (1965) assumes that the kink-band is triggered by a local micro-buckling of the fibres, whereas Argon (1972) assumes that the kink-band is promoted by the failure of the matrix due to small misalignment of the fibre. Following the above hypotheses, it is feasible to consider the following assumptions regarding longitudinal compressive strength. On one hand, X_C is reduced when longitudinal shear stresses (σ_{12} or σ_{13}) and tensile transverse stresses ($\sigma_{22} > 0$ or $\sigma_{33} > 0$) are applied as they promote the initiation of the micro-buckling. On the other hand, X_C is increased when compressive transverse stresses ($\sigma_{22} < 0$ or $\sigma_{33} < 0$) are applied due to the fibre confinement effect that prevents the micro-buckling. As can be appreciated in Fig. 1a and b, both hypotheses are correctly captured by the proposed loading functions. In addition, the X_C behaviour is driven by two shape parameters η_S and η_S^q (or η_T and η_T^q) which control the slope and curvature, respectively.

As can be appreciated in Fig. 1c, the model is also capable of accounting for the failure under high values of hydrostatic compressive pressure. It should be pointed out that the apparent transverse strength is governed by the parameter μ_T. If $\mu_T > \frac{(Y_C-Y_T)^2}{4Y_TY_C}$, the envelope of the loading function is closed under biaxial transverse compression.

Finally, the combination of longitudinal shear stresses (σ_{12} or σ_{13}) and compressive transverse stresses (σ_{22} or σ_{33}) influence the onset of transversal damage. This influence is governed by means of the parameter μ_{LT} as depicted in Fig. 1d. When $\mu_{LT} > 0$, low values of transverse stresses increase the onset stress for transversal damage.

2.5. Damage threshold variables

The damage threshold variables, r_N, are those variables that set the deformation necessary for a damage mechanism to grow. In the current formulation, the damage variables related to cracks parallel to the fibers, r_T, and the ones related with the normal degradation modes to the fibers, r_{L+} and r_{L-}, are uncoupled. However, it is assumed that, in the longitudinal direction, the tensile damage state is influenced by the compressive damage state. These hypotheses are considered in the temporal integration of the damage threshold variables, which are defined using Eq. (12) as:

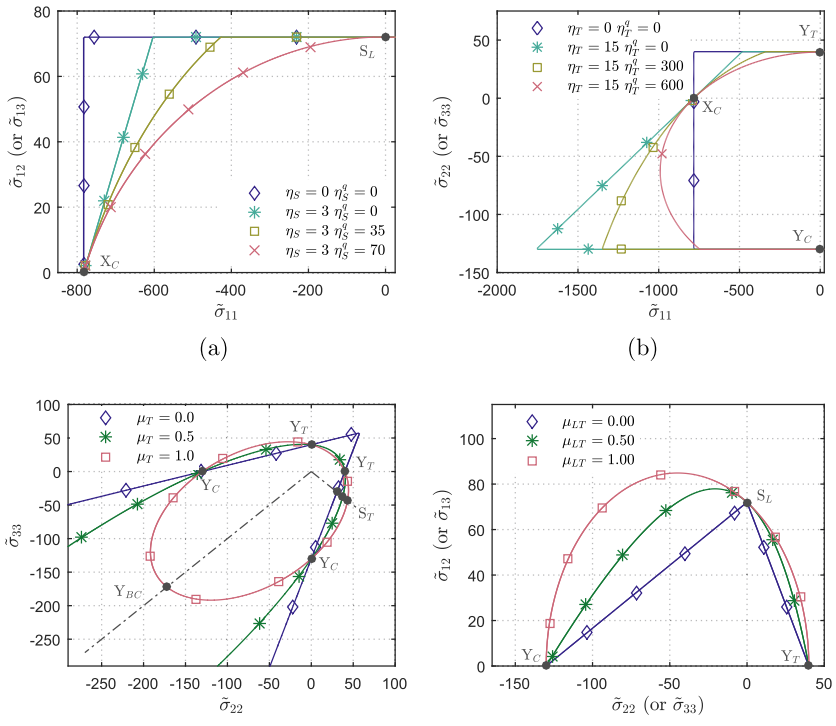

Fig. 1. Loading functions for the material E-Glass/LY556 at different stress space: (a) $\tilde{\sigma}_{11}$ - $\tilde{\sigma}_{12}$ with different values of η_S and η_S^q; (b) $\tilde{\sigma}_{11}$ - $\tilde{\sigma}_{22}$ with different values of η_T and η_T^q; (c) $\tilde{\sigma}_{22}$ - $\tilde{\sigma}_{33}$ for different values of μ_T; and (d) $\tilde{\sigma}_{22}$ - $\tilde{\sigma}_{12}$ with different values of μ_{LT}.

Table 1
E-Glass/LY556 material properties used for the contour plots.

Prop.	Value	Units	Source
G_{12}	5830	MPa	Soden et al. (1998)
X_T	1266.7	MPa	Soden et al. (2002)
X_C	783.3	MPa	Soden et al. (2002)
Y_T	40	MPa	Soden et al. (2002)
Y_{BT}	25.6	MPa	Camanho et al. (2015)
Y_C	130	MPa	Catalanotti et al. (2013)
Y_{BC}	860	MPa	Soden et al. (2002)
S_L	72	MPa	Catalanotti et al. (2013)

$$r_{L+} = \max_{s\in[0,t]}(1, \phi^s_{L+}, \phi^s_{L-}) \tag{38}$$

$$r_{L-} = \max_{s\in[0,t]}(1, \phi^s_{L-}) \tag{39}$$

$$r_T = \max_{s\in[0,t]}(1, \phi^s_T) \tag{40}$$

2.6. Damage evolution laws

The damage evolution law, d_M, relates the degradation of the elastic properties, i.e. the loss of stiffness, with the damage mechanisms. In the current formulation, five laws are defined: $d_{1+}(r_{L+})$ and $d_{1-}(r_{L-})$ that relate the breaking and kinking of the fibers with the degradation of the stiffness associated to the longitudinal stress, σ_{11}; $d_K(r_T)$ that relates the mode-I matrix cracking associated with the transverse stresses, σ_{22} and σ_{33}; $d_G(r_T)$ that relates the mode-II matrix cracking with the transverse shear stress, σ_{23}; and $d_6(r_T, r_{L+})$ that relates the longitudinal tensile and matrix damage mechanism, r_T and r_{L+}, with the longitudinal shears, σ_{12} and σ_{13}.

The current formulation considers the distributed damage negligible up to the onset of the nucleation (or localization) of a crack. This hypothesis is suitable for most of industrial applications with laminated composites materials, where the stacking sequences usually contain not only ± 45° plies, but also 0° and 90°. As consequence, the development of large non-linearities in the shear direction due to the plastic behaviour of the matrix is limited. However, the above hypothesis may not be valid in such cases where the compressive failure plays a dominant role (Ahn and Waas, 2002). In those cases, the shear non-linearities should be included (see for example Pineda and Waas (2013); Joseph et al. (2015); Camanho et al. (2013); Pineda and Waas (2013) and Joseph et al. (2015) or Camanho et al. (2013)).

Once the localization takes place, the strains are not defined in the continuum due to the formation of a crack at the corresponding failure plane. Therefore, the material constitutive relationship must be expressed with respect to crack openings, known as cohesive law. It is assumed that the cohesive law is a material property that can be obtained experimentally (Ortega et al., 2016, 2017). As shown in Fig. 2a, each cohesive law is defined as a C^0-piecewise linear function of the form:

$$\sigma_M(w_M) = -a^i_M w_M + b^i_M \;\forall\, i \in \{1,...,n\} \tag{41}$$

where w_M is the crack opening. Hence, $w^i_M = (b^{i+1}_M - b^i_M)/(a^{i+1}_M - a^i_M)$ defines the intersection point between two consecutive segments of the cohesive law (Fig. 2a). Furthermore, the area under the cohesive law is equal to the fracture toughness ($\mathscr{G}_M$) associated to a particular failure mode M and the traction when $w_M = 0$ is equal to the material strength.

Considering the crack band model (Bažant and Oh, 1983), it is

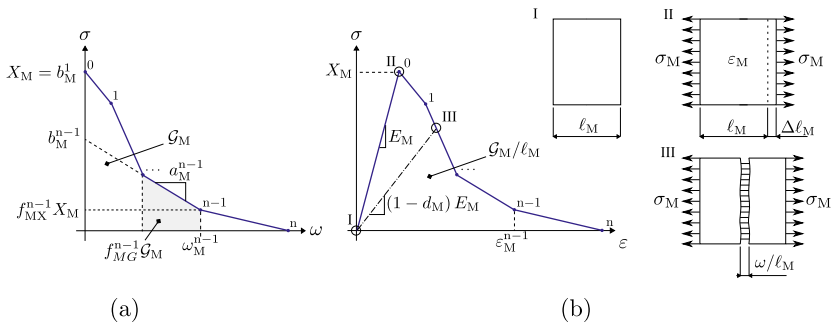

Fig. 2. Cohesive law: (a) cohesive traction-crack opening and (b) stress-strain.

Table 2a
Coefficients and expressions of the damage laws for each uni-axial case.

–	$\sigma_{11} > 0$	$\sigma_{11} < 0$	σ_{23}	σ_{12} (or σ_{13})
M:	1+	1-	G	6*
N:	L+	L-	T	T
E_M:	E_{11}	E_{11}	G_{23}	G_{12}
b_M^1:	X_T	X_C	S_T	S_L
d_M^i:	Exp. A	Exp. B	Exp. A	Exp. A
φ_M^i	1	Exp. C	1	1

possible to consider the cohesive law in a continuum manner ensuring a correct dissipation of the energy. The crack band model assumes that the crack opening is distributed in a finite band that, in the finite element framework, corresponds to the characteristic element length, ℓ_M. Hence, the stress-strain constitutive relationship for each of the uni-axial load cases can be written as (see Table 2a):

$$\sigma_M(\varepsilon_M) = (1 - d_M) E_M \varepsilon_M \tag{42}$$

where E_M is the undamaged slope related the uni-axial load case M and d_M is the damage state variable (see Table 2b and Fig. 2b). Finally, according to the crack band model, the mean strain ε_M in the element and the crack opening w_M can be related through

$$w_M = d_M \ell_M \varepsilon_M \tag{43}$$

At this point, it is possible to determine $d_M(\varepsilon_M)$ using Eqs. 41 and 42 and $\varepsilon_M(r_N)$ using Eqs. 32–34 and Eqs. 38–40. In this way, the damage laws with respect to the damage threshold variables, $d_M(r_N)$, can be defined as:

$$d_M = \begin{cases} 0 & \text{if} \quad r_N \le r_M^0 \\ d_M^i & \text{if} \quad r_M^{i-1} < r_N \le r_M^i \quad \forall\, i \in \{1,...,n\} \\ 1 & \text{if} \quad r_M^n < r_N \end{cases} \tag{44}$$

where the expression d_M^i for $r_M^{i-1} < r_N \le r_M^i$ is defined in Table 2b. Finally, in order to determine which is the active segment i, the value of the damage threshold variable in an inflection point, r_M^i, has to be determined as:

$$r_M^i = \begin{cases} 1 & \text{if} \quad i = 0 \\ \left(\dfrac{(b_M^i - b_M^{i+1}) E_M + (a_M^i b_M^{i+1} - a_M^{i+1} b_M^i)\ell_M}{(a_M^i - a_M^{i+1})\ell_M b_M^1} \right) \varphi_M^i & \text{if} \quad i \in \{1,...,\, n-1\} \\ \dfrac{b_M^n E_M}{a_M^n \ell_M b_M^1} & \text{if} \quad i = n \end{cases} \tag{45}$$

where φ_M^i is also defined in Table 2b.

Notice that in Table 2b it is defined d_{6^*} instead of d_6. Then, considering the aforementioned hypothesis, the latter law is defined as

$$d_6 = 1 - (1 - d_{6^*})(1 - d_{1+}) \tag{46}$$

where $d_{6^*}(r_T)$ is related with the longitudinal shear stresses, σ_{12} and σ_{13}.

Finally, the damage laws for tensile transverse stress, $\sigma_{22} > 0$ or $\sigma_{33} > 0$, are computed considering that both transverse damages laws, d_{K+} and d_G, are linked. It is assumed that the matrix, when it is fully damaged, is not able to support transverse tensile pressure and transverse shear stresses. As a consequence, both transverse damages have to initiate and finalize at the same moment. Under this hypothesis, the

Table 2b
Coefficients and expressions of the damage laws for each uni-axial case.

Exp. A

$$d_M^i = \frac{E_M}{E_M - a_M^i \ell_M} \left(1 - \frac{b_M^i}{r_N b_M^1} \right) \quad \forall\, i \in \{1,...,n\}$$

Exp. B

$$d_{1-}^i = -\sqrt{\frac{1}{4}\left(\frac{\kappa_2^i}{\kappa_1^i}\right)^2 - \frac{\kappa_3^i}{\kappa_1^i}} - \frac{\kappa_2^i}{2\kappa_1^i} \quad \forall\, i \in \{1,...,n\}$$

Exp. C

$$\varphi_{1-}^i = \left(-\sqrt{(\nu_T)^2 - (4\nu_{12}\nu_{21}\nu_T)\hat{d}_{1-}^{\,i} + (\eta_T + 4\nu_{12}^2)\left(\nu_{21}\hat{d}_{1-}^{\,i}\right)^2} + \eta_T \nu_{21} \hat{d}_{1-}^{\,i} \right) \frac{1}{\nu_T}$$

where $\forall\, i \in \{1,...,n\}$ the coefficients are:

$$\kappa_1^i = (\eta_T \nu_{21} + \nu_T \lambda_1^i \lambda_2^{i\,2} - \nu_{21}^2 (4\nu_{12}^2 + \eta_T^q)$$

$$\kappa_2^i = 2\nu_T (2\nu_{12}\nu_{21} - (\eta_T \nu_{21} + \nu_T \lambda_1^i \lambda_2^i)\lambda_2^i)$$

$$\kappa_3^i = \nu_T^2 ((\lambda_2^i)^2 - 1)$$

$$\lambda_1^i = 1 - \frac{a^i \ell_{1-}}{E_{11}}$$

$$\lambda_2^i = \frac{b_{1-}^1}{b_{1-}^i} r_{L-}$$

$$\nu_T = \nu_{23} + 2\nu_{12}\nu_{21} - 1$$

$$\hat{d}_{1-}^{\,i} = \left(\frac{(a_{1-}^i b_{1-}^{i+1} - a_{1-}^{i+1} b_{1-}^i)\ell_{1-}}{E_{11}(b_{1-}^i - b_{1-}^{i+1})} + 1 \right)^{-1}$$

Table 3
IM7/8552 material properties for the current model and the Camanho's et al. failure criteria.

Prop.	Camanho	Current	Units	Source
G_{12}	5290	–	MPa	Camanho and Lambert (2006)
ν_{12}	–	0.32	–	
X_T	2323.5	2323.5	MPa	Catalanotti et al. (2013)
X_C	1017.5	1017.5	MPa	Catalanotti et al. (2013)
Y_T	62.3	62.3	MPa	Camanho and Lambert (2006)
Y_{BT}	38.7	–	MPa	Vogler et al. (2013)
Y_C	253.7	253.7	MPa	Koerber et al. (2010)
Y_{BC}	600.0	–	MPa	Vogler et al. (2013)
S_L	89.6	89.6	MPa	Catalanotti et al. (2013)
S_T	62.3	–	MPa	Camanho et al. (2015)
β	0.0	–	MPa^{-3}	Camanho et al. (2015)
μ_T	–	0.904	–	Eq. (36) [a]
μ_{LT}	–	1.0	–	Eq. (37) [b]
η_T	–	12.0	–	Adjusted
η_T^q	–	385.0	–	Adjusted
η_S	–	9.5	–	Adjusted
η_S^q	–	0.0	–	Adjusted

[a] Assuming $Y_{BC} = 600.0$ MPa.
[b] Assuming $\eta_L = 0.5$ Catalanotti et al. (2013).

following expression for d_{K+} is proposed:

$$d_{K+} = 1 - (1 - d_G)\frac{1 + k + (r_T - 1)G_T/E_T}{k + r_T} \tag{47}$$

Where k is a parameter that depends on the material properties and the characteristic element length. In Algorithm 1, a numerical procedure to compute this parameter is presented. It is worth mentioning that this procedure has to be done just once at the beginning of the analysis.

Algorithm 1. Adjust k parameter

Let $g_K = \mathscr{G}_K/\ell_K$ be the mode-I transverse energy that an element of length ℓ_K must dissipate, a_G and b_G be the softening parameters related with the mode-II transverse energy, and $\Xi(k, \ell_K) = \int \Xi dt$ be computed by means of numerical quadrature, such that standard Simpson's rule.
1: Evaluate the transversal threshold variable when the element has been dissipated the mode-II transverse energy $\mathscr{G}_G$, in other words, compute r_T when $d_G = 1$.
2: Compute the admissible range of mode-I transverse energy:
$\Xi_{min} = \Xi(0, \ell_K)$ and $\Xi_{max} = \Xi(\infty, \ell_K)$
3: **if** $\Xi_{min} < g_{IT} < \Xi_{max}$ **then**
4: Bracket the solution between k_1 and k_2.
5: Find k by means of the Ridder's method (Ralston and Rabinowitz, 2001).
6: **else**
7: The parameter k cannot be adjusted for the current $\mathscr{G}_K$ and ℓ_K. Modify the element size or modify the relation between d_G and d_K.
8: **end if**

3. Model algorithm

In this section the main features related to the implementation of the present damage model into the Alya system (Casoni et al., 2014) are briefly outlined.

Discretization method: The numerical model for solving the equations

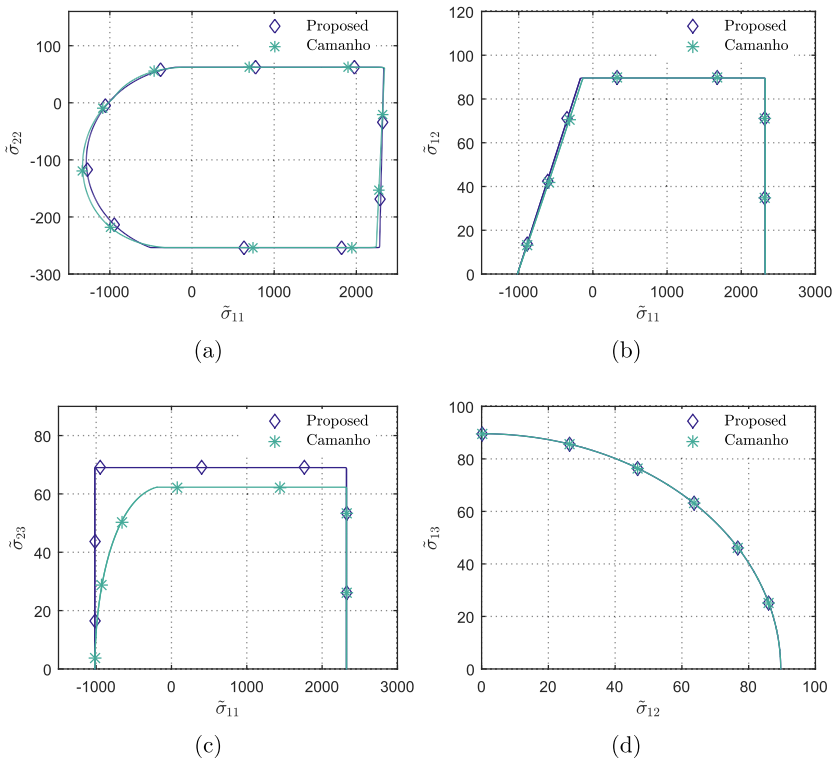

Fig. 3. a: Proposed loading functions vs failure criteria (Camanho et al., 2015) for the IM7/8552 material at different stress spaces: (a) $\tilde{\sigma}_{11}$ - $\tilde{\sigma}_{22}$, (b) $\tilde{\sigma}_{11}$ - $\tilde{\sigma}_{12}$, (c) $\tilde{\sigma}_{11}$ - $\tilde{\sigma}_{23}$, (d) $\tilde{\sigma}_{12}$ - $\tilde{\sigma}_{13}$, (e) $\tilde{\sigma}_{12}$ - $\tilde{\sigma}_{23}$, (f) $\tilde{\sigma}_{22}$ - $\tilde{\sigma}_{33}$, (g) $\tilde{\sigma}_{22}$ - $\tilde{\sigma}_{12}$ and (h) $\tilde{\sigma}_{22}$ - $\tilde{\sigma}_{23}$.

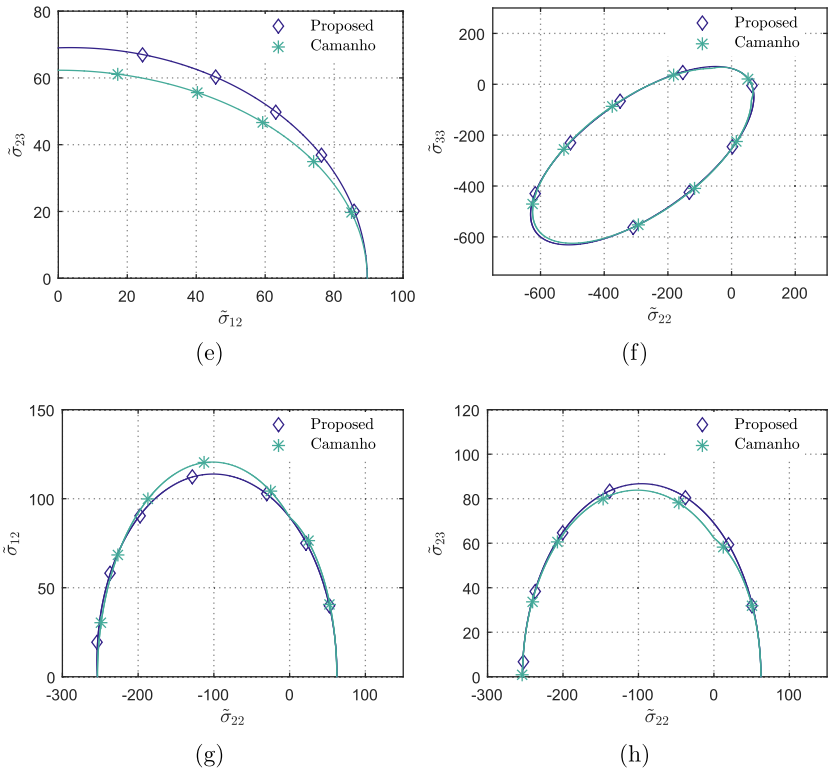

Fig. 3. (*continued*)

is based on a total Lagrangian formulation. In this approach, the discrete equations are formulated with respect to the reference configuration, hence using the Second Piola Kirchoff stress and Green Lagrangian strain measures.

Focusing on the Alya implementation, the damage model is implemented as a constitutive model within the framework of the nonlinear finite element method, with the continuous loading process replaced by incremental time steps. Thanks to the modular architecture of the Alya system, it does not present any limitation for running either in explicit or implicit time integration scheme. For the implicit case, in each step the boundary value problem is solved using an incremental-iterative solution strategy, the standard Newton-Raphson iteration.

The current formulation is implemented as an independent material model, which work-flow is summarized in Algorithm 2. The integration of the constitutive law is performed at the gauss point level, where the contribution of each element to the model during the analysis is to provide the stresses and the external load vector at each node.

Algorithm 2. Material model work-flow

Input: strains $\boldsymbol{\varepsilon}$ and internal variables r_N
Output: nominal stress tensor $\boldsymbol{\sigma}$ and internal variables r_N
1: Compute the effective stresses: $\tilde{\boldsymbol{\sigma}} = \mathbf{H}_0^{-1}$: $\boldsymbol{\varepsilon}$ Eq. (29)
2: Compute the effective invariants: $\tilde{\sigma}_L$, $\tilde{p}_T$, $\tilde{\tau}_T$, $\tilde{\tau}_{LT}$ Eqs. 16–19
3: Evaluate the loading failure functions: ϕ_{L+}, ϕ_{L-}, ϕ_T Eqs. 32–34
4: Integrate the internal variables: r_{L+}, r_{L-}, r_T Eqs. 38–40
5: Evaluate the damage state variables: d_{1+}, d_{1-}, d_{K+}, d_G, d_{6^*} Eqs. 44–47
6: Evaluate the active damage state variables: d_1, d_K, d_6 Eqs. (30), (31) and (46)
7: Compute the nominal stress tensor: $\boldsymbol{\sigma} = \mathbf{H}^{-1}$: $\boldsymbol{\varepsilon}$ Eq. (29)

Parallelization: The Alya code is written in Fortran 90/95 and parallelized with an hybrid OpenMP/MPI. The partition of the mesh is carried out on-the-fly with the METIS library (Casoni et al., 2014). The time for the partition is only a few seconds. The mechanical solver consists mainly of two basic steps, the assembly of the matrix and the right hand side of the system, and the solution of this system using iterative solvers. The assembly step does not require any communication during the matrix-vector products. However, the parallelization of the solver is based on MPI gather functions, as described by Löhner et al. (2011).

4. Demonstration cases

This section presents two examples that demonstrate the capabilities of the model to capture the onset and propagation of the damage induced by complex 3D stress states. The first example consists of a cross-ply laminate in which the central ply clustering thickness is increased, whereas the second one is an open-hole specimen under tensile loading. In both cases, the laminate is made of IM7/8552 CFRP unidirectional tape with a nominal thickness of 0.125 mm. The loading functions at the onset of failure are validated in Section 4.1. The validation is performed through the physically based failure criteria proposed by Camanho et al. (2015). The input parameters required by the model are summarized in Section 4.2. Finally, the numerical setup and simulation results are presented and discussed in Section 4.3 and Section 4.4, respectively. All the simulations are performed using the Alya FE code run in the Marenostrum IV supercomputer (Casoni et al., 2014).

Table 4
Model input parameters for an IM7/8552 unidirectional ply.

		Prop.	Value	Units	Source
Elastic		E_{11}	171420	MPa	Camanho et al. (2007)
		E_{22}	9080	MPa	Camanho et al. (2007)
		G_{12}	5290	MPa	Camanho et al. (2007)
		ν_{12}	0.32	–	Camanho et al. (2007)
		ν_{23}	0.45	–	Camanho et al. (2007)
Strength		X_T	2323.5	MPa	Catalanotti et al. (2013)
		X_C	1017.5	MPa	Catalanotti et al. (2013)
		Y_T	62.3	MPa	Camanho and Lambert (2006)
		Y_C	253.7	MPa	Koerber et al. (2010)
		S_L	89.6	MPa	Catalanotti et al. (2013)
		μ_T	0.904	–	Section 4.1
		μ_{LT}	1.0	–	Section 4.1
		η_T	12.0	–	Section 4.1
		η_T^q	350.0	–	Section 4.1
		η_S	9.5	–	Section 4.1
		η_S^q	0.0	–	Section 4.1
Softening	1+	a_{1+}^1	55200.94	$mm^3\ N^{-1}$	–
		a_{1+}^2	2123.11	$mm^3\ N^{-1}$	–
		b_{1+}^1	2323.5	MPa	–
		b_{1+}^2	536.19	MPa	–
	1-	a_{1-}^1	19478.95	$mm^3\ N^{-1}$	–
		a_{1-}^2	256.3	$mm^3\ N^{-1}$	–
		b_{1-}^1	1017.5	MPa	–
		b_{1-}^2	214.21	MPa	–
	K	k	111.5	–	–
	G	a_G^1	2165.15	$Mm^3\ N^{-1}$	–
		b_G^1	69.02	MPa	–
	6	a_6^1	5094.01	$mm^3\ N$	–
		b_6^1	89.6	MPa	–

Table 5
Cohesive material properties of the IM7/8552 material.

	Prop.	Value	Units	Source
1+	$\mathscr{G}_{1+}$	97.8	kJ/m^2	Gutkin and Pinho (2011)
	$f_{\mathscr{G}1+}^1$	0.5	–	
	X_T	2323.5	MPa	Catalanotti et al. (2013)
	f_{XT}^1	0.2	–	
1-	$\mathscr{G}_{1-}$	106.3	kJ/m^2	Camanho et al. (2007)
	$f_{\mathscr{G}1-}^1$	0.25	–	
	X_C	1017.5	MPa	Catalanotti et al. (2013)
	f_{XC}^1	0.2	–	
K	$\mathscr{G}_K$	0.277	kJ/m^2	Camanho et al. (2007)
G	$\mathscr{G}_G$	1.1	kJ/m^2	Estimated
	S_T	69.01	MPa	Estimated
6	$\mathscr{G}_6$	0.788	kJ/m^2	Camanho et al. (2007)
	S_L	89.6	MPa	Catalanotti et al. (2013)

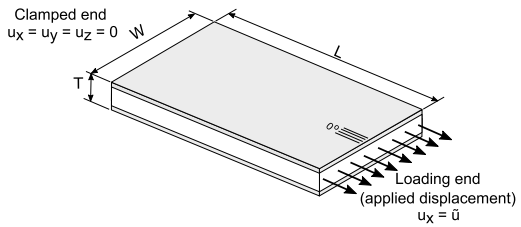

Fig. 4. Geometric definition for the matrix cracking tests.

4.1. Loading functions validation

In this section, the failure criteria proposed by Camanho et al. (2015) are used to adjust and to validate the loading functions at the onset of failure. Their criteria are based on a 3D physically invariant formulation that is capable to accurately predict the onset of failure in a single unidirectional ply of a fibre reinforced polymer under a complex loading state. As demonstrated in their work, the numerical predictions of the failure criteria are in good agreement with the data available in the literature and with the numerical predictions computed using the micro-mechanical approach developed by Melro et al. (2013a, b) and Arteiro et al. (2014).

The material properties and parameters for the IM7/8552 that are required for the failure criteria and the loading functions are listed in Table 3. The ones referring to the loading functions are adjusted as following: μ_T is computed by means of the biaxial compression strength, Y_{BC}, using Eq. (36) in order to accurately describe the closed surface in $\bar{\sigma}_{22} - \bar{\sigma}_{33}$ stress space; μ_{LT} is computed through Eq. (37) considering $\eta_L = 0.5$, which is the longitudinal slope used by Catalanotti et al. (2013); and η_T, η_T^q, η_S and η_S^q are adjusted through a least squares method.

The surfaces representing the different stress spaces at the onset of damage are depicted in Fig. 3a–h. A very good agreement between the failure criteria and the loading functions is obtained. The differences that can be observed in Fig. 3c, e, h for the transversal shear strength, S_T, are due to the adjustment of μ_T. As aforementioned, it is adjusted in the current work by means of Y_{BC} instead of S_T and therefore, using Eq. (35) it is obtained that $S_T = 69.0$ MPa, whereas in the failure criteria it is $S_T = 62.3$ MPa. However, it must be pointed out that it is possible to match the transversal shear strength, but at cost of the biaxial compression strength. Additionally, it can be observed in Fig. 3c that the influence of transversal shear stress on the longitudinal compression strength is not accounted in the proposed loading functions.

4.2. Model input parameters

The model input parameters for an IM7/8552 unidirectional ply are listed in Table 4. The softening parameters are obtained by means of the cohesive properties summarized in Table 5, following the relations explained in Section 2. The cohesive laws along the longitudinal direction are assumed bilinear laws, whereas linear along the transverse and shear directions. The slope, a_M, and the ordinate, b_M, are computed by means of the fracture toughness, $\mathscr{G}_M$, and the uniaxial strength, X_M. Note that, in the first segment, $b_M^1 = X_M$. Moreover, in order to completely describe the longitudinal cohesive law, two extra properties are required: the strength at inflection point, $f_{XM}^1 X_M$, and the energy under the first part of the cohesive law, $f_{\mathscr{G}M}^1 \mathscr{G}_M$, see Fig. 2. It is worth mentioning that $\mathscr{G}_{1+}$ and $\mathscr{G}_{1-}$ are the fracture toughness associated with the breaking and kinking of the fiber, $\mathscr{G}_K$ and $\mathscr{G}_G$ with the cracking of the matrix in mode-I and mode-II, and $\mathscr{G}_6$ with the formation of in-plane shear cracks. Finally, the parameter k in Eq. (47) is constant for all the elements thanks to the definition of a structured mesh with a constant characteristic element size.

4.3. Matrix cracking test

The matrix cracking test consist on three cross-ply laminates subjected to tensile loading, whose stacking sequence consist of: $[0_2/90_n]_s$ with $n = 1,2,4$. The geometric definition is shown in Fig. 4 and the nominal dimensions are: length $L = 20$ mm, width $W = 20$ mm, and thickness $T = 0.125(n + 4)$ mm. Each model is discretized with a structured mesh conformed by eight-node cubic elements with full integration and an approximated aspect ratio of 1. The element size is set to $\ell_e = 0.05$ mm that corresponds to five elements per each two plies, e.g. for $n = 1$ there are 6 plies and therefore, 15 elements through the specimen thickness. This discretization results in meshes of 2.4, 3.2 and 4.8 million elements, for $n = 1$, 2, and 4, respectively. Finally, the loading of the specimen is performed by means of a monotonically increasing displacement applied at one end, whereas it is prohibited at the opposite end, see Fig. 4.

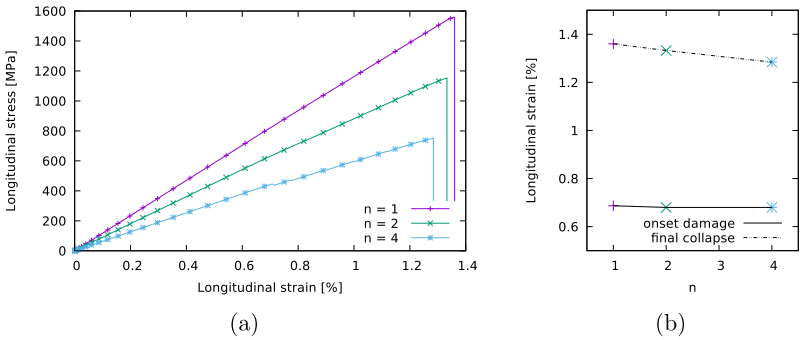

Fig. 5. (a) Longitudinal stress - strain response and (b) Longitudinal strain at the onset of the damage and at the final collapse of the specimen for the matrix cracking tests.

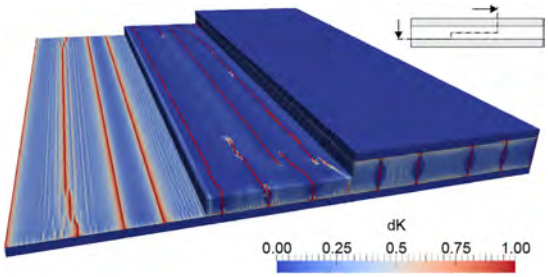

Fig. 6. Matrix damage, d_K, at $\varepsilon_{xx} = 1.0\%$ for $[0_2/90_4]_s$.

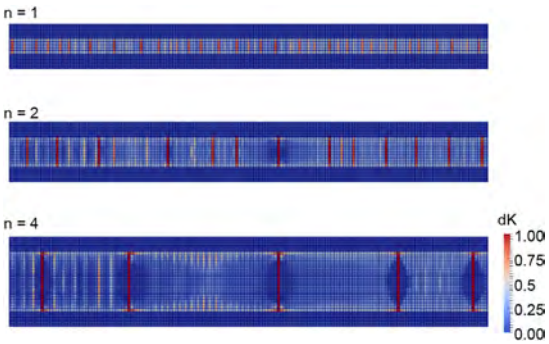

Fig. 7. Matrix damage, d_K, at $\varepsilon_{xx} = 0.9\%$ for $[0_2, 90_n]_s$, where $n = 1,2,4$.

The simulations are performed under a quasi-static regime using the β-Newmark temporal integration scheme (Newmark, 1959). The material tangent stiffness is approximated by the secant matrix computed as the inverse of the compliance matrix, defined in Eq. (29). It is well known that standard solution techniques lead to instabilities near discontinuity threshold, thus precluding the convergence of the algebraic solver. In the present work, it has been observed that at the beginning of the damage, the secant matrix increases the robustness of the algebraic solver, which in turn helps to find the solution of the Newton-Raphson, i.e. the equilibrium state. Taking benefit of the wide range of options that the Alya code offers, several combinations of algebraic solvers and preconditioners have been tested. It has been observed that, for the current case, a GMRES solver with a diagonal preconditioning gives a good compromise between efficiency and robustness (Magoulès et al., 2016).

The overall behaviour of a cross-ply laminate under tensile loading

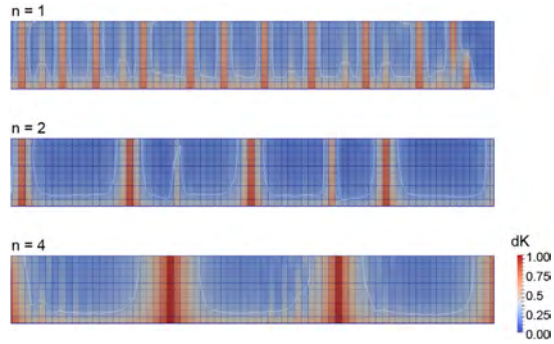

Fig. 8. Matrix damage, d_K, at the free-edge at $\varepsilon_{xx} = 0.9\%$ for $[0_2/90_n]_s$, where $n = 1,2,4$. The solid line is an isoline corresponding to $d_K = 0.3$.

Table 6
Computation time of the matrix cracking cases.

n	#Elements	#CPUs	CPU time [hh:mm]
1	2,400,000	312	00: 58
2	3,200,000	416	00: 59
4	4,800,000	624	01: 13

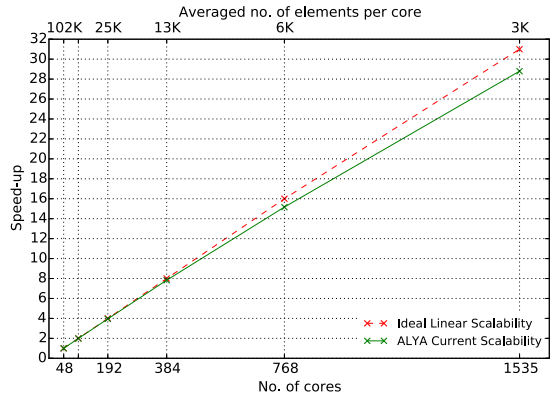

Fig. 9. Strong scalability curve for the matrix cracking test with 4.8 million of elements.

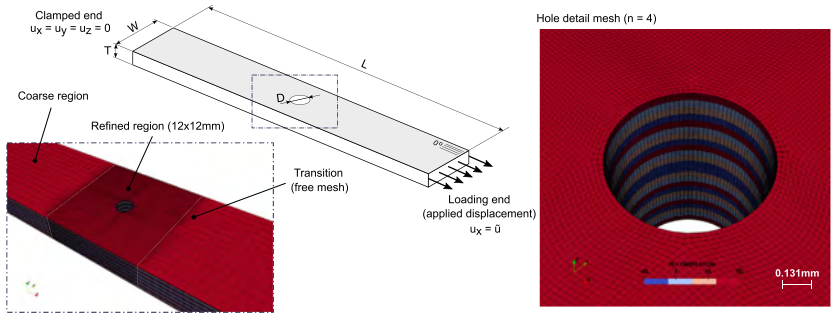

Fig. 10. Geometric definition and mesh detail for the open hole test.

Table 7
Mesh and computational time summary for the open hole test, where n indicates the number of elements per ply.

n	#Elements	#CPUs	CPU time [hh:mm]
1	258,000	48	2: 43
2	515,472	96	3: 06
4	4,123,776	624	18: 01

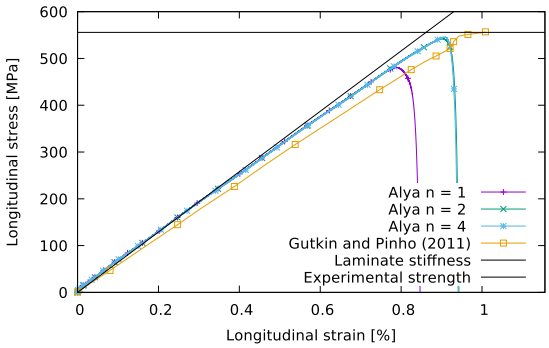

Fig. 11. Longitudinal stress - strain response for the open hole test.

Table 8
Experimental and numerical ultimate strength of the laminate for the open hole test.

Case	Laminate strength [MPa]	Error [%]
Exp.	555.70	–
$n = 1$	480.78	13.48
$n = 2$	541.89	2.49
$n = 4$	545.64	1.81

conditions is correctly captured by the proposed model. The matrix cracks appear in the inner plies of 90° up to the final collapse of the specimen, which is triggered by fibre tensile fracture of the adjoining plies (Maimí et al., 2008; Meyer and Waas, 2016).

The longitudinal stress-strain response for the different layups is shown in Fig. 5a. The onset of damage occurs at a similar strain level, whereas the final collapse occurs at a lower strain level as thicker is the central ply clustering, see 5b. This is because the failure in the outer plies is initiated where there is a matrix crack in the central plies. Therefore, if the central ply is thicker, the stress intensity factor is higher, which leads to a premature initiation of the failure.

In Fig. 6, the transversal matrix damage, d_K, for the $[0_2/90_4]_s$ specimen at $\varepsilon_{xx} = 1.0\%$ is depicted for two different views. It should be noted that the matrix damage is extended along the elements that surround the interface, whereas it is located around the cracks in the rest of the laminate thickness. This is in agreement with the experimental observations, which indicate that the nucleation of a matrix crack is followed by its propagation up to the interface triggering a delamination (Thorsson et al., 2016).

As can be appreciated in Fig. 7, the obtained crack pattern is different as a function of the central ply clustering. The crack density increases as the thickness of 90° plies cluster decreases.

Another interesting phenomena that can be observed in the simulation results is the effect of the free-edge at the interface. According to the experimental observations (Guillamet et al., 2016), the high normal and shear interlaminar stresses in addition to the lower in-situ strengths in the thicker laminates involve a premature development of the matrix damage at the free-edge. Fig. 8 depicts the matrix damage developed between the 0° and 90° plies at the free-edge for $\varepsilon_{xx} = 0.9\%$. It can be appreciated that the thicker the 90° ply clustering is, the larger the damaged area close to the free-edge is. Moreover, the damaged area between two neighbouring cracks follows the same trend. It is larger as thicker the 90° ply clustering is.

With regards to the computational performance, the number of CPUs used in each simulation as well as the total elapsed computational time are listed in Table 6. It is worth mentioning that the simulation time for all cases is less than 1 h and 15 min. In Fig. 9, it is shown the strong scalability curve for the largest specimen with 4.8 million of elements, i.e. $n = 4$. The scalability is measured based on the total time of the solver computation as it runs in an increasing number of processors. The straight line shows the ideal scalability, which indicates that if the number of processors is multiplied by a factor, the speed-up of the simulation should be increased proportionally. It can be seen that the current implementation maintains the excellent performance of the Alya code (Casoni et al., 2014; Vázquez et al., 2016), with an efficiency higher than 80% up to 1,535 cores, i.e. 3,000 elements per CPU.

4.4. Open hole test

An open-hole test tension subjected to tensile loading is presented here in order to strengthen the validation of the proposed damage formulation. The stacking sequence of the specimen under consideration is $[90/0/+45/-45]_{3s}$. The geometric configuration under consideration was previously studied by Camanho et al. (2007), Gutkin and Pinho (2011) and more recently by Reinoso et al. (2017). The nominal dimensions of the model are: length $L = 100$ mm, width $W = 12$ mm and thickness $T = 3.144$ mm with a hole diameter of $d = 2$ mm. The model is discretized with a structured mesh conformed by eight-node cubic elements with full integration. Two regions with different mesh sizes are distinguished: a refined mesh region defined in a 12x12 mm central square and a coarse mesh region that extends in the remaining part, see Fig. 10. Three meshes with different number of elements

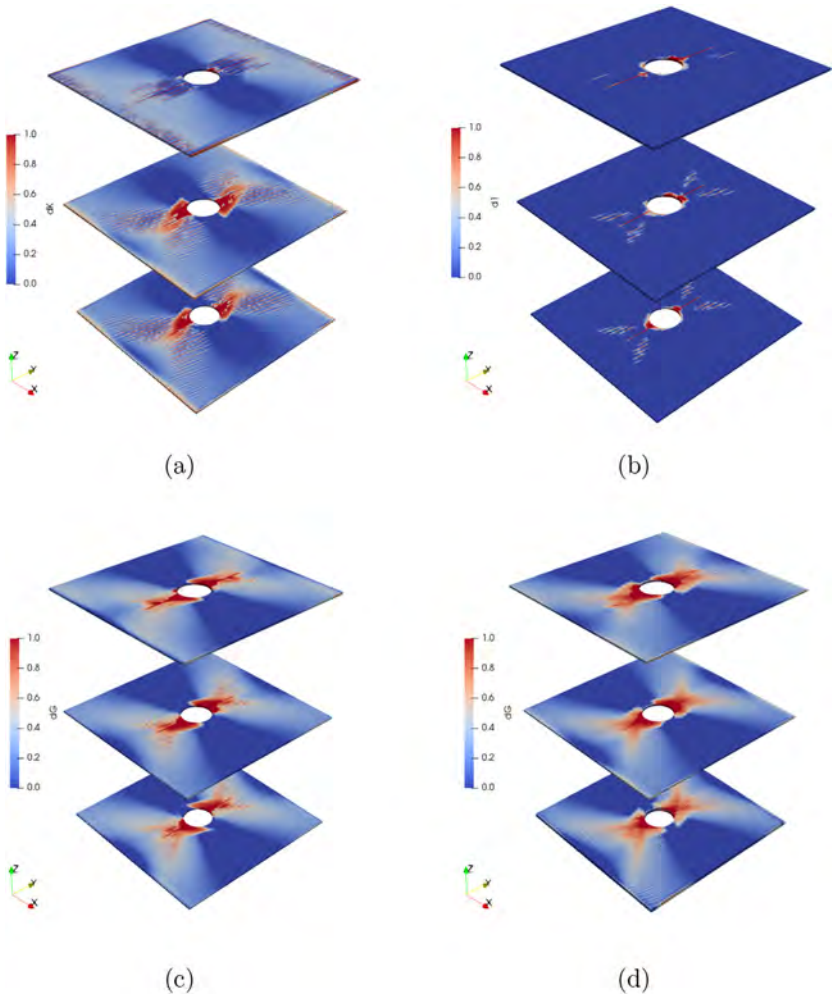

Fig. 12. Damage pattern at the different plies for the open hole test with four elements per ply, $n = 4$, just before the failure: (a) 90° plies - matrix damage, d_K, (b) 0° plies - fiber damage, d_{1+}, (c) +45° plies - matrix damage, d_G, (d) -45° plies - matrix damage, d_G.

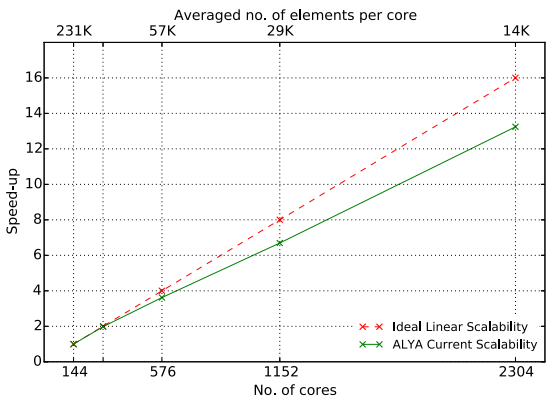

Fig. 13. Strong scalability curve for the open hole test with 30 million of elements.

through the thickness (denoted by n) are analysed in order to demonstrate the proper regularization of the current formulation at coupon level. Table 7 summarizes the computational resources and time for each discretization.

The simulations are performed using a central-difference temporal integration scheme, i. e an explicit scheme. The initial stable time increment used is $\Delta t \approx 7.45{\cdot}10^{-7}$s, which guarantees the stability of the scheme (Belytschko et al., 2013). In addition, a displacement control loading with smooth step is applied in order to vanish the initial velocities and accelerations. Thus minimizing the inertial forces at the beginning of the simulation.

The longitudinal stress-strain response for the different element sizes is shown in Fig. 11. A good correlation between numerical predictions and experimental data for those models with more than one element through the ply thickness can be observed in Table 8. It is worth mentioning that the nominal strengths given in Table 4 have been used in the simulations, instead of modifying some properties according to the ply thickness, as it is usually done in the literature, and referred as in-situ strengths (Dvorak and Laws, 1987; Camanho et al.,

2007). This have some implications if the discretization of the plies in the thickness direction is not refined enough. It can be appreciated with the numerical prediction for one element per ply, $n = 1$, which has an error of 13.5%. In contrast, when more than one element through the thickness is used, $n > 1$, the current formulation captures the in-situ effect as demonstrate with an error below 3%.

As shown in Fig. 11, the stress-strain curve has an inflection point $\approx 200MPa$, which is in agreement with the experimental results reported by Reinoso et al. (2017). According to their work, this inflection point marks the transition between a first stage without damage and a second stage with interlaminar and intralaminar damage evolution. The current simulations do not include cohesive elements, so interlaminar damage is captured by the 3D nature of the intralaminar model and cannot be precisely separated from intra-laminar damage. This is in concordance with the results shown in the matrix cracking tests, see Fig. 6. It must be pointed that in problems where the matrix rich layer plays an important role, such as those involving bolted joints (Joseph et al., 2017, 2018) or stiffeners (Krueger et al., 2002; Psarras et al., 2011), the interlaminar damage should be explicitly modelled using, for instance, a cohesive zone model (Turon et al., 2006, 2018).

The damage pattern for the open hole test using the mesh with four elements per ply, $n = 4$, is represented in Fig. 12 at a load level close to the maximum load, $\sigma_{xx} = 542$ MPa. Due to symmetry, only top-half of the stacking sequence is represented. In this figure, the most relevant damage mechanisms are represented for each orientation: plies at 90° mostly have matrix failure under tension (d_K); plies at $\pm$ 45° have matrix failure under shear (d_G) as the most predominant; and plies oriented at 0° show fiber failure (d_1). The first ply failure occurs at the 90° outer ply and it is concentrated around the hole, approximately at $\varepsilon_{xx} = 0.3\%$, in agreement with Reinoso et al. (2017). This ply exhibits tensile matrix cracking failure (d_K) in two locations: around the hole and at the free-edge, the former in agreement also with the results predicted by Gutkin and Pinho (2011). With regard to the $\pm$ 45° plies a similar damage pattern is obtained, as shown in Fig. 12c and d. In these cases, matrix failure under shear (d_G) is the most predominant damage mechanism. Damage is initiated at the hole and propagates perpendicularly to the loading direction, in accordance with the failure mode observed in the experiments (Camanho et al., 2007). Finally, the progression of the matrix failure around the hole leaves the 0° plies sustaining the major part of the load and leads to a net-fiber failure damage (d_1) just before the total failure of the specimen, see Fig. 12b.

The computational times are listed in Table 7. Fig. 13 shows a scalability analysis for a mesh of 30 million elements. In this case, the scalability is measured excluding pre- and post-process tasks and increasing the number of processors from 144 to 2,304. From this figure, it can be conclude that the current case scales well until 2,304 cores with an efficiency close to 80%. For this case the sweet spot is around 14,000 element per core.

5. Conclusions

A 3D continuum damage model able to predict the progressive failure of laminated composite materials under complex stress states has been proposed. The formulation of the model is based on the continuum damage mechanics framework in order to ensure its thermodynamic consistence. The loading functions have been defined to describe a large number of materials. The envelope of the load functions proposed have been compared with the envelopes obtained using a physically based failure criteria, showing a good agreement. The damage laws are piecewise functions of n linear segments that have been formulated using the crack band model in order to ensure the energy mesh-independent prediction.

The model has been implemented in the Alya code, a high performance computing based finite element software. The simulated loading cases demonstrate the capability of the model to capture the kinematics of the propagation of transverse matrix cracks for cross-plies and the damage pattern developed in the open hole tensile test. The model correctly captures the complex phenomena associated with these specimens, such as the in-situ effect and the complex stress state at the free-edges due to the mismatch of the Poisson ratios of adjacent layers. In addition, the matrix damage arising at the interfaces between two plies is also captured if more than one element through the thickness is used. This damage can be identified as delamination damage showing the potential of the current formulation. Finally, the scalability curves are shown for meshes of 4.8 and 30 million elements, showing the good scalability and efficiency of Alya code up to thousands of cores.

Acknowledgements

The first author would like to thank the Spanish Government (Ministerio de Educación, Cultura y Deporte) for the pre-doctoral grant FPU 15/06287. This works has been partially funded by the Spanish Government (Ministerio de Economía y Competitividad) under contracts TRA2015-71491-R, MAT2013-46749-R and MAT2015-69491-C3-1-R.

References

Abisset, E., Daghia, F., Ladevèze, P., 2011. On the validation of a damage mesomodel for laminated composites by means of open-hole tensile tests on quasi-isotropic laminates. Compos. Appl. Sci. Manuf. 42 (10), 1515–1524.
Ahn, J., Waas, A., 2002. Prediction of compressive failure in laminated composites at room and elevated temperature. AIAA J. 42 (2), 346–358.
Argon, A., 1972. TReatise on Materials Science and Technology: Materials Science Series, vol. 1. Academic Press, New York, pp. 79–114.
Arteiro, A., Catalanotti, G., Melro, A., Linde, P., Camanho, P., 2014. Micro-mechanical analysis of the in situ effect in polymer composite laminates. Compos. Struct. 116 (1), 827–840.
Barbero, E., de Vivo, L., 2001. A constitutive model for elastic damage in fiber-reinforced pmc laminae. Int. J. Damage Mech. 10 (1), 73–93.
Bažant, Z.P., Oh, B.H., 1983. Crack band theory for fracture of concrete. Matériaux et Construction et Construction 16 (3), 155–177.
Belytschko, T., Liu, W.K., Moran, B., Elkhodary, K., 2013. Nonlinear Finite Elements for Continua and Structures. Wiley.
Camanho, P., Arteiro, A., Melro, A., Catalanotti, G., Vogler, M., 2015. Three-dimensional invariant-based failure criteria for fibre-reinforced composites. Int. J. Solid Struct. 55, 92–107.
Camanho, P., Bessa, M., Catalanotti, G., Vogler, M., Rolfes, R., 2013. Modeling the inelastic deformation and fracture of polymer composites part ii: smeared crack model. Mech. Mater. 59 (Suppl. C), 36–49.
Camanho, P., Lambert, M., 2006. A design methodology for mechanically fastened joints in laminated composite materials. Compos. Sci. Technol. 66 (15), 3004–3020.
Camanho, P., Maimí, P., Dávila, C., 2007. Prediction of size effects in notched laminates using continuum damage mechanics. Compos. Sci. Technol. 67 (13), 2715–2727.
Casoni, E., Jérusalem, A., Samaniego, C., Eguzkitza, B., Lafortune, P., Tjahjanto, D., Sáez, X., Houzeaux, G., Vázquez, M., 2014. Alya: computational solid mechanics for supercomputers. Arch. Comput. Meth. Eng. 22 (4), 557–576.
Catalanotti, G., Camanho, P., Marques, A., 2013. Three-dimensional failure criteria for fiber-reinforced laminates. Compos. Struct. 95, 63–79.
Cho, J., Fenner, J., Werner, B., Daniel, I., 2013. Numerical analysis of size effects on open-hole tensile composite laminates. Compos. Appl. Sci. Manuf. 47 (Suppl. C), 52–62.
Dvorak, G., Laws, N., 1987. Analysis of progressive matrix cracking in composite laminates ii. first ply failure. J. Compos. Mater. 21 (4), 309–329.
Guillamet, G., Turon, A., Costa, J., Linde, P., 2016. A quick procedure to predict free-edge delamination in thin-ply laminates under tension. Engineering Fracture Mechanics 168, Part B 28–39.
Gutkin, R., Pinho, S., 2011. Practical Application of Failure models to Predict the Response of Composite Structures.
Hill, R., 1998. The Mathematical Theory of Plasticity. Oxford Classic Texts in the Physical Sciences. Clarendon Press.
Houlsby, G., Puzrin, A., 2000. A thermomechanical framework for constitutive models for rate-independent dissipative materials. Int. J. Plast. 16 (9), 1017–1047.
Houzeaux, G., de la Cruz, R., Owen, H., Vázquez, M., 2013. Parallel uniform mesh multiplication applied to a navierstokes solver. Computers & Fluids 80, 142–151 selected contributions of the 23rd International Conference on Parallel Fluid Dynamics ParCFD2011.
Houzeaux, G., Vázquez, M., Aubry, R., Cela, J., 2009. A massively parallel fractional step solver for incompressible flows. J. Comput. Phys. 228 (17), 6316–6332.
Joseph, A., Davidson, P., Waas, A., 2017. Intra-inter Crack Band Model (I2cbm) for Progressive Damage and Failure Analysis of Joints.
Joseph, A., Davidson, P., Waas, A.M., 2018. Intra-inter Crack Band Model (I2cbm) for Progressive Damage and Failure Analysis of Joints.
Joseph, A., Waas, A.W., Ji, E.P., Liguore, S., Wanthal, S., 2015. Progressive Damage and Failure Prediction of Open Hole Tension and Open Hole Compression Specimens.
Koerber, H., Xavier, J., Camanho, P., 2010. High strain rate characterisation of

unidirectional carbon-epoxy im7-8552 in transverse compression and n-plane shear using digital image correlation. Mech. Mater. 42 (11), 1004–1019.
Krueger, R., Paris, I., O'Brien, T., Minguet, P., 2002. Comparison of 2d finite element modeling assumptions with results from 3d analysis for composite skin-stiffener debonding. Compos. Struct. 57 (1), 161–168.
Ladevèze, P., Dantec, E.L., 1992. Damage modelling of the elementary ply for laminated composites. Compos. Sci. Technol. 43 (3), 257–267.
Lemaitre, J., Chaboche, J., 1990. Mechanics of Solid Materials. Cambridge University Press, cambridge Books Online.
Löhner, R., Mut, F., Cebral, J., Aubry, R., Houzeaux, G., 2011. Deflated preconditioned conjugate gradient solvers for the pressure-Poisson equation: extensions and improvements. Int. J. Numer. Meth. Eng. 87 (1–5), 2–14.
Magoulès, F., Roux, F., Houzeaux, G., 2016. Parallel Scientific Computing. Computer Engineering Series. ISTE-John Wiley & Sons.
Maimí, P., Camanho, P., Mayugo, J., Dávila, C., 2007a. A continuum damage model for composite laminates: Part {I} constitutive model. Mech. Mater. 39 (10), 897–908.
Maimí, P., Camanho, P., Mayugo, J., Dávila, C., 2007b. A continuum damage model for composite laminates: Part {II} computational implementation and validation. Mech. Mater. 39 (10), 909–919.
Maimí, P., Camanho, P., Mayugo, J., Turon, A., 2011. Matrix cracking and delamination in laminated composites. part i: ply constitutive law, first ply failure and onset of delamination. Mech. Mater. 43 (4), 169–185.
Maimí, P., Mayugo, J., Camanho, P., 2008. A three-dimensional damage model for transversely isotropic composite laminates. J. Compos. Mater. 42 (25), 2717–2745.
Martín-Santos, E., Maimí, P., González, E., Cruz, P., 2014. A continuum constitutive model for the simulation of fabric-reinforced composites. Compos. Struct. 111, 122–129.
Matzenmiller, A., Lubliner, J., Taylor, R., 1995. A constitutive model for anisotropic damage in fiber-composites. Mech. Mater. 20 (2), 125–152.
Melro, A., Camanho, P., Pires, F.A., Pinho, S., 2013a. Micromechanical analysis of polymer composites reinforced by unidirectional fibres: Part i constitutive modelling. Int. J. Solid Struct. 50 (1112), 1897–1905.
Melro, A., Camanho, P., Pires, F.A., Pinho, S., 2013b. Micromechanical analysis of polymer composites reinforced by unidirectional fibres: Part {II} micromechanical analyses. Int. J. Solid Struct. 50 (1112), 1906–1915.
Meyer, P., Waas, A., 2016. Fem predictions of damage in continous fiber ceramic matrix composites under transverse tension using the crack band method. Acta Mater. 102 (Suppl. C), 292–303.
Newmark, N.M., 1959. A method of computation for structural dynamics. Journal of the Eng. Mech. Div 85 (3), 67–94.
Oller, S., Botello, S., Miquel, J., Oñate, E., 1995. An anisotropic elastoplastic model based on an isotropic formulation. Eng. Comput. 12 (3), 245–262.
Ortega, A., Maimí, P., Gonzlez, E., de Aja, J.S., de la Escalera, F., Cruz, P., 2017. Translaminar fracture toughness of interply hybrid laminates under tensile and compressive loads. Compos. Sci. Technol. 143, 1–12.
Ortega, A., Maimí, P., Gonzlez, E., Trias, D., 2016. Characterization of the translaminar fracture cohesive law. Compos. Appl. Sci. Manuf. 91 (Part 2), 501–509 compTest 2015.
Pineda, E., Waas, A., 2013. Numerical implementation of a multiple-isv thermo-dynamically-based work potential theory for modeling progressive damage and failure in fiber-reinforced laminates. Int. J. Fract. 182 (1), 93–122.
Pinho, S., Iannucci, L., Robinson, P., 2006. Physically based failure models and criteria for laminated fibre-reinforced composites with emphasis on fibre kinking. part ii: Fe implementation. Composites Part A: Applied Science and Manufacturing 37 (5), 766–777.
Psarras, S., Pinho, S., Falzon, B., 2011. Design of composite stiffener run-outs for damage tolerance. Finite Elem. Anal. Des. 47 (8), 949–954 computational Mechanics and Design.
Ralston, A., Rabinowitz, P., 2001. A First Course in Numerical Analysis. Dover Books on Mathematics. Dover Publications.
Reinoso, J., Blázquez, A., 2016. Application and finite element implementation of 7-parameter shell element for geometrically nonlinear analysis of layered cfrp composites. Compos. Struct. (Suppl. C), 263–276.
Reinoso, J., Catalanotti, G., Blázquez, A., Areias, P., Camanho, P., París, F., 2017. A consistent anisotropic damage model for laminated fiber-reinforced composites using the 3d-version of the puck failure criterion. Int. J. Solid Struct. 126–127 (Suppl. C), 37–53.
Rosen, B., 1965. Mechanics of composite strengthening. Fiber Composite Materials 28–32.
Simo, J., Ju, J., 1987. Strain- and stress-based continuum damage modelsi. formulation. Int. J. Solid Struct. 23 (7), 821–840.
Soden, P., Hinton, M., Kaddour, A., 1998. Lamina properties, lay-up configurations and loading conditions for a range of fibre-reinforced composite laminates. Compos. Sci. Technol. 58 (7), 1011–1022.
Soden, P., Hinton, M., Kaddour, A., 2002. Biaxial test results for strength and deformation of a range of e-glass and carbon fibre reinforced composite laminates: failure exercise benchmark data. Compos. Sci. Technol. 62 (1213), 1489–1514.
Sun, C., Chen, J., 1989. A simple flow rule for characterizing nonlinear behavior of fiber composites. J. Compos. Mater. 23 (10), 1009–1020.
Thorsson, S., Xie, J., Marek, J., Waas, A., 2016. Matrix crack interacting with a delamination in an impacted sandwich composite beam. Eng. Fract. Mech. 163 (1011), 476–486.
Tsai, J., Sun, C., 2002. Constitutive model for high strain rate response of polymeric composites. Compos. Sci. Technol. 62 (1011), 1289–1297.
Turon, A., Camanho, P., Costa, J., Dávila, C., 2006. A damage model for the simulation of delamination in advanced composites under variable-mode loading. Mech. Mater. 38 (11), 1072–1089.
Turon, A., González, E., Sarrado, C., Guillamet, G., Maimí, P., 2018. Accurate simulation of delamination under mixed-mode loading using a cohesive model with a mode-dependent penalty stiffness. Compos. Struct. 184 (1011), 506–511.
Van Der Meer, F., 2016. Micromechanical validation of a mesomodel for plasticity in composites. Eur. J. Mech. Solid. 60 (5), 58–69.
Van Der Meer, F., Sluys, L., Hallett, S., Wisnom, M., 2012. Computational modeling of complex failure mechanisms in laminates. J. Compos. Mater. 46 (5), 603–623.
Vasiukov, D., Panier, S., Hachemi, A., 2015. Non-linear material modeling of fiber-reinforced polymers based on coupled viscoelasticityviscoplasticity with anisotropic continuous damage mechanics. Compos. Struct. 132, 527–535.
Vázquez, M., Houzeaux, G., Koric, S., Artigues, A., Aguado-Sierra, J., Arís, R., Mira, D., Calmet, H., Cucchietti, F., Owen, H., Taha, A., Derin, E., Cela, J., Valero, M., 2016. Alya: multiphysics engineering simulation toward exascale. Journal of Computational Science 14, 15–27.
Vogler, M., Rolfes, R., Camanho, P., 2013. Modeling the inelastic deformation and fracture of polymer composites part i: plasticity model. Mech. Mater. 59, 50–64.
Weeks, C., Sun, C., 1998. Modeling non-linear rate-dependent behavior in fiber-reinforced composites. Compos. Sci. Technol. 58 (34), 603–611.
Williams, K., Vaziri, R., Poursartip, A., 2003. A physically based continuum damage mechanics model for thin laminated composite structures. Int. J. Solid Struct. 40 (9), 2267–2300.
Yokozeki, T., Ogihara, S., Yoshida, S., Ogasawara, T., 2007. Simple constitutive model for nonlinear response of fiber-reinforced composites with loading-directional dependence. Compos. Sci. Technol. 67 (1), 111–118.

Paper B

A phase field approach to simulate intralaminar and translaminar fracture in long fiber composite materials

Published in *Composite Structures* (ISSN: 0263-8223)
Impact factor according to the 2017 Journal Citation Reports: 4.101, ranked 5/26 in category *Materials Science, Composites* (1st quartile)

Composite Structures 220 (2019) 899–911

Contents lists available at ScienceDirect

Composite Structures

journal homepage: www.elsevier.com/locate/compstruct

A phase field approach to simulate intralaminar and translaminar fracture in long fiber composite materials

A. Quintanas-Corominas[a], J. Reinoso[b,*], E. Casoni[c], A. Turon[a], J.A. Mayugo[a]

[a] AMADE, Polytechnic School, Universitat de Girona, Campus Montilivi s/n, 17071 Girona, Spain
[b] Elasticity and Strength of Materials Group, School of Engineering, Universidad de Sevilla, Camino de los Descubrimientos s/n, 41092 Seville, Spain
[c] Barcelona Supercomputing Center, Edificio NEXUS I, Campus Nord UPC, Gran Capitán 2–4, 08034 Barcelona, Spain

ARTICLE INFO

Keywords:
A. Composite materials
B. FE-modeling
C. Damage modeling
D. Fracture
E. Phase Field

ABSTRACT

The development of predictive numerical methods, which accurately represent the progressive failure of long fiber composite materials, is nowadays required for the achievement of optimized mechanical responses in terms of load bearing capacities of modern composite structures. In this investigation, two characteristic failure mechanisms of long fiber composites, denominated as intralaminar and translaminar fracture, are simulated by means of a novel version of the phase field (PF) approach of fracture. This numerical strategy encompasses a sort of gradient-enhanced damage formulation rooted in the Griffith theory of fracture, which is herewith extended for its use in composite laminates applications. In order to assess its verification and validation, the predictions obtained using the present formulation are compared against experimental results and two well-established alternative computational methods, which correspond to an anisotropic local-based continuum damage model and a cohesive zone model. The comparisons demonstrate that the PF approach with the proposed formulation provides reliable and robust predictions under quasi-static loading, but with a higher versatility regarding the potential of triggering arbitrarily complex crack paths with intricate topology over alternative techniques.

1. Introduction

The production of highly efficient structures made from Long Fiber Reinforced Composites (LFRCs) has been a recurrent objective during the last decades. Current production demands aim to obtain optimized designs with higher damage tolerance, which intrinsically imply a comprehensive understanding of the mechanisms involved during the failure processes. At mesoscopic length scale, the typical failure mechanisms in LFRCs can be classified as: (*i*) intralaminar failure, which includes breaking and kinking of the fibers and cracking of the matrix, (*ii*) interlaminar failure that is the delamination between plies, and (*iii*) translaminar failure, which is a fracture event within the laminate thickness involving different plies. These different mechanisms in conjunction with the orthotropic mechanical response at the lamina level generally induce to the occurrence of complex mechanical responses that are difficult to predict in a faithful manner. For this reason, the development of robust and reliable simulations methods is nowadays mandatory in order to achieve an improved level of exploitation of the load-bearing capacities of modern composite structures.

In the context of Finite Element Method (FEM) based tools, satisfactory results have been achieved through the exploitation of Cohesive Zone Models (CZM) [1–3] and local-based anisotropic Continuum Damage Models (CDM) [4–9]. However, one of the main drawbacks of these techniques is the necessity of aligning the mesh with the fiber direction [10], which leads to difficult mesh generations and reduces the predictive capabilities. To overcome this issue, different enriched FE-based formulations have been proposed in the related literature so far, such as the eXtended FEM (X-FEM) [11], the Enhanced FEM (E-FEM) [12], the Floating Point Method (also denominated as the Phantom Node Method) [13]. Despite their effectiveness, the aforementioned techniques can suffer from tracking the actual crack path topology, especially in 3D applications, whereby intricate crack coalescence and branching scenarios may potentially occur. In addition, their implementation can be especially challenging and problematic in parallel environments and High Performance Computing (HPC) platforms.

A promising alternative for modeling the progressive failure is the recent Phase Field (PF) approach for fracture, which has gained a notable relevance during the last years in the scientific community [14,15]. In particular, this approach allows the accurate simulation of complex crack paths, including crack branching and coalescence, without the need of cumbersome crack tracking algorithms. The PF

* Corresponding author.
E-mail address: jreinoso@us.es (J. Reinoso).

https://doi.org/10.1016/j.compstruct.2019.02.007
Received 3 November 2018; Received in revised form 11 January 2019; Accepted 4 February 2019
Available online 06 February 2019

approach is rooted in the seminal work developed by Francfort and Marigo [16], who proposed a modified variational approach to brittle fracture exploiting the classical Griffith fracture theory [17]. In particular, this technique has been successfully applied to brittle, cohesive and ductile fracture in 2D and 3D analyses [18–21], shells [22,23], heterogeneous media in combination with the CZM [24,25], and multiphysics environments [26,27]. The results presented in these studies showed that the strain localization path has a reduced mesh dependency when the spatial discretization (mesh size) is small enough to resolve the fracture process zone.

However, at present, the use of the PF to perform progressive damage analysis of long fiber composite materials has received very limited attention, see [28,29]. Regarding the modeling of anisotropic behavior in the context of the PF approach, there are recent investigations that modeled the anisotropy using structural tensors, see for instance [30–34]. The main drawback of this strategy is that it accounts only for a unique critical energy release rate. This limitation is not in line with the actual nature of composite materials, in which each failure mechanisms have associated a different critical energy. Bleyer and Alessi [35] proposed a pioneering incursion on this matter via the definition of several PF variables, one for each intralaminar failure mechanism, i.e. fiber and matrix failures. Despite the promising results, their strategy increases the computational efforts (since a set of phase field variables with their corresponding evolution equations are considered [35]), and therefore this fact can potentially complicate the numerical solution scheme.

Based on the previous arguments, the purpose of the current research is the development, assessment and application of the PF approach to model the progressive failure of long fiber reinforced composites subjected to quasi-static tensile conditions. A salient aspect of the current study regards the development of a new PF formulation suitable for modeling damage events in composite laminates from different signature, specifically for the treatment of intralaminar and translaminar failure. In this concern, differing from previous methods, the strategy herein adopted combines the structural tensor with an additive split of crack driving forces, requiring a single damage-like variable that encompasses the contribution of each failure mode. In this sense, the developed formulation can be conceived as an approach falling between the mesoscopic and macroscopic modeling assumptions. Correspondingly, from an operative standpoint, the complete set of elastic properties are degraded at the same rate but taking into account the anisotropic response and different damage mechanisms as those specified above. A similar strategy has been recently adopted by Gültekin et al. [36,37] for biomechanics systems. Recalling thermodynamic arguments, the fundamental ingredients of the underlying theoretical and numerical implementation are herein outlined. Moreover, in order to perform high-fidelity massive composite simulations, this strategy is implemented into the FE-code `Alya`, which is a multiphysics parallel software developed at Barcelona Supercomputing Center [38]. Finally, the potential and accuracy of the proposed PF approach is demonstrated by comparing the current numerical predictions for intralaminar and translaminar failure with available experimental data and with alternative computational results using an anisotropic CDM [9] and CZM [39].

The manuscript is organized as follows. Section 2 briefly introduces the fundamental theoretical and numerical aspects of the PF method for fracture. The constitutive assumptions regarding the long fiber composite materials are presented in Section 3. In Section 4, current predictions regarding intralaminar and translaminar failure with two alternative predictive techniques are presented. Moreover, current results associated with translaminar failure are correlated with experimental and linear elastic fracture mechanics (LEFM) results, showing a very satisfactory agreement. Finally, the main conclusions are summarized in Section 5.

2. Phase field approach to fracture

In this section, the fundamental aspects of the current PF formulation are presented. Firstly, the PF approach for brittle fracture are briefly revisited in Section 2.1. For a more comprehensive derivation, the readers are referred to the seminal works of Miehe et al. [18] and Bourdin et al. [40]. Subsequently, in Section 2.2, it is outlined the numerical strategy developed in the current study, pinpointing the novel aspects herewith addressed. Finally, the role of the length scale parameter ℓ and the effective energy release rate $\mathscr{G}_c$ are briefly discussed in Section 2.3.

2.1. Fundamentals of the PF approach

The PF approach to brittle fracture is conceived as a regularized version of the evolutionary problem of crack propagation under quasi-static conditions. Therefore, the crack evolution is studied by the minimization of the functional that describes the potential energy of the body under consideration in the spirit of the Griffith's theory of fracture. For the current investigation concerning fiber reinforced composites, we focus our attention on a body subjected to infinitesimal deformation in the general Euclidean space of dimension N. In this sense, let $\mathscr{B} \in \mathbb{R}^N$ be an arbitrary body with an existing crack network represented by the boundary Γ as illustrated in Fig. 1. Moreover, let $\partial\mathscr{B}$ be the exterior boundary of the body, whose outward normal unit vector is represented by $\boldsymbol{n}$. The material points within the body are identified by the position vector $\boldsymbol{x} \in \mathscr{B}$, whereas its displacement field is identified by the vector field $\boldsymbol{u}(\boldsymbol{x}, t)$. Finally, we assume that $\mathscr{B}$ is subjected to body forces $\boldsymbol{b}$ as well as boundary conditions in form of prescribed displacements ($\bar{\boldsymbol{u}}$ on $\partial\mathscr{B}_u$) and prescribed tractions ($\bar{\boldsymbol{t}}$ on $\partial\mathscr{B}_t$). These boundary conditions are subjected to the Neumann-Dirichlet conditions, i.e. $\partial\mathscr{B}_t \cup \partial\mathscr{B}_u = \partial\mathscr{B}$ and $\partial\mathscr{B}_t \cap \partial\mathscr{B}_u = \varnothing$.

Recalling the variational approach to brittle fracture [40], the energy functional governing a cracked body subjected to external mechanical loadings, such as the one defined previously, reads:

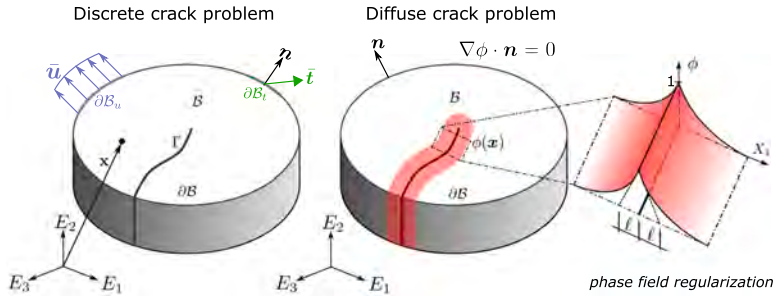

Fig. 1. Schematic representation of an arbitrary body with a discrete or a diffuse crack regularized by means of the phase field variable.

$$\Pi(\boldsymbol{u}, \Gamma) = \Pi_{\text{int}}(\boldsymbol{u}, \Gamma) + \Pi_{\text{ext}}(\boldsymbol{u}) \tag{1}$$

where Π_{int} and Π_{ext} account for the internal and the external (which is associated with the external mechanical loadings) counterparts, respectively. Here, the internal energy density functional Π_{int} can be defined as the sum of the elastic energy stored in the body $\Pi_{\mathscr{B}}$ and the energy dissipated through different mechanisms Π_{Γ}. Then, considering only dissipative mechanisms stemming from the formation and propagation of a cracks network, it is postulated through Griffith's theory [17] that:

$$\Pi_{\text{int}}(\boldsymbol{u}, \Gamma) = \Pi_{\mathscr{B}}(\boldsymbol{u}) + \Pi_{\Gamma}(\Gamma) = \int_{\mathscr{B}\setminus\Gamma} \Psi(\boldsymbol{u})\mathrm{dV} + \int_{\Gamma} \mathscr{G}_c \mathrm{dA} \tag{2}$$

where Ψ is the specific elastic bulk energy, $\mathscr{G}_c$ is the critical energy release rate and $\boldsymbol{u}$ is the displacement vector field. Here, the Griffith criterion is used to evaluate the fracture energy dissipated during the formation of Γ through the initiation and propagation of the crack network. Note that in the context of a minimization energy problem, the previous expression defines a direct competition between the elastic energy stored in the body and the fracture energy dissipated in the cracks network.

The evaluation of Eq. (2) can become a complex and computationally intensive task when numerical methods based on space discretization are used (FEM, mesh-less methods, among others). The difficulty arises from the evolution of the discrete boundary representing the crack path Γ, which is necessary to evaluate both (volume and surface) integrals expressions concomitantly. Taking into account that cracks generally propagate along the most favorable energetic path, which can exhibit bifurcation and coalescence phenomena, the resulting path can be arbitrarily complex. This aspect leads to the use of tracking algorithms, which increases the costs of implementation and computation, especially in 3D analysis. In order to circumvent the use of tracking algorithms, there exists the possibility to use non-local damage approaches. In particular, the current work is focused on the PF approach, which was seminally conceived by Bourdin et al. [40] as a regularization technique that smears the discrete boundary of a crack over the entire domain of the body. Concretely, it is rooted in the framework developed by Francfort and Marigo [16], which exploits the Γ-convergence concept to approximate an internal boundary avoiding its explicit representation [41]. In other words, the PF approach is a regularized version of the variational problem of brittle fracture, in the same line that gradient damage formulations [42].

Correspondingly, within the context of the PF approach, the surface integral in the dissipated energy can be approximated by a volume integral:

$$\int_{\Gamma} \mathscr{G}_c \mathrm{dA} \approx \int_{\mathscr{B}} \mathscr{G}_c \gamma(\phi, \nabla\phi)\mathrm{dV} \tag{3}$$

where $\gamma(\phi, \nabla\phi)$ is a functional representing the crack surface density and $\phi(\boldsymbol{x})$ is a continuous scalar field representing the amount of surface crack created at a material point. In turn, $\nabla\phi(\boldsymbol{x})$ is the spatial gradient of the PF. Thanks to these new variables, the discrete boundary of a crack γ is regularized over the body domain inducing the diffuse representation illustrated in Fig. 1. Note that this approach can be interpreted as a smooth representation of the Griffith fracture criterion. Moreover, the PF can be related to the damage state of a material point, similarly to the state variable used in the continuum damage models [18]. Henceforth, $\phi = 0$ represents a virgin state, whereas $\phi = 1$ identifies a fully damaged one. The dependency of ϕ on the material coordinates vector $\boldsymbol{x}$ is avoided in the sequel in order to alleviate the formulation.

Next, the crack surface density functional introduced in the previous expression is herein defined using a modified version of the Ambrosio-Tortorelli functional [37]:

$$\gamma(\phi, \nabla\phi) = \frac{1}{2\ell}(\omega(\phi) + \nabla\phi\cdot\mathcal{L}\nabla\phi) \tag{4}$$

where $\omega(\phi)$ is a function such that $\omega(0) = 0$ and $\omega(1) = 1$; ℓ is the length scale parameter that controls the transition between a virgin and a damage state, see Fig. 1; and $\mathcal{L}$ is a structural tensor that aligns the PF with a preferred direction. In the case of an isotropic surface density, it is defined as $\mathcal{L} = \ell^2\mathbf{I}$. A comprehensive description of the ℓ role is explained in Section 2.3.

Furthermore, in the PF approach, Ψ is redefined to include the influence of the PF variable, i.e. $\Psi(\boldsymbol{u}) \approx \Psi(\boldsymbol{u}, \phi)$. This modification is motivated by the fact that, to ensure the thermodynamic equilibrium, the elastic energy density in the transition zone has to decrease as the dissipated energy increases due to the crack formation. Moreover, in the current approach, the elastic energy density is energetically split into active Ψ_{act} and passive Ψ_{pas} contributions as proposed by Miehe et al. [43]. This split allows the possibility to affect with the PF only the active contribution endowing the modeling of asymmetric damage behaviors. Under reversal loading, the closing of the crack flanks precludes the damage evolution and provokes a stiffness recovery. Based on the aforementioned observations, Ψ is defined as:

$$\Psi(\boldsymbol{u}, \phi) = (\alpha(\phi) + \eta_\ell)\Psi_{\text{act}}(\boldsymbol{u}) + \Psi_{\text{pas}}(\boldsymbol{u}) \tag{5}$$

where $\alpha(\phi)$ is a monotonic function that models the degradation of energy as the crack density increases, fulfilling that $\alpha(0) = 1$ and $\alpha(1) = 0$, and $\eta_\ell = \mathcal{O}(\ell)$ is a numerical parameter associated with a residual elastic energy that is defined to mitigate instabilities during the solution process.

Taking into account Eqs. (3)–(5), the regularized version of the internal energy density functional defined in Eq. (2) is given by:

$$\Pi_{\text{int}}(\boldsymbol{u}, \Gamma) \approx \Pi_{\text{int}}(\boldsymbol{u}, \phi) = \Pi_{\mathscr{B}}(\boldsymbol{u}, \phi) + \Pi_{\Gamma}(\phi) \tag{6}$$

with:

$$\Pi_{\mathscr{B}}(\boldsymbol{u}, \phi) = \int_{\mathscr{B}} [((1-\phi)^2 + \eta_\ell)\Psi_{\text{act}}(\boldsymbol{u}) + \Psi_{\text{pas}}(\boldsymbol{u})]\mathrm{dV} \tag{7a}$$

$$\Pi_{\Gamma}(\phi) = \frac{\mathscr{G}_c}{4c_\omega\ell}\int_{\mathscr{B}} [\omega(\phi) + \nabla\phi\cdot\mathcal{L}\nabla\phi]\mathrm{dV} \tag{7b}$$

where $c_\omega = \int_0^1 \sqrt{\omega(\phi)}\mathrm{d}\phi$ is a normalization parameter [44].

As can be appreciated, the formulation presented up to this point is applicable to a wide range of materials and damage models by the proper choice of Ψ_{act}, Ψ_{pas}, $\alpha(\phi)$ and $\omega(\phi)$. The specific expressions of the active and passive specific elastic bulk energy, which models the anisotropic nature of long fiber composite materials, are detailed in Section 3.2. Regarding the degradation functions, the quadratic formulation proposed by Bourdin et al. [45] is used, which reads:

$$\alpha(\phi) = (1-\phi)^2, \quad \omega(\phi) = \phi^2 \quad \text{and} \quad w_c = 1/2. \tag{8}$$

Finally, the regularized version of the internal energy considering the quadratic formulation is given by:

$$\Pi_{\text{int}}(\boldsymbol{u}, \phi) = \int_{\mathscr{B}} [((1-\phi)^2 + \eta_\ell)\Psi_{\text{act}}(\boldsymbol{u}) + \Psi_{\text{pas}}(\boldsymbol{u})]\mathrm{dV} + \frac{\mathscr{G}_c}{2\ell}\int_{\mathscr{B}} [\phi^2 + \nabla\phi\cdot\mathcal{L}\nabla\phi]\mathrm{dV} \tag{9}$$

It should be pointed out that an explicit definition of an elastic threshold for the damage activation is not considered in the previous expression and therefore, the PF monotonically grows from the very beginning of the simulation [46]. Another aspect to note here is that using the quadratic formulation, the width of the damaged band extends over all the domain, which can lead to numerical issues in analysis where the PF length scale ℓ is close to the domain size [47,44]. Under such conditions, the linear crack density functional proposed by Pham et al. [14] and the degradation functions presented by Sagrado et al. [48] can be plausible methods in order to mitigate the previous issues.

2.2. Numerical strategy

The numerical strategy used in the current investigation relies on the use of the standard Finite Element (FE) method for the spatial approximation. In turn, no temporal integration scheme is required since the scope of the current formulation is restricted to quasi-static analysis. Therefore, the numerical strategy adopted in the present study leads to an equilibrium problem at each pseudo-time step.

In the two following subsections, the finite element approximation and the solution scheme used for the demonstration cases are briefly presented. Specific details regarding the FE discretization are omitted here for the sake of brevity. For more details, the reader should refer to Msekh et al. [49] and Molnár and Gravouil [50] for standard linear elements and Reinoso et al. [23,28] for continuum shells and thin-ply laminates, respectively. In addition, an alternative time evolution scheme for dynamical problems can be found in Borden et al. [51].

2.2.1. Finite element formulation

According to Eq. (6), the regularization of the energy density functional given in Eq. (1) results in a coupled displacement-phase field problem. Recalling a standard Galerkin procedure, the two primary fields, $\boldsymbol{u}$ and ϕ, are extended with the corresponding admissible test function, $\delta\boldsymbol{u}$ and $\delta\phi$, which are respectively subjected to $\mathscr{V}_{\mathrm{u}} = \{\delta\boldsymbol{u} \in \mathrm{H}^1 | \delta\boldsymbol{u} = 0 \,\mathrm{on}\, \partial\mathscr{B}_{\mathrm{u}}\}$ and $\mathscr{V}_{\phi} = \{\delta\phi \in \mathrm{H}^1 | \delta\phi = 0 \,\mathrm{on}\, \partial\mathscr{B}_{\phi}\}$. Thus, the weak form of the coupled problem is constructed as follows:

$$\begin{aligned}\delta\Pi(\boldsymbol{u}, \delta\boldsymbol{u}, \phi, \delta\phi) &= \delta\Pi_{\mathrm{int}}(\boldsymbol{u}, \delta\boldsymbol{u}, \phi, \delta\phi) + \delta\Pi_{\mathrm{ext}}(\boldsymbol{u}) \\ &= 0, \quad \forall\, \delta\boldsymbol{u} \in \mathscr{V}_{\mathrm{u}}, \quad \forall\, \delta\phi \in \mathscr{V}_{\phi}\end{aligned} \tag{10}$$

where $\delta\Pi_{\mathrm{int}}(\boldsymbol{u}, \delta\boldsymbol{u}, \phi, \delta\phi)$ and $\delta\Pi_{\mathrm{ext}}(\boldsymbol{u})$ identify the internal and external variation terms, respectively. Taking into account the expression given in Eq. (9), the internal variation term can be split as:

$$\delta\Pi_{\mathrm{int}}(\boldsymbol{u}, \delta\boldsymbol{u}, \phi, \delta\phi) = \delta\Pi^{\mathrm{u}}_{\mathrm{int}}(\boldsymbol{u}, \phi, \delta\boldsymbol{u}) + \delta\Pi^{\phi}_{\mathrm{int}}(\boldsymbol{u}, \phi, \delta\phi) \tag{11}$$

Then, if the infinitesimal strain regime as the modeling framework, the variations with respect to primary fields according to the quadratic formulation given in Eq. (8) results in:

$$\delta\Pi^{\mathrm{u}}_{\mathrm{int}}(\boldsymbol{u}, \delta\boldsymbol{u}, \phi) = \int_{\mathscr{B}} \delta\boldsymbol{\varepsilon} : \boldsymbol{\sigma}\, \mathrm{dV} \tag{12a}$$

$$\delta\Pi^{\phi}_{\mathrm{int}}(\boldsymbol{u}, \phi, \delta\phi) = \int_{\mathscr{B}} (\phi - 2(1-\phi)\mathscr{H})\delta\phi + \nabla(\delta\phi)\cdot\mathcal{L}\nabla\phi\, \mathrm{dV} \tag{12b}$$

where $\boldsymbol{\sigma} = \partial_{\boldsymbol{\varepsilon}}\Psi(\boldsymbol{\varepsilon}(\boldsymbol{u}), \phi)$ is the nominal stress tensor and $\boldsymbol{\varepsilon}(\boldsymbol{u}) = \nabla^S_x \boldsymbol{u}$ is the infinitesimal strain tensor, which variation with respect to the displacement field is $\delta\boldsymbol{\varepsilon} = \partial_{\boldsymbol{u}}\boldsymbol{\varepsilon}(\delta\boldsymbol{u})$. In turn, $\mathscr{H}$ is the history field that enforces the irreversibly condition and prevents healing effects. Following Miehe et al. [26], this historical variable can be defined by means of the crack driving state function $\mathscr{D}$ as:

$$\mathscr{H} = \max_{s\in[0,t]}(\mathscr{D}^s) \quad \text{with} \quad \mathscr{D}^s = \frac{\Psi^s_{\mathrm{act}}}{\mathscr{G}_c/\ell} \tag{13}$$

where s represents the fully story process and t is the current time step.

The linearized expressions of the weak form are herewith presented here because they are required in order to solve the nonlinear set of equation that appears in the Newton-Raphson method as a consequence of Taylor's expansion around the solution of the primary fields [52]. This consistent linearization can be obtained through the Gâteaux derivative, resulting in:

$$\begin{aligned}\Delta\delta\Pi^{\mathrm{u}}_{int}(\boldsymbol{u}, \delta\boldsymbol{u}, \phi; \Delta\boldsymbol{u}) = &\int_{\mathscr{B}} \nabla^S_x(\delta\boldsymbol{u}) : \mathbb{C} : \nabla^S_x(\Delta\boldsymbol{u})\, \mathrm{dV} + \int_{\mathscr{B}} \nabla_x(\delta\boldsymbol{u}) \\ &: \nabla_x(\Delta\boldsymbol{u})\boldsymbol{\sigma}\, \mathrm{dV}\end{aligned} \tag{14a}$$

$$\Delta\delta\Pi^{\phi}_{int}(\boldsymbol{u}, \phi, \delta\phi; \Delta\phi) = \int_{\mathscr{B}} \delta\phi(1 + 2\mathscr{H})\Delta\phi\, \mathrm{dV} + \int_{\mathscr{B}} \nabla(\delta\phi)\cdot\mathcal{L}\nabla(\Delta\phi)\, \mathrm{dV} \tag{14b}$$

where the nominal tangent material operator is defined as:

$$\mathbb{C} = \frac{\partial^2\Psi(\boldsymbol{\varepsilon}(\boldsymbol{u}), \phi)}{\partial\boldsymbol{\varepsilon} \otimes \partial\boldsymbol{\varepsilon}} \tag{15}$$

The spatial discretization of the decoupled weak forms in Eq. (12) is performed considering first-order elements. Complying with the isoparametric approach, the displacement and phase fields ($\boldsymbol{u}$, ϕ) as well as, their variations ($\delta\boldsymbol{u}$, $\delta\phi$), increments ($\Delta\boldsymbol{u}$, $\Delta\phi$) and gradients ($\nabla\boldsymbol{u}$, $\nabla\phi$) are discretized by means of the $\mathscr{C}^0$ continuous shape functions $\mathscr{N}^I$ where the super-script I indicates the nodal support. Arranging them into the operator $\mathcal{N}$, the spatial discretization of the continuum quantities at the element level are given by:

$$\boldsymbol{u} \approx \mathcal{N}_{\mathrm{d}}\mathbf{d}, \quad \delta\boldsymbol{u} \approx \mathcal{N}_{\mathrm{d}}\delta\mathbf{d}, \quad \Delta\boldsymbol{u} \approx \mathcal{N}_{\mathrm{d}}\Delta\mathbf{d}, \quad \nabla\boldsymbol{u} \approx \mathbf{B}_{\mathrm{d}}\mathbf{d} \tag{16a}$$

$$\phi \approx \mathcal{N}_{\mathfrak{d}}\mathfrak{d}, \quad \delta\phi \approx \mathcal{N}_{\mathfrak{d}}\delta\mathfrak{d}, \quad \Delta\phi \approx \mathcal{N}_{\mathfrak{d}}\Delta\mathfrak{d}, \quad \nabla\phi \approx \mathbf{B}_{\mathfrak{d}}\mathfrak{d} \tag{16b}$$

where $\mathbf{d}$ and $\mathfrak{d}$ are the vectors arranging the nodal values of the displacement and phase fields, respectively. In turn, $\mathbf{B}_{\mathrm{d}}$ and $\mathbf{B}_{\mathfrak{d}}$ are the kinematic compatibility operators arranging the partial derivatives of the shape functions with respect to the spatial coordinate $\nabla_x\mathcal{N}$, which specific expressions can be found in Msekh et al. [49] and Reinoso et al. [23]. At this point, the insertion of Eq. (16) into Eq. (12) and Eq. (14) leads to the semi-discrete form of the residual vectors:

$$\mathbf{R}_{\mathrm{d}} = \int_{\mathscr{B}} \mathbf{B}^{\mathrm{T}}_{\mathrm{d}}\boldsymbol{\sigma}\, \mathrm{dV} \tag{17a}$$

$$\mathbf{R}_{\mathfrak{d}} = \int_{\mathscr{B}} [(\mathfrak{d} - 2(1-\mathfrak{d})\mathscr{H})\mathcal{N}_{\mathrm{d}} + \mathbf{B}^{\mathrm{T}}_{\mathfrak{d}}\mathcal{L}\nabla\mathfrak{d}]\, \mathrm{dV}, \tag{17b}$$

and the corresponding stiffness matrices:

$$\mathbf{K}_{\mathrm{dd}} = \int_{\mathscr{B}} [\mathbf{B}^{\mathrm{T}}_{\mathrm{d}}\mathbb{C}\mathbf{B}_{\mathrm{d}} + \nabla^{\mathrm{T}}_x\mathcal{N}_{\mathrm{d}}\boldsymbol{\sigma}\nabla_x\mathcal{N}_{\mathrm{d}}]\, \mathrm{dV} \tag{18a}$$

$$\mathbf{K}_{\mathfrak{d}\mathfrak{d}} = \int_{\mathscr{B}} [((1 + 2\mathfrak{d})\mathscr{H})\mathcal{N}^{\mathrm{T}}_{\mathfrak{d}}\mathcal{N}_{\mathfrak{d}} + \mathbf{B}^{\mathrm{T}}_{\mathfrak{d}}\mathcal{L}\mathbf{B}_{\mathfrak{d}}]\, \mathrm{dV} \tag{18b}$$

where $\mathbb{C}$ is the nominal tangent material operator expressed in compact form according to Eq. (15).

2.2.2. Solution scheme

According to the spatial discretization outlined above, the PF approach yields to a multi-field finite element problem. The global solution is composed of two fields, whose respective solutions can be obtained using either a **monolithic** or an **alternate minimization** numerical scheme.

Monolithic scheme On the one hand, the monolithic solution scheme solves the following linearized system of equations in order to find the incremental solution of both fields at time t_{n+1} as follows:

$$\begin{bmatrix}\mathbf{d} \\ \mathfrak{d}\end{bmatrix}_{t+1} = \begin{bmatrix}\mathbf{d} \\ \mathfrak{d}\end{bmatrix}_{t} + \begin{bmatrix}\mathbf{K}_{\mathrm{dd}} & \mathbf{K}_{\mathrm{d}\mathfrak{d}} \\ \mathbf{K}_{\mathfrak{d}\mathrm{d}} & \mathbf{K}_{\mathfrak{d}\mathfrak{d}}\end{bmatrix}^{-1} \begin{bmatrix}\mathbf{R}_{\mathrm{d}} \\ \mathbf{R}_{\mathfrak{d}}\end{bmatrix}_{t} \tag{19}$$

where $\mathbf{R}_{\mathrm{d}}$ and $\mathbf{R}_{\mathfrak{d}}$ are the right hand side vectors for the displacement and phase fields, respectively; $\mathbf{K}_{\mathrm{dd}}$, $\mathbf{K}_{\mathrm{d}\mathfrak{d}}$, $\mathbf{K}_{\mathfrak{d}\mathrm{d}}$ and $\mathbf{K}_{\mathfrak{d}\mathfrak{d}}$ are the tangent matrices after the consistent linearisation of the residual vectors.

Alternate minimization. On the other hand, in an alternate minimization scheme, the solution is obtained by solving alternately the displacement field and the phase field sub-problems. From a mathematical point of view, this alternate minimization algorithm is preferable due to the non-convexity of the regularized energy functional. It means that Eq. (9) admits many local minimizers that might lead to erroneous solutions, see [45,53]. Furthermore, this strategy allows the use of different algebraic solvers, which can considerably increase the numerical performance.

In light of the previous arguments and based on operative implementation aspects, the solution strategy herein adopted is the alternate minimization scheme proposed by [45]. Hence, the global minimization problem is solved by alternately fixing either $\mathbf{d}$ or $\mathfrak{d}$ and

solving the sub-problem for the corresponding free variable. The process is performed iteratively until the difference in the PF variable between two consecutive iterations fulfill the desired tolerance.

2.3. Role of the length scale parameter

According to the Γ-convergence concept, the regularized solution stemming from the variational formalism of the PF method approximates to the original (sharp) crack representation as the length scale parameter ℓ tends to zero [45]. Therefore, it seems logical that setting lower values for the length scale would produce more accurate results. However, Borden et al. [51] indicate that if an infinitesimal length scale is used, the crack nucleation stress becomes infinite, which can induce a non-physical behavior. For this reason, they propose that the length scale not only should be considered as a numerical parameter to ensure the convergence, but also as a material property since it influences the critical stress. An extensive discussion on this matter can be found in [54].

In line with this discussion, some studies analyzed the homogeneous analytical solution for a one-dimensional quasi-static problem finding that the length scale parameter can be related to the material characteristic length $\ell_c = \mathscr{G}_c E/\sigma_c^2$ where E is the Young modulus and σ_c is the nominal strength of the material under study [51,55]. Thus, the variational PF models are uniquely characterized by physical parameters since the internal length ℓ is now linked to the material strength σ_c. Particularizing the analysis to the quadratic form of the crack density functional given in [45], the length scale parameter can be expressed as:

$$\ell = \frac{27}{256}\frac{\mathscr{G}_c E}{\sigma_c^2} \tag{20}$$

In addition to the previous considerations, through the conduction of different numerical experiments, Bourdin et al. [40] showed that, in the current modeling framework, the fracture energy is slightly overestimated due to the space approximation of the domain. As a consequence, an effective energy release rate $\mathscr{G}_e$ should be defined as function of the discretization parameter ℓ_e in order to compensate this amplification. In the current work, we propose a modification of the relation between the effective $\mathscr{G}_e$ and the critical $\mathscr{G}_c$ energy release rates according to the following expression:

$$\mathscr{G}_e = \mathscr{G}_c\left(1 - \frac{\ell_e}{\ell}\right) \tag{21}$$

where in a finite element space approximation ℓ_e is the characteristic element length. It should be noted that this relationship has only been used with linear isoparametric elements and its particular expression stems from numerical experiments. A more careful discussion about the current proposal falls beyond the scope of the present investigation and it will be treated in future contributions. The sensibility of the numerical predictions for different PF length scale values ℓ as well as the necessity of correcting the fracture toughness $\mathscr{G}_c$ are illustrated in Appendix A.

3. Constitutive assumptions

One of the main aspects of the long fiber composite materials is the anisotropic behavior of the mechanical response due to the elastic properties and failure mechanisms. For instance, the cracks tend to be aligned with the fiber direction because the energy required for cracking the matrix is lower than that corresponding to fibers rupture. Hence, the general formulation presented in Section 2.1 is extended in the sequel for long fiber composite materials. In Section 3.1the strategy used to model the different failure modes is described, whereas the specific bulk energy for transversal isotropic materials in Section 3.2. It is worth mentioning that the framework presented in the following subsections is valid for 2D and 3D cases through plane-stress or plane-strain modeling conditions [56].

3.1. Specific crack density

Motivated by the works of Miehe et al. [46] and Zhang et al. [57], the anisotropic behavior of the fracture process is modeled by splitting the crack driving function $\mathscr{D}$ into several contributions. This split allows the association of a different critical energy release rate to each of the contributions and therefore, the modeling of different failure mechanism. Considering that the PF approach is rooted in the minimization of the internal potential energy, the crack network will tend to grow along the most energetically favorable path. This trend is in line with the actual response of long fiber composite materials. In practice, $\mathscr{D}$ is additively decomposed into M contributions such that Eq. (13) is defined as:

$$\mathscr{D} = \sum_{i=1}^{M} \frac{\Psi_i}{\mathscr{G}_{ci}/\ell_i} \tag{22}$$

where the subscript i indicates a different damage mode, e.g. fiber breaking and matrix cracking. It is worth mentioning that the isotropic behavior can be recovered by simply setting $\mathscr{G}_{ci}$ and ℓ_i as constant values. Furthermore, an elastic threshold can be defined to prevent the stiffness loss before the localization of the crack, which is necessary for applications where the distributed damage is negligible. Following Miehe et al. [46], this threshold is defined in Eq. (13) leading to:

$$\mathscr{D} = \sum_{i=1}^{M} \zeta_i \left\langle \frac{\Psi_i}{\Psi_{0i}} - 1 \right\rangle_+ = \sum_{i=1}^{M} \zeta_i \left\langle \left(\frac{\widetilde{\sigma}_i}{\sigma_{0i}}\right)^2 - 1 \right\rangle_+ \tag{23}$$

where $\langle\bullet\rangle_\pm$ is the Macauly operator defined as $\langle x\rangle_\pm = (x \pm |x|)/2$. In turn, Ψ_{0i} is the critical fracture energy per unit volume and ζ_i is a dimensionless parameter that governs the post-peak behavior. It should be noted that the right-hand-side of Eq. (23) is obtained through the advocation of Eq. (20). At this point, and following Gültekin et al. [36,37], the structural tensor $\mathcal{L}$ in Eq. (4) is modified to account for different regularization lengths, which in turn aligns the PF with the preferred direction. Because the nature of long fiber composite materials, two lengths are considered: ℓ_f for the fiber and ℓ_m for the matrix. Thus, the structural tensor can be defined as: $\mathcal{L} = \ell_f^2(\mathbf{n}_f \otimes \mathbf{n}_f + \beta(\mathbf{I} - \mathbf{n}_f \otimes \mathbf{n}_f))$, where $\mathbf{n}_f$ is the fiber direction vector with respect to the global directions and $\beta = \ell_m/\ell_f^2$.

3.2. Specific elastic bulk energy

The constitutive modeling of anisotropic composite materials at the macroscopic scale is generally expressed in terms of the specific elastic bulk energy through the Helmholtz free energy $\Psi(\boldsymbol{\varepsilon})$. Alternatively, the complementary Gibbs free energy Ψ^*, which is the dual form of the Helmholtz free energy, can be used to describe the mechanical response using the Legendre-Fenchel transformation. Exploiting this concept, the free energy density proposed in Quintanas-Corominas et al. [9] for long fiber composite material is herein employed as the specific bulk energy:

$$\Psi(\boldsymbol{\varepsilon}) = \Psi^*(\widetilde{\boldsymbol{\sigma}}) = \frac{1}{2}\left(\frac{(\widetilde{\sigma}_L)^2 - 4\nu_{12}\widetilde{\sigma}_L\widetilde{p}_T}{E_{11}} + \frac{(\widetilde{p}_T)^2}{E_T} + \frac{(\widetilde{\tau}_T)^2}{G_T} + \frac{(\widetilde{\tau}_L)^2}{G_{12}}\right) \tag{24}$$

where $\widetilde{\sigma}_L$, $\widetilde{p}_T$, $\widetilde{\tau}_L$ and $\widetilde{\tau}_T$ are the effective stress quantities that have rotational invariance with respect to the longitudinal axis. These quantities are defined as:

$$\widetilde{\sigma}_L = \widetilde{\sigma}_{11}, \quad \widetilde{p}_T = \frac{\widetilde{\sigma}_{22} + \widetilde{\sigma}_{33}}{2}, \quad \widetilde{\tau}_L = \sqrt{(\widetilde{\sigma}_{12})^2 + (\widetilde{\sigma}_{13})^2} \quad \text{and} \quad \widetilde{\tau}_T = \frac{1}{2}\sqrt{(\widetilde{\sigma}_{22} - \widetilde{\sigma}_{33})^2 + 4(\widetilde{\sigma}_{23})^2}. \tag{25}$$

The elastic material properties required in Eq. (24) are: E_{11} is the longitudinal Young's modulus; ν_{12} is the longitudinal Poisson's coefficient; G_{12} is the longitudinal shear modulus; and E_T and G_T are the

transversal and shear modulus of the transverse isotropy plane, which are given by:

$$E_T = \frac{E_{22}}{2(1-\nu_{23})} \quad \text{and} \quad G_T = \frac{E_{22}}{2(1+\nu_{23})} \tag{26}$$

where E_{22} is the transversal Young's modulus and ν_{23} is the transversal Poisson's coefficient.

Moreover, crack closure effects under reversal loading is modeled assuming that it is only induced by $\widetilde{\sigma}_{\mathrm{L}}$ and $\widetilde{p}_{\mathrm{T}}$, whereas $\widetilde{\tau}_{\mathrm{L}}$ and $\widetilde{\tau}_{\mathrm{T}}$ do not have any influence [6,9]. Invoking this assumption, the degradation of the specific bulk energy for fiber reinforced composites within the context of the PF approach, Eq. (5), finally leads to:

$$\Psi^*(\widetilde{\boldsymbol{\sigma}}, \phi) = ((1-\phi)^2 + \eta_\ell)\Psi^*_{\mathrm{act}}(\widetilde{\boldsymbol{\sigma}}) + \Psi^*_{\mathrm{pas}}(\widetilde{\boldsymbol{\sigma}}) \tag{27}$$

with the active and passive contributions defined as:

$$\Psi^*_{\mathrm{act}}(\widetilde{\boldsymbol{\sigma}}) = \frac{1}{2}\left(\frac{\langle (\widetilde{\sigma}_{\mathrm{L}})^2 - 4\nu_{12}\widetilde{\sigma}_{\mathrm{L}}\widetilde{p}_{\mathrm{T}}\rangle_+}{E_{11}} + \frac{\langle \widetilde{p}_{\mathrm{T}}\rangle_+^2}{E_T} + \frac{(\widetilde{\tau}_{\mathrm{T}})^2}{G_T} + \frac{(\widetilde{\tau}_{\mathrm{L}})^2}{G_{12}} \right) \tag{28}$$

$$\Psi^*_{\mathrm{pas}}(\widetilde{\boldsymbol{\sigma}}) = \frac{1}{2}\left(\frac{\langle (\widetilde{\sigma}_{\mathrm{L}})^2 - 4\nu_{12}\widetilde{\sigma}_{\mathrm{L}}\widetilde{p}_{\mathrm{T}}\rangle_-}{E_{11}} + \frac{\langle \widetilde{p}_{\mathrm{T}}\rangle_-^2}{E_T} \right) \tag{29}$$

Using the appropriate thermodynamic arguments, the effective compliance tensor in compact notation $\widetilde{\mathbf{H}}$ (vector form) is defined as:

$$\widetilde{\mathbf{H}} = \left[\frac{\partial^2 \Psi^*}{\partial \widetilde{\boldsymbol{\sigma}} \otimes \partial \widetilde{\boldsymbol{\sigma}}} \right] = \begin{bmatrix} \frac{1}{E_{11}} & -\frac{\nu 12}{E_{11}} & -\frac{\nu 12}{E_{11}} & 0 & 0 & 0 \\ & \frac{1}{4}\left(\frac{1}{E_T}+\frac{1}{G_T}\right) & \frac{1}{4}\left(\frac{1}{E_T}-\frac{1}{G_T}\right) & 0 & 0 & 0 \\ & & \frac{1}{4}\left(\frac{1}{E_T}+\frac{1}{G_T}\right) & 0 & 0 & 0 \\ & & & \frac{1}{G_T} & 0 & 0 \\ & sym. & & & \frac{1}{G_{12}} & 0 \\ & & & & & \frac{1}{G_{12}} \end{bmatrix} \tag{30}$$

The conjugate effective stress tensor in compacted form can be obtained through $\{\widetilde{\boldsymbol{\sigma}}\} = [\widetilde{\mathbf{H}}]^{-1}\{\boldsymbol{\varepsilon}\}$ where $\{\boldsymbol{\varepsilon}\}$ is the strain tensor in compacted form. Taking into account the formulation presented here and the framework described in Section 3.1, four damage modes can be captured, one for each material directions: (11) fiber, (22/33) matrix, (12/13) shear in-plane and (23) transversal shear. Correspondingly, each failure mode is, in turn, related to one of the stress invariants leading to the following expressions:

$$\Psi^*_{11} = \frac{1}{2}\frac{\langle \widetilde{\sigma}_{\mathrm{L}}\rangle_+^2}{E_{11}}, \quad \Psi^*_{22} = \frac{1}{2}\frac{\langle \widetilde{p}_{\mathrm{T}}\rangle_+^2}{E_T}, \quad \Psi^*_{12} = \frac{1}{2}\frac{(\widetilde{\tau}_{\mathrm{L}})^2}{G_{12}}, \quad \text{and} \quad \Psi^*_{23} = \frac{1}{2}\frac{(\widetilde{\tau}_{\mathrm{T}})^2}{G_T} \tag{31}$$

which are the energetic contributions used in the evaluation of the crack driving force, $\mathscr{D}$, in Eq. (22). Another option is to use directly the energy associated to each material direction. The implications of both options are currently under investigation. Thus, the failure modes under consideration in the present model can be associated with the corresponding uniaxial strengths: σ_{11c} for the fiber under tensile loading, σ_{22c} for the matrix under mode-I, σ_{23c} for the matrix under mode-II, and σ_{12c} for the in-plane shear.

It is worth mentioning that the formulation herewith outlined provides a general numerical framework for modeling damage events in long fiber composites, which can be accordingly modified to consider further capabilities. Therefore, a particular stress-based criterion can be incorporated into the formulation by means of a simple manipulation of the expressions given in Eq. (23). In addition, the current formulation only uses a single damage variable assuming that all the elastic properties start the degradation at the same moment. This simplification can lead to a premature triggering of the failure in full laminate analysis. For those cases, the herein formulation could be combined with the Bleyer and Alessi [35] strategy, which defines a PF for the fiber and other one for the matrix.

4. Applications

This section presents the predictive capabilities of the PF approach regarding the initiation and propagation of damage events in long fiber composite laminates. Firstly, the anisotropic failure behavior of the current approach is shown through a demonstration problem in Section 4.1. Then, two intralaminar failure tests are presented in Section 4.2 and Section 4.3. The first one compares the current numerical results of cross-ply test subjected to tensile loading against those predicted with a continuum damage model. The second example shows the capabilities for capturing the strength and crack orientation in an off-axis tensile test. Finally, the capabilities to simulate translaminar failure are analyzed in Section 4.4 by means of a compact tension test. In this case, the numerical predictions are compared with experimental data and the linear elastic fracture mechanics (LEFM) and cohesive zone model (CZM) predictions. Current simulations are performed using the parallel FE-code `Alya` [58].

4.1. Demonstration problem

The first test herein proposed is a demonstration problem to demonstrate the potential of the current formulation to capture the anisotropic behavior. For this purpose, the properties of a unidirectional IM7/8552 CFRP tape are used, which are listed in Table 1. The geometry of the specimen and the boundary conditions applied onto the two vertical edges are illustrated in Fig. 2. As can be appreciated, the problem consists of a square plate of size $1 \times 1\,\mathrm{mm}^2$ with an initial notch, which is divided into four zones, allowing a different fiber orientation in each one. Two configurations are simulated, where fiber orientation in the different zones is: {0°/−22.5°/0°/22.5°} and {0°/0°/ −22.5°/ 22.5°}. Regarding the boundary conditions, the specimen is subjected to an uniform prescribed displacement $\bar{u}$ onto the leftmost vertical edges, whereas the rightmost edge is fully clamped. The application of the external loading is performed under displacement control with monotonic increments of $\Delta\bar{u} = 5{\cdot}10^{-4}$ mm until $\bar{u} = 1{\cdot}10^{-2}$ mm. The domain is discretized using 104, 013 isoparametric triangular elements, whose maximum characteristic element size is 0.0025 mm. Finally, plane stress conditions are considered with a thickness of 0.125 mm.

Analyzing the results shown in Fig. 3, it is observable that the crack is predicted to grow parallel to the fibers. As was previously discussed, this crack pattern can be considered as an expected behavior because the energy that is required to crack the matrix is lower than that corresponding to fiber failure. Moreover, it can be seen in Fig. 3b that, in advanced stages of the simulation, the crack path within the matrix is

Table 1
Material properties for an IM7/8552 unidirectional ply [9].

	Prop.	Value	Unit
Elastic	E_{11}	171,000	MPa
	E_{22}	9,080	MPa
	G_{12}	5,290	MPa
	ν_{12}	0.32	–
	ν_{23}	0.45	–
Strength	σ_{c11}	2325	MPa
	σ_{c22}	62.3	MPa
	σ_{c12}	89.6	MPa
	σ_{c23}	63.7	MPa
Fracture	$\mathscr{G}_{11}$	97.8	N/mm^2
	$\mathscr{G}_{22}$	0.277	N/mm^2
	$\mathscr{G}_{23}$	1.1	N/mm^2
	$\mathscr{G}_{12}$	0.788	N/mm^2

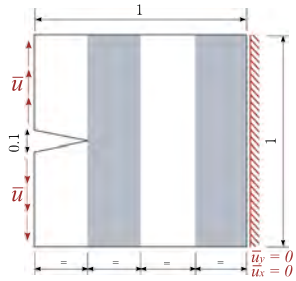

Fig. 2. Demonstration problem: specimen geometry and boundary conditions.

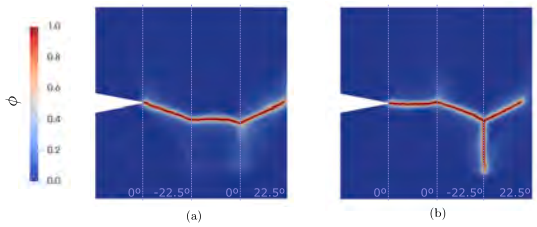

Fig. 3. Demonstration problem: failure pattern for a) {0°/−22.5°/0°/22.5°} and b) {0°/0°/−22.5°/22.5°} configurations ($\bar{u}$ = 0.05 mm).

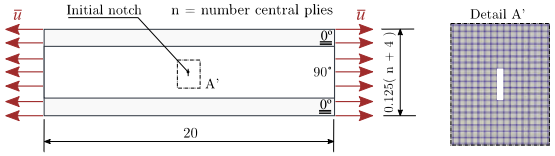

Fig. 4. Matrix cracking test specimen geometry subjected to tensile loading. Detail of the mesh with the initial notch.

divided in two branches, showing the capabilities of the current approach to trigger crack branching in a consistent and efficient manner. In particular, one path follows the direction parallel to the fibers, whereas the second crack path is aligned with the existing interface between the two regions (note that this interface is not specifically modeled in the current study, being a matter of future investigations). This fact can be explained by the abrupt change of the material orientation between adjacent regions.

4.2. Matrix cracking tensile test

Two configurations of a cross-ply $[0_2/90_n]$ laminate subjected to tensile loading are examined to show the predictive capabilities of the current approach for intralaminar failure. The laminate of both configurations is made from unidirectional IM7/8552 CFRP plies with a nominal thickness of 0.125 mm, whose properties are reported in Table 1. The unique difference between the present laminate configurations is the number of the central plies, which are $n = 1$ and $n = 4$. Hence, the length and boundary conditions are the same for both cases, while the thickness depends on the particular configuration, see Fig. 4.

Regarding the loading conditions, Dirichlet boundary conditions are prescribed at both ends of the specimen (Fig. 4). The specimen is loaded under displacement control with constant increments of $\Delta\bar{u} = 1{\cdot}10^{-3}$ mm until the final collapse of the laminate. For this problem, quadrilateral isoparametric elements with a characteristic length of 0.025 mm are used to approximate the domain under study, which results in a FE-mesh of 24, 000 elements for $n = 1$ case and 48, 000 elements for $n = 4$. It is worth mentioning that the characteristic element size is defined in such a way that at least five elements through the thickness per each ply are considered. Moreover, an initial notch is modeled at the centre of the specimen, whose size corresponds to a column of five elements as illustrated in Fig. 4. Finally, the simulations are performed assuming plane stress conditions with a thickness equal to 20 mm.

The longitudinal stress-strain response and the crack path at different strain levels for $n = 4$ are depicted in Fig. 5. The response curve has multiple drops that correspond to the formation of matrix cracks in the inner plies along the transverse direction, i.e. through the ply-thickness. Moreover, the occurrence of such matrix cracking events follow the expected sequence as was described in [59]. Subsequently, the matrix cracks that are formed just before the final collapse are initiated along the interface between the 0° and 90° plies instead of the center of the ply clustering. Finally, it is possible to see that laminate collapse is caused by the fiber breaking of the outer plies, which in turn is triggered by the transverse cracks of the inner plies. These numerical predictions in terms of failure sequence and qualitative results are in good agreement with the behavior reported in [60].

A comparison between the numerical predictions of the current approach and the anisotropic CDM formulated by Quintanas and

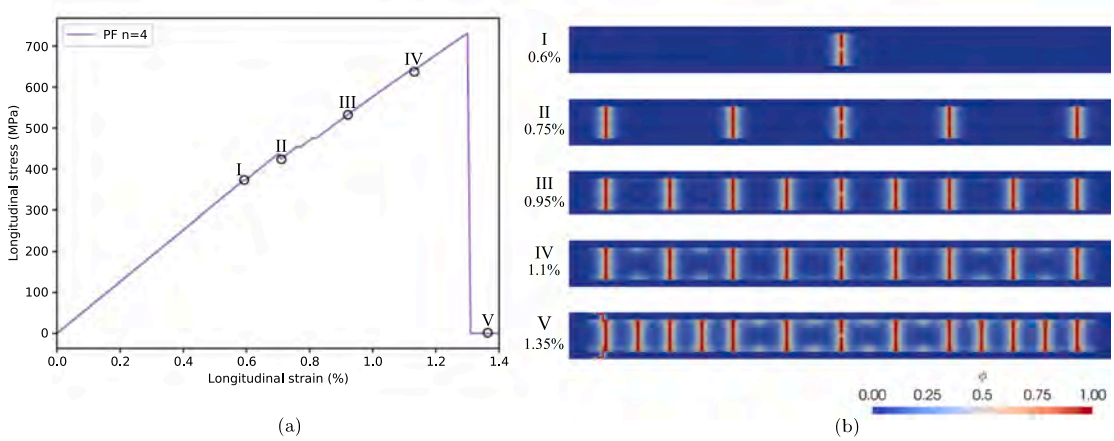

Fig. 5. Matrix cracking test: a) longitudinal stress-strain curve for the laminate $[0_2/90_4]_s$ and b) crack pattern at different strain levels.

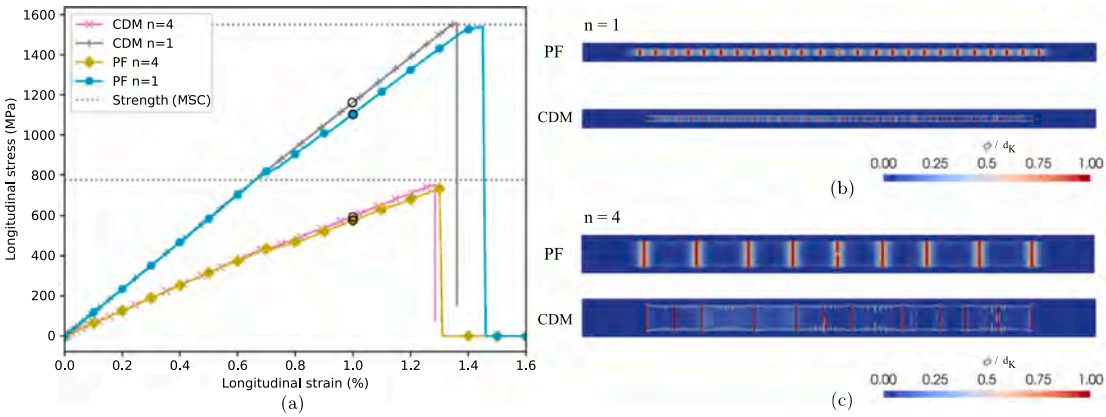

Fig. 6. Matrix cracking test. Comparison between the numerical predictions obtained using the current approach (PF), the Continuum Damage Model (CDM) of Quintanas-Corominas et al. [9] and a Maximum Stress Criteria for the fiber (MSC): a) longitudinal stress-strain curve, b) crack pattern for the laminate $[0_2/90_1]_s$ (1% of longitudinal strain) and c) failure pattern for the laminate $[0_2/90_4]_s$ (1% of longitudinal strain).

Table 2
Off-axis tensile test: material properties (taken from [61]) and phase field properties.

	Prop.	Value	Unit	
Elastic	E_{11}	38,900	MPa	
	E_{22}	13,380	MPa	
	ν_{12}	0.26	–	
Strength	σ_{c11}	901	MPa	
	σ_{c22}	36.5	MPa	
	σ_{c12}	52	MPa	
Phase-field	ℓ_f	1.00	mm^2	Assumed
	β	5.00	–	Assumed
	ξ_{11}	0.01	N/mm^2	Assumed
	ξ_{22}	0.50	N/mm^2	Assumed
	ξ_{12}	1.00	N/mm^2	Assumed

coauthors [9] can be found in Fig. 6. It can be seen in Fig. 6a that both approaches, i.e the current PF formulation and the previous CDM, predict similar longitudinal stress-strain response. Moreover, the maximum longitudinal stress predicted for both approaches is very similar to each other and in satisfactory agreement with the maximum stress criterion for the fiber [6]. The slight under-prediction of the current method can be attributed to the stress concentration induced by inner matrix cracks. It is also worth mentioning that the PF approach has a more pronounced stiffness loss in comparison with the CDM because the damage extends through the 0/90 interface. This in turn reduces the rigidity of the 0 plies which are the main load bearing plies. In addition, for $n = 4$ the crack density is very similar in both approaches, whereas for $n = 1$ is higher in the CDM, see Fig. 6b–c. In turn, from the depicted results it can be observed that the crack density increases as the thickness of 90° ply cluster decreases, which is consistent with the experimental observations.

4.3. Off-axis tensile test

In the present Section, an off-axis tensile test on a 10° unidirectional laminate is used to simulate a case in which the orientation of the crack propagation is governed by the fiber direction rather than an existing stress intensity region. For this purpose, the configuration studied by Van der Meer and Sluys [61] is herewith reproduced. The material is representative of glass/epoxy, which properties are listed in Table 2.

The specimen geometry, boundary conditions and mesh details are given in Fig. 7. As can be appreciated, the specimen is a plate of size $80 \times 8\,mm^2$ (length × width) and 3 mm in thickness, with oblique edges with an angle of 54° at both ends to suppress the edge effect, which outcome a homogeneous stress state. Regarding the boundary condition, the left edge of the specimen is restrained to horizontal displacements, whereas the right one is loaded under displacement control ($\Delta\bar{u}_x = 0.1$ mm until 0.7 mm and $\Delta\bar{u}_x = 0.001$ mm until its final collapse). The FE-mesh is created using 73, 347 isoparametric elements divided into two zones: (*i*) a central region which is discretized with quadrilateral elements, and (*ii*) two secondary regions close to the oblique ends with triangular elements. The characteristic element size in both zones is 0.1 mm. Finally, a weak zone of $0.3 \times 0.3\,mm^2$ is defined in the center of the specimen using the PF formulation without the elastic threshold and setting a $\mathscr{G}_c = 0.3$ N/mm for all the directions.

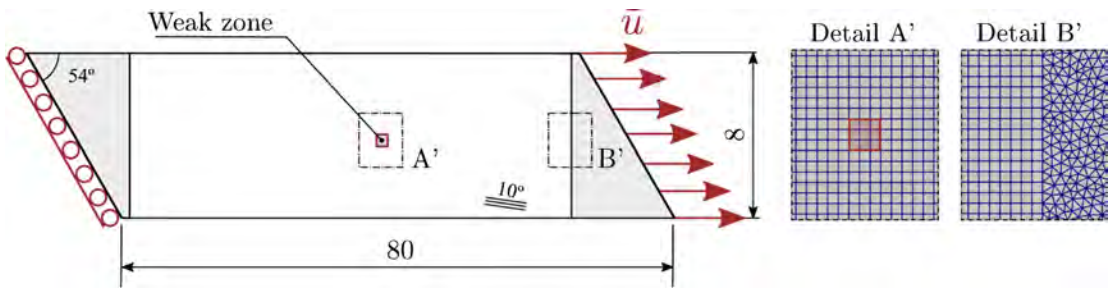

Fig. 7. Off-axis tensile test: specimen geometry and boundary conditions, including details of the mesh and the weak zone.

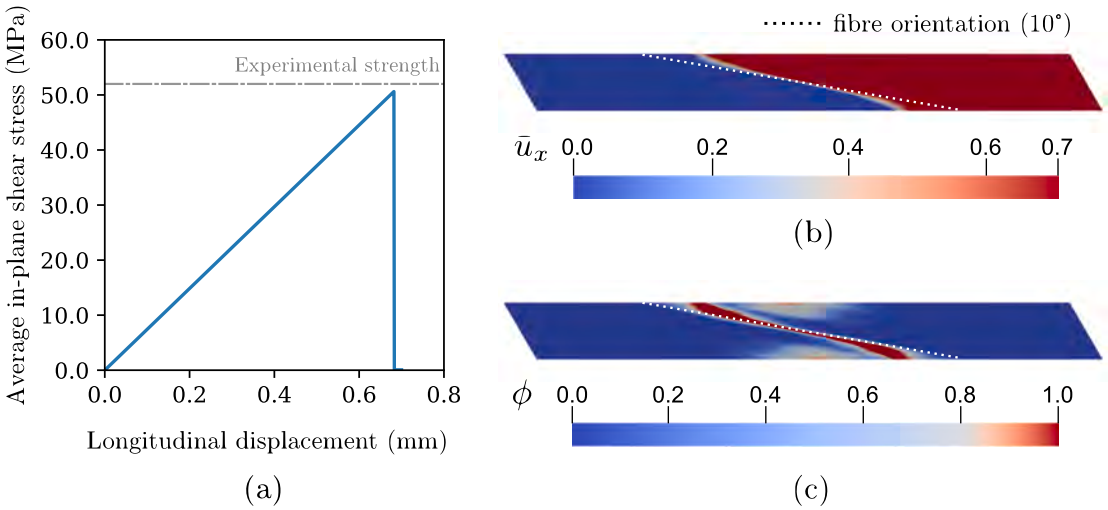

Fig. 8. Off-axis tensile test: a) average in-plane shear stress with respect to the applied displacement, b) longitudinal displacement field and c) phase field ($\bar{u}$ = 0.7 mm).

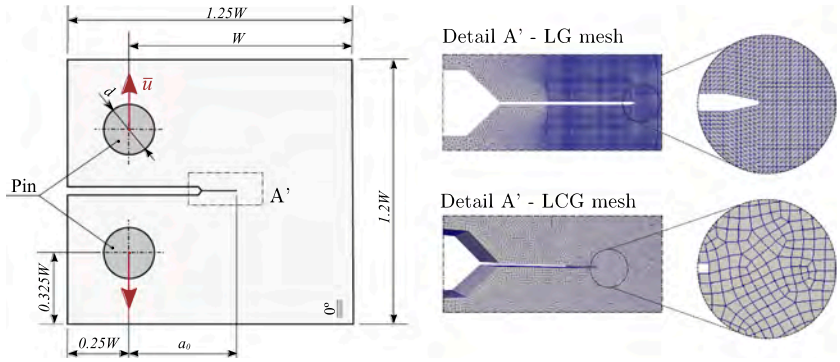

Fig. 9. Compact tension test: geometry, loading conditions and details of the mesh around the crack tip.

Table 3
Compact tensions. Laminate thickness, elastic and fracture properties [62], phase field parameters and mesh information.

	Prop.	LG	LCG	Unit
Thickness	h	4.58	4.31	mm
Elastic	E	19, 050	34, 000	MPa
Strength	σ_c	521.2	469.5	MPa
Fracture	$\mathscr{G}_c$	75	105	N/mm
Phase Field	ℓ[1]	0.5	1.709	mm
Mesh	n_{dim}	2D	3D	–
	ℓ_e	0.055	0.189	mm
	type[2]	TRI	HEX	–
	size[3]	600 K	2.7 M	–

[1] Computed using Eq. (20).
[2] Isoparametric linear elements: 3-nodes (triangles) and 8-nodes (hexahedral).
[3] Number of elements: K10[3] and M = 10^6.

The corresponding results using the present PF method are shown in Fig. 8. In this plot, it can be seen in the curve of Fig. 8.a that the specimen response features a linear elastic evolution up to an abrupt collapse which occurs reasonably close to the in-plane shear strength of the laminate (50 MPa vs 52 MPa). Furthermore, the orientation of the crack path at the central region is also very close to the expected one, see Fig. 8b and.c.

However, it should be pointed out that, close to the horizontal free edges (topmost and bottommost regions) of the specimen, present predictions gradually loss the correct orientation due to the normality condition $\nabla\phi\cdot\mathbf{n} = 0$, which is a natural condition of PF formulations. Despite this limitation, the current results show better accuracy regarding the orientation of the crack path in comparison with the results presented in [61] using a continuum damage model. Taking into account that the current approach also homogenize the material structure, similar to most of the existing CDMs, the better accuracy regarding the orientation is attributed to the non-local character of the PF method.

4.4. Compact tension test

Two Compact Tension (CT) specimens subjected to tensile loading studied by Ortega et al. [62] and González et al.[63] are simulated to examine the capabilities of the current approach regarding the modeling of translaminar failure. The geometric description and boundary conditions are shown in Fig. 9. In both cases the nominal dimensions are: W = 51 mm, d = 8 mm and a_0 = 25 mm. In relation to the laminate

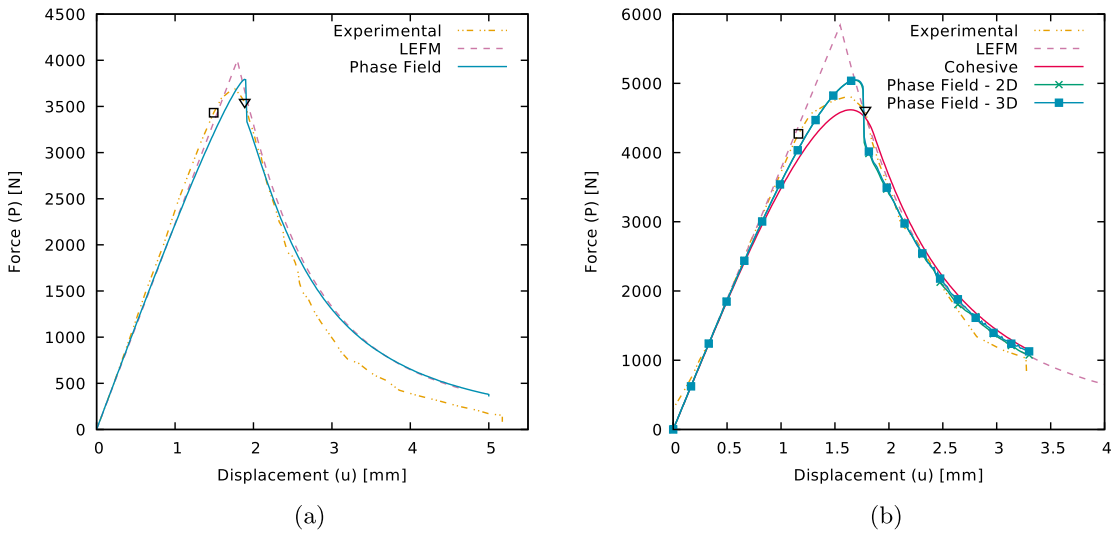

Fig. 10. Compact tension experimental [62], analytical and numerical load-displacement curves for: (a) LG and (b) LCG configurations.

Table 4
Compact tension peak force comparison between the experimental and the numerical predictions.

Config.	Approach	Predicted	Exper.	Unit	Rel. Err.
LG	PF	3.79	3.69	kN	2.71 %
LCG	PF	5.05	4.82	kN	4.77 %
	CZM	4.61	4.82	kN	4.36 %

disposals, the stacking sequence of the first specimen (LCG) is $[(0^C/45^C)_2/0^G/60^G/-60^G]_s$, wherein C stands for carbon fabric woven plies and G for glass fabric woven plies. Differing from the previous case, the stacking sequence of the second specimen (LG) is $[(0^G/45^G)_5]_s$. As can be appreciated, equivalent homogeneous material properties can be used due to the fact that both laminates are quasi-isotropic in-plane, leading to the equivalent material properties summarized in Table 3.

In contrast to the previous applications, a PF formulation without elastic threshold is used for this problem. Here, Eq. (20) is used to compute the length scale parameter, which complies with the

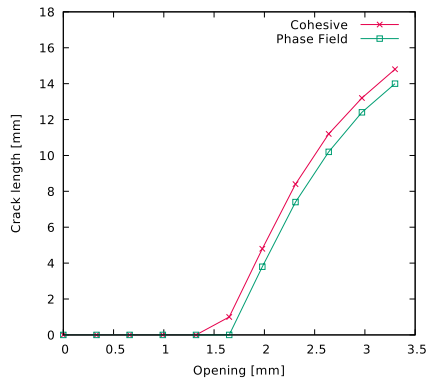

Fig. 12. Crack path for CT test (LCG): cohesive prediction.

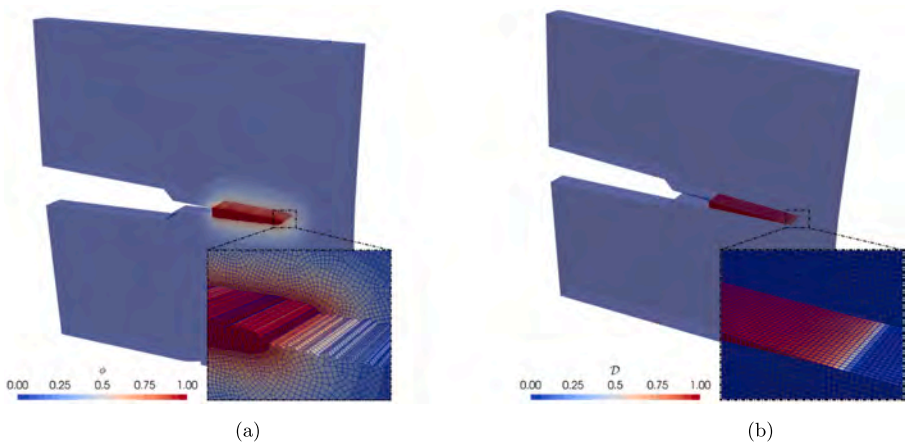

Fig. 11. Compact tension failure patterns for the LCG configuration at the end of the simulation predicted by: (a) PF and (b) CZM approach.

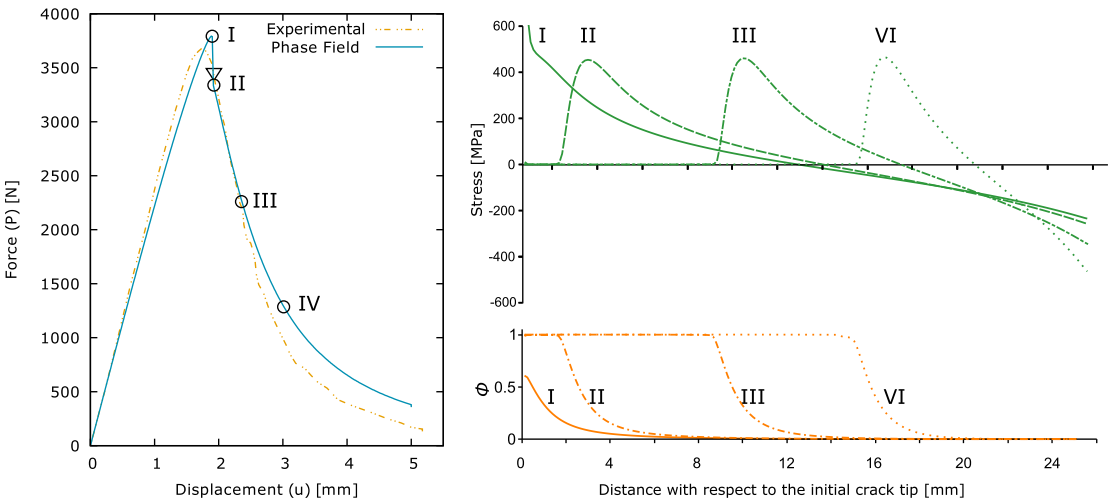

Fig. 13. Normal stress and phase field along the crack path for the LG configuration.

recommended mesh size according to the guidelines discussed in [43]. In this sense, the current PF parameters and the FE-mesh information are also listed in Table 3.

Regarding the boundary conditions, the specimens are loaded under displacement control with constant displacement increments of $\Delta\bar{u} = 1{\cdot}10^{-3}$ mm (Fig. 9a). Finally, it must be pointed out that the damage events are precluded in the pins, which are considered to be made from steel ($E = 210$ GPa and $\nu = 0.3$).

The load-displacement curves for both laminates are plotted together with the PF and LEFM in Fig. 10. In addition, the CZM prediction using the formulation proposed by Turon et al. [39] is also plotted for the LCG laminate. As can be appreciated, the predictions of the present PF formulation are in very good agreement with the experimental data and the LEFM and CZM results. On one hand, the loss of stiffness during the formation of the fracture process zone (from □ to ▽) in the PF response is not so pronounced as the CZM one, which results in a response closer to the experimental data. From a quantitative point of view, on the other hand, the PF method slightly overestimates the experimental peak force, whereas the CZM underestimates it. However, the relative error for both numerical approaches is below 5%, see Table 4). It is worth mentioning that the scatter of the peak load value obtained during the experimental campaign may induces deviations which precludes the accurate calibration of the critical stress and fracture toughness.

Fig. 11 depicts the damage pattern predicted by the PF and CZM approaches for the LCG laminate at the end of the simulation. As expected, the estimated crack path in both cases extends from the initial crack tip along a fracture plane perpendicular to the loading direction, which maximizes the mode-I stress intensity factor K_I. Notice that in the PF approach the damage is not only extended along the crack path, but also perpendicular to it, whereas in CZM the damage is confined to the interface elements. This can explain the small offset in the load-displacement curves. Finally, it is worth mentioning that the PF approach follows the expected path independent of the mesh orientation.

Continuing the comparison of the current method with respect to the CZM, the crack tip evolution as a function of the displacement is shown in Fig. 12. Numerically, the crack tip is identified as the last element along the crack path that is almost fully damaged, i.e. the PF variable is close to 1. It can be seen that in both methods the crack propagates at the same rate, inducing a similar slope in both curves. However, there is an offset between both methods of approximately 1 mm, which is a consequence of the failure initiation. As expected, due to the localization of the PF approach, the crack initiates with a small delay with respect to the CZM.

In order to understand the overestimation of the peak load and the delay at the crack localization, the normal stress field and ϕ along the expected crack path of the LG configuration is depicted at four intermediate stages in Fig. 13. In this graph, it can be seen that at stage (*I*), which corresponds to the localization of ϕ, the normal stress field in the vicinity of the crack tip has a singular behaviour that provokes the overestimation of the maximum load. Considering the results presented by Mesgarnejad et al. [47], a possible explanation of this overshoot is that the solution induced by the singularity is not the global minimizer, which in turn overestimates the total energy and the peak force. Continuing with the analysis, after the localization of ϕ, stage (*II*), the normal stress field no longer presents the asymptotic trend. After this stage, the normal stress field around the crack tip is constant denoting that the crack is growing self-similarly during the propagation, see stages (*II*, *III* and *IV*). Furthermore, it is worth mentioning that the localization of the PF corresponds to the moment when the fracture process zone is fully developed, marked with (▽) in the experimental curve [62]. Finally, it is also noticeable that the PF variable ϕ remains null in the compression region of the specimen, hence demonstrating the unilateral damage growth.

5. Concluding remarks

In this study, a novel phase field approach for triggering failure events in long fiber reinforced composite materials has been presented and implemented into a massively parallel simulation framework `Alya`. The potential of the approach for modeling anisotropic failure events has been shown for quasi-static loading problems by means of several representative applications. Firstly, a demonstration problem has been presented demonstrating the anisotropic behavior of the formulation. Then, the capability for modeling the intralaminar failure has been examined through a matrix crack test and off-axis test, both subjected to tensile loading. Finally, a compact tension has been simulated to explore the capability to capture translaminar failure. Moreover, the performance of the current approach has been contrasted with different modeling techniques, continuum damage models and cohesive zone models, showing excellent accuracy.

Considering the results obtained, it can be concluded that the proposed formulation based on the PF approach of fracture provides a competitive alternative to the classical approaches for modeling failure events in long fiber composite materials. From different perspectives,

the most appealing aspects are:

- The formulation captures responses with a soft evolution (quasi-brittle) or with abrupt jumps (perfect-brittle).
- The formulation models correctly anisotropic behaviors.
- The input parameters rely on measurable physical properties of the material.
- The non-local character minimizes the reliance of the crack path on the mesh topology.From the last point, it can be concluded that the PF approach precludes the use of adaptive tearing of the spatial mesh as the crack propagates. Nevertheless, for large structures with complex crack propagation paths, a combination of the PF approach with re-meshing algorithms are worth to be exploited in line with the methodology presented in [22].

Correspondingly, the PF method will be a matter of future investigations in order to tackle some open issues such as the use of phenomenological damage initiation criteria, the extension of dynamic fracture in composites or the calibration of an equivalent cohesive law stemming from the PF data. These activities are beyond the scope of the present study and will be addressed in forthcoming studies.

Acknowledgements

The first author would like to thank the Spanish Government (Ministerio de Educación, Cultura y Deporte) for the pre-doctoral grant FPU 15/06287. This works has been partially funded by the Spanish Government (Ministerio de Economia y Competitividad) under contracts TRA2015-71491-R and MAT2015-71036-P. The authors gratefully acknowledge Prof. Marco Paggi (IMT Lucca, Italy) for many fruitful discussions, which have undoubtedly contributed for the substantial improvement of the present investigation.

Appendix A. Sensitivity of the PF model

In this appendix, two basic aspects of the PF method are discussed: (*i*) the sensibility of the numerical predictions with respect to the PF length parameter ℓ_c and (*ii*) the necessity of correcting the fracture toughness $\mathscr{G}_c$.

The sensitivity of the model to the PF length scale parameter ℓ is analyzed. The load-displacement curve of the LCG configuration of the CT specimen described in Section 4.4 is obtained for three different length scales: ℓ = 1.7, 3.4 and 5.1 mm, see Fig. A.1a. Using Eq. (20), the corresponding nominal strength is: σ_c = 469.4, 331.9 and 271.0 MPa. The behavior predicted is similar in all cases: the initial stiffness is gradually decreases up to a critical point in which the crack propagation starts. As ℓ increases, the rate of growth of ϕ decreases. In turn, crack localization and initiation of crack growth is delayed. In addition, an abrupt jump in the load-displacement curve as well as an small offset in the softening part is obtained. This behavior not only highlights the sensibility of the PF approach with ℓ, but also the necessity of a correct experimentally estimation of σ_c to obtain reliable numerical predictions.

The importance of using an effective fracture toughness $\mathscr{G}_c$, is demonstrated by means of Fig. A.1b. In this figure, the load-displacement curve of the CT specimen obeying a LCG configuration is shown for the corrected (effective) and the non-corrected fracture toughness $\mathscr{G}_c$. Despite the similar behavior in both curves, the non-corrected value has an offset with respect to the corrected one. In this particular case, this results in an increase of approximately 10% of the peak load and fracture toughness, 5.35 KN and 115.5 N/mm, respectively. It should be pointed out that the increase of $\mathscr{G}_c$ is computed using the LEFM curves.

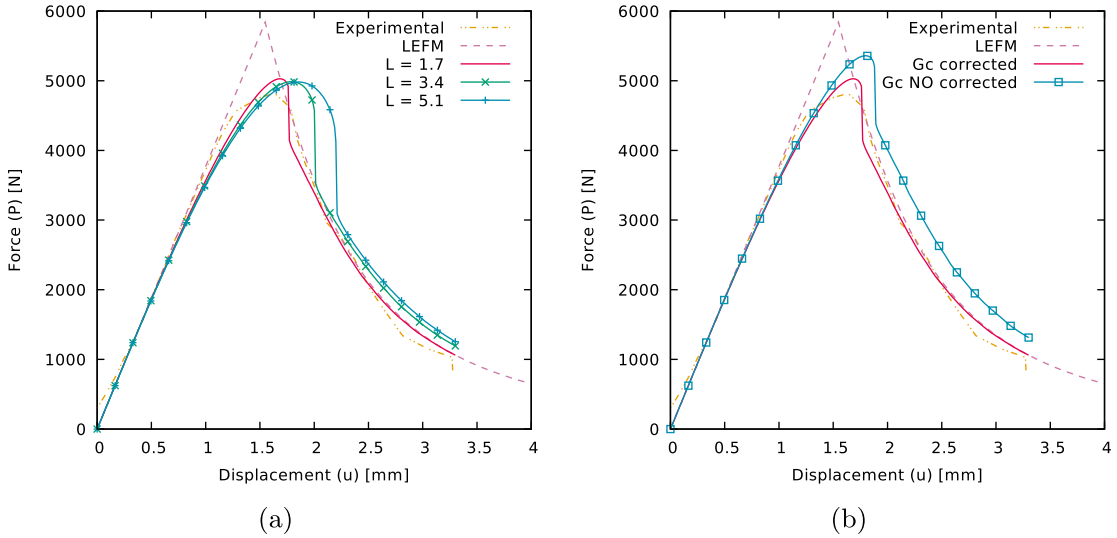

Fig. A.1. Load-displacement curve of the LCG configuration considering: a) three different phase field length, ℓ_c = 1.7, 3.4 and 5.1 mm and b) corrected and non-corrected $\mathscr{G}_c$.

References

[1] Turon A, Dávila CG, Camanho PP, Costa J. An engineering solution for mesh size effects in the simulation of delamination using cohesive zone models. Eng Fract Mech 2007;74(10):1665–82.

[2] Guillamet G, Turon A, Costa J, Linde P. A quick procedure to predict free-edge delamination in thin-ply laminates under tension. Eng. Fract. Mech. 2016;168(Part B):28–39.

[3] Reinoso J, Paggi M, Blázquez A. A nonlinear finite thickness cohesive interface

element for modeling delamination in fibre-reinforced composite laminates. Compos Part B: Eng 2017:116–28.
[4] Ladevèze P, Le Dantec E. Damage modelling of the elementary ply for laminated composites. Compos Sci Technol 1992;43(3):257–67.
[5] Camanho PP, Maimí P, Dávila CG. Prediction of size effects in notched laminates using continuum damage mechanics. Compos Sci Technol 2007;67(13):2715–27.
[6] Maimí P, Camanho PP, Mayugo JA, Dávila CG. A continuum damage model for composite laminates: Part I – Constitutive model. Mech Mater 2007;39(10):897–908.
[7] Maimí P, Camanho PP, Mayugo JA, Dávila CG. A continuum damage model for composite laminates: Part II – Computational implementation and validation. Mech Mater 2007;39(10):909–19.
[8] Reinoso J, Catalanotti G, Blázquez A, Areias P, Camanho PP, París F. A consistent anisotropic damage model for laminated fiber-reinforced composites using the 3d-version of the puck failure criterion. Int J Solids Struct 2017:37–53.
[9] Quintanas-Corominas A, Maimí P, Casoni E, Turon A, Mayugo JA, Guillamet G, Vázquez M. A 3D transversally isotropic constitutive model for advanced composites implemented in a high performance computing code. Eur J Mech A Solids 2018;71:278–91.
[10] Falcó O, Ávila RL, Tijs B, Lopes CS. Modelling and simulation methodology for unidirectional composite laminates in a virtual test lab framework. Compos Struct 2018;190:137–59.
[11] Moës N, Dolbow J, Belytschko T. A finite element method for crack growth without remeshing. Int J Numerical Methods Eng 1999;46(1):131–50.
[12] Linder C, Armero F. Finite elements with embedded strong discontinuities for the modeling of failure in solids. Int J Numer Meth Eng 2007;72(12):1391–433.
[13] Van Der Meer FP, Sluys LJ, Hallett SR, Wisnom MR. Computational modeling of complex failure mechanisms in laminates. J Compos Mater 2012;46(5):603–23.
[14] Pham K, Amor H, Marigo JJ, Maurini C. Gradient damage models and their use to approximate brittle fracture. Int J Damage Mech 2011;20(4):618–52.
[15] Borden Michael J, Hughes Thomas JR, Landis Chad M, Verhoosel Clemens V. A higher-order phase-field model for brittle fracture: formulation and analysis within the isogeometric analysis framework. Comput Methods Appl Mech Eng 2014;273:100–18.
[16] Francfort GA, Marigo J-J. Revisiting brittle fracture as an energy minimization problem. J Mech Phys Solids 1998;46(8):1319–42.
[17] Griffith A. The phenomena of rupture and flow in solids. Philos Trans R Soc London. Series A 1921;221:163–98. containing papers of a mathematical or physical character.
[18] Miehe C, Hofacker M, Welschinger F. A phase field model for rate-independent crack propagation: robust algorithmic implementation based on operator splits. Comput Methods Appl Mech Eng 2010;199(45):2765–78.
[19] Kuhn C, Müller R. A continuum phase field model for fracture. Eng Fract Mech 2010;77(18):3625–34.
[20] Wu JY. A unified phase-field theory for the mechanics of damage and quasi-brittle failure. J Mech Phys Solids 2017;103:72–99.
[21] Wu JY, Nguyen VP. A length scale insensitive phase-field damage model for brittle fracture. J Mech Phys Solids 2018;119:20–42.
[22] Areias P, Rabczuk T, Msekh MA. Phase-field analysis of finite-strain plates and shells including element subdivision. Comput Methods Appl Mech Eng 2016;312:322–50.
[23] Reinoso J, Paggi M, Linder C. Phase field modeling of brittle fracture for enhanced assumed strain shells at large deformations: formulation and finite element implementation. Comput Mech 2017;59(6):981–1001.
[24] Paggi M, Reinoso J. Revisiting the problem of a crack impinging on an interface:a modeling framework for the interaction between the phase field approach for brittle fracture and the interface cohesive zone model. Comput Methods Appl Mech Eng 2017;321:145–72.
[25] Carollo V, Reinoso J, Paggi M. A 3D finite strain model for intralayer and interlayer crack simulation coupling the phase field approach and cohesive zone model. Compos Struct 2017;182:636–51.
[26] Miehe C, Hofacker M, Schänzel L-M, Aldakheel F. Phase field modeling of fracture in multi-physics problems. Part II. coupled brittle-to-ductile failure criteria and crack propagation in thermo-elastic-plastic solids. Comput Methods Appl Mech Eng 2015;294:486–522.
[27] Martínez-Pañeda E, Golahmar A, Niordson CF. A phase field formulation for hydrogen assisted cracking. Comput Methods Appl Mech Eng 2018;342:742–61.
[28] Reinoso J, Arteiro A, Paggi M, Camanho PP. Strength prediction of notched thin ply laminates using finite fracture mechanics and the phase field approach. Compos Sci Technol 2017;150:205–16.
[29] Carollo V, Reinoso J, Paggi M. Modeling complex crack paths in ceramic laminates: a novel variational framework combining the phase field method of fracture and the cohesive zone model. J Eur Ceram Soc 2018;38(8):2994–3003.
[30] Li B, Peco C, Millán D, Arias I, Arroyo M. Phase field modeling and simulation of fracture in brittle materials with strongly anisotropic surface energy. Int J Numer Meth Eng 2014;102(3–4):711–27.
[31] Teichtmeister S, Kienle D, Aldakheel F, Keip MA. Phase field modeling of fracture in anisotropic brittle solids. Int J Non-Linear Mech 2017;97:1–21.
[32] Nguyen TT, Réthoré J, Baietto M. Phase field modelling of anisotropic crack propagation. Eur J Mech A Solids 2017;65:279–88.
[33] Nguyen TT, Réthoré J, Yvonnet J, Baietto MC. Multi-phase-field modeling of anisotropic crack propagation for polycrystalline materials. Comput Mech 2017;60(2):289–314.
[34] Kakouris EG, Triantafyllou SP. Material point method for crack propagation in anisotropic media: a phase field approach. Arch Appl Mech 2018;88(1):287–316.
[35] Bleyer J, Alessi R. Phase-field modeling of anisotropic brittle fracture including several damage mechanisms. Comput Methods Appl Mech Eng 2018;336:213–36.
[36] Gültekin O, Dal H, Holzapfel GA. A phase-field approach to model fracture of arterial walls: theory and finite element analysis. Comput Methods Appl Mech Eng 2016;312:542–66.
[37] Gültekin O, Dal H, Holzapfel GA. Numerical aspects of anisotropic failure in soft biological tissues favor energy-based criteria: a rate-dependent anisotropic crack phase-field model. Comput Methods Appl Mech Eng 2018;331:23–52.
[38] Casoni E, Jérusalem A, Samaniego C, Eguzkitza B, Lafortune P, Tjahjanto DD, Sáez X, Houzeaux G, Vázquez M. Alya: computational solid mechanics for supercomputers. Arch Comput Methods Eng 2014;22(4):557–76.
[39] Turon A, González EV, Sarrado C, Guillamet G, Maimí P. Accurate simulation of delamination under mixed-mode loading using a cohesive model with a mode-dependent penalty stiffness. Compos Struct 2018;184(10–11):506–11.
[40] Bourdin B, Francfort GA, Marigo JJ. The variational approach to fracture. J Elast 2008;91(1):5–148.
[41] Ambrosio L, Tortorelli VM. Approximation of functional depending on jumps by elliptic functional via t-convergence. Commun Pure Appl Math 1990;43(8):999–1036.
[42] Forest S. Micromorphic approach for gradient elasticity, viscoplasticity, and damage. J Eng Mech 2009;135(3):117–31.
[43] Miehe C, Welschinger F, Hofacker M. Thermodynamically consistent phase-field models of fracture: variational principles and multi-field FE implementations. Int J Numer Meth Eng 2010;83(10):1273–311.
[44] Tanné E, Li T, Bourdin B, Marigo JJ, Maurini C. Crack nucleation in variational phase-field models of brittle fracture. J Mech Phys Solids 2018;110:80–99.
[45] Bourdin B, Francfort GA, Marigo JJ. Numerical experiments in revisited brittle fracture. J Mech Phys Solids 2000;48(4):797–826.
[46] Miehe C, Schänzel L, Ulmer H. Phase field modeling of fracture in multi-physics problems. Part I. balance of crack surface and failure criteria for brittle crack propagation in thermo-elastic solids. Comput Methods Appl Mech Eng 2015;294:449–85.
[47] Mesgarnejad A, Bourdin B, Khonsari MM. Validation simulations for the variational approach to fracture. Comput Methods Appl Mech Eng 2015;290:420–37.
[48] Sargado JM, Keilegavlen E, Berre I, Nordbotten JM. High-accuracy phase-field models for brittle fracture based on a new family of degradation functions. J Mech Phys Solids 2018;111:458–89.
[49] Msekh M, Sargado JM, Jamshidian M, Areias P, Rabczuk T. Abaqus implementation of phase-field model for brittle fracture. Comput Mater Sci 2015;96(12):472–84.
[50] Molnár G, Gravouil A. 2D and 3D Abaqus implementation of a robust staggered phase-field solution for modeling brittle fracture. Finite Elem Anal Des 2017;130:27–38.
[51] Borden MJ, Verhoosel CV, Scott MA, Hughes T, Landis CM. A phase-field description of dynamic brittle fracture. Comput Methods Appl Mech Eng 2012;217–220(8):77–95.
[52] Wriggers P. Nonlinear finite element methods. Springer Science & Business Media; 2008.
[53] Farrell P, Maurini C. Linear and nonlinear solvers for variational phase-field models of brittle fracture. Int J Numer Meth Eng 2015;109(5):648–67.
[54] Zhang X, Vignes C, Sloan SW, Sheng D. Numerical evaluation of the phase-field model for brittle fracture with emphasis on the length scale. Comput Mech 2017;59(5):737–52.
[55] Pham K, Marigo JJ. From the onset of damage to rupture: construction of responses with damage localization for a general class of gradient damage models. Continuum Mech Thermodyn 2013;25(2):147–71.
[56] Barbero EJ, de Vivo L. A constitutive model for elastic damage in fiber-reinforced PMC laminae. Int J Damage Mech 2001;10(1):73–93.
[57] Zhang X, Sloan SW, Vignes C, Sheng D. A modification of the phase-field model for mixed mode crack propagation in rock-like materials. Comput Methods Appl Mech Eng 2017;322:123–36.
[58] Houzeaux G, Vázquez M, Aubry R, Cela JM. A massively parallel fractional step solver for incompressible flows. J Comput Phys 2009;228(17):6316–32.
[59] Maimí P, Camanho PP, Mayugo JA, Turon A. Matrix cracking and delamination in laminated composites. Part I: Ply constitutive law, first ply failure and onset of delamination. Mech Mater 2011;43(4):169–85.
[60] Maimí P, Mayugo JA, Camanho PP. A three-dimensional damage model for transversely isotropic composite laminates. J Compos Mater 2008;42(25):2717–45.
[61] Van der Meer FP, Sluys LJ. Continuum models for the analysis of progressive failure in composite laminates. J Compos Mater 2009;43(20):2131–56.
[62] Ortega A, Maimí P, González EV, Trias D. Characterization of the translaminar fracture cohesive law. Compos Part A: Appl Sci Manuf 2016;91(Part 2):501–9. CompTest 2015.
[63] González EV, Maimí P, Sainz de Aja JR, Cruz P, Camanho PP. Effects of interply hybridization on the damage resistance and tolerance of composite laminates. Compos Struct 2014;108:319–31.

Paper C

A phase field approach enhanced with a cohesive zone model for modelling delamination induced by matrix cracking

Published in *Computer Methods in Applied Mechanics and Engineering* (ISSN: 0045-7825).
Impact factors according to the 2017 Journal Citation Reports: 4.441, ranked 5/86 in category *Engineering, Multidisciplinary* (1st quartile), ranked 7/134 in category *Mechanics* (1st quartile), and ranked 2/103 in category *Mathematics, Interdisciplinary applications* (1st quartile)

Available online at www.sciencedirect.com
ScienceDirect
Comput. Methods Appl. Mech. Engrg. 358 (2020) 112618
Computer methods in applied mechanics and engineering
www.elsevier.com/locate/cma

A phase field approach enhanced with a cohesive zone model for modeling delamination induced by matrix cracking

A. Quintanas-Corominas[a,*], A. Turon[a], J. Reinoso[b], E. Casoni[c], M. Paggi[d], J.A. Mayugo[a]

[a] AMADE, Polytechnic School, Universitat de Girona, Campus Montilivi s/n, 17071 Girona, Spain
[b] Elasticity and Strength of Materials Group, School of Engineering, Universidad de Sevilla, Camino de los Descubrimientos s/n, 41092, Seville, Spain
[c] Barcelona Supercomputing Center (BSC-CNS), Edificio NEXUS I, Campus Nord UPC, Gran Capitán 2–4, 08034, Barcelona, Spain
[d] IMT School for Advanced Studies Lucca, Piazza San Francesco 19, 55100, Lucca, Italy

Received 13 May 2019; received in revised form 30 August 2019; accepted 1 September 2019
Available online xxxx

Abstract

The progressive damage analysis of fiber-reinforced composite materials is a challenging task, especially when complicated cracking scenarios arise due to the onset and progression of several damage mechanisms. From a modeling point of view, a particularly complex failure scenario is the interaction between intralaminar and interlaminar cracks. This work proposes a novel framework accounting for this interaction through the coupling of a nonlocal damage model based on the phase field approach for the intralaminar failure with a cohesive zone model for the interlaminar one. The modular variational formalism of the method presented leads to a very compact and efficient numerical strategy, which endows the fulfillment of the thermodynamic consistency restrictions and provides a relatively simple basis for its finite element implementation due to the preclusion of complex crack tracking procedures with standard element architectures. After addressing its implementation in the context of the finite element method in a high performance computing environment, the capabilities of the proposed formulation are explored through a numerical investigation of a cross-ply laminate subjected to a 4-point bending configuration. The comparison of the numerical predictions against the experimental observations demonstrates the reliability of the proposed framework for capturing the delamination induced by matrix cracking failure scenario.

Keywords: Composite materials; FE-modeling; Damage modeling; Fracture; Interlaminar

1. Introduction

Long Fiber-Reinforced Composites (LFRC) laminates proportionate a well-suited option for light-weight applications thanks to their excellent specific strength and stiffness ratios. The intricate and heterogeneous internal arrangement of these materials not only provides their strengths but also hints the prediction of their bearing capacities. The principal reason that makes difficult the estimation of the bearing capacities is the failure process of a LFRC laminates can be driven by several damage mechanisms which, moreover, can interact between them. For this reason, a Progressive Damage Analysis (PDA) is normally necessary to predict under arbitrary loading

* Corresponding author.
E-mail address: adria.quintanas@udg.edu (A. Quintanas-Corominas).

https://doi.org/10.1016/j.cma.2019.112618
0045-7825/

conditions the bearing capacities of a LFRC structure. At the mesoscopic level, a PDA of LFRC laminates needs to model the mechanical response of two clearly differentiated regions: the intralaminar that refers to the region inside a ply and the interlaminar that refers to the region between two adjacent plies, which is named interface.

In the context of Finite Element Method (FEM), a commonly-adopted strategy for performing PDFA of LFRC on the mesoscopic level is to model the intralaminar and interlaminar regions independently. Hence, different models are employed without a direct coupling between the failure events occurring in both regions. Following this strategy, local Continuum Damage Models (CDMs) have been extensively used for capturing the intralaminar damage mechanisms, namely: breaking and kinking of the fibers and cracking of the matrix [1–4]. In turn, Cohesive Zone Models (CZMs) have been successfully employed for describing the main interlaminar damage, the so-called interface debonding or delamination [5–8]. Despite the excellent results [9–12], this strategy has some flaws that arise from the local character of the models. On the one hand, the local CDMs suffer from localization problems due to the loss of the ellipticity of the governing equations, which leads to mesh-dependent results [13]. On the other hand, the local character of formulations makes difficult the interchanges of information regarding the damage state between both regions. This interchange can be essential to model complex failure scenarios, such as the case of delamination induced by transverse cracks.

In the last decades, the Phase Field (PF) approach to brittle fracture has emerged as a reliable alternative beyond the classical nonlocal CDMs for modeling progressive failure events without the aforementioned localization issue. The PF approach, in essence, is a regularization strategy of the variational problem for the brittle fracture proposed by Francfort and Marigo [14]. After the pioneering work of Bourdin et al. [15,16] and later of Miehe et al. [17], the PF approach has been used to model the onset and progression of different types of fractures: (i) brittle [18–21], (ii) ductile [22–25], (iii) hydraulic and hydrogen driven [26,27], (v) thermo-elastic–plastic [28–30], and (v) anisotropic behaviors [31–37].

Despite the potential of PF approach, few works have addressed their application for modeling the failure of composite materials. For instance, Reinoso et al. [38] successfully predicted the failure of thin-ply laminates by combining the PF with a continuum shell theory. Later, Alessi and Fredi [25] proposed a one-dimensional PF model to predict the failure of unidirectional hybrid laminates under uniaxial loading conditions. Subsequently, Bleyer and Alessi [39] extended their approach to a multi-dimensional model that employs several PFs to account for the failure induced by the fiber breaking and matrix cracking separately. In line with the previous approach, Quintanas-Corominas et al. [40] presented a formulation to model the anisotropic mechanical response of LFRC using a single damage-type variable. In this last study, they demonstrated the capabilities of their formulation by making a comparison of the intralaminar and translaminar failure predictions against the Linear Elastic Fracture Mechanics (LEFM) and the most common modeling approaches: CDM and CZM.

The existence of interfaces make difficult the employment of the PF approach via a physically sound variational formalism. To overcome this issue, Paggi and Reinoso [41] recently presented an approach that combines the PF approach for the bulk region with a CZM for the interface one. In this sense, they proposed a physically consistent strategy to couple via the PF variable a tension cut-off interface behavior with the damage state of the surrounding bulk region by reducing the apparent stiffness of the interface as the PF increases. This hypothesis is suitable for relatively brittle interface behavior as they demonstrated in several studies: (i) layered ceramics [42,43], (ii) micro-mechanics of poly-crystalline [44], and (iii) micro-mechanics of FRC [45].

This work aims to present a PF–CZM approach for modeling the interaction between the intralaminar and interlaminar damage mechanisms, constituting an alternative to the classical CDM–CZM approaches [46]. The main innovative aspects herein presented are: (i) the usage of the PF model proposed by Quintanas-Corominas et al. [40] for the intralaminar failure events and the CZM proposed by Turon et al. [47] for the interlaminar one, (ii) the coupling strategy between both constitutive models via the PF variable, and (iii) the numerical implementation in a High Performance Computing (HPC) simulation code. Indeed, it is presented a new interface model that attempts to provide a more general scenario for progressive damage model of solids with internal interfaces suitable for brittle and cohesive responses. After addressing the verification of the numerical implementation through mode-I and mode-II delamination tests, a thorough analysis of a cross-ply LFRC laminate subjected to a 4-Point Bending Test (4PBT) configuration is performed. The comparison between the numerical predictions and experimental observations demonstrate the capabilities of the presented PF–CZM approach to capture the main behavior on such complex failure scenario as the delamination induced by matrix cracking.

The manuscript is organized as follows. Section 2 briefly outlines the fundamental theoretical and numerical aspects of the PF–CZM approach. The constitutive assumptions regarding the bulk and interface regions are

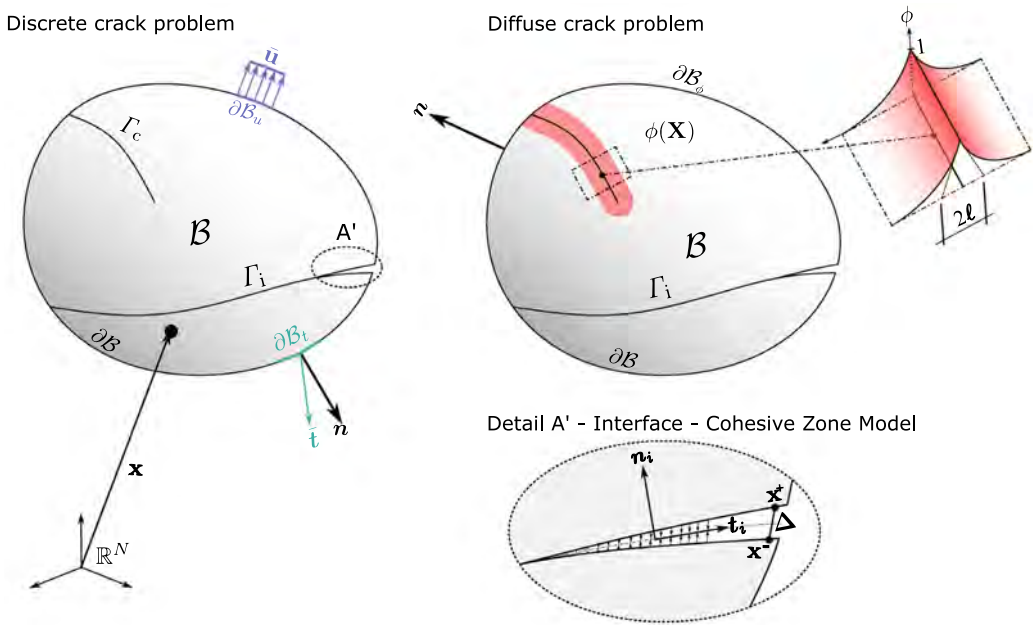

Fig. 1. Schematic representation of an arbitrary body with a discontinuity in the domain and an interface.

presented in Section 3. Section 4 introduces the implementation and applicability of the proposed formulation. In particular, the HPC environment employed is outlined in Section 4.1, while, in Section 4.3, the numerical study of the 4PBT is conducted, demonstrating predictive capabilities in very satisfactory agreement with the experimental observations. Finally, the main conclusions are summarized in Section 5.

2. Phase field approach to fracture

This section outlines the fundamental aspects of the current modeling framework, In particular, the present methodology is derived by taking the formulation of Paggi and Reinoso [41] as the fundamental result, which sets the basis for the combination of the PF approach for bulk fracture with a consistent interface formulation relying on the cohesive-like approach. Along these lines, the variational form of the internal energy functional of a general cracked body with internal interfaces is described in Section 2.1, while the weak and discrete forms of the energy functional are summarized in Sections 2.2 and 2.3, respectively.

2.1. Modeling hypotheses and variational formalism

As stated above, combining the PF and CZM methods for fracture in heterogeneous media was intuitively motivated in different investigations [41,48,49]. Complying with this idea, we consider an arbitrary body in the general Euclidean space of dimension $N \in [2, 3]$. Restricting the analysis to the infinitesimal deformation setting, the body occupies the domain $\mathcal{B} \subset \mathbb{R}^N$ with the external boundary denoted as $\partial\mathcal{B} \subset \mathbb{R}^{N-1}$, whose outward normal unit vector is represented by $\boldsymbol{n}$. As illustrated in Fig. 1, we postulate the existence of an internal interface Γ_{i} in the system, and a discrete cracks network Γ_{c} in the bulk. The material points within the body are identified by the individual position vectors $\boldsymbol{x} \in \mathcal{B}$, whereas the displacement field is identified by $\mathbf{u}(\boldsymbol{x}, t)$. For convenience, we define the displacement jump at the interface as the relative displacement between two homologous points, i.e. $\boldsymbol{\Delta} = \mathbf{u}_a^+ - \mathbf{u}_a^-$, denoting the difference between the kinematic field along the interface flanks Γ_{i}^+ and Γ_{i}^- (Fig. 1). Finally, we assume that $\mathcal{B}$ is subjected to body forces $\boldsymbol{b}$ as well as to boundary conditions in the form of prescribed displacements ($\bar{\mathbf{u}}$ on $\partial\mathcal{B}_u$) and prescribed tractions ($\bar{\boldsymbol{t}}$ on $\partial\mathcal{B}_t$). These boundary conditions are subjected to the Neumann–Dirichlet conditions, i.e. $\partial\mathcal{B}_t \cup \partial\mathcal{B}_u = \partial\mathcal{B}$ and $\partial\mathcal{B}_t \cap \partial\mathcal{B}_u = \emptyset$.

By establishing the variational approach to fracture as the point of departure of the current formulation, it is postulated that the energy functional governing the fracture process of the system is given by

$$\Pi(\mathbf{u}, \Gamma) = \Pi_{int}(\mathbf{u}, \Gamma) - \Pi_{ext}(\mathbf{u}) \tag{1}$$

Following Bourdin et al. [15] and [41], the internal energy density functional $\Pi_{int}(\mathbf{u}, \Gamma)$ of the system under consideration can be defined as the sum of elastic energy stored in the body $\Pi_{\mathcal{B}}$ and the energy dissipated through the different potential mechanisms of fracture Π_{Γ}, i.e. bulk and interface fracture processes in the current analysis. Based on these modeling assumptions, $\Pi_{int}(\mathbf{u}, \Gamma)$ takes the particular form:

$$\Pi_{int}(\mathbf{u}, \Gamma) = \Pi_{\mathcal{B}}(\mathbf{u}) + \Pi_{\Gamma}(\Gamma), \tag{2}$$

where Γ is the union between the bulk and interface cracks that are associated with the respectively fracture events, such that $\Gamma = \Gamma_{\mathrm{c}} \cup \Gamma_{\mathrm{i}}$. Accordingly, the fracture energy of the system can be accounted for by adding the split of the two corresponding counterparts:

$$\Pi_{int}(\mathbf{u}, \Gamma) = \Pi_{int}(\mathbf{u}, \Gamma_{\mathrm{c}}, \Gamma_{\mathrm{i}}) = \Pi_{\mathcal{B}}(\mathbf{u}) + \Pi_{\Gamma_{\mathrm{c}}}(\Gamma_{\mathrm{c}}) + \Pi_{\Gamma_{\mathrm{i}}}(\Gamma_{\mathrm{i}}) \tag{3}$$

where $\Pi_{\Gamma_{\mathrm{c}}}$ and $\Pi_{\Gamma_{\mathrm{i}}}$ are the dissipated energies that stem from the cracking events within the bulk and the debonding effects along the interfaces, respectively. Note that to evaluate the above expression, the topology of the cracks network is required. This evaluation can be very challenging due to the complex crack paths arising from the branching and coalescence phenomena, as well as the interaction with the cracks which induces the debonding processes along the existing interfaces. As proposed in [41], evaluating such complex crack patterns in heterogeneous media can be done by combining the PF approach within the bulk region and the interface elements, relying on the concept of the cohesive zone at the prescribed interfaces. In the continuation, the particular expression of the internal energy density is consistently derived but also including two new features: (i) the use of the recent anisotropic PF method for bulk fracture proposed in [40], and (ii) the consideration of cohesive-like interface crack obeying the bilinear Traction–Separation Law (TSL) [47].

2.1.1. Bulk region

The energy density of the bulk region Π_b includes the elastic energy stored for the body and the energy required to create and propagate the bulk cracks. Within the context of LFRCs, these events are also known as intralaminar damage mechanisms [1,4]. Considering the energetic criterion proposed by Griffith [50], Π_b can be defined as [15]:

$$\Pi_b(\mathbf{u}, \Gamma_{\mathrm{c}}) = \Pi_{\mathcal{B}}(\mathbf{u}) + \Pi_{\Gamma_{\mathrm{c}}}(\Gamma_{\mathrm{c}}) = \int_{\mathcal{B}\setminus\Gamma} \Psi_{\mathrm{e}}(\boldsymbol{\varepsilon}(\mathbf{u}))\, \mathrm{d}V + \int_{\Gamma_{\mathrm{c}}} \mathcal{G}_c\, \mathrm{d}S \tag{4}$$

where Ψ_{e} is the specific elastic energy function and $\mathcal{G}_{\mathrm{c}}$ is the critical energy release rate of the bulk material. The infinitesimal strain tensor $\boldsymbol{\varepsilon}$ is the symmetric gradient of the displacement field ($\boldsymbol{\varepsilon} := \nabla^s \mathbf{u}$), which is introduced here because Ψ_{e} is generally expressed with respect to the strain state.

The PF approach postulates that the discrete boundary representing a crack network Γ_{c} can be smeared over the domain $\mathcal{B}$ through the exploitation of the Γ-convergence concept [51], allowing the definition of the crack surface density functional $\gamma(\phi, \nabla\phi)$ to be defined [17]. This new functional is governed by the phase field variable ϕ and its spatial gradient $\nabla\phi$, endowing the current approach with non-local character in the spirit of gradient enhanced models [52]. Formally, the phase field variable ϕ accounts for the amount of equivalent crack surface at a material point. Therefore, in line with CDM models, ϕ can be interpreted as the damage state of the material point tracking the stiffness degradation. Following the notation introduced by Miehe et al. [17], Π_b reads:

$$\Pi_b(\mathbf{u}, \Gamma_{\mathrm{c}}) \approx \Pi_b(\mathbf{u}, \phi) = \int_{\mathcal{B}} \Psi_{\mathrm{b}}(\boldsymbol{\varepsilon}(\mathbf{u}), \phi)\, \mathrm{d}V + \int_{\mathcal{B}} \mathcal{G}_{\mathrm{c}} \gamma(\phi, \nabla\phi)\, \mathrm{d}V \tag{5}$$

where Ψ_{b} is the bulk free energy functional that takes into account the degradation of elastic energy within the smearing transition zone that is characterized by ℓ, i.e. between a pristine ($\phi = 0$) and a fully-damaged ($\phi = 1$) state. It is worth mentioning that the expression of Ψ_{b} depends on the material model, which is presented in Section 3.1. Note that fracture toughness in Eq. (5) requires a simple modification following [16] in order to prevent the overestimation of the released energy. This modification is performed via the use of an effective energy release

rate $\mathcal{G}_{\mathrm{c}}^{\mathrm{eff}}$ that depends on the spatial discretization parameter (finite element size) ℓ_{e} and the phase field length scale ℓ, according to the expression: $\mathcal{G}_{\mathrm{c}}^{\mathrm{eff}} = \mathcal{G}_{\mathrm{c}}\left(1 - \frac{\ell_{\mathrm{e}}}{\ell}\right)$.

Regarding the specialization of crack density functional for intralaminar failure in LFRCs, the modified version of the Ambrosio–Tortorelli functional [51] encompassing the anisotropic character at lamina level proposed in [40] is herewith recalled:

$$\gamma(\phi, \nabla\phi) = \frac{1}{2\ell}\left(\phi^2 + \nabla\phi \cdot \boldsymbol{\mathcal{L}}\nabla\phi\right) \tag{6}$$

where $\boldsymbol{\mathcal{L}}$ is a structural tensor that aligns the phase field with a preferred direction and ℓ is the so-called length scale parameter of the PF method that controls the damage diffusion around the process region [32]. In the case of isotropic surface density, it is defined as $\boldsymbol{\mathcal{L}} = \ell^2\mathbf{I}$, whereas for an anisotropic surface this yields to $\boldsymbol{\mathcal{L}} = \ell_p^2(\mathbf{n}_p \otimes \mathbf{n}_p + \beta(\mathbf{I} - \mathbf{n}_p \otimes \mathbf{n}_p))$, where $\mathbf{n}_p$ is the principal direction vector (coinciding with the fiber direction in this work), and β is a factor governing the anisotropy [40]. As can be seen, the fracture energy contribution in Eq. (5) is integrated over $\mathcal{B}$ instead of Γ_{c} eliminating the explicit need to compute the crack surface topology.

2.1.2. Interface region

The energy density of the interface Π_i accounts for the debonding process along the prescribed interfaces of the system under study. This phenomenon is denominated as interlaminar damage in composite materials, which is induced by micro-cracks at the fracture process zone [53]. Differing from the previous investigations [41–43], which employed a relatively simple tension cut-off interface formulation and whose coupling with the PF method for bulk fracture regarded the modification of the interface apparent stiffness, the current method encompasses the consideration of a bilinear TSL to account for the interface debonding according to [53]. This interface model allows interlaminar failure to be triggered through a gradual stiffness reduction upon failure initiation up to the complete decohesion. Therefore, the crack opening governs the damage state at the interface, requiring the definition of an internal variable to ensure the irreversible condition of the process. In this sense, Π_i can be defined as:

$$\Pi_i(\Gamma_{\mathrm{i}}) \approx \Pi_i(\boldsymbol{\Delta}(\mathbf{u}), \phi) = \int_{\Gamma_{\mathrm{i}}} \Psi_{\mathrm{i}}(\boldsymbol{\Delta}(\mathbf{u}), \phi, \boldsymbol{h})\, \mathrm{d}S \tag{7}$$

where Ψ_{i} is the specific interface energy function. The CZM is formulated according to the continuum damage theory and, therefore, Ψ_{i} depends on a set of historical variables $\boldsymbol{h}$. Finally, Ψ_{i} incorporates the PF variable of the bulk as an additional argument, which is introduced in order to model the interaction between the bulk and interface cracks. Both Ψ_{i} and interaction process are presented in Section 3.2.

2.1.3. Final variational form

Relying on the previous considerations in Eqs. (5) and (7), the internal energy functional of a cracked body with interfaces is herein approximated as:

$$\Pi_{int}(\mathbf{u}, \Gamma) \approx \Pi_{int}(\mathbf{u}, \phi) = \int_{\mathcal{B}} \left[\Psi_{\mathrm{b}}(\boldsymbol{\varepsilon}(\mathbf{u}), \phi) + \frac{\mathcal{G}_{\mathrm{c}}}{2\ell}\left(\phi^2 + \nabla\phi \cdot \boldsymbol{\mathcal{L}}\nabla\phi\right)\right] \mathrm{d}V + \int_{\Gamma_{\mathrm{i}}} \Psi_{\mathrm{i}}(\boldsymbol{\Delta}(\mathbf{u}), \phi, \boldsymbol{h})\, \mathrm{d}S \tag{8}$$

Moreover, in the current framework, the active–passive decomposition of the bulk free energy density function is used to account for a fracture-induced stress degradation via the volumetric–deviatoric decomposition [54]:

$$\Psi_{\mathrm{b}}(\boldsymbol{\varepsilon}, \phi) = \left((1-\phi)^2 + \eta_\ell\right)\Psi_{act}(\boldsymbol{\varepsilon}) + \Psi_{pas}(\boldsymbol{\varepsilon}) \tag{9}$$

where $\Psi_{e,act}$ and $\Psi_{e,pass}$ are the active and passive parts, respectively, of the elastic free energy density; and η_ℓ stands for the residual stiffness parameter to prevent numerical issues. In line with [40], we herewith adopt the previous decomposition in order to activate the driving forces for cracking evolution in the bulk under tensile load conditions (Section 3.1). Thus, through the use of this decomposition, the phase field only affects the so-called active term, allowing the crack closure under loading reversal to be modeled.

2.2. Weak form

Recalling the standard continuous Bubnov–Galerkin method [55], the two primary fields, $\mathbf{u}$ and ϕ, are extended with the corresponding admissible test function, $\delta\mathbf{u}$ and $\delta\phi$. Thus, the weak form of the governing functional can

be constructed by its first variation with respect to the primary fields mentioned above:

$$\delta\Pi(\mathbf{u},\delta\mathbf{u},\phi,\delta\phi)=\delta\Pi_{int}(\mathbf{u},\delta\mathbf{u},\phi,\delta\phi)-\delta\Pi_{ext}(\mathbf{u}),\quad \forall\delta\mathbf{u}\in\mathcal{V}_u,\quad \forall\delta\phi\in\mathcal{V}_\phi \tag{10}$$

where $\delta\Pi_{int}$ and $\delta\Pi_{ext}$ are respectively the internal and external variations. Here, $\mathcal{V}_u=\{\delta\mathbf{u}\in \mathrm{H}^1|\delta\mathbf{u}=0 \text{ on } \partial\mathcal{B}_u\}$ and $\mathcal{V}_\phi=\{\delta\phi\in \mathrm{H}^1|\delta\phi=0 \text{ on } \Gamma_\mathrm{c}\}$ are the functional spaces of the admissible test functions [21,42].

Focusing on the internal energy variation, this term can be split according to the variation of the primary fields as:

$$\delta\Pi_{int}(\mathbf{u},\delta\mathbf{u},\phi,\delta\phi)=\delta\Pi^{u}_{int}(\mathbf{u},\delta\mathbf{u},\phi)+\delta\Pi^{\phi}_{int}(\mathbf{u},\phi,\delta\phi),\quad \forall\delta\mathbf{u}\in\mathcal{V}_u,\quad \forall\delta\phi\in\mathcal{V}_\phi. \tag{11}$$

Complying with the infinitesimal strain setting as the modeling framework, the weak form of the variation of the internal energy with respect to the displacement field reads as:

$$\delta\Pi^{u}_{int}(\mathbf{u},\delta\mathbf{u},\phi)=\int_{\mathcal{B}}\boldsymbol{\sigma}(\phi):\delta\boldsymbol{\varepsilon}\,\mathrm{d}V+\int_{\Gamma_\mathrm{i}}\boldsymbol{\tau}(\phi):\delta\boldsymbol{\Delta}\,\mathrm{d}S,\quad \forall\delta\mathbf{u}\in\mathcal{V}_u \tag{12}$$

where $\boldsymbol{\sigma}(\phi)=\partial_{\boldsymbol{\varepsilon}}\Psi_\mathrm{b}$ is the stress tensor which depends on the phase field variable via the so-called degradation function $g(\phi)=(1-\phi)^2$ and $\delta\boldsymbol{\varepsilon}=\partial_{\mathbf{u}}\boldsymbol{\varepsilon}(\delta\mathbf{u})$ is the variation of the strain tensor $\boldsymbol{\varepsilon}$; both are associated to the bulk region. Similarly, $\boldsymbol{\tau}(\phi)=\partial_{\boldsymbol{\Delta}}\Psi_\mathrm{i}$ is the cohesive tractions and $\delta\boldsymbol{\Delta}=\partial_{\mathbf{u}}\boldsymbol{\Delta}(\delta\mathbf{u})$ is the variation of the displacement jumps; both are associated with the interface region. It is worth noting that both stress tensors, $\boldsymbol{\sigma}$ and $\boldsymbol{\tau}$, formally depend on the displacement and phase fields as is denoted in the corresponding terms.

In a similar way, the weak form resulting from the variation of the internal energy with respect to the phase field renders

$$\delta\Pi^{\phi}_{int}(\mathbf{u},\phi,\delta\phi)=\int_{\mathcal{B}}\left[\mathcal{F}_b\delta\phi+\frac{\mathcal{G}_c}{\ell}\left(\phi\delta\phi+\nabla(\delta\phi)\cdot\boldsymbol{\mathcal{L}}\nabla\phi\right)\right]\mathrm{d}V+\int_{\Gamma_\mathrm{i}}\mathcal{F}_i\delta\phi\,\mathrm{d}S,\quad \forall\delta\phi\in\mathcal{V}_\phi \tag{13}$$

where $\mathcal{F}_b=\partial_\phi\Psi_\mathrm{b}=-2(1-\phi)\Psi_\mathrm{act}$ and $\mathcal{F}_i=\partial_\phi\Psi_\mathrm{i}$ stand for the bulk and the interface contributions to the energetic force that drives the phase field evolution, respectively. Note that $\mathcal{F}_b$ is obtained assuming the active–passive energy decomposition defined in Eq. (9). After some algebraic manipulations, the variation of the coupled functional associated with the phase field contribution can be rewritten as:

$$\delta\Pi^{\phi}_{int}(\mathbf{u},\phi,\delta\phi)=\frac{\mathcal{G}_c}{\ell}\int_{\mathcal{B}}\left[(\phi-2(1-\phi)\mathcal{H})\,\delta\phi+\nabla(\delta\phi)\cdot\boldsymbol{\mathcal{L}}\nabla\phi\right]\mathrm{d}V+\int_{\Gamma_\mathrm{i}}\mathcal{F}_i\delta\phi\,\mathrm{d}S,\quad \forall\delta\phi\in\mathcal{V}_\phi \tag{14}$$

For isotropic crack density surfaces, the fracture toughness $\mathcal{G}_\mathrm{c}$ is a constant value, and therefore the corresponding expression can be evaluated without any further assumptions. Otherwise, for anisotropic crack density surfaces, $\mathcal{G}_\mathrm{c}$ represents the nominal fracture toughness accounting for the current local mixed-mode opening. At present, a particular expression for the evaluation of $\mathcal{G}_\mathrm{c}$ for mixed-mode fracture conditions is not available and requires further research, which is a matter beyond the scope of the current study. In addition, although this is still an open issue within the context of the PF method, assuming a constant value of $\mathcal{G}_\mathrm{c}$ yields to predictions with very good accuracy in comparison with the experimental data as will be reported in forthcoming sections.

In Eq. (14), $\mathcal{H}$ is a field variable that accounts for the historical value of the crack driving state function $\tilde{\mathcal{D}}$ by setting:

$$\mathcal{H}=\max_{s\in\{0,t\}}\left(\tilde{\mathcal{D}}^s\right)\quad\text{with}\quad\tilde{\mathcal{D}}^s=\frac{\Psi^s_\mathrm{act}}{\mathcal{G}_c/\ell} \tag{15}$$

where s represents the fully story process and t is the current time step. Thus, this history field ensures two conditions required to correctly model the evolution of a crack: (i) the irreversible condition preventing healing effects and (ii) the positiveness of the crack driving force enforcing for fracture growth. In addition, following Miehe et al. [29], the dimensionless character of the crack driving force allows an elastic behavior up to the onset of the failure to be included by setting a threshold $\tilde{\mathcal{D}}^s=\left\langle\Psi^s_\mathrm{act}\ell/\mathcal{G}_c-1\right\rangle_+$.

Finally, the external energy variation can be written, in its most general form, as:

$$\delta\Pi_{ext}(\mathbf{u},\delta\mathbf{u})=\int_{\mathcal{B}}\boldsymbol{b}\cdot\delta\mathbf{u}\,\mathrm{d}V+\int_{\partial\mathcal{B}_u}\bar{\boldsymbol{t}}\cdot\delta\mathbf{u}\,\mathrm{d}S \tag{16}$$

2.3. Discrete form

The FEM is used in the current work to solve the displacement-phase coupled field problem. The interpolation of the continuum variables at the element level is performed in the isoparametric space using the first-order Lagrangian shape functions. In this sense, the interpolation operator $\boldsymbol{\mathcal{N}}$ is defined as a matrix arranging the $\mathcal{C}^0$-continuous shape functions, $\boldsymbol{\mathcal{N}}^I$ giving the required support to the node I of the element. It must be pointed out that this operator can have a different expression depending on the region and primary field.

In accordance with the isoparametric concept within FEM, firstly introduced by Irons [56], the spatial approximation and the semi-discrete version of the residual vectors and consistent tangent matrices of the two primary fields ($\mathbf{u}$, ϕ) are presented in the following.

2.3.1. Bulk region

The displacement and phase fields ($\mathbf{u}$, ϕ), as well as their variations ($\delta\mathbf{u}$, $\delta\phi$) and their spatial gradients ($\nabla\mathbf{u}$, $\nabla\phi$) are approximated at the element level as follows:

$$\mathbf{u} \approx \boldsymbol{\mathcal{N}}\mathbf{d}, \quad \delta\mathbf{u} \approx \boldsymbol{\mathcal{N}}\delta\mathbf{d}, \qquad \nabla\mathbf{u} \approx \mathbf{B}_{\mathbf{d}}\mathbf{d} \tag{17}$$

$$\phi \approx \boldsymbol{\mathcal{N}}_{\mathfrak{d}}\mathfrak{d}, \quad \delta\phi \approx \boldsymbol{\mathcal{N}}_{\mathfrak{d}}\delta\mathfrak{d}, \quad \nabla\phi \approx \mathbf{B}_{\mathfrak{d}}\mathfrak{d} \tag{18}$$

where $\mathbf{d}$ and $\mathfrak{d}$ are the vectors arranging the nodal values of the displacement and phase fields, respectively. In turn, $\mathbf{B}_{\mathbf{d}}$ is the strain–displacement kinematic operator and $\mathbf{B}_{\mathfrak{d}}$ is the compatibility operator with the spatial derivatives of the shape functions corresponding to the phase field variable. As the particular expressions of these operators can be found in Msekh et al. [57], they are omitted here for the sake of brevity.

2.3.2. Interface region

Complying with the formulation of an interface element, the displacement jumps vector ($\boldsymbol{\Delta}$) is expressed in the local frame across the interface [6,53,58]. Therefore, the interpolation of $\boldsymbol{\Delta}$ and its variation with respect to the displacement field ($\delta\boldsymbol{\Delta}$) can be expressed at the element level as:

$$\boldsymbol{\Delta} \approx \mathbf{B}_{\Delta}\mathbf{d}, \quad \delta\Delta \approx \mathbf{B}_{\Delta}\delta\mathbf{d} \tag{19}$$

where $\mathbf{B}_{\Delta} = \mathbf{R}(\mathbf{d})\boldsymbol{\mathcal{N}}_{\Delta}\mathbf{L}$ is the kinematic jump-displacement operator that approximates the nodal displacement jump into the integration points of the middle plane of the interface. Here, $\mathbf{L}$ provides the difference between the displacements of the upper and the lower interface points and $\mathbf{R}(\mathbf{d})$ rotates the integration point value from the global to the local frame. Since $\mathbf{R}$ depends on $\mathbf{d}$, this aspect induces a geometric contribution in both the residual vector of the internal forces and the consistent tangent matrix, those cases with large displacements should be accounted for [58]. Taking into account that for a small displacement regime the geometric contribution can be neglected, in the current investigation, this effect has not been considered to approximate the variation of the displacement jumps.

The phase field across the interface is defined as the averaged value between the two homologous points of the upper and bottom interface boundaries, i.e. $\hat{\phi} = (\phi^+ + \phi^-)/2$ [41]. Hence, the approximation of the phase field (ϕ) and its variation ($\delta\phi$) at the element level is given by

$$\phi \approx \hat{\mathbf{B}}_{\mathfrak{d}}\mathfrak{d}, \quad \delta\phi \approx \hat{\mathbf{B}}_{\mathfrak{d}}\delta\mathfrak{d} \tag{20}$$

where $\hat{\mathbf{B}}_{\mathfrak{d}} = \boldsymbol{\mathcal{N}}_{\hat{\phi}}\mathbf{M}$ is a compatibility operator of the averaged phase field in which $\mathbf{M}$ is the average operator. More details about the geometrical contribution as well as the particular form of the above operators can be found in [58,59].

2.3.3. FE residual vectors

The discrete version of the residual vectors of the displacement and phase fields are defined as:

$$\mathbf{R}_{\mathbf{d}}^{int} = \int_{\mathcal{B}} \mathbf{B}_{\mathbf{d}}^{\mathrm{T}}\boldsymbol{\sigma}(\phi)\,\mathrm{d}V + \int_{\Gamma_{\mathrm{i}}} \mathbf{B}_{\Delta}^{\mathrm{T}}\boldsymbol{\tau}(\phi)\,\mathrm{d}S \tag{21}$$

$$\mathbf{R}_{\mathfrak{d}} = \frac{\mathcal{G}_c}{\ell}\int_{\mathcal{B}} \left[(\mathfrak{d} - 2(1-\mathfrak{d})\mathcal{H})\,\boldsymbol{\mathcal{N}}_{\mathfrak{d}} + \mathbf{B}_{\mathfrak{d}}^{\mathrm{T}}\boldsymbol{\mathcal{L}}\nabla\mathfrak{d}\right]\,\mathrm{d}V + \int_{\Gamma_{\mathrm{i}}} \hat{\mathbf{B}}_{\mathfrak{d}}^{\mathrm{T}}\mathcal{F}_i\,\mathrm{d}S \tag{22}$$

In the first expression, $\mathbf{R}_{\mathbf{d}}^{int}$ stands for the contribution of the internal forces in the out-of-balance force residual of the displacement field. The complete expression including the contribution of body forces and external traction, is given by

$$\mathbf{R}_{\mathbf{d}} = \mathbf{R}_{\mathbf{d}}^{int} - \int_{\mathcal{B}} \boldsymbol{\mathcal{N}}^{\mathrm{T}} \boldsymbol{b} \, \mathrm{d}V - \int_{\partial \mathcal{B}_t} \boldsymbol{\mathcal{N}}^{\mathrm{T}} \bar{\boldsymbol{t}} \, \mathrm{d}S \tag{23}$$

2.3.4. FE consistent tangent matrices

The consistent tangent matrices can be obtained by differentiating the residual vectors with respect to the increment of the primary fields:

$$\mathbf{K}_{\mathbf{dd}} = \int_{\mathcal{B}} \mathbf{B}_{\mathbf{d}}^{\mathrm{T}} \mathbb{C}(\phi) \mathbf{B}_{\mathbf{d}} \, \mathrm{d}V + \int_{\Gamma_{\mathrm{i}}} \mathbf{B}_{\Delta}^{\mathrm{T}} \mathbb{D}(\phi) \mathbf{B}_{\Delta} \, \mathrm{d}S \tag{24}$$

$$\mathbf{K}_{\mathfrak{d}\mathfrak{d}} = \frac{\mathcal{G}_c}{\ell} \int_{\mathcal{B}} \left[((1 + 2\mathfrak{d})\mathcal{H}) \boldsymbol{\mathcal{N}}_{\mathfrak{d}}^{\mathrm{T}} \boldsymbol{\mathcal{N}}_{\mathfrak{d}} + \mathbf{B}_{\mathfrak{d}}^{\mathrm{T}} \boldsymbol{\mathcal{L}} \mathbf{B}_{\mathfrak{d}} \right] \mathrm{d}V + \int_{\Gamma_{\mathrm{i}}} \hat{\mathbf{B}}_{\mathfrak{d}}^{\mathrm{T}} \mathbf{F} \hat{\mathbf{B}}_{\mathfrak{d}} \, \mathrm{d}S \tag{25}$$

where $\mathbb{C} = \partial_{\boldsymbol{\varepsilon}} \boldsymbol{\sigma}$ and $\mathbb{D} = \partial_{\boldsymbol{\Delta}} \boldsymbol{\tau}$ are the nominal tangent operators of the bulk material and cohesive zone model, respectively. In turn, $\mathbf{F} = \partial_{\phi} \mathcal{F}_i$ is the tangent operator of the phase field driving force across the interface with respect to the average phase field. Finally, the coupling matrices $\mathbf{K}_{\mathfrak{d}\mathbf{d}}$ and $\mathbf{K}_{\mathbf{d}\mathfrak{d}}$ are not derived here because they are not necessary for the staggered solution scheme used in the numerical examples. It is worth mentioning that the adoption of a staggered incremental-iterative scheme in conjunction with the Newton–Raphson method is herewith adopted due to its robustness, being of especial interest in the current investigation where several energy dissipation mechanisms can evolve simultaneously.

Remark 1. In the current approach the nominal tangent operators ($\mathbb{C}$, $\mathbb{D}$ and $\mathbf{F}$) are computed using the Complex-Step Derivative Approximation (CSDA) [60], which is briefly summarized in Appendix B. This approach is used with the aim of increasing the robustness in the face of the perturbation parameter, not the accuracy of the approximation. In this sense, CSDA approximates the derivate at $\mathcal{O}(x^2)$ like the classical perturbation step approximation which is used, for instance, in [47,61].

3. Constitutive material models

3.1. Bulk model

The constitutive model used to model the anisotropic behavior characteristic of LFRCs reproduces the formulation proposed by Quintanas-Corominas et al. [40], and which is summarized in the sequel. Accordingly, the complementary Gibbs free energy Ψ^*, which is the dual form of the Helmholtz free energy, for long fiber composite material can be expressed as (see [2,28] for a more comprehensive treatment):

$$\Psi(\boldsymbol{\varepsilon}) = \Psi^*(\tilde{\boldsymbol{\sigma}}) = \frac{1}{2} \left(\frac{(\tilde{\sigma}_{\mathrm{L}})^2 - 4\nu_{12}\tilde{\sigma}_{\mathrm{L}}\tilde{p}_{\mathrm{T}}}{E_{11}} + \frac{(\tilde{p}_{\mathrm{T}})^2}{E_T} + \frac{(\tilde{\tau}_{\mathrm{T}})^2}{G_T} + \frac{(\tilde{\tau}_{\mathrm{L}})^2}{G_{12}} \right) \tag{26}$$

where $\tilde{\sigma}_{\mathrm{L}}$, $\tilde{p}_{\mathrm{T}}$, $\tilde{\tau}_{\mathrm{L}}$ and $\tilde{\tau}_{\mathrm{T}}$ identify the effective stress quantities, whose definitions are given by

$$\tilde{\sigma}_{\mathrm{L}} = \tilde{\sigma}_{11}, \quad \tilde{p}_{\mathrm{T}} = \frac{\tilde{\sigma}_{22} + \tilde{\sigma}_{33}}{2}, \quad \tilde{\tau}_{\mathrm{L}} = \sqrt{(\tilde{\sigma}_{12})^2 + (\tilde{\sigma}_{13})^2} \quad \text{and} \quad \tilde{\tau}_{\mathrm{T}} = \frac{1}{2}\sqrt{(\tilde{\sigma}_{22} - \tilde{\sigma}_{33})^2 + 4(\tilde{\sigma}_{23})^2}, \tag{27}$$

where E_{11} is the Young's modulus along the fiber direction, ν_{12} stands for the longitudinal Poisson's coefficient, G_{12} is the shear modulus and E_T and G_T are the transverse and the shear modulus:

$$E_T = \frac{E_{22}}{2(1 - \nu_{23})} \quad \text{and} \quad G_T = \frac{E_{22}}{2(1 + \nu_{23})}, \tag{28}$$

where E_{22} is the Young's modulus in-plane transverse to the fiber direction and ν_{23} denotes the transverse Poisson's coefficient.

Recalling the modeling hypotheses of [40], the degradation of the specific bulk energy for fiber-reinforced composites within the context of the PF approach is given by

$$\Psi^*(\tilde{\boldsymbol{\sigma}}, \phi) = \left((1 - \phi)^2 + \eta_\ell \right) \Psi^*_{\mathrm{act}}(\tilde{\boldsymbol{\sigma}}) + \Psi^*_{\mathrm{pas}}(\tilde{\boldsymbol{\sigma}}) \tag{29}$$

being

$$\Psi^*_{\text{act}}(\tilde{\boldsymbol{\sigma}}) = \frac{1}{2}\left(\frac{\left\langle(\tilde{\sigma}_{\text{L}})^2 - 4\nu_{12}\tilde{\sigma}_{\text{L}}\tilde{p}_{\text{T}}\right\rangle_+}{E_{11}} + \frac{\langle\tilde{p}_{\text{T}}\rangle_+^2}{E_T} + \frac{(\tilde{\tau}_{\text{T}})^2}{G_T} + \frac{(\tilde{\tau}_{\text{L}})^2}{G_{12}}\right) \tag{30}$$

$$\Psi^*_{\text{pas}}(\tilde{\boldsymbol{\sigma}}) = \frac{1}{2}\left(\frac{\left\langle(\tilde{\sigma}_{\text{L}})^2 - 4\nu_{12}\tilde{\sigma}_{\text{L}}\tilde{p}_{\text{T}}\right\rangle_-}{E_{11}} + \frac{\langle\tilde{p}_{\text{T}}\rangle_-^2}{E_T}\right) \tag{31}$$

Then, the effective compliance tensor in compact notation $\tilde{\mathbf{H}}$ (vector form) reads

$$\tilde{\mathbf{H}} = \left[\frac{\partial^2\Psi^*}{\partial\tilde{\boldsymbol{\sigma}}\otimes\partial\tilde{\boldsymbol{\sigma}}}\right] = \begin{bmatrix} \frac{1}{E_{11}} & -\frac{\nu_{12}}{E_{11}} & -\frac{\nu_{12}}{E_{11}} & 0 & 0 & 0 \\ & \frac{1}{4}(\frac{1}{E_T}+\frac{1}{G_T}) & \frac{1}{4}(\frac{1}{E_T}-\frac{1}{G_T}) & 0 & 0 & 0 \\ & & \frac{1}{4}(\frac{1}{E_T}+\frac{1}{G_T}) & 0 & 0 & 0 \\ & & & \frac{1}{G_T} & 0 & 0 \\ & sym. & & & \frac{1}{G_{12}} & 0 \\ & & & & & \frac{1}{G_{12}} \end{bmatrix} \tag{32}$$

Based on the previous definitions, it is worth mentioning that the crack driving state function can be associated with four different material directions that are in turn related to the following intralaminar damage mechanisms: (11) fiber failure, (22/33) matrix failure, (12/13) shear in-plane and (23) transversal shear failures. See Quintanas-Corominas et al. [40] for further details.

3.2. Interface model

The constitutive model herein envisaged for the interface region is based on the formulation proposed by Turon et al. (TM) [8,47,53]. The principal differences of this interface formulation with respect to that proposed by Paggi and Reinoso (PRM) [41] are: (i) the post-peak behavior, (ii) the mixed-mode interaction, and (iii) the initiation criteria. Thus, while a cut-off upon failure is defined in the PRM, the TM sets a softening law after reaching the maximum strength of the interface. Therefore, the PRM can be conceived as a more suitable model for interfaces with moderately low fracture process zones, whereas the TM is inherently formulated to capture the response of cohesive interfaces. Regarding the propagation criterion under mixed-mode interaction, on the one hand, PRM used a standard quadratic one whereas, on the other hand, TM employed the Benzeggagh and Kenane criterion [62].

Taking into account the aforementioned characteristics of the TM formulation, the coupling strategy between the PF and CZM proposed herein differs from the one in the PRM. The current strategy assumes that the damage state in the fracture process zone of a crack originated in the bulk region can induce damage in the interface resulting in a loss of stiffness. Considering that the PF variable and the damage state of the TM formulation represent the ratio of a cracked area at a material point, the coupling between both approaches is performed through the integrity function $m(\boldsymbol{\Delta}, \phi)$. In particular, this coupling function has to be a continuous monotonically decreasing function defined between 1 (pristine material) and 0 (fully damaged material). In a general manner, the coupling strategy herein proposed is expressed in terms of the integrity functions associated with the displacement jump and PF fields, i.e. $m_{\Delta}(\boldsymbol{\Delta})$ and $m_{\phi}(\phi)$, respectively. Assuming a complementary effect in the stiffness loss, the coupling function proposed for the current framework is:

$$m\left(\boldsymbol{\Delta}, \phi\right) \equiv m\left(m_{\Delta}, m_{\phi}\right) = m_{\Delta} m_{\phi} \tag{33}$$

where m_{Δ} is computed according to the TM formulation (see Algorithm 1) and m_{ϕ} to the following evolution law:

$$m_{\phi} = \left(1 - r_{\phi}\right)^2 \tag{34}$$

where r_{ϕ} is the PF damage threshold that is integrated over the time t satisfying Kuhn–Tucker conditions as:

$$\text{Activation function}: \quad F_{\phi} = H_{\phi} - r_{\phi} \tag{35}$$

$$\text{Loading function}: \quad H_{\phi} = \begin{cases} 0 & \text{if} \quad \phi \leq \phi_{\min} \\ \dfrac{\phi - \phi_{\min}}{\phi_{\max} - \phi_{\min}} & \text{if} \quad \phi_{\min} < \phi < \phi_{\max} \\ 1 & \text{if} \quad \phi \geq \phi_{\max} \end{cases} \tag{36}$$

Table 1
4PBT material properties and input parameters [63,64].

Bulk region	E_{11}	140 GPa	Young's modulus (fiber dir.)
	E_{22}	10 GPa	Young's modulus (matrix dir.)
	G_{12}	5.2 GPa	Shear modulus
	ν_{12}	0.3	Poisson ratio
	ν_{13}	0.42	Poisson ratio (isotropy plane)
	Y_T	70 MPa	Tensile transverse strength
	ξ[a]	1	PF post-peak control parameter
	ℓ_f[a]	1.5	PF length scale (fiber dir.)
	ℓ_m[a]	0.1	PF length scale (matrix dir.)
Interface region	τ_I[a]	70 MPa	Cohesive strength: mode-I
	τ_{II}[a]	110 MPa	Cohesive strength: mode-II
	$\mathcal{G}_I$	0.432 kJ/m^2	Fracture toughness: mode-I
	$\mathcal{G}_{II}$	1.002 kJ/m^2	Fracture toughness: mode-II
	η	1.75	BK interpolation parameter
	K_I	$1.5{\cdot}10^5$ kN/mm^3	Penalty stiffness: mode-I
	$\phi_{\min}$[a]	0.1	PF–CZM coupling limits: min.
	$\phi_{\max}$[a]	0.5	PF–CZM coupling limits: max.

[a]Assumed values.

$$\text{Temporal integration:} \quad r_\phi = \max_{s\in\{0,t\}} \left[H_\phi^s\right] \tag{37}$$

where ϕ is the averaged PF value at the integration point according to the interface element formulation presented in Section 2.3.

As can be appreciated in the previous expression, two limits, $\phi_{\min}$ and $\phi_{\max}$, control the initiation and finalization of the coupling. By setting $\phi_{\min} > 0$, the degradation of the interface properties due to the cracking of the bulk region is delayed which, in turn, precludes the driving of the PF from the very beginning of the analysis. On the other hand, an upper limit for the coupling is established by setting $\phi_{\max} < 1$. Moreover, it is also possible to model a brittle behavior of the interface due to the stiffness loss in the bulk region by setting $\phi_{\min} \approx \phi_{\max}$.

Remark 2. As described in Section 2.3, the quantities of the primary fields are extrapolated into the mid-plane of the interface region through an interface element technology. Hence, in the current approach, ϕ governing the interface constitutive model is the averaged quantity at the mid-plane of the interface region.

To illustrate the behavior associated to the proposed coupling, the equivalent cohesive traction is shown in Fig. 2 for an interface with the properties listed in Table 1 and $\phi_{\min} = 0.2$ and $\phi_{\min} = 0.8$ as coupling limits. The colored lines in Fig. 2b–c illustrate the degradation of the stiffness as the PF increases, whereas the black line corresponds to the loading cycle depicted in Fig. 2a. This cycle combines steps in which the opening of the interface increases and the PF is kept fixed (A, C, and E), with others in which the opening is kept fixed and the PF increases (B and D). In the following, the black curve behavior is analyzed in terms of the cohesive traction τ, mixed-mode equivalent opening λ and PF ϕ. In step A, the cohesive traction increases according to the effective penalty stiffness due to the opening of the interface. Then, in step B, the traction remains constant until the PF reaches the bottom limit $\phi_{\min}$, after which the cohesive traction decreases as a consequence of the damage growth. Note that, from the point of view of the traction — opening law, this behavior is similar to a relaxation of the interface. In step C, the cohesive traction increases according to the nominal penalty stiffness until reaching the corresponding critical opening. After this point, the cohesive traction decreases due to the opening of the interface according to a nominal cohesive law which has less available free energy density as consequence of the bulk damage. Moving to step D, the cohesive traction decreases due to the increase of the PF up to the rupture of the interface, which happens when the $\phi > \phi_{\max}$. Finally, in step E, the equivalent opening is increased without any effect on the cohesive tractions, demonstrating the complete rupture of the interface.

The work-flow of the interface model accounting for the coupling between TM and PF is presented in Algorithm 1. Nevertheless, it is worth mentioning that through the coupling herein proposed, the fundamental hypotheses of TM are preserved. Therefore, for situations in which failure processes are confined to the interface, we retrieved

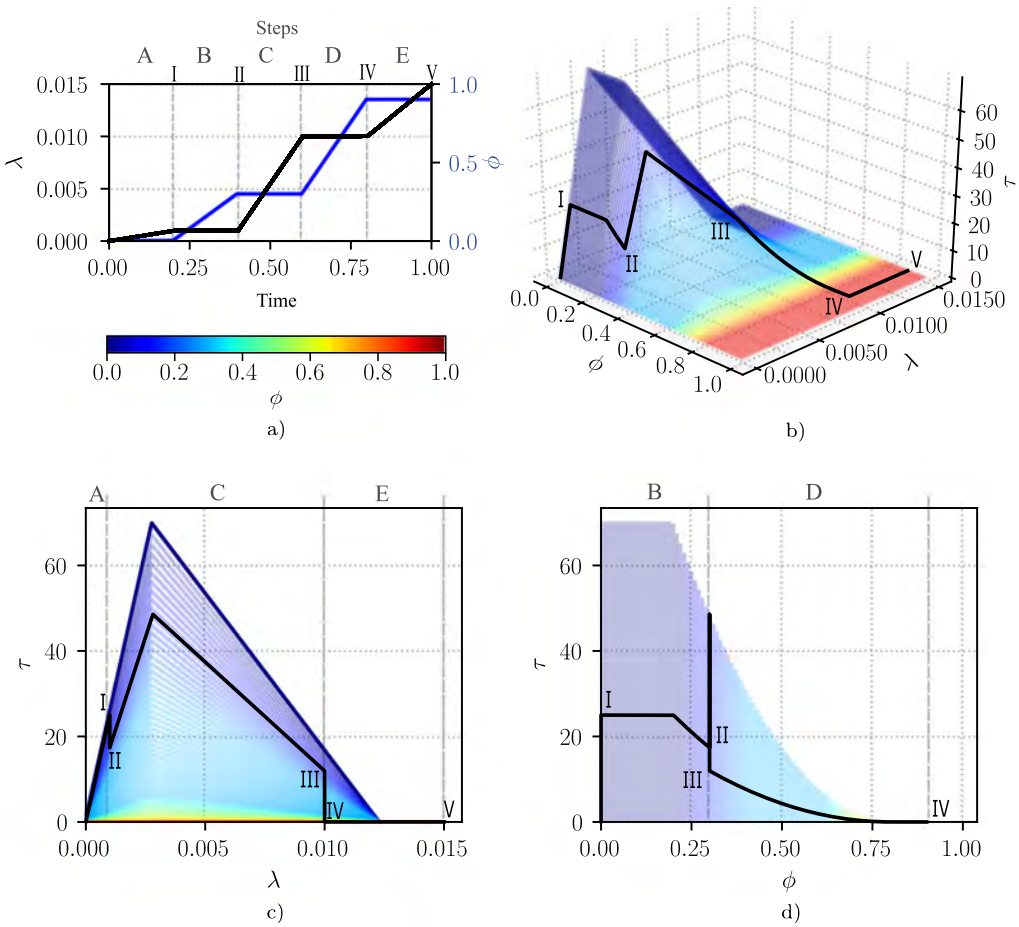

Fig. 2. Cohesive traction (τ) behavior for a loading cycle combining equivalent displacement jumps (λ) and phase field (ϕ): (a) loading cycle representation (b) $\tau - \lambda - \phi$ curves, (c) $\tau - \lambda$ and (d) $\tau - \phi$. The labels A, B, C and D denote the time interval (step), whereas I, II, III, IV and V a particular instant of time. The black curve in b–d illustrates the response of the loading cycle defined in a. Finally, the rainbow-colored map illustrates the response of the cohesive law for an initial and fixed value of ϕ.

previous results obtained with such an interface model. To illustrate this claim, we examine the accuracy of the TM for pure interface failure under mixed-mode fracture conditions in Section 4.2. Moreover, for the sake of brevity, the specific details of the TM are herewith omitted and interested readers are referred to [8,47,53].

3.2.1. PF driving force and thermodynamic consistency

In this section, we outline the derivations of the PF driving force and the examination of the thermodynamic consistency of the model in the following paragraphs. Recalling the coupling function herein derived, the cohesive interface free energy density function of the TM model can be rewritten as:

$$\Psi_{\mathrm{i}}(\boldsymbol{\Delta}, \phi) = m(\boldsymbol{\Delta}, \phi)\, \Psi_{\mathrm{i,ela}} \tag{38}$$

where $\Psi_{\mathrm{i,ela}} = (\boldsymbol{\Delta})^{\mathrm{T}} \mathbf{K} \boldsymbol{\Delta}$ is the elastic energy stored in the interface. Here, $\mathbf{K}$ is the elastic stiffness matrix. Note that the dependency of the integrity function with respect to the displacement jumps and PF is here explicitly represented here to emphasize the coupling strategy. Then, considering the previous expression and the coupling functions given

in Eqs. (33)–(37), the contribution of the interface to the driving force of the PF is defined as:

$$\mathcal{F}_i = \begin{cases} m_\Delta \dfrac{\partial m_\phi}{\partial r_\phi} \dfrac{\partial r_\phi}{\partial \phi} \Psi_{\text{i,ela}} & \text{if} \quad 0 < r_\phi < 1 \\ 0 & \text{otherwise} \end{cases} \tag{39}$$

where m_Δ is the integrity function defined in the original TM formulation (see step 9 in Algorithm 1), whereas the partial derivatives accounting for the coupling herein proposed are given by:

$$\frac{\partial m_\phi}{\partial r_\phi} = -2(1 - r_\phi) \tag{40}$$

$$\frac{\partial r_\phi}{\partial \phi} = \frac{1}{(\phi_{\max} - \phi_{\min})} \tag{41}$$

It should be noted that for a fixed displacement jump and, therefore, a fixed m_Δ and $\Psi_{\text{i,ela}}$, the dissipated energy by PF will be the free energy available because of $-\int_0^1 \mathcal{F}_i \mathrm{d}\phi = m_\Delta \Psi_{\text{i,ela}}$.

Algorithm 1 Work-flow for the interface model: cohesive zone model coupled with the phase field approach.

The input material properties are the mode-I and mode-II initial and final jumps (Δ_{Io}, Δ_{IIo}, Δ_{Ic} and Δ_{IIc}) as well as the mode-I and mode-II penalty stiffness (K_{I} and K_{II}). In addition, the Benzeggagh and Kenane parameter η is also given as an input property. It is worth mentioning that Δ_{o} and Δ_{c} can be defined using the fracture toughness and cohesive strength [9]. Here, r_Δ^h and r_ϕ^h are the maximum historical values of the damage threshold variable. Finally, the compact notation is herein used, which means that for a 3D case $\{\boldsymbol{\Delta}\} = \{\Delta_1, \Delta_2, \Delta_3\}^{\text{T}}$ is the displacement jump, $\{\boldsymbol{\tau}\} = \{\tau_1, \tau_2, \tau_3\}^{\text{T}}$ is the tractions and $[\mathbf{K}] = [\mathbf{I}]\{K_{\text{II}}, K_{\text{II}}, K_{\text{I}}\}$ is the penalty stiffness matrix, where $[\mathbf{I}]$ is the identity matrix.

Input: $\{\boldsymbol{\Delta}\}$, ϕ, r_Δ^h, r_ϕ^h, material properties

Output: $\{\boldsymbol{\tau}\}$, $\mathcal{F}_i$, r_Δ, r_ϕ

Compute mixed-mode dependent quantities:

1: Effective cohesive tractions: $\tilde{\tau} = \sqrt{K_{\text{II}}^2 \Delta_1^2 + K_{\text{II}}^2 \Delta_2^2 + K_{\text{I}}^2 \langle \Delta_3 \rangle_+^2}$

2: Mixed-mode ratio: $B = (K_{\text{II}} \Delta_1^2 + K_{\text{II}} \Delta_2^2)/(\tilde{\tau})^2$

3: Equivalent penalty stiffness: $K_B = (1 - B) K_{\text{I}} + B K_{\text{II}}$

4: Equivalent onset jump: $\lambda_{\text{o}} = \sqrt{(K_{\text{I}} \Delta_{\text{Io}}^2 + (K_{\text{II}} \Delta_{\text{IIo}}^2 - K_{\text{I}} \Delta_{\text{Io}}^2) B^\eta) K_B^{-1}}$

5: Equivalent critical jump: $\lambda_{\text{c}} = (K_{\text{I}} \Delta_{\text{Io}} \Delta_{\text{Ic}} + (K_{\text{II}} \Delta_{\text{IIo}} \Delta_{\text{IIc}} - K_{\text{I}} \Delta_{\text{Io}} \Delta_{\text{Ic}}) B^\eta)(K_B \lambda_{\text{o}})^{-1}$

6: Equivalent jump: $\lambda = (K_{\text{II}} \Delta_1^2 + K_{\text{II}} \Delta_2^2 + K_{\text{I}} \langle \Delta_3 \rangle_+^2)(\tilde{\tau})^{-1}$

Compute the integrity function associated to the equivalent jump:

7: Activation function: $H_\Delta = \min\left[1, \max\left[0, \frac{\lambda - \lambda_{\text{o}}}{\lambda_{\text{c}} - \lambda_{\text{o}}}\right]\right]$

8: Historical threshold: $r_\Delta = \max\left[r_\Delta^h, H_\Delta\right]$

9: Integrity function: $m_\Delta = 1 - \frac{r_\Delta \lambda_{\text{c}}}{r_\Delta \lambda_{\text{c}} + (1 - r_\Delta)\lambda_{\text{o}}}$

Compute the integrity function associated to the phase field:

10: Activation function: $H_\phi = \min\left[1, \max\left[0, \frac{\phi - \phi_{\min}}{\phi_{\max} - \phi_{\min}}\right]\right]$

11: Historical threshold: $r_\phi = \max\left[r_\phi^h, H_\phi\right]$

12: Integrity function: $m_\phi = \left(1 - r_\phi\right)^2$

Compute the integrity function according to the coupling function:

13: Integrity function: $m = \min\left[m_\Delta, m_\phi\right]$

Compute cohesive tractions:

14: Cohesive tractions: $\{\boldsymbol{\tau}\} = m[\mathbf{K}]\{\boldsymbol{\Delta}\}$

Compute phase field driving force:

15: Elastic energy: $\Psi_{\text{i,ela}} = \frac{1}{2}\{\boldsymbol{\Delta}\}^T [\mathbf{K}]\{\boldsymbol{\Delta}\}$

16: Phase field driving force: $\mathcal{F}_i = \begin{cases} m_\Delta \frac{-2(1-r_\phi)}{\phi_{\max} - \phi_{\min}} \Psi_{\text{i,ela}} & \text{if} \quad 0 < r_\phi < 1 \\ 0 & \text{otherwise} \end{cases}$

4. Numerical treatment and applications

This section briefly introduces the implementation of the proposed formulation in High Performance Computing (HPC) environments, and demonstrates the predictive capabilities in a coupon-based composite specimen.

4.1. HPC implementation and solution scheme

4.1.1. Basic architecture

The proposed model is programmed in the Alya system, which is a multi-physics code conceived for HPC environments, see for instance [4,65,66]. This code is written in Fortran 90/95 using a hybrid OpenMP/MPI strategy for efficient parallelization. Thus, the assembly procedure of the right-hand side and the Jacobian matrix do not require communication between nodes. Otherwise, the solution of the algebraic system is performed using built-in iterative solvers and pre-conditioners, which need several communications during the matrix–vector products. In this last case, the MPI gather functions are used, as described by Löhner et al. [67].

4.1.2. Solution scheme

The solution scheme used to compute the numerical predictions of the current coupled displacement-phase field problem is summarized in Algorithm 2. Specifically, the global solution of the coupled problem is obtained via a modified iterative procedure based on the alternate minimization of the two primary fields. The particular modifications from standard staggered solution processes are introduced in the minimization of the PF in order to preclude the necessity of using a bound-constrained optimization solver, which greatly increases the computational costs of the solution procedure.

Moreover, it is worth remarking that the requirement of using these type of solvers arises from the irreversibly condition of the damage evolution imposed in the minimization of the PF in the bulk. Specifically, the strategy herein used is a combination of a posterior projection of the solution used by Lancioni and Royer-Carfagni [68] with a fixation of the solution for values close to 1, which is similar to that employed by Bourdin et al. [15]. In this sense, the solution of PF at the current time step is firstly obtained by solving the unconstrained minimization problem, (step 6). Then, it is imposed that the current solution cannot be smaller than the one at the beginning of the current time step (step 7). Finally, the projected solution of PF is set to 1 wherever it is greater than a threshold value close to 1 (step 8). For the current work, this threshold is considered as 0.95. As pointed out by Amor et al. [54], the posterior projection performed in (step 7) ensures the irreversibly condition of the damage evolution, but it cannot guarantee that the solution found is the global minimum of the constrained problem. However, according to their numerical experiments, there is no significant difference between the results obtained using a bound-constrained optimization solver and the posteriori strategy. Finally, it is worth mentioning that in the related literature, at present, there are alternative solution schemes, such as the so-called over-relaxed alternate minimization proposed by Farrel and Maurini [69] or the primal–dual active set method and predictor–corrector mesh adaptivity used by Heister and coworkers [70], among many others. The numerical performance of these solution schemes with respect to that proposed here, will be a matter of future investigations.

4.2. Verification examples: Mode I and II delamination tests

In this section, two simple simulations are performed to demonstrate that the proposed formulation preserves the original qualities of the cohesive zone model to capture those failure cases driven purely by delamination. The purpose of these tests also encompasses the assessment of the implementation of the cohesive model proposed in [47] in HPC environments. In this sense, the specimen depicted in Fig. 3 is simulated considering a Double Cantilever Beam (DCB) configuration as well as an End-Notched Flexural (ENF) one.

Regarding the material, the specimen consists of unidirectional carbon fiber reinforced plies, whose material properties can be found in [47]. The specimen is discretized using a 2D structured mesh conformed by 4-node isoparametric finite elements, whose characteristic element size is 0.15×0.13 mm^2 at the bulk region and 0.15×0.001 mm^2 at the interface region. This leads to a domain formed by a mesh of 17,350 elements. Finally, the boundary conditions corresponding to each configuration are also illustrated in Fig. 3.

Algorithm 2 Solution scheme: quasi-alternate minimization with posteriori projection.

Let the subscript t and $t-1$ denote the quantities at the current and previous pseudo-time steps along the simulation, respectively. Hence, $(\mathbf{u}_{t-1}, \phi_{t-1})$ is the initial solution of the displacement and the phase field at the beginning of the current time step before applying the Dirichlet–Neumann boundary conditions. Then, $(\mathbf{u}_t, \phi_t)$ is the solution of the primary fields at the current time step, which is evaluated for a fixed tolerance $s_{\max}$ and phase field threshold $\phi_{\text{threshold}}$ with the following iterative procedure:

Input: $\mathbf{u}_{t-1}$, ϕ_{t-1}, $\phi_{\text{threshold}}$, $s_{\max}$

Output: $\mathbf{u}_t$, ϕ_t

1: Initialize $(\epsilon, p) = (1, 0)$
2: Set $\left(\mathbf{u}^{(0)}, \phi^{(0)}\right) = (\mathbf{u}_{t-1}, \phi_{t-1})$
3: While $s \geq s_{\max}$ do
4: Increase iteration counter: $p = p + 1$.
5: Compute $\mathbf{u}^{(p)}$ by the minimization of $\Pi(\mathbf{u}^{(p-1)}, \phi^{(p-1)})$ subjected to boundary conditions at fixed ϕ .
6: Compute $\phi^{(p)}$ by the minimization of $\Pi(\mathbf{u}^{p}, \phi^{(p-1)})$ at fixed $\mathbf{u}$.
7: Impose irreversibly condition by setting $\phi^{(p)} = \phi^{(0)}$ wherever $\phi^{(p)} \leq \phi^{(0)}$.
8: Impose fully damage condition by setting $\phi^{(p)} = 1$ wherever $\phi^{(p)} \geq \phi_{\text{threshold}}$.
9: Compute current residual: $s = \left\| \phi^{(p)} - \phi^{(p-1)} \right\|_{\infty}$.
10: Set $(\mathbf{u}_t, \phi_t) = \left(\mathbf{u}^{(p)}, \phi^{(p)}\right)$

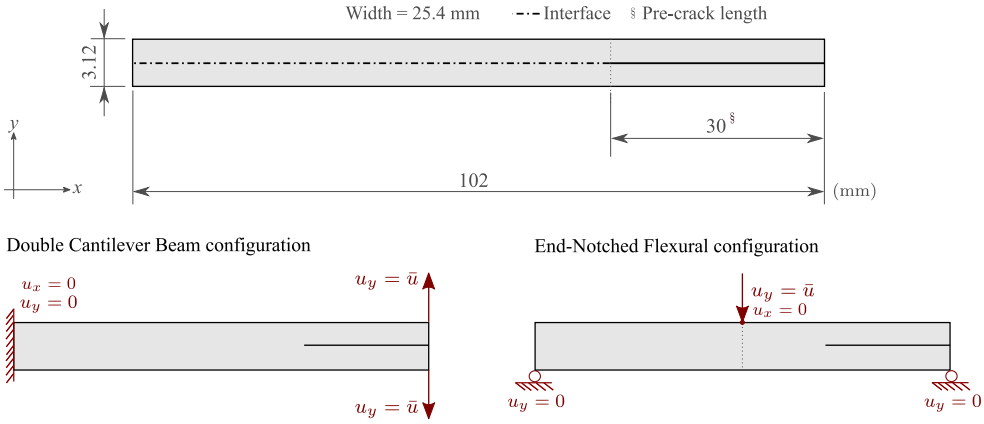

Fig. 3. Pure delamination tests: Geometry and boundary conditions for the DCB and ENF configurations.

The load versus displacement curve for the DCB and ENF predicted by the current framework and the Linear Elastic Fracture Mechanics (LEFM) theory are shown in Fig. 4. As can be appreciated, both predictions display an excellent agreement with respect to LEFM results. It should be pointed that for this investigation several configurations with different $(\phi_{\min}, \phi_{\max})$ have been investigated without any noticeable differences in the corresponding response. In this analysis, the bulk region is not affected by the opening of the interface thanks to the driving force that governs the increase of the PF in the proposed formulation is not affected when the failure is driven purely by a delamination mechanism. Thus, it is expected that the current framework can be used in those cases that have previously been analyzed with the original CZM.

4.3. Representative application: 4-points bending test

In this section, a four-point bending test is investigated to show the capabilities of the current framework to model the delamination induced by the cracking of the matrix. The specimen considered is a $[90_4/0_7/90_4]$ cross-ply laminate made from HTA/6376 carbon fiber-reinforced plies, which was experimentally studied by Mortell et al. [63]. The description of the geometric disposals and dimensions are depicted in Fig. 5, while the mechanical properties of the unidirectional ply and interface are listed in Table 1.

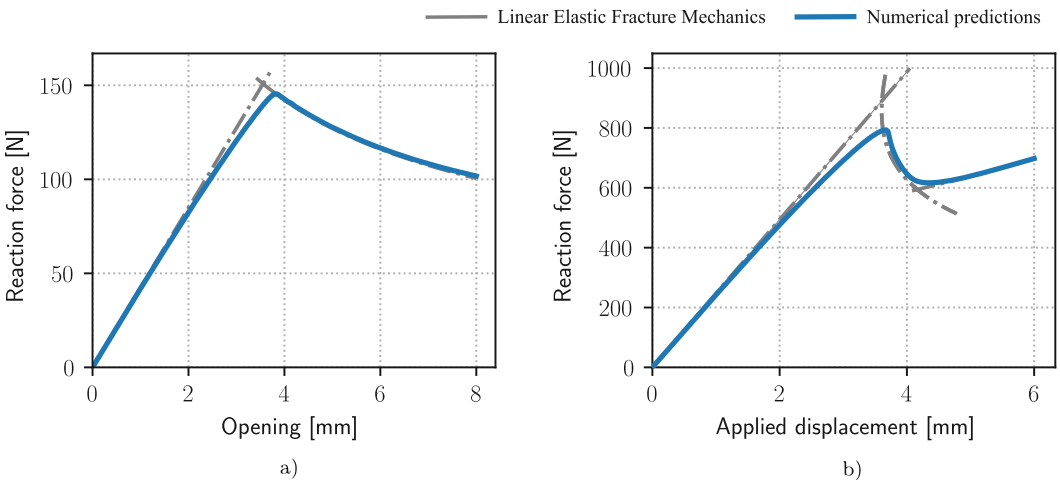

Fig. 4. Pure delamination response curves: (a) DCB and (b) ENF configurations.

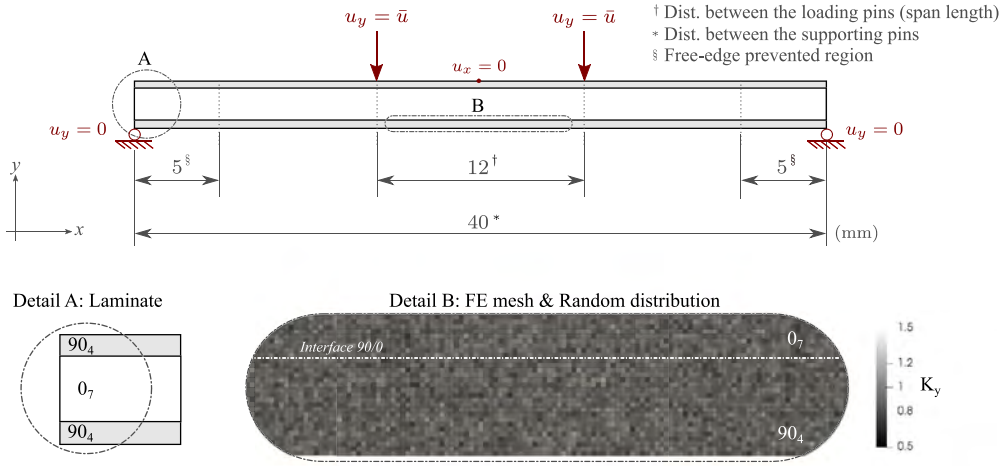

Fig. 5. 4PBT scheme: Geometry, boundary conditions and details of the FE mesh with the random distribution. The nominal strength at the elemental level is defined as $Y_T = K_Y Y_{0,T}$.

Regarding the computational method, the domain is approximated using a 2D structured mesh conformed by 4-node isoparametrical finite elements whose characteristic element size is 0.05 x 0.05 mm^2 at the bulk region and 0.05 x 0.001 mm^2 at the interface. This leads to a mesh of 124,800 elements and 374,400 degrees of freedom. According to the experimental setup, the loading and support conditions can be applied by modeling the contact between the specimen and steel pins as performed by Reiner et al. [64]. However, in the current application, the boundary conditions are applied as point displacements at the positions illustrated in Fig. 5. The loading is smoothly applied until a total vertical displacement of $\bar{u} = 6$ mm is reached.

In addition to the aforementioned numerical setup, two more aspects, which are related to the material properties, must be considered:

- The first issue concerns the uniformity of the stress field that takes place along the length between loading pins (span length) due to a constant moment region [63,64]. From a numerical point of view, this situation provokes the failure onset being able to initiated at any arbitrary location along the span length because the PF will

Table 2
4PBT: FE models considered to justify the coupling strategy.

Label	Bulk	Interface	Coupling
ELASTIC	Elastic	Elastic	–
CZM	Elastic	CZM	–
PF–CZM	PF	CZM	Off
PF–CZM (COU)	PF	CZM	On

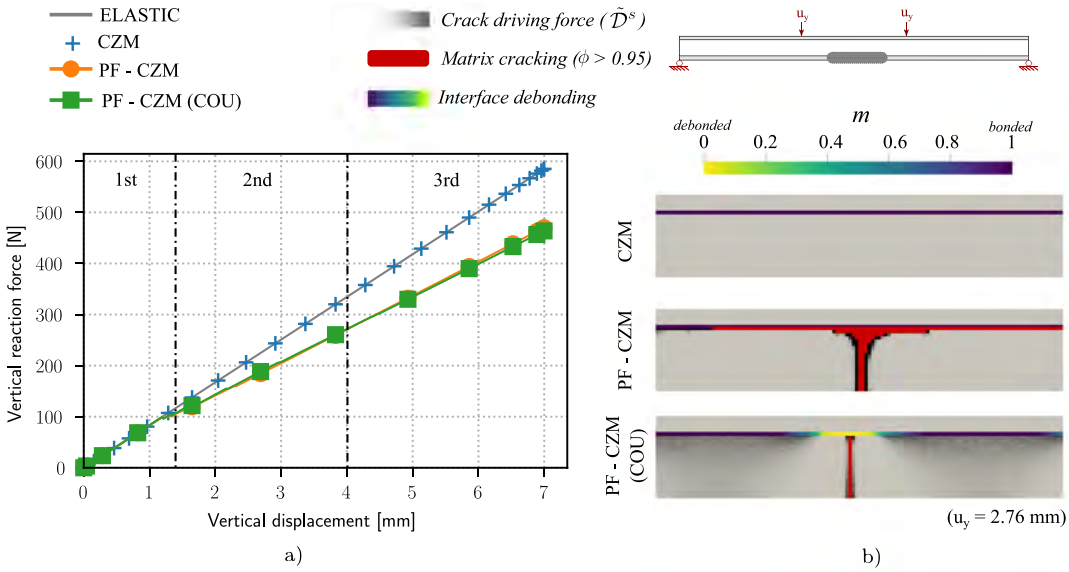

Fig. 6. 4PBT results: (a) vertical reaction–displacement curve predicted four approaches: (i) elastic, (ii) CZM, (iii) CZM and PF without coupling and (iv) CZM and PF with coupling, (b) fracture pattern around a transverse crack for approaches (ii)–(iv). The gray-scale color map illustrates the crack driving force of the transverse cracks, the red color represents fully damaged elements (i.e. wherever $\phi \geq 0.95$) and in the blue-to-yellow colored map the interface debonding in accordance with the integrity function m. Warping scale = 0. (For interpretation of the references to color in this figure legend, the reader is referred to the web version of this article.)

tend to simultaneous and homogeneous growth, only affected by the round-off errors. In turn, this precludes the correct localization of the strain affecting the reliability of the predictions. In this work, this limitation is originally overcome by defining a random field in the finite element mesh affecting only the transverse strength. The correct application of any alternative statistically-based distribution of the corresponding material strength can be considered in forthcoming investigations. Nevertheless, to illustrate this issue of random field by accounting for and complying with the objectives of the current work, a normal distribution with a coefficient of variance of 10% is applied, see Fig. 5.

- The second aspect concerns the sensitivity of the delamination onset close to the free-edges. It is well known that the mismatch between the Poisson ratios of the plies infers a stress concentration at the interfaces triggering delamination [71]. This issue can be prevented by increasing the fracture toughness of the interface at the regions close to the free-edges as illustrated in Fig. 5.

As a starting point of the analysis, the need for a coupling strategy between the PF and CZM approaches to capture the delamination induced by matrix cracking is justified. For this purpose, the 4PBT is simulated considering four different FE models, which are listed in Table 2. The fully elastic case is considered here as a reference case, whereas the CZM one is used to illustrate that the delamination is only induced by the transverse cracks. Fig. 6a shows the reaction force at the supports as a function of the applied displacement. From this figure, it can be seen that the curve predicted by the FEM model using only CZM case does not differ from the fully elastic one.

Otherwise, a change of slope is predicted by those FE models that use the PF in the bulk region, indicating the onset of transverse cracks.

Focusing on the interaction of a transverse crack when it impinges the interface, it is observed that the delamination onset only occurs in the FE model using the coupling strategy between the PF and CZM, see Fig. 6b. In the FE model without the coupling strategy, the PF grows parallel to the interface because of the difference in the elastic properties between the 90 and 0 plies. In fact, this mismatch combined with the impossibility of the stresses to relax induces an increase of the PF driving force close to the interface. Moreover, it is noted that without the coupling strategy the crack density is lower than that corresponding to the experimental observations. Therefore, based on this discussion, the coupling strategy becomes a required feature in order to capture the experimental evidence which is characterized by a very complex failure scenario combining intralaminar and interlaminar failure events.

Next, the influence of the $\mathcal{G}_c/\ell$ in Eq. (14) is examined by comparing the stiffness loss in the load direction as a function of the applied displacement for $\mathcal{G}_c/\ell = 0.5, 1, 5, 10, 100$. The normalized curves are plotted in Fig. 7a. Low values of $\mathcal{G}_c/\ell$ induce a more pronounced stiffness loss. This trend is because of the contribution of interface in the driving force of the PF increases as $\mathcal{G}_c/\ell$ decreases affecting the 0 plies. In this sense, if $\mathcal{G}_c/\ell$ is fixed, it plays a role as a scale factor between both contributions: the bulk and interface. To illustrate the affectation of the central plies, the PF across specimen thickness at the location of the first transverse crack is plotted in Fig. 7b. Notice that the PF value in the 0 plies is lower as increases $\mathcal{G}_c/\ell$. Another observation associated with this parameter is related to the onset of the delamination and the crack density. It is observed that the interface debonding takes place prematurely for low values of $\mathcal{G}_c/\ell$. In turn, a relaxation of the stress occurs precluding the onset of new transverse cracks. This observation is shown in Fig. 7c. As can be appreciated, no significant differences regarding the fracture pattern take places for $\mathcal{G}_c/\ell > 5$. Accordingly, in the following, the $\mathcal{G}_c/\ell = 10$ case is analyzed by comparing the numerical predictions against the experimental data.

Compared with the experimental observations the failure sequence predicted is in agreement with the one reported by Mortell et al. [63]. In the following, the curve predicted by the FE model with the coupling strategy depicted in Fig. 6 is taken as guideline with which to compare the results. In the first stage, the curve displays a quasi-elastic evolution up to the onset of the cracking of the bottom plies. The average stress level at the span length of the outermost ply at first transverse crack initiation predicted (67.5 MPa), which is in close agreement with the experimental findings. Analyzing the failure sequence, the transverse cracking is provoked by a macro-crack that rapidly grows from the bottom edge of the 90 to the 0 plies impinging the 0/90 interface with a micro-delamination, but not reaching the intralaminar region of the central 0 plies. After that, in the second stage, the slope of the curve decreases gradually due to the onset of several transverse cracks across the span length. As expected, the new cracks are predicted to be initiated at the center of the span between existing cracks. This is a direct consequence of the fact that it corresponds to the location where the maximum stress occurs since it is outside the free-stress region, see Fig. 8. Note also that this relaxed zone is confined in the typical triangular zone [72,73].

In line with the previous discussion, the number of transverse cracks in which the crack length saturates (6 cracks) and the total number of transverse cracks between the supporting pins at the end before the final collapse (14 cracks) are in reasonable agreement with the experimental observations. In addition, the average space between cracks at the end of the simulation (2.25 mm) is close to that recorded in the experiments.

Finally, the third stage commences with the coalescence of the micro-delaminations that debounds the interface which, in turn, triggers the catastrophic collapse of the specimen. Table 3 lists the correlation between the experimental values and the numerical predictions using the proposed PF–CZM coupling method.

Another interesting phenomenon observed in the experiments is with regard to delamination growth as a function of the horizontal location of the transverse crack associated with its triggering. Mortell et al. [63] found that the delamination grows more asymmetrically with respect to the transverse crack far from the center of the specimen than close to it. Moreover, they observed that the preferred direction for the growth is away from the center of the span length. As can be appreciated in Figs. 8 and 9, this behavior has been correctly captured by the current simulations.

Finally, it should be pointed that Mortell et al. [63] also observed that not all the transverse cracks initiate micro-delamination. With the current numerical setup, this behavior is not captured because all transverse cracks damage the interface when they impinge on it. This phenomenon could be modeled by defining a random field for the PF couplings parameters. However, this is not a critical point in the current study.

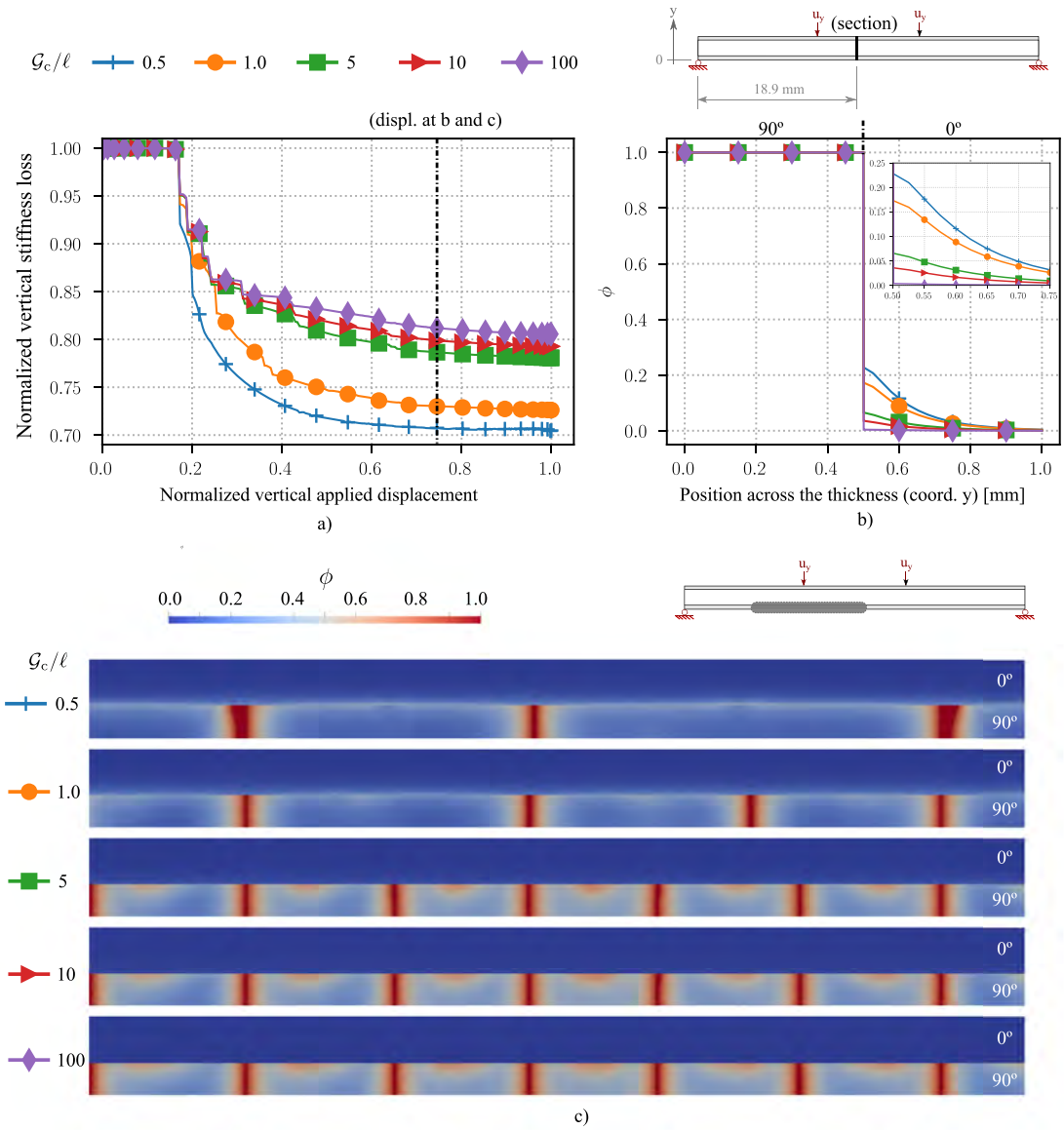

Fig. 7. 4PBT results: study of $\mathcal{G}_c/\ell$ influence for 0.5, 1, 5, 10, 100: (a) loss of vertical rigidity–normalized applied displacement, (b) PF through the specimen thickness, and (c) crack pattern (PF). Warping scale = 0.

5. Conclusions

In the present work, a novel PF–CZM numerical method has been developed to model the delamination induced by matrix cracks in long fiber composite materials.

The current method is characterized by considering the anisotropic PF formulation for the intralaminar damage proposed by Quintanas-Corominas et al. [40], which has been coupled with the cohesive zone model formulation developed by Turon et al. [47]. For this purpose, an alternative coupling strategy between the PF method and the CZM for heterogeneous media with respect to that outlined in [41] has been formulated according to the fundamental aspects of both approaches. In particular, the integrity function of the CZM, which defines the loss of

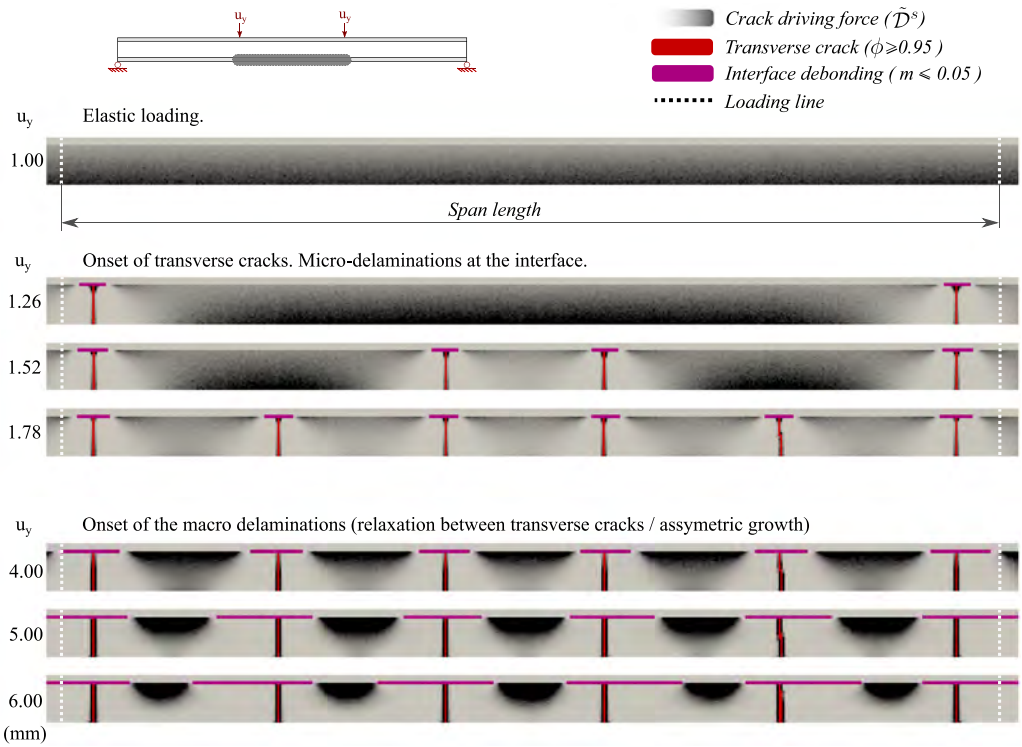

Fig. 8. 4PBT results: Fracture pattern of the bottom 90 plies in the span-length region for different applied vertical displacements. The gray-scale color palette illustrates the crack driving force of the transverse cracks, the purple color represents the interface debonding (i.e. wherever $m \leq 0.05$) and the red color represents the transverse cracks (i.e. wherever $\phi \geq 0.95$). Warping scale = 0. (For interpretation of the references to color in this figure legend, the reader is referred to the web version of this article.)

Table 3
4PBT results: Quantitative comparison of the numerical predictions and the experimental observations found by Mortell and co-workers [63,64].

Observation	Experimental	Numerical	Units
Onset of the first transverse crack[a]	62	67.5	MPa
Transverse cracks saturation[a]	0.7	0.5	crack/mm
Total number of cracks[b]	15	14	–
Average space between cracks[b]	2	2.25	mm

[a]Between the loading pins (span length).
[b]Between the supporting pins.

interface rigidity, has been modified, considering the role of the bulk PF variable in the interface response through the definition of a suitable coupling function. The proposed framework has been implemented in the Alya FE code [66].

The capabilities of the proposed formulation have been demonstrated by means of several examples which included the verification of the current interface model in HPC environments and the simulation of a 4-Points Bending Test. The obtained numerical predictions showed that the general trend regarding the failure sequence was correctly captured by the proposed modeling method. Moreover, a direct comparison with experimental observations demonstrated that the proposed framework was also capable of capturing the onset and number of transverse cracks. Finally, the need for a coupling strategy between the CZM and the PF approach to correctly capture the delamination induced by transverse cracking has been shown.

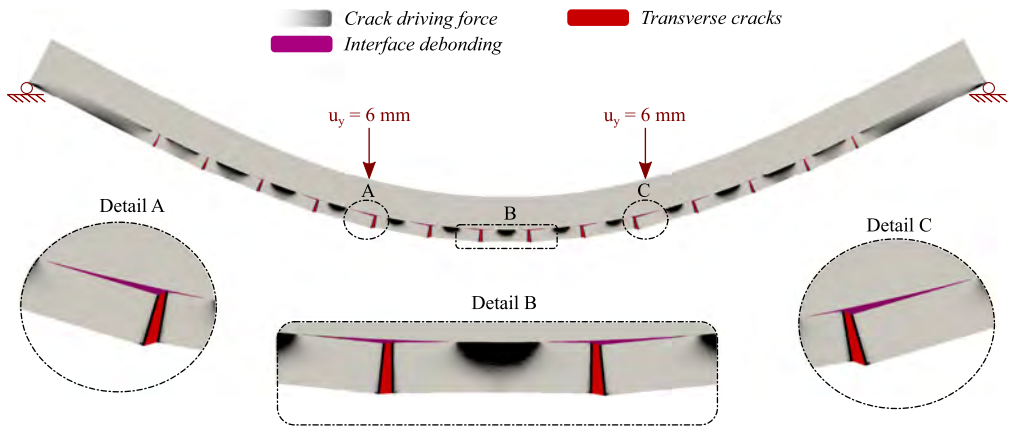

Fig. 9. 4PBT results: Fracture pattern for an applied vertical displacement of 6 mm. The gray-scale color map illustrates the crack driving force of the transverse cracks, whereas the red color represents a fully damage elements (i.e. wherever $\phi \geq 0.95$). Warping scale = 1.

In light of the previous arguments, the formulation herein presented is expected to provide a suitable modeling framework for other engineering problems concerning progressive failure analysis in long fiber composite materials. Future developments might regard the extension of the current framework for performing 3-dimensional simulations of more complex loading scenarios, such as Double-Notched or Open Hole under tensile loading, in conjunction with the incorporation of mesh-adaptive schemes as those proposed in [74,75] among others, in order to preserve the computational efficiency. In those cases, the approach here presented could be combined with the proposal of Belyer and Alessi [39] to include several phase field variables, achieving a better representation of the different failure mechanisms.

Acknowledgments

The Government of Spain has partially funded this work through Ministerio de Educación, Cultura y Deporte under the grant FPU15/06287, Ministerio de Economía y Competitividad under the contract MAT2015-71036-P, and Ministerio de Economía y Empresa under the contract RTI2018-099373-B-I00. JR would like to thank the Consejería de Economía y Conocimiento of the Junta de Andalucía (Spain) for financial support under the contract US-1265577 that belongs to the Programa Operativo FEDER Andalucía 2014-2020. MP would like to acknowledge the financial support from the Italian Ministry of Education, University and Research (MIUR) to the research project of relevant national interest (PRIN 2017) "XFAST-SIMS: Extra fast and accurate simulation of complex structural systems" (Prot. 20173C478N). Finally, the authors would like to thank the Red Española de Surpercomputación for giving access to the supercomputer MareNostrum IV based in Barcelona (Spain) through the project FI-2018-3-0022.

Appendix A. Thermodynamic consistency

The thermodynamic consistency of the coupling proposed here is ensured by means of the Clausius–Duhem inequality. Thus, the thermodynamic irreversible condition of the damage process holds if the rate of energy dissipation is positive, i.e.

$$\mathbf{Y} \cdot \dot{\boldsymbol{\mathcal{D}}} \geq 0 \tag{A.1}$$

where $\mathbf{Y}$ is the thermodynamic forces vector conjugated to a set of internal damage variables $\boldsymbol{\mathcal{D}}$ accounting for the dissipative mechanisms. Considering the formulation herein proposed, two internal state variables are defined to measure the damage threshold associated to the displacement and phase fields, which are denoted by r_{Δ} and r_{ϕ}, respectively. It is worth mentioning that the mixed-mode ratio does not affect the damage state as demonstrated by [47] and therefore, it is not considered in the following derivations. Then, the previous inequality can be expressed as:

$$\mathbf{Y} = [-\partial_{m_{\Delta}} \Psi_{\mathrm{i}}, -\partial_{m_{\phi}} \Psi_{\mathrm{i}}]^T \tag{A.2}$$

$$\dot{\mathcal{D}} = [\dot{r}_{\mathbf{\Delta}}, \dot{r}_{\phi}] \tag{A.3}$$

which, after some algebraic manipulations, is reduced to

$$-\Psi_{\text{i,ela}} \left(m_{\phi} \frac{\partial m_{\Delta}}{\partial r_{\Delta}} \dot{r}_{\mathbf{\Delta}} + m_{\Delta} \frac{\partial m_{\phi}}{\partial r_{\phi}} \dot{r}_{\phi} \right) \geq 0 \tag{A.4}$$

Recalling the demonstration presented by Turon et al. [47] and considering that $m_{\phi} \geq 0$, the first term in the parenthesis is always less than or equal to zero. Hence, the second term should be also less than or equal to zero in order to ensure a positive rate of energy dissipation, i.e.

$$m_{\Delta} \frac{\partial m_{\phi}}{\partial r_{\phi}} \dot{r}_{\phi} \leq 0 \tag{A.5}$$

where, in light of the expressions summarized in Algorithm 1, it is postulated that

$$m_{\Delta} = 1 - \frac{r_{\mathcal{D}} \lambda_{\text{c}}}{r_{\mathcal{D}} \lambda_{\text{c}} + (1 - r_{\mathcal{D}}) \lambda_{\text{o}}} \geq 0 \tag{A.6}$$

$$\frac{\partial m_{\phi}}{\partial r_{\phi}} = -2(1 - r_{\phi}) \qquad \leq 0 \tag{A.7}$$

At this point, the thermodynamic consistency of the proposed formulation holds thanks to the irreversibly conditions imposed on the damage threshold associated to the phase field variable Eq. (37), i.e. stating that $\dot{r}_{\phi} \geq 0$.

Appendix B. Complex-step derivative approximation

The Complex-Step Derivative Approximation (CSDA) is used in the current framework to obtain the tangent operator of the material models [60]. When compared to the classical difference approximation, CSDA is more robust than the perturbation parameter h, but it is also more expensive computationally.

Outlining the concept of CSDA, the derivative of a scalar function f can be approximated by perturbing its argument x along the imaginary axis. Thus, the Taylor series expansion of the function around the perturbation is expressed as:

$$f(x + ih) = f(x) + ihf'(x) + \mathcal{O}(x^2) \tag{B.1}$$

where h is the perturbation and $i^2 = -1$ is the imaginary unit number. Then, discarding the high order terms $\mathcal{O}(x^2)$, the first derivative can be approximated as:

$$f'(x) \approx \frac{\text{Im}[f(x + ih)]}{h} \tag{B.2}$$

where Im[•] is an operator that takes only the imaginary part of the argument. Note that, unlike the traditional method, h can be very small thanks to the above operation is not being subjected to subtractive cancellation [76]. However, the order of the approximation is the same, i.e. $\mathcal{O}(x^2)$.

According to Tanaka and coworkers [77], this concept of CSDA can be extended to directional derivatives of vector fields which, in turn, allows the method for the approximation of the tangent derivative of a material model to be applied. For instance, considering a 2-dimensional analysis and adopting the Voigt notation, the material tangent operator for the bulk region can be explicitly represented as:

$$\mathbb{C} = \frac{\partial \boldsymbol{\sigma}}{\partial \boldsymbol{\varepsilon}} \approx \frac{1}{h} \begin{bmatrix} \text{Im}[\sigma_{11}(\boldsymbol{\varepsilon} + ih\tilde{\boldsymbol{\varepsilon}}_{(11)})] & \text{Im}[\sigma_{11}(\boldsymbol{\varepsilon} + ih\tilde{\boldsymbol{\varepsilon}}_{(22)})] & \text{Im}[\sigma_{11}(\boldsymbol{\varepsilon} + ih\tilde{\boldsymbol{\varepsilon}}_{(12)})] \\ \text{Im}[\sigma_{22}(\boldsymbol{\varepsilon} + ih\tilde{\boldsymbol{\varepsilon}}_{(11)})] & \text{Im}[\sigma_{22}(\boldsymbol{\varepsilon} + ih\tilde{\boldsymbol{\varepsilon}}_{(22)})] & \text{Im}[\sigma_{22}(\boldsymbol{\varepsilon} + ih\tilde{\boldsymbol{\varepsilon}}_{(12)})] \\ \text{Im}[\sigma_{12}(\boldsymbol{\varepsilon} + ih\tilde{\boldsymbol{\varepsilon}}_{(11)})] & \text{Im}[\sigma_{12}(\boldsymbol{\varepsilon} + ih\tilde{\boldsymbol{\varepsilon}}_{(22)})] & \text{Im}[\sigma_{12}(\boldsymbol{\varepsilon} + ih\tilde{\boldsymbol{\varepsilon}}_{(12)})] \end{bmatrix} \tag{B.3}$$

where $\tilde{\boldsymbol{\varepsilon}}_{(ij)} = \{\delta_{1(i)}\delta_{1(j)} \quad \delta_{2(i)}\delta_{2(j)} \quad \delta_{1(i)}\delta_{2(j)}\}^T$ is the directional perturbation vectors and δ_{ij} is the Kronecker delta. In turn, the material operator for the cohesive zone model reads as:

$$\mathbb{D} = \frac{\partial \boldsymbol{\tau}}{\partial \mathbf{\Delta}} \approx \frac{1}{h} \begin{bmatrix} \text{Im}[\tau_1(\mathbf{\Delta} + ih\mathbf{g}_{(11)})] & \text{Im}[\tau_1(\mathbf{\Delta} + ih\mathbf{g}_{(22)})] \\ \text{Im}[\tau_2(\mathbf{\Delta} + ih\mathbf{g}_{(11)})] & \text{Im}[\tau_2(\mathbf{\Delta} + ih\mathbf{g}_{(22)})] \end{bmatrix} \tag{B.4}$$

where $\mathbf{g}_{(ij)} = \{\delta_{1(i)}\delta_{1(j)} \quad \delta_{2(i)}\delta_{2(j)}\}^T$.

References

[1] P. Maimí, P.P. Camanho, J.A. Mayugo, C.G. Dávila, A continuum damage model for composite laminates: Part I – Constitutive model, Mech. Mater. 39 (10) (2007) 897–908.

[2] P. Maimí, P.P. Camanho, J.A. Mayugo, C.G. Dávila, A continuum damage model for composite laminates: Part II – Computational implementation and validation, Mech. Mater. 39 (10) (2007) 909–919.

[3] J. Reinoso, G. Catalanotti, A. Blázquez, P. Areias, P.P. Camanho, F. París, A consistent anisotropic damage model for laminated fiber-reinforced composites using the 3d-version of the puck failure criterion, Int. J. Solids Struct. (2017) 37–53.

[4] A. Quintanas-Corominas, P. Maimí, E. Casoni, A. Turon, J.A. Mayugo, G. Guillamet, M. Vázquez, A 3D transversally isotropic constitutive model for advanced composites implemented in a high performance computing code, Eur. J. Mech. A Solids 71 (2018) 278–291.

[5] M. Ortiz, A. Pandolfi, Finite deformation irreversible cohesive elements for three-dimensional crack-propagation analysis, Internat. J. Numer. Methods Engrg. 44 (1999) 1267–1282.

[6] A. Turon, P.P. Camanho, J. Costa, C.G. Dávila, A damage model for the simulation of delamination in advanced composites under variable-mode loading, Mech. Mater. 38 (11) (2006) 1072–1089.

[7] P.P. Camanho, C.G. Davila, M.F. de Moura, Numerical simulation of mixed-mode progressive delamination in composite materials, J. Compos. Mater. 37 (16) (2003) 1415–1438.

[8] A. Turon, P.P. Camanho, J. Costa, J. Renart, Accurate simulation of delamination growth under mixed-mode loading using cohesive elements: Definition of interlaminar strengths and elastic stiffness, Compos. Struct. 92 (8) (2010) 1857–1864.

[9] E.V. González, P. Maimí, J.R. Sainz de Aja, P. Cruz, P.P. Camanho, Effects of interply hybridization on the damage resistance and tolerance of composite laminates, Compos. Struct. 108 (2014) 319–331.

[10] A. Soto, E.V. González, P. Maimí, F. Martín de la Escalera, J.R. Sainz de Aja, E. Alvarez, Low velocity impact and compression after impact simulation of thin ply laminates, Composites A 109 (2018) 413–427.

[11] L. Carreras, E. Lindgaard, J. Renart, B.L.V. Bak, A. Turon, An evaluation of mode-decomposed energy release rates for arbitrarily shaped delamination fronts using cohesive elements, Comput. Methods Appl. Mech. Engrg. 347 (2019) 218–237.

[12] A. Sasikumar, J. Costa, D. Trias, E.V. González, S.M. García-Rodríguez, P. Maimí, Unsymmetrical stacking sequences as a novel approach to tailor damage resistance under out-of-plane impact loading, Compos. Sci. Technol. 173 (2019) 125–135.

[13] R.H.J. Peerlings, M.G.D. Geers, R. De, W.A.M. Brekelmans, A critical comparison of nonlocal and gradient-enhanced softening continua, Int. J. Solids Struct. 38 (2001) 7723–7746.

[14] G.A. Francfort, J.-J. Marigo, Revisiting brittle fracture as an energy minimization problem, J. Mech. Phys. Solids 46 (8) (1998) 1319–1342.

[15] B. Bourdin, G.A. Francfort, J.J. Marigo, Numerical experiments in revisited brittle fracture, J. Mech. Phys. Solids 48 (4) (2000) 797–826.

[16] B. Bourdin, G.A. Francfort, J.J. Marigo, The variational approach to fracture, J. Elasticity 91 (1) (2008) 5–148.

[17] C. Miehe, F. Welschinger, M. Hofacker, Thermodynamically consistent phase-field models of fracture: Variational principles and multi-field FE implementations, Internat. J. Numer. Methods Engrg. 83 (10) (2010) 1273–1311.

[18] M.J. Borden, C.V. Verhoosel, M.A. Scott, T. Hughes, C.M. Landis, A phase-field description of dynamic brittle fracture, Comput. Methods Appl. Mech. Engrg. 217–220 (8) (2012) 77–95.

[19] M. Hofacker, C. Miehe, A phase field model of dynamic fracture: Robust field updates for the analysis of complex crack patterns, Internat. J. Numer. Methods Engrg. 93 (2013) 276–301.

[20] M.F. Wheeler, T. Wick, W. Wollner, An augmented-lagrangian method for the phase-field approach for pressurized fractures, Comput. Methods Appl. Mech. Engrg. 271 (2014) 69–85.

[21] J. Reinoso, M. Paggi, C. Linder, Phase field modeling of brittle fracture for enhanced assumed strain shells at large deformations: formulation and finite element implementation, Comput. Mech. 59 (6) (2017) 981–1001.

[22] H. Ulmer, M. Hofacker, C. Miehe, Phase field modeling of brittle and ductile fracture, PAMM 13 (2013) 533–536.

[23] M. Ambati, T. Gerasimov, L. De Lorenzis, Phase-field modeling of ductile fracture, Comput. Mech. 55 (2015) 1017–1040.

[24] M. Ambati, L. De Lorenzis, Phase-field modeling of brittle and ductile fracture in shells with isogeometric nurbs-based solid-shell elements, Comput. Methods Appl. Mech. Engrg. 312 (2016) 351–373.

[25] R. Alessi, J.J. Marigo, C. Maurini, S. Vidoli, Coupling damage and plasticity for a phase-field regularisation of brittle, cohesive and ductile fracture: One-dimensional examples, Int. J. Mech. Sci. 149 (2018) 559–576.

[26] Z.A. Wilson, C.M. Landis, Phase-field modeling of hydraulic fracture, J. Mech. Phys. Solids 96 (2016) 264–290.

[27] E. Martínez-Pañeda, A. Golahmar, C.F. Niordson, A phase field formulation for hydrogen assisted cracking, Comput. Methods Appl. Mech. Engrg. 342 (2018) 742–761.

[28] C. Miehe, L. Schänzel, H. Ulmer, Phase field modeling of fracture in multi-physics problems. Part I. balance of crack surface and failure criteria for brittle crack propagation in thermo-elastic solids, Comput. Methods Appl. Mech. Engrg. 294 (2015) 449–485.

[29] C. Miehe, M. Hofacker, L.-M. Schänzel, F. Aldakheel, Phase field modeling of fracture in multi-physics problems. Part II. coupled brittle-to-ductile failure criteria and crack propagation in thermo-elastic–plastic solids, Comput. Methods Appl. Mech. Engrg. 294 (2015) 486–522.

[30] C. Miehe, S. Mauthe, Phase field modeling of fracture in multi-physics problems. part iii. crack driving forces in hydro-poro-elasticity and hydraulic fracturing of fluid-saturated porous media, Comput. Methods Appl. Mech. Eng. 304 (2016) 619–655.

[31] B. Li, C. Peco, D. Millán, I. Arias, M. Arroyo, Phase field modeling and simulation of fracture in brittle materials with strongly anisotropic surface energy, Internat. J. Numer. Methods Engrg. 102 (2014) 711–727.

[32] O. Gültekin, H. Dal, G.A. Holzapfel, A phase-field approach to model fracture of arterial walls: Theory and finite element analysis, Comput. Methods Appl. Mech. Engrg. 312 (2016) 542–566.
[33] X. Zhang, S.W. Sloan, C. Vignes, D. Sheng, A modification of the phase-field model for mixed mode crack propagation in rock-like materials, Comput. Methods Appl. Mech. Engrg. 322 (2017) 123–136.
[34] T. Tung, J. Réthoré, M.C. Baietto, Phase field modelling of anisotropic crack propagation, Eur. J. Mech. A Solids 65 (2017) 279–288.
[35] S. Teichtmeister, D. Kienle, F. Aldakheel, M.A. Keip, Phase field modeling of fracture in anisotropic brittle solids, Int. J. Non-Linear Mech. 97 (2017) 1–21.
[36] T.T. Nguyen, J. Réthoré, J. Yvonnet, M.C. Baietto, Multi-phase-field modeling of anisotropic crack propagation for polycrystalline materials, Comput. Mech. 60 (2) (2017) 289–314.
[37] E.G. Kakouris, S.P. Triantafyllou, Material point method for crack propagation in anisotropic media: a phase field approach, Arch. Appl. Mech. 88 (1) (2018) 287–316.
[38] J. Reinoso, A. Arteiro, M. Paggi, P.P. Camanho, Strength prediction of notched thin ply laminates using finite fracture mechanics and the phase field approach, Compos. Sci. Technol. 150 (2017) 205–216.
[39] J. Bleyer, R. Alessi, Phase-field modeling of anisotropic brittle fracture including several damage mechanisms, Comput. Methods Appl. Mech. Engrg. 336 (2018) 213–236.
[40] A. Quintanas-Corominas, J. Reinoso, E. Casoni, A. Turon, J.A. Mayugo, A phase field approach to simulate intralaminar and translaminar fracture in long fiber composite materials, Compos. Struct. (2019).
[41] M. Paggi, J. Reinoso, Revisiting the problem of a crack impinging on an interface:a modeling framework for the interaction between the phase field approach for brittle fracture and the interface cohesive zone model, Comput. Methods Appl. Mech. Engrg. 321 (2017) 145–172.
[42] V. Carollo, J. Reinoso, M. Paggi, A 3D finite strain model for intralayer and interlayer crack simulation coupling the phase field approach and cohesive zone model, Compos. Struct. 182 (2017) 636–651.
[43] V. Carollo, J. Reinoso, M. Paggi, Modeling complex crack paths in ceramic laminates: a novel variational framework combining the phase field method of fracture and the cohesive zone model, J. Eur. Ceram. Soc. 38 (8) (2018) 2994–3003.
[44] M. Paggi, M. Corrado, J. Reinoso, Fracture of solar-grade anisotropic polycrystalline silicon: A combined phase field–cohesive zone model approach, Comput. Methods Appl. Mech. Engrg. 330 (2018) 123–148.
[45] T. Guillén-Hernández, I.G. García, J. Reinoso, M. Paggi, A micromechanical analysis of inter-fiber failure in long reinforced composites based on the phase field approach of fracture combined with the cohesive zone model, Int. J. Fract. (under rev.) (2019).
[46] Kumchol Yun, Songhun Kwak, Zhenqing Wang, Mengzhou Chang, Jonggun Kim, Jingbiao Liu, Cholsu Ri, A damage model reflecting the interaction between delamination and intralaminar crack for failure analysis of frp laminates, Appl. Sci. 9 (2) (2019) https://www.mdpi.com/2076-3417/9/2/314.
[47] A. Turon, E.V. González, C. Sarrado, G. Guillamet, P. Maimí, Accurate simulation of delamination under mixed-mode loading using a cohesive model with a mode-dependent penalty stiffness, Compos. Struct. 184 (10–11) (2018) 506–511.
[48] T-T Nguyen, J Yvonnet, Q-Z Zhu, M Bornert, C Chateau, A phase-field method for computational modeling of interfacial damage interacting with crack propagation in realistic microstructures obtained by microtomography, Comput. Methods Appl. Mech. Engrg. 312 (2016) 567–595.
[49] T.-T. Nguyen, J. Yvonnet, M. Bornert, C. Chateau, Initiation and propagation of complex 3d networks of cracks in heterogeneous quasi-brittle materials: direct comparison between in situ testing-microct experiments and phase field simulations, J. Mech. Phys. Solids 95 (2016) 320–350.
[50] A. Griffith, The phenomena of rupture and flow in solids, Phil. Trans. R. Soc. Lond. Ser. A Contain. Pap. Math. Phys. Charact. 221 (1921) 163–198.
[51] L. Ambrosio, V.M. Tortorelli, Approximation of functional depending on jumps by elliptic functional via t-convergence, Comm. Pure Appl. Math. 43 (8) (1990) 999–1036.
[52] J.J. Marigo, M. Corrado, K. Pahm, An overview of the modelling of fracture by gradient damage models, Meccanica 51 (12) (2016) 3107–3128.
[53] A. Turon, C.G. Dávila, P.P. Camanho, J. Costa, An engineering solution for mesh size effects in the simulation of delamination using cohesive zone models, Eng. Fract. Mech. 74 (10) (2007) 1665–1682.
[54] H. Amor, J.J. Marigo, C. Maurini, Regularized formulation of the variational brittle fracture with unilateral contact: Numerical experiments, J. Mech. Phys. Solids 57 (2009) 1209–1229.
[55] T.J.R. Hughes, The Finite Element Method: Linear Static and Dynamic Finite Element Analysis, in: Dover Civil and Mechanical Engineering, Dover Publications, 2000.
[56] B.M. Irons, Engineering applications of numerical integration in stiffness methods, AIAA J. 11 (4) (1966) 2035—2037.
[57] M. Msekh, J.M. Sargado, M. Jamshidian, P. Areias, T. Rabczuk, Abaqus implementation of phase-field model for brittle fracture, Comput. Mater. Sci. 96 (12) (2015) 472–484.
[58] J. Reinoso, M. Paggi, A consistent interface element formulation for geometrical and material nonlinearities, Comput. Mech. 54 (2014) 1569–1581.
[59] M. Paggi, J. Reinoso, An anisotropic large displacement cohesive zone model for fibrillar and crazing interfaces, Int. J. Solids Struct. 69 (2015) 106–120.
[60] J.R.R.A. Martins, P. Sturdza, J.J. Alonso, The complex-step derivative approximation, ACM Trans. Math. Software 29 (3) (2003) 245–262.
[61] X. Martínez, S. Oller, F. Rastellini, A.H. Barbat, A numerical procedure simulating {RC} structures reinforced with {FRP} using the serialparallel mixing theory, Computers & Structures 86 (2008) 1604–1618.

[62] M.L. Benzeggagh, M. Kenane, Measurement of mixed-mode delamination fracture toughness of unidirectional glass/epoxy composites with mixed-mode bending apparatus, Compos. Sci. Technol. 56 (4) (1996) 439–449.
[63] D.J. Mortell, D.A. Tanner, C.T. McCarthy, In-situ sem study of transverse cracking and delamination in laminated composite materials, Compos. Sci. Technol. 105 (2014) 118–126.
[64] J. Reiner, M. Veidt, M. Dargusch, L. Gross, A progressive analysis of matrix cracking-induced delamination in composite laminates using an advanced phantom node method, J. Compos. Mater. 51 (20) (2017) 2933–2947.
[65] E. Casoni, A. Jérusalem, C. Samaniego, B. Eguzkitza, P. Lafortune, D.D. Tjahjanto, X. Sáez, G. Houzeaux, M. Vázquez, Alya: Computational solid mechanics for supercomputers, Arch. Comput. Methods Eng. 22 (2014) 557–576.
[66] M. Vázquez, G. Houzeaux, S. Koric, A. Artigues, J. Aguado-Sierra, R. Arís, D. Mira, H. Calmet, F. Cucchietti, H. Owen, A. Taha, E. Derin, J.M. Cela, M. Valero, Alya: Multiphysics engineering simulation toward exascale, J. Comput. Sci. 14 (2016) 15–27.
[67] R. Löhner, F. Mut, J.R. Cebral, R. Aubry, G. Houzeaux, Deflated preconditioned conjugate gradient solvers for the pressure-poisson equation: Extensions and improvements, Internat. J. Numer. Methods Engrg. 87 (2011) 2–14.
[68] G. Lancioni, G. Royer-Carfagni, The variational approach to fracture mechanics. A practical application to the French Panthéon in Paris, J. Elasticity 95 (1) (2009) 1–30.
[69] P. Farrell, C. Maurini, Linear and nonlinear solvers for variational phase-field models of brittle fracture, Int. J. Numer. Methods Eng. 109 (5) (2017) 648–667.
[70] T. Heister, M.F. Wheeler, T. Wick, A primal-dual active set method and predictor-corrector mesh adaptivity for computing fracture propagation using a phase-field approach, Comput. Methods Appl. Mech. Engrg. 290 (2015) 466–495.
[71] G. Guillamet, A. Turon, J. Costa, P. Linde, A quick procedure to predict free-edge delamination in thin-ply laminates under tension, Eng. Fract. Mech. 168, Part B (2016) 28–39.
[72] J.A. Mayugo, P.P. Camanho, P. Maimí, C.G. Dávila, Analytical modelling of transverse matrix cracking of 0/90ns composite laminates under multiaxial loading, Mech. Adv. Mater. Struct. 17 (4) (2010) 237–245.
[73] P. Maimí, P.P. Camanho, J.A. Mayugo, A. Turon, Matrix cracking and delamination in laminated composites. Part I: Ply constitutive law, first ply failure and onset of delamination, Mech. Mater. 43 (4) (2011) 169–185.
[74] H. Badnava, M.A. Msekh, E. Etemadi, T. Rabczuk, An h-adaptive thermo-mechanical phase field model for fracture, Finite Elem. Anal. Des. 138 (4) (2018) 31–47.
[75] Hirshikesh, A.L.N. Pramod, R.K. Annabattula, E.T. Ooi, C. Song, S. Natarajan, Adaptive phase-field modeling of brittle fracture using the scaled boundary finite element method, Comput. Methods Appl. Mech. Engrg. 355 (2019) 284–307.
[76] S. Kim, J. Ryu, M. Cho, Numerically generated tangent stiffness matrices using the complex variable derivative method for nonlinear structural analysis, Comput. Methods Appl. Mech. Engrg. 200 (1) (2011) 403–413.
[77] M. Tanaka, M. Fujikawa, D. Balzani, J. Schr oder, Robust numerical calculation of tangent moduli at finite strains based on complex-step derivative approximation and its application to localization analysis, Comput. Methods Appl. Mech. Engrg. 269 (2014) 454–470.